NATIONAL SCIENCE FOUNDATION

Journal

of the

National Science Foundation of Sri Lanka

www.nsf.gov.lk

CONTENTS

Guidelines for Contributors

Journal
of the
National Science Foundation
of Sri Lanka

Cover: Top left: Oval and completely confluent dorsal blotch pattern of Russell's viper (*Daboia russelli*). Bottom left: Oval and completely separated dorsal blotch pattern of Russell's viper (*Daboia russelli*). Top right: Fangs of Russell's viper (*Daboia russelli*). Middle right: A closer view of the scales on the lateral head of Russell's viper (*Daboia russelli*). Bottom right: Scales of the lateral head of Russell's viper (*Daboia russelli*).
See *J.Natn.Sci.Foundation Sri Lanka* 2024 **52**(2): 125 – 156

EDITORIAL

Scientific literacy in the age of misinformation

Many of the important issues that confront society today such as, mitigating climate change, alternative energy sources, genetically modified organisms and the use of pesticides and weedicides in agriculture, require the general public to possess scientific literacy to understand and decide amongst different proposals presented by policy makers and politicians. However, it is clear that in today's world, scientific literacy which is limited only to a knowledge of some basic theories and facts regarding the natural world does not enable society to take reasonable decisions on these issues.

This is mainly due to the fact that the controls that existed in the flow of scientific information, such as boards of scientific and academic organizations, editors and knowledgeable science journalists are now being by-passed via social media and the internet. Various ideological and political campaigns are now behind much of what passes as "science". Fidelity to the truth is no longer a concern. The anti-vaccine drive in many technologically advanced countries during the Covid-19 pandemic, and the banning of chemical fertilizers in Sri Lanka in 2021 stand as illustrative examples. An unfortunate by-product of the digital revolution has been the current age of misinformation.

While the implications of these developments for democracy and freedom of expression are being debated, it is evident that being a scientifically literate person implies the ability to evaluate the trustworthiness of science related information that is so readily available on the internet. The different fields of science are so highly specialized today, that it may not be possible even for a scientist to evaluate the evidence for a particular claim outside one's own specialty with certainty. Thus, the starting point for both scientists and the general public has to be to assess the trustworthiness of their sources of information. This may not be as straightforward as it seems, but the kinds of questions that should be looked into are conflict of interest, ideological bias, credentials for expertise and level of agreement with other experts in the field. Being able to evaluate 'who' is making a claim becomes as important as considering 'what' is being claimed.

Ajit Abeysekera

RESEARCH ARTICLE

Construction Materials
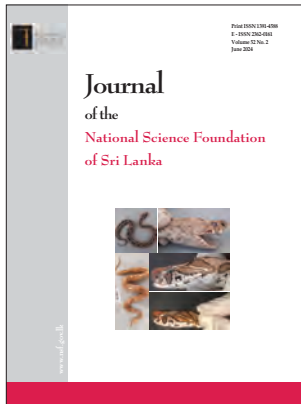
Proposed mix design improvements of compressed stabilized earth blocks (CSEB) with particle packing optimization and coir reinforcement

SN Malkanthi[1*], KGK Sathsara[1], PD Dharmaratne[2] and H Galabada[3]

[1] *Department of Civil & Environmental Engineering, Faculty of Engineering, University of Ruhuna, Sri Lanka.*
[2] *Department of Civil Engineering, Faculty of Engineering, Sri Lanka Institute of Information Technology, Malambe, Sri Lanka.*
[3] *Esoft Metro campus, Colombo, Sri Lanka.*

Abstract: The use of the earth as a building material has been practiced since the beginning of human civilization. Unburnt bricks, rammed earth, adobe, and burnt bricks are some of them. As a result of technological development, adobe has developed into a compressed stabilized earth block (CSEB). The clay percentage of the soil significantly affects the strength of the CSEB. This study focused on controlling the clay percentage by adding larger particles externally using building construction waste and reinforcing them with coconut coir. Different coir amounts by weight from 0.1% to 0.5% with different lengths of 2 cm, 4 cm, 6 cm, and 8 cm were considered for block production. For dry compressive strength and wet compressive strength, the combination of 0.3% coir amount with 6 cm coir length gave the maximum strength, and it also satisfied the required water absorption limit as per the Grade 1 category of the SLS 1382, part 1. After that, using the above combination, the industrial scale (350 × 100 ×175) mm size block was prepared, and its strength also satisfied the SLS 1382 Grade 1 requirements. According to the study, the manufacturing cost for the CSEB is lower than that of cement blocks and clay bricks. The cost for a 1 m² wall panel preparation using CSEB is 41.52% lower than preparing using burnt clay brick and 8.56% lower than preparing using cement blocks. Therefore, the CSEB can be used as a load-bearing walling material at a low cost and with eco-friendliness.

Keywords: Coconut coir, compressed stabilized earth blocks (CSEB), compressive strength, cost-effectiveness, particle packing optimization.

INTRODUCTION

Masonry is one of the most popular building construction materials because of its durability, cost-effectiveness, availability, and sound and heat insulation. Nowadays the consumer demand is for environmentally friendly construction materials. Compressed Stabilized Earth Block (CSEB) is a relatively new eco-friendly construction material. Generally available sandy soil and gravel soil are used as the main raw material while stabilizing with cement, lime, or other different additives to improve the properties of CSEB (Kongkajun *et al.*, 2020). The main advantage of the CSEB is its eco-friendliness due to low cement usage, and it is an unburnt block (Riza *et al.*, 2010). The manufacturing cost of CSEB is significantly lower than that of fired clay bricks and conventional concrete blocks.

Though CSEB is a sustainable building material, there are some issues associated with durability and strength (Abdullah *et al.*, 2017). The best known method for enhancing the properties of CSEB is stabilization. Stabilization agents such as cement, fly ash (Gurumoorthy & Shanmugapriyan, 2020), bottom ash (Danso *et al.*, 2015) and lime (Malkanthi *et al.*, 2020) can be added to enhance the properties of the soil. According to past

studies (Hall *et al.*, 2012), the inclusion of cement significantly causes an increase in the strength of the soil, but higher cement content will increase the manufacturing cost of the CSEB. Walker (1995) highlighted that the use of more than 10% cement is not very economical during this process. Alam *et al.* (2015) and Segetin *et al.* (2007) also suggested that the 5–10% and 3–10% range of cement stabilization is more effective, respectively. Further, the availability of suitable material is a major concern in this CSEB production because it is an earth-based product. So, the variation of the soil properties highly affects CSEB production. The dry density and compressive strength decrease due to the poor bond of cement with soil particles, as well as finer clay and silt particles (Walker, 1995). Also, water absorption is higher when the clay and silt content is in the high range (Guettala *et al.*, 2002). The higher water absorption decreases the durability of the blocks. Some researchers have suggested different methods like soil washing to overcome this issue (Malkanthi & Perera, 2018) and adding larger particles to modify the soil (Malkanthi *et al.*, 2021). The use of recycled waste, such as building construction waste, can reduce the finer percentage in the mix and increase the number of larger particles. However, there is a limit to adding other sources. With that limit, further enhancement of the properties of CSEB can be carried out by reinforcing with fibres such as coconut coir (Thanushan *et al.*, 2021).

This study used building construction waste to modify the soil according to the particle packing concept and coconut coir as a reinforcement to enhance the properties of CSEB. Further, the study focused on the cost-effectiveness of the CSEB with coconut coir.

Applicability of particle packing concept for CSEB production

The particle packing concept states that the particles should be selected to fill the voids between soil particles to achieve the maximum packing density (Senthil & Santhanam, 2003). This theory has been used in concrete technology (Wong *et al.*, 2013) and later to produce interlocking blocks (Hettiarachchi & Mampearachchi, 2019). It is a very useful concept to select the most suitable soil and densify the improper soils by adding the required particle sizes in CSEB production. Several past studies on particle packing density with this optimization concept are available. The particles are considered as a continuous distribution in Fuller's curve theory (Fennis & Walraven, 2012).

According to Malkanthi *et al.* (2021) and Malkanthi & Perera (2019), native soil extracted from different activities can be modified by adding larger particles according to the theoretical curves, as explained in the particle packing concept. This helps to achieve the maximum packing density. At the same time, this helps to reduce the clay content in the soil. The theoretical curves developed according to Fuller's equation (Equation 1) and Funk and Dinger's equation (Equation 2) (Fennis & Walraven, 2012) were used to modify the soil grading with the purpose of reducing clay content and maximizing the packing density.

$$P_d = (d / d_{max})^q \qquad (...01)$$

$$P_d = \frac{d^q - d_{min}^q}{d_{max}^q - d_{min}^q} \qquad (...02)$$

where,

P_d = size cumulative distribution function
d = considered particle diameter
d_{max} = maximum particle diameter in the mixture
d_{min} = minimum particle diameter in the mixture
q = parameter (0.33-0.5), which adjusts the curve for fineness or coarseness.

Fibre-reinforced compressed stabilized earth blocks

For the purpose of increasing the strength and durability of the cement-stabilized earth blocks, different materials like glass fibre, synthetic fibre, and natural fibres (coconut husk fibre, banana fibre, oil palm, wool, straw, etc.) are used as the reinforcing material of CSEB (Bahar *et al.*, 2004; Thanushan *et al.*, 2021). Further, most of the researchers have shown that the properties of CSEB have improved with the addition of coconut fibre in different quantities (Raj *et al.*, 2017; Rangkuti & Siregar, 2020; Thanushan *et al.*, 2021).

Nowadays, synthetic fibres are gaining more popularity than natural fibres. There are experimental investigations on the application of natural fibres due to environmental concerns. This research mainly focused on CSEB reinforced with coconut. Coconut coir is a low-cost, widely available material that can be easily incorporated with cement soil mixture and increase the durability and strength of the CSEB. Researchers state that the average coconut fibre diameter is approximately 0.2 mm, cut into 15 mm pieces to mix better with soil. In Sri Lanka, the cost of 1 kg of coconut fibre varies from 300 to 650 LKR (Sri Lankan Rupees) according to its grade.

Coconut fibre is a readily available material that can be obtained from the husk of the coconut fruit. Countries like Sri Lanka, India, Thailand, Vietnam, etc. supply coconut coir to the world. Generally, there are two types of coconut fibre. They are brown fibre and white fibre. Brown fibres are thick and strong and are obtained from matured coconuts, and the white fibres which are extracted from immature coconuts are smoother, finer, and weaker (Wazir, 2020). Commercially, coconut coir is available in three forms: Bristle fibre – long fibres, mattress fibre – short fibres, and Decorated fibre – mixed fibres. According to Dharmaratne *et al.* (2021), the average diameter and the density of the coir fibre are 0.31 mm and 1.018 g/cm^3. These values may change from region to region. In the tensile test, ultimate tensile strength, Young's modulus, and elongation of the coir fibre ranged from 94–159 MPa, 1.2–1.8 GPa, and 21–67%, respectively. Also, Sri Lankan coir fibres are thermally stable below 220 $^\circ$C.

MATERIALS AND METHODS

Soil is the main raw material of the compressed stabilized earth blocks. In this study, the soil was collected from a borrow pit in the Karapitiya area (southern region of Sri Lanka) and ordinary Portland Cement was added to stabilize the soil. Considering past research findings, 10% of cement addition by weight was used in this study to achieve the required strength with cost-effectiveness. The clay percentage of the selected soil was 18.98%. It has a plasticity index of 3.5%, and this soil can be categorized as slightly plastic. Most of the research has shown that soil with a plasticity index of less than 15% is suitable for CSEB production (Raj *et al*., 2017; Malkanthi *et al*., 2020). The low clay percentage significantly increases the strength and durability of the CSEB. The reduction of clay percentage in the soil was achieved by adding larger particles using building construction waste according to the particle packing optimization. Construction waste mainly consists of crushed concrete waste. Further, coconut coir was used as reinforcement. There are three types of coconut coir available in Sri Lanka: bristle fibre, mixed fibre, and decorticated fibre. Bristle fibre was selected for the research because it is lengthy and stronger than the other two. The diameter of the coir is approximately 0.2 mm.

Using the particle packing concept, the soil was modified to fit the particle distribution of soil to theoretical particle curves. Particle packing theory says how to optimize the particle size to minimize the void ratio. According to the optimization curves, as explained in particle packing theories, soil particles of different sizes are added to the mixture to improve the packing density by reducing the voids, as shown in Figure 1. It shows that the large particles have filled the container with large voids, and smaller particles are added to reduce the voids. Then, tiny particles are filled to further reduce voids and increase the density.
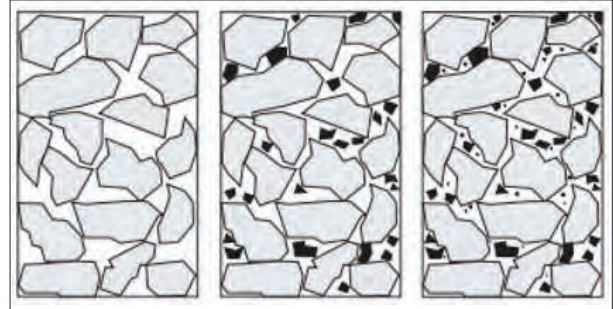
Figure 1: Particle packing concept (Senthil & Santhanam, 2003)

Figure 2 shows the graphical representation of Equation 1 and Equation 2. Further, it includes particle size distribution of the selected soil and construction waste. Finally, the particle size distribution of the modified soil by adding construction waste is illustrated. Coconut coir was added to the soil mixture as a reinforcement.

The clay reduction of the soil by adding building construction waste has limitations. The clay percentage of the selected soil was reduced from 18.98% to 12%. The governing factor for the properties of CSEB is the clay content, and most of the past studies have shown that limiting the clay content to 15% would give desirable properties to CSEB (Jayasinghe, 1999; Senthil & Santhanam, 2003; Reddy & Kumar, 2011a; 2011b). Further reduction of clay is not very practicable. So, further improvement of the CSEB was performed by adding coconut coir. After going through several research papers, the fibre length was varied as 2 cm, 4 cm, 6 cm, and 8 cm, with the amount of coir being 0.1%, 0.2%, 0.3%, 0.4%, and 0.5% of the total weight of the dry soil. The coir was combed using a wire brush to remove unwanted particles attached to the fibre and to get a straight fibre bundle. Then, those were cut into predefined lengths using a knife or scissors. All the materials were mixed by weight. For 10 kg of soil, 6.46 kg of construction waste and 1.0 kg of cement were used. Water addition was 8%-10% of the soil weight. The cubes (150 × 150 × 150 mm) were cast, and the properties of the cubes were tested. For each test, three specimens were used.

The optimum coconut coir combination, which showed the optimum desirable properties, was selected and using that combination, industrial scale $350 \times 100 \times 175$ mm blocks were produced, and their properties were tested. Block preparation and testing were done following SLS 1382 Part 2: Test Methods.
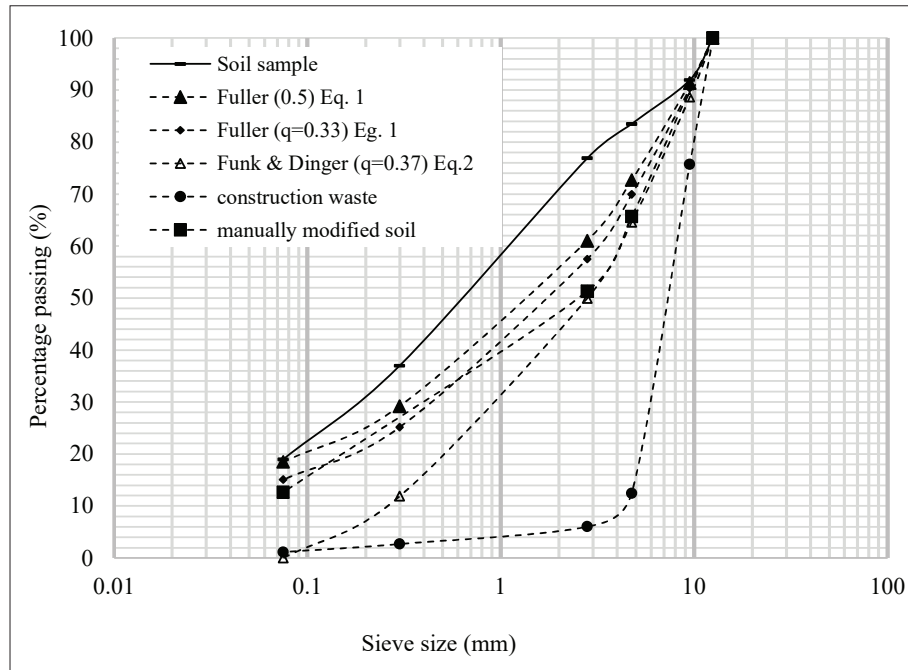
Figure 2:   Particle size distribution of soil and theoretical particle packing curves

Finally, the cost of coir-reinforced CSEB was calculated considering the market rates of materials in August 2022. Furthermore, the cost of produced CSEB was compared with the market price of cement blocks of the same size. The unit rate of 1 m² of CSEB wall was calculated and compared to that of cement blocks and burnt bricks.

RESULTS AND DISCUSSION

The cubes were cast using modified soil with 10% Portland cement and different coir combinations. After 28 days of the curing period, cubes were tested and compared with Sri Lankan standards (SLSI, 2010a; 2010b). The 28 days of dry compressive strength values are shown in Figure 3. It shows that compressive strength first increases with the coir length and amount, and then it tends to decrease. When increasing the coir amount, the bond between soil particles and coir increases. Further addition of coir reduces the interfacial bond between soil particles and coir. In other words, the bond performance will loosen due to the high density of fibre. Similar behaviour has been shown in the studies done by Raj *et al.* (2017) and Thanushan *et al.* (2021).

According to Figure 3, the maximum dry compressive strength value was 8.0 MPa with the combination of 0.3% coir amount and 6 cm coir length. Also, it satisfies the SLS 1382, grade 1 strength condition (should be more than 6.0 N/mm²). Based on the study done by Thanushan *et al.* (2021), the maximum compressive strength achievement was around 3.3 N/mm² when varying the coir amount from 0.0% to 0.6%. Raj *et al.* (2017) have achieved a compressive strength of 10.42 N/mm² at 0.8% of coir content.

The wet compressive strength variation with the different coir combinations is also shown in Figure 4. As for dry compressive strength, the maximum wet compressive strength was given from 0.3%, 6 cm coir combination, and the strength value was 5.60 MPa. Also, all wet compressive strength values are in Grade 1 as per SLS 1382 strength requirement (should be more than 2.4 N/mm²).

Figure 5 shows the water absorption variation of the different combinations.
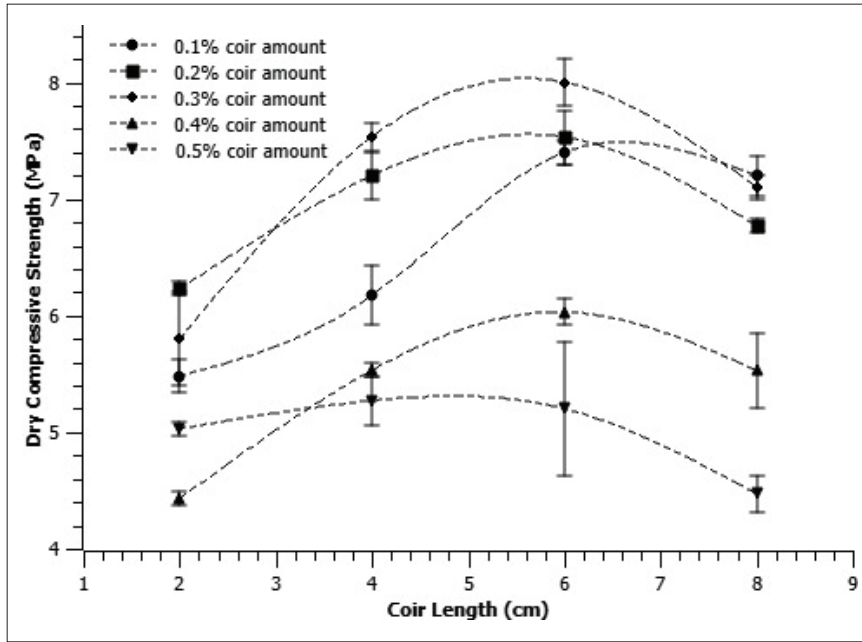
Figure 3: 28 days dry compressive strength vs coir length of CSEB
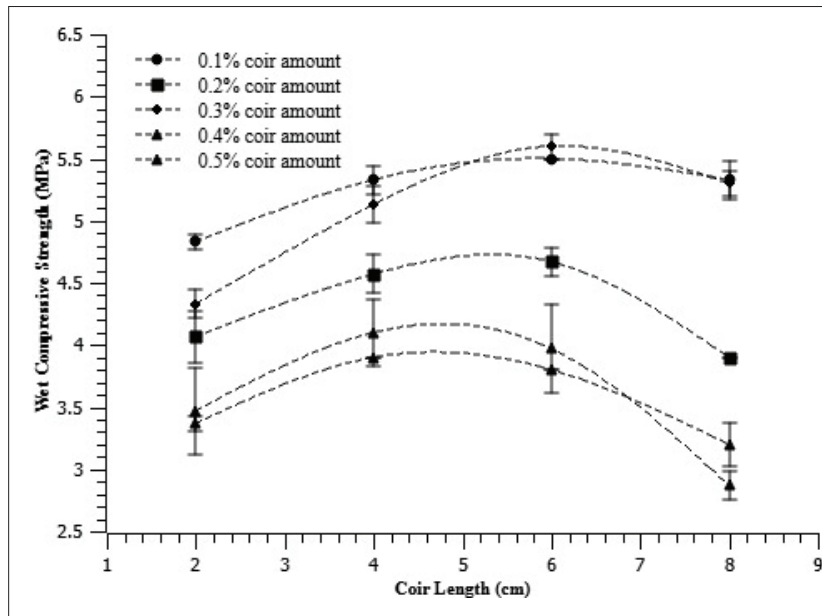
Figure 4: 28 days wet compressive strength vs coir length of CSEB

According to Figure 5, the water absorption of the CSEB increased with the coir length and the amount of coir. The maximum water absorption should be limited to 15% as SLS 1382; Part 1. Finally, Table 1 shows the summary of the test results. Considering all the requirements, the standing of CSEB in SLS 1382 is also listed.
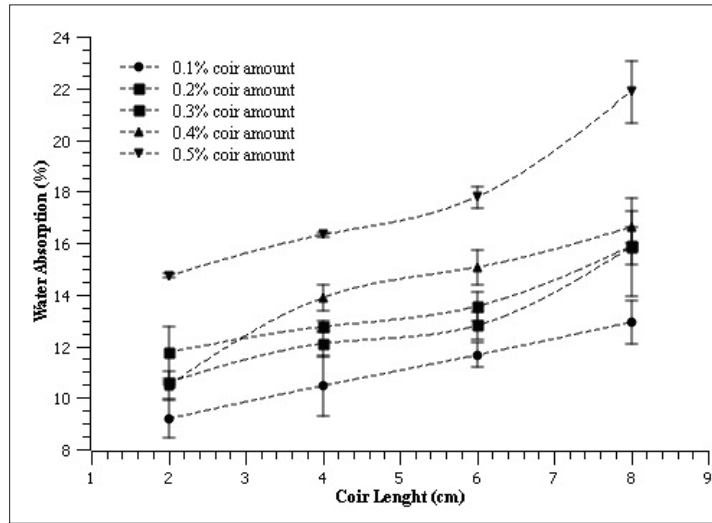
Figure 5: Water absorption of the CSEB with different coir combinations

Table 1: Summary of the test results

Coir amount	Length (cm)	28 days compressive strength (MPa)		Dry density (kg/m³)	Water absorption (%)	Standing of CSEB in SLS 1382
		Dry	Wet			
0.1%	2	5.48	4.83	1,640	9.18	Grade 2
	4	6.17	5.33	1,649	10.46	Grade 1
	6	7.40	5.50	1,738	11.65	Grade 1
	8	7.20	5.33	1,719	12.93	Grade 1
0.2%	2	6.23	4.07	1,684	10.59	Grade 1
	4	7.20	4.57	1,669	12.09	Grade 1
	6	7.53	4.67	1,664	12.80	Grade 1
	8	6.77	3.90	1,610	15.83	Not satisfied
0.3%	2	5.80	4.33	1,763	11.75	Grade 2
	4	7.53	5.13	1,728	12.75	Grade 1
	6	8.00	5.60	1,723	13.54	Grade 1
	8	7.10	5.30	1,649	15.87	Not satisfied
0.4%	2	4.43	3.37	1,743	10.48	Grade 2
	4	5.53	3.90	1,649	13.87	Grade 2
	6	6.03	3.80	1,640	15.06	Grade 1
	8	5.53	3.20	1,546	16.61	Not satisfied
0.5%	2	5.03	3.47	1,615	14.72	Grade 2
	4	5.27	4.10	1,635	16.31	Not satisfied
	6	5.20	3.97	1,556	17.78	Not satisfied
	8	4.47	2.87	1,491	21.86	Not satisfied

6.0 MPa, 4.0 MPa, and 2.8 MPa are the dry compressive strength limits for Grade 1, Grade 2, and Grade 3, respectively. 2.4 MPa, 1.6 MPa, and 1.2 MPa are the wet compressive strength limits for Grade 1, Grade 2. and Grade 3, respectively. Water absorption should be less than 15% (SLSI, 2010a).

The optimum combination for the CSEB was selected as a 0.3% coir amount with a 6 cm coir length because that combination obtained the maximum dry and wet compressive strength with an acceptable water absorption value. Then, using that combination, an industrial scale block (350 × 100 × 175 mm) was produced. The 28-day test results of the industrial scale CSEB block are shown in Table 2.

Table 2: Test results of the Industrial-scale block

Clay percentage (%)	Cement percentage (%)	28 days compressive strength (MPa)		Dry density (kg/m³)	Water absorption (%)	Grade (As per SLS 1382)
		Dry	Wet			
12	10	Avg = 7.01	Avg = 4.41	1,677.64	12.79	Grade1
		SD = 0.07	SD = 0.08			

The industrial-scale block properties also satisfied SLS Grade 1 requirements.

The cost of the coconut fibre-reinforced compressed stabilized earth block is calculated for the laboratory cast block, which is 150 mm × 150 mm × 150 mm in size. After that, it was converted into an industrial-scale block. It is assumed that the manufacturing process for cement blocks can also be applied to this CSEB production. So, the same labour requirement was assumed. During the testing procedure, the average dry weight of a block is around 5.82 kg. Materials (dry soil, construction waste, cement, coir) requirement for one block production was calculated, and rates were calculated for these units of material considering market prices of August 2022. Finally, the estimated manufacturing cost for the compressed stabilized earth block was 91.00 LKR (Sri Lankan Rupees). If the CSEB market price is listed as Rs 105.00 with a 15% profit, the cost reduction by comparing with a normal cement block is Rs. 15, and the estimated cost reduction percentage is 14.28%, considering the market value of cement blocks (average) was 120.00 LKR. So, the industrial-scale compressed stabilized earth block usage is more economical than the usage of normal cement block.

Furthermore, a 1 m², 4.5-inch thick wall panel with burnt clay brick needs 3136.86 LKR, and a 1 m², 4-inch thick wall with CSEB needs 2216.45 LKR, which is a 41.52% cost reduction over burnt clay brick usage. A 4-inch thick 1 m² wall with cement block needs 2,406.26 LKR, and it is 8.56% more costly than the CSEB wall cost. The unit rate calculations are shown in Table 3 and Table 4. The quantities were extracted from the Building Schedule of the Department of Buildings. Most of the CSEB walls are not plastered because of their external appearance, which results in further reductions in construction costs. Construction waste usage is also an eco-friendly method to reduce waste generation in the country.

Table 3: Unit rate calculation for CSEB wall and cement block wall

Item description	Unit	Quantity	Rate (Rs.)	Amount for CSEB (Rs.)	Amount for cement block (Rs.)
Hollow cement blocks (16" × 8"× 6")	No	112	105.00 for CSEB and 120 for cement blocks	11,760.00	13,440.00
Allow 5% for wastage	-	-		588.00	672.00
Cement	Bag	0.75	3,000.00	2,250.00	2,250.00
Sand	Cube	0.06	23,000.00	1,380.00	1,380.00
Mason	Day	1.5	3,000.00	4,500.00	4,500.00
U / SK laborer	Day	2.25	2,000.00	4,000.00	4,000.00
	Total for 1 square			24,478.00	26,242.00
	Rate for 1 m²			2,631.40	2,821.00

Table 4: Unit rate calculation for brick masonry wall

Item description	Unit	Quantity	Rate (Rs.)	Amount (Rs.)
Bricks	No	550	25.00	3,750.00
Allow 5% for wastage	-	-		687.50
Cement	Bag	1.3	3,000.00	3,900.00
Sand	Cube	0.1	23,000.00	2,300.00
Water	Gal	50	0.30	15.00
Mason	Day	1.5	3,000.00	4,500.00
U / SK laborer	Day	2	2,000.00	4,000.00
	Total for 1 square			29,152.50
	Rate for 1 m^2			**3,133.90**

CONCLUSION

Green building techniques can help to create a better, environmentally friendly future. Compressed stabilized earth block is one of the eco-friendly building construction materials. The clay percentage of the soil significantly affects the strength of CSEB. The particle packing concept was used to modify the soil by adding different sizes of building construction waste to obtain the maximum packing density, and it helped reduce the clay percentage of the soil from 18.98% to 12%. Further reduction of clay percentage is not possible by adding waste particles. Therefore, fibre reinforcing of CSEB was done using coconut coir. It helps to improve the properties of CSEB. Both the coir length and the amount were varied.

To minimize the cost and to obtain the desired strength, 10% of Portland cement was used as the stabilizer. The maximum dry and wet compressive strengths were given with the combination of 0.3% coir amount and 6 cm coir length. The water absorption was increased with the increase of the coir amount and coir length. The 0.3%, 6 cm coir combination test results satisfied the SLS 1382 Grade 1 requirements. The cost reduction of industrial-scale CSEB was 8.56% compared to cement blocks and 41.52% compared to clay bricks. The use of CSEB for low-rise buildings is a cost-effective and eco-friendly solution.

This study focused on changing the coir amount and the length only. Due to the unavailability of facilities, other physical, mechanical, and chemical properties of coir, such as tensile strength, elastic modulus, and lignin of coir were not tested. Further, durability issues related to wetting expansion and drying shrinkage were not considered in the present study.

To enhance the properties of CSEB further, it is recommended to consider the durability of CSEB reinforced with natural fibres. Artificial fibre reinforcements also can be considered with different stabilization agents. The effectiveness of using fly ash, bottom, and plant resin can be tested as stabilizers.

Acknowledgement

REFERENCES

Abdullah A.H., Nagapan S., Antonyova A., Rasiah K., Yunus R. & Sohu S. (2017). Strength and absorption rate of compressed stabilized earth bricks (CSEBs) due to different mixture ratios and degree of compaction. *MATEC Web of Conferences* **103**: 1–8.
DOI: https://doi.org/10.1051/matecconf/201710301028

Alam I., Naseer A. & Shah A.A. (2015). Economical stabilization of clay for earth buildings construction in rainy and flood prone areas. *Construction and Building Materials* **77**: 154–159.
DOI: https://doi.org/10.1016/j.conbuildmat.2014.12.046

Bahar R., Benazzoug M. & Kenai S. (2004). Performance of compacted cement-stabilised soil. *Cement and Concrete Composites* **26**(7): 811–820.
DOI: https://doi.org/10.1016/j.cemconcomp.2004.01.003

Danso H., Martinson D.B., Ali M. & Williams J.B. (2015). Physical, mechanical and durability properties of soil building blocks reinforced with natural fibres.

Construction and Building Materials **101**: 797–809. DOI: https://doi.org/10.1016/j.conbuildmat.2015.10.069

Dharmaratne P.D., Galabada H., Jayasinghe R., Nilmini R. & Halwatura R.U. (2021). Characterization of physical, chemical and mechanical properties of Sri Lankan coir fibers. *Journal of Ecological Engineering* **22**(6): 55–65. DOI: https://doi.org/10.12911/22998993/137364

Fennis S.A.A.M. & Walraven J.C. (2012). Using particle packing technology for sustainable concrete mixture design. *Heron* **57**(2): 73–101.

Guettala A., Mezghiche B., Chebili R. & Houari H. (2002). Durability of lime stabilised earth blocks. *Sustainable Concrete Construction* **5**: 645–654. DOI: https://doi.org/10.1680/scc.31777.0064

Gurumoorthy C. & Shanmugapriyan R. (2020). Compressed stabilized earth block using fly ash and quarry dust. *International Journal of Recent Technology and Engineering* **9**(1): 714–716. DOI: https://doi.org/10.35940/ijrte.A1165.059120

Hall M.R., Najim K.B. & Keikhaei Dehdezi P. (2012). Soil stabilisation and earth construction: Materials, properties and techniques. *Modern Earth Buildings: Materials, Engineering, Constructions and Applications* **2012**: 222–255. DOI: https://doi.org/10.1533/9780857096166.2.222

Hettiarachchi H.A.C.K. & Mampearachchi W.K. (2019). Validity of aggregate packing models in mixture design of interlocking concrete block pavers (ICBP). *Road Materials and Pavement Design* **20**(2): 462–474. DOI: https://doi.org/10.1080/14680629.2017.139300

Jayasinghe C. (1999). Alternative Building Materials and Technologies. *PhD thesis*, University of Moratuwa, Sri Lanka.

Kongkajun N., Laitila E., Ineure P., Prakaypan W., Cherdhirunkorn B. & Chakartnarodom P. (2020). Soil-cement bricks produced from local clay brick waste and soft sludge from fibre cement production. *Case Studies in Construction Materials* **13**: e00448. DOI: https://doi.org/10.1016/j.cscm.2020.e00448

Malkanthi S.N., Balthazaar N. & Perera A.A.D.A.J. (2020). Lime stabilization for compressed stabilized earth blocks with reduced clay and silt. *Case Studies in Construction Materials* **12**: e00326 DOI: https://doi.org/10.1016/j.cscm.2019.e00326

Malkanthi S.N. & Perera A.A.D.A.J. (2018). Durability of compressed stabilized earth blocks with reduced clay and silt. *IOP Conference Series: Materials Science and Engineering* **431**(8): 082010. DOI: https://doi.org/10.1088/1757-899X/431/8/082010

Malkanthi S.N. & Perera A.A.D.A.J. (2019). Particle packing application for improvement in the properties of compressed stabilized earth blocks with reduced clay and silt. *Technology and Applied Science Research* **9**(4): 4538–4542. DOI: https://doi.org/10.48084/etasr.3002

Malkanthi S.N., Wickramasinghe W.G.S. & Perera A.A.D.A.J. (2021). Use of construction waste to modify soil grading for compressed stabilized earth blocks (CSEB) production.

Case Studies in Construction Materials **15**: e00717. DOI: https://doi.org/10.1016/j.cscm.2021.e00717

Raj S., Mohammad S., Das R. & Saha S. (2017). Coconut fibre reinforced cement stabilized rammed earth blocks. *World Journal of Engineering* **14**(3): 208–216. DOI: https://doi.org/10.1108/WJE-10-2016-0101

Rangkuti N.M. & Siregar N. (2020). Coconut fibre usage for the compressive strength brick materials. *International Journal of Civil Engineering, Construction and Estate Management* **8**: 90–99. DOI: https://doi.org/10.30546/2616-4418.13.2020.90

Reddy B.V. & Kumar P. (2011a). cement stabilized rammed earth. Part A: Compaction characteristics and physical properties of compacted cement stabilised soils. *Materials and Structures* **44**(3): 681–693. DOI: https://doi.org/10.1617/s11527-010-9658-9

Reddy B.V. & Kumar P. (2011b). Cement stabilized rammed earth. Part B: Compressive strength and stress-strain characteristics. *Materials and Structures* **44**(3): 695–707. DOI: https://doi.org/10.1617/s11527-010-9659-8

Riza F.V., Rahman I.A. & Zaidi A.M.A. (2010). A brief review of compressed stabilized earth brick (CSEB). *Proceedings of International Conference on Science and Social Research* (CSSR 2010), 5–7 December. Kuala Lumpur, Malaysia, pp. 1011–1016. DOI: https://doi.org/10.1109/CSSR.2010.5773936

Senthil K.V. & M. Santhanam (2003). Particle packing theories and their application in concrete mixture proportioning: a review. *Indian Concrete Journal* **77**(9): 1324–1331.

Segetin M., Jayaraman K. & Xu X. (2007). Harakeke reinforcement of soil-cement building materials: Manufacturability and properties. *Building and Environment* **42**(8): 3066–3079. DOI: https://doi.org/10.1016/j.buildenv.2006.07.033

SLSI (2010a). *Specification for compressed stabilized earth blocks: Part 1 Requirements*. Sri Lanka Standard Institution, Colombo, Sri Lanka.

SLSI (2010b). *Specification for compressed stabilized earth blocks: Part 2 Test Methods*. Sri Lanka Standard Institution, Colombo, Sri Lanka.

Thanushan K., Yogananth Y., Sangeeth P., Coonghe J.G. & Sathiparan N. (2021). Strength and durability characteristics of coconut fibre reinforced earth cement blocks. *Journal of Natural Fibers* **18**(6): 773–788. DOI: https://doi.org/10.1080/15440478.2019.1652220

Walker P.J. (1995). Strength, durability and shrinkage characteristics of cement stabilized soil blocks. *Cement and Concrete Composites* **17**(4): 301–310. DOI: https://doi.org/10.1016/0958-9465(95)00019-9

Wazir H. (2020). *Coconut/Coir Fiber: Properties, Manufacturing Process and Uses*. Available at *https://textilelearner.net/coconut-coir-fiber-properties-manufacturing/*.

Wong V., Chan K.W. & Kwan A.K.H. (2013). Applying theories of particle packing and rheology to concrete for sustainable development. *Organization, Technology and Management in Construction* **5**(2): 844–851. DOI: https://doi.org/10.5592/otmcj.2013.2.3

RESEARCH ARTICLE

Operations Research

Meta-heuristic method to schedule vehicle routing with moving shipments at the cross-docking facility

SR Gnanapragasam[1,2*] and WB Daundasekera[3]

[1] *Department of Mathematics, Faculty of Natural Sciences, The Open University of Sri Lanka, Nawala, Nugegoda, Sri Lanka.*
[2] *Postgraduate Institute of Science, University of Peradeniya, Peradeniya, Sri Lanka.*
[3] *Department of Mathematics, Faculty of Science, University of Peradeniya, Peradeniya, Sri Lanka.*

Abstract: Cross-Docking (CD) is a modern distribution strategy in a supply chain. The optimal scheduling of vehicle routing, known as the Vehicle Routing Problem (VRP), is one of the influential factors of the efficiency of a supply chain. In recent years, researchers and business consultants in different organizations have been interested in integrating the VRP with CD (VRPCD). Since VRPCD is a NP-hard problem, heuristic or meta-heuristic methods are always recommended to solve large-scale VRPCD. The Genetic Algorithm (GA) is a population based meta-heuristic algorithm and also, it is based on the principles of genetic and natural selections. The GA is capable of finding near optimal solutions to large-scale optimization problems which are extremely difficult to solve using traditional optimization algorithms. Therefore, in this study, a meta-heuristic approach based on the GA is proposed to solve the vehicle routing problem with moving shipments at the cross-docking facility (VRPCD&MS). The data are extracted from benchmark instances in the literature. The optimum solutions obtained to small-scale instances by the GA are compared with the exact solutions obtained by the Branch and Bound (BB) algorithm, which is a traditional algorithm to solve problems of this nature. The GA and BB algorithms are respectively coded in *MATLAB* and *LINGO*. The results reveal that the relative difference between the exact solution and the near–optimal solution is below 5%. Therefore, it can be concluded that the proposed GA is a better alternative method, considering its overall performance, to solve the VRPCD&MS models. Moreover, since the computational time is low, the proposed GA can be used to schedule the vehicles to the routes of VRPCD&MS at the last moment prior to the start of the time horizon.

Keywords: Cross-dock, genetic algorithm, meta-heuristic, moving shipments, vehicle routing.

INTRODUCTION

The efficiency of supply chains is crucial to maintain competitiveness in the globalised market around the world. The optimal scheduling of vehicle routing, known as the Vehicle Routing Problem (VRP), is one of the influential factors for a fast supply chain. Also, the VRP is one of the well-studied problems in the area of operations research and since the study of Dantzig and Ramser (1959), VRP has been subject to very intensive research by considering the different variants of the problem. In order to satisfy the demand of the customers in terms of time, quality, and cost, organizations always attempt new logistics strategies. Cross-docking is one of the key strategies in which business consultants in different organizations are interested. A Cross-Docking Facility (CDF) is an intermediate component of a supply chain. Generally, at a CDF, incoming products, after the consolidation process, are immediately dispatched to outgoing vehicles with minimum time delay. By doing so, cross docking reduces the cost incurred by traditional warehousing up to 70%, by eliminating some costly operations, such as storing and order picking, at those respective warehousing centres (Vahdani & Zandieh, 2010). In 1980, after a successful implementation of Cross

* Corresponding author (srgna@ou.ac.lk; https://orcid.org/0000-0003-1411-4853)

Docking at *Walmart*, which is a major multinational retail corporation (Apte & Viswanathan, 2000), other giant companies such as *Goodyear GB Ltd*, *Toyota*, *Eastman Kodak Co*, *Dots,* and *LLC* also successfully implemented Cross Docking in their supply chains (Van Belle *et al.*, 2012).

Initially 'Vehicle Routing Problem' and 'Cross Docking' have been treated separately in most studies, but after the study on the Vehicle Routing Problem with Cross Docking (VRPCD) by Lee *et al.* (2006), studies on the integration of the VRP with Cross Docking have attracted more attention among researchers and practitioners. For an effective VRPCD, there should be synchronization among the incoming vehicles which collect products from the suppliers and outgoing vehicles which distribute products to the customers. According to the literature, several characteristics of the VRP with Cross Docking technique with different methods of solution have been experimented with. However, the internal operations were not taken into consideration in almost all the past studies on VRPCD. In the literature review survey by Buakum and Wisittipanich (2019), it was recommended to consider the internal operations at the CDF to develop the models for VRPCD. Therefore, Gnanapragasam and Daundasekera (2022) integrated the component of 'Moving Shipments inside a CDF' with VRPCD and referred it as 'VRPCD&MS'.

In the study (Gnanapragasam & Daundasekera, 2022), not only the moving shipments from indoors to outdoors of the CDF, but also loading and unloading shipments at all the nodes (suppliers or customers), including the CDF, were taken into consideration in VRPCD&MS. However, the solution method applied in this study was only capable of obtaining optimal solutions to small-scale instances, in which the total number of suppliers and customers was only up to 20. In general, reaching an exact optimal solution when the number of suppliers and customers exceeding 20, which is considered as a large-scale instance, is time consuming and hence, impractical in the business world. Therefore, Gnanapragasam & Daundasekera (2022) recommended applying meta-heuristic methods to reach near-optimal solutions to large-scale instances of VRPCD&MS. In this current study, a modified version of the Mixed Integer Non-Linear Programming model formulated by Gnanapragasam & Daundasekera is developed without considering time related constraints. Therefore, in this study, a meta-heuristic method based on the Genetic Algorithm is developed to reach near-optimal solutions to the large-scale instances of VRPCD&MS. It should be emphasized that, in the development of the Mixed Integer Liner Programming model to VRPCD&MS, this study focuses only on the operation cost and does not include any time related constraints which were considered in the previous study.

The study on the integration of the VRP with Cross Docking was initiated in 2006 by Lee *et al.* (2006). In this initial study on VRPCD, two different sets of homogeneous vehicles, one for the pickup process and one for the delivery process, were used. Also, the simultaneous arrival of inbound vehicles to the CDF was assumed. Wen *et al.* (2009) extended the initial study by assigning the Time Windows to all the suppliers and customers. Moreover, the assumptions regarding the simultaneous arrival of inbound vehicles and two different sets of vehicles, made by Lee *et al.* (2006), were removed. On the other hand, the consolidation decisions with dependency rules and the same set of vehicles for pickup and delivery processes were introduced by Wen *et al.* (2009). Hence in the literature, this model has become a more generalized version of VRPCD. Different methods of solution have been tried out in the past to solve the variants of VRPCD, which are mentioned in the following paragraphs.

Since the VRPCD is a NP-hard problem, obtaining the exact solution is possible only for small-scale instances. The exact solution to the small-scale instances of the variants of VRPCD were obtained in the following studies which are stated in this paragraph. Santos *et al.* (2011a) used the Branch and Price algorithm to the model developed by Wen *et al.* (2009). This Branch and Price method outperformed the Branch and Bound approach for the same instances. In the same year, a Column Generation method was introduced by the same authors (Santos *et al.*, 2011b) and the overall results outperformed the results of Santos *et al.* (2011a). Multi commodity, splitting and heterogeneous characteristics were incorporated by Hasani-Goodarzi & Tavakkoli-Moghaddam (2012). Dondo (2013) applied a Branch and Price algorithm to solve the model of Wen *et al.* (2009). In the study by Gnanapragasam & Daundasekera (2022), a Branch and Bound algorithm is employed to reach the optimal solution to the VRPCD&MS.

Since the VRPCD is an optimization problem with high complexity, reaching an exact solution to a large-scale problem is extremely challenging. Meta-heuristic approaches to reach near optimal solutions to large-scale problems were also examined in the integrated research on the VRPCD, and the following studies in this paragraph

highlights them. Initially in the study of Lee *et al.* (2006), a Tabu Search approach was used. Subsequently the model of Wen *et al.* (2009) was also tested using a Tabu Search algorithm with Adaptive Memory Procedure. Later Liao *et al.* (2010) made use of another Tabu Search algorithm to obtain a better optimal solution than the one obtained by Lee *et al.* (2006). The open versus closed configurations to the VRPCD, described by Wen *et al.* (2009), were compared by Tarantilis (2013), by using a Tabu Search algorithm. Morais *et al.* (2014) attempted six different Iterative Local Search methods to solve the model of Wen *et al.* (2009) and obtained more promising solutions than Tarantilis (2013). The soft Time Windows characteristic was adapted with the model of Wen *et al.* (2009) by Fakhrzad & Sadri Esfahani (2014), using the Tabu Search and Variable Neighbourhood Search methods, and the Tabu Search outperformed the Variable Neighbourhood Search method in this attempt.

Furthermore, hybrid methods built by combining two or more meta-heuristics methods were also applied to solve the variants of VRPCD. A method by hybridizing Ant Colony System and Simulated Annealing was employed by Moghadam *et al.* (2014), with the added characteristic: splitting the order in the delivery process, to the model of Wen *et al.* (2009). It was revealed that the hybridized approach outperformed the method of using Simulated Annealing alone. Another hybridized approach combining the methods Variable Neighbourhood Search, Simulated Annealing, and Particle Swarm Optimization to the model of Lee *et al.* (2006) was utilized by Vahdani *et al.* (2012), who obtained more encouraging solutions than the previous. It was observed that a remarkable improvement to the solutions was obtained using the Simulated Annealing algorithm by Yu *et al.* (2014), compared to the solutions obtained by Liao *et al.* (2010). A mix of open and closed network configurations with splitting characteristics were tested on the VRPCD system by Alinaghian *et al.* (2016). Yin & Chuang (2016) adapted the environmental factor with the heterogeneous property to the model developed by Lee *et al.* (2006). The Adaptive Memory Artificial Bee Colony (AMABC) technique was applied to solve the Green VRPCD model presented by Yin & Chuang (2016), and AMABC has produced a more promising solution than was obtained by Liao *et al.* (2010). The model formulated by Wen *et al.* (2009) was enhanced by Nikolopoulou *et al.* (2016) by incorporating some characteristics such as many-to-many correspondence between suppliers and customers, different sets of heterogeneous vehicles, and splitting. The results obtained by the Adaptive Memory Procedure with Tabu Search by Nikolopoulou *et al.* (2016) were

parallel to the results obtained by Wen *et al.* (2009), and better than the results obtained by Morais *et al.* (2014). In the study of Larioui & Reghioui (2017), the solutions were compared by a Tabu Search and Memetic Algorithm to the model of Wen *et al.* (2009) and it was observed that the Memetic Algorithm outperformed the Tabu Search.

Moreover, the solutions to the additional characteristics with VRPCD have been attempted in the past and are highlighted as follows. The Open VRPCD developed by Yu *et al.* (2016) and the heterogeneous property added by Birim (2016) were modified versions of the method of Lee *et al.* (2006). The Simulated Annealing strategies were examined to solve both models by Yu *et al.* (2016) and Birim (2016). Early arrivals were allowed in the model of Wen *et al.* (2009) by Grangier *et al.* (2017) and a Large Neighbourhood Search with Set Partitioning and Matching approach generated some better solutions than the results from the studies of Wen *et al.* (2009), Tarantilis (2013), and Morais *et al.* (2014). A Two-phase Genetic Algorithm was employed in the study by Baniamerian *et al.* (2018b) by adding customer satisfaction to the model of Wen *et al.* (2009). The solutions obtained by a method developed by Gunawan *et al.* (2020a) with the combination of Adaptive Large Neighbourhood Search (ALNS) with Set Partitioning Problem and by Gunawan *et al.* (2020b) using ALNS were better than the solutions obtained from the studies conducted by Lee *et al.* (2006), Liao *et al.* (2010), and Yu *et al.* (2016).

It can be observed from the literature on VRPCD, that several solution methods were applied not only to the small-scale instances but also to the large-scale instances. Many models were developed to different variants of VRPCD. However, the internal operations of CDF were not taken into consideration. Moreover, as per the recommendation made by the literature survey of Buakum and Wisittipanich (2019), the component of moving shipments from indoors to outdoors of a CDF was incorporated with VRPCD by Gnanapragasam & Daundasekera (2022). However, in the previous study, exact solutions were obtained only for small-scale (total number of suppliers and customers not exceeding 20) instances of VRPCD&MS using the Branch and Bound algorithm and it was recommended to apply meta-heuristic methods to solve large-scale instances of VRPCD&MS.

It can be observed that the Genetic Algorithm was applied in some of the studies in the literature to solve VRPCD. For instance, VRPCD with multiple objectives

was considered in several studies (Hasani Goodarzi *et al.*, 2018; Kargari Esfand Abad *et al.*, 2018; Ieva *et al.*, 2022). Moreover, the study by Baniamerian *et al.* (2018a) followed an approach hybridized with the Genetic Algorithm to maximize the total profit of the system. A two-phase Genetic Algorithm was developed by Baniamerian *et al.* (2018b) by considering customer satisfaction and time windows with VRPCD. For a VRPCD with a queuing approach, the Genetic Algorithm was proposed by Hasani Goodarzi *et al.* (2022). Besides, there is no study found in the literature that uses the Genetic Algorithm to minimize the total cost with a single objective. Therefore, in this current study, the Genetic Algorithm is employed to solve the VRPCD&MS constructed by Gnanapragasam & Daundasekera (2022).

METHODS AND MATERIALS

The integrated problem of Vehicle Routing with Cross Docking and Moving Shipments is described in the next section. The 'moving shipments' is a component of the internal operations at the cross-docking facility. Also, the developed mathematical model for the integrated problem has been presented.

Vehicle routing problem with cross-docking and moving shipments

The Vehicle Routing Problem with Cross-docking and Moving Shipment (VRPCD&MS) is a problem already studied by Gnanapragasam & Daundasekera (2022). Also, it is an extension of the problem defined by Lee *et al.* (2006) by incorporating internal operations at the CDF. This study focuses on solutions to the large-scale instances of VRPCD&MS without considering the time related constraints considered by Gnanapragasam & Daundasekera (2022).

The phases of VRPCD&MS

The VRPCD&MS model is partitioned into three main phases as follows:

Phase 1: The process of collecting products from all the suppliers.

The first vehicle routing problem is that of picking up the products from the suppliers. Initially all the inbound vehicles should start their trips from the CDF simultaneously.

Phase 2: The process of internal operations at the CDF.

This is a consolidation process occurring inside the CDF. First, the products accumulated by every inbound vehicle should be unloaded indoors at the CDF. Then the unloaded products should be moved to the outdoors of the CDF. Ultimately, the moved products should be loaded to the outbound vehicles.

Phase 3: The process of distributing products to all the customers.

The second vehicle routing problem is that of delivering the products to the customers. Eventually, all the outbound vehicles should terminate their trips at the CDF.

The assumptions

The following specific assumptions are taken into account when formulating the model for the problem VRPCD&MS:

- A single product is cross docked at a single facility and all the inbound vehicles should unload their accumulated products at the CDF.
- All the vehicles in both Phase 1 and Phase 3 should start their tours from the CDF and at the end they should return to the CDF.
- Two different homogeneous fleets of vehicles are used so that the fleet with larger capacity belongs to Phase 1 and the fleet with smaller capacity belongs to Phase 3. The capacities of the vehicles are always higher than the supply/demand by any supplier/customer so that the splitting the orders is not necessary.

The elements of the total cost due to the VRPCD&MS model are described with their respective formulas.

Mathematical formulation

The VRPCD&MS is formulated as a Mixed Integer Linear Programming (MILP) model as follows, which is based on the model proposed in the previous study (Gnanapragasam & Daundasekera, 2022). The indices, sets, parameters and variables used to develop MILP for the VRPCD&MS are described in the following Table 1:

Routing constraints

$$\sum_{j \in N} x_{hj}^k \le 1 \qquad \forall\, k \in V \,,\ \forall\, h \in O \qquad \qquad ...(1)$$

Table 1: Notations and their descriptions

Notation	Description
i, j	Indices for suppliers in Phase 1 or customers in Phase 3
h	Index for receiving or shipping doors of CDF in Phase 2
k	Index for inbound vehicles in Phase 1 or outbound vehicles in Phase 3
$S = \{S_1, S_2, ..., S_n\}$	Set of n suppliers in Phase 1
$C = \{C_1, C_2, ..., C_{n'}\}$	Set of n' customers in Phase 3
$N = S \cup C$	Set of $(n + n')$ suppliers and customers
$V_S = \{v_1^S, v_2^S, ..., v_m^S\}$	Set of m inbound vehicles used in Phase 1
$V_C = \{v_1^C, v_2^C, ..., v_{m'}^C\}$	Set of m' outbound vehicles used in Phase 3
$V = V_S \cup V_C$	Set of $(m + m')$ inbound and outbound vehicles
$O = \{o, o'\}$	Set of receiving (o) and shipping (o') doors of CDF in Phase 2
tc_{ij}	Transportation cost between destinations i and j in Phase 1 and Phase 3
q_i	Quantity at supplier i in Phase 1 or customer i in Phase 3
Q_S	Maximum capacity of inbound vehicles in Phase 1
Q_C	Maximum capacity of outbound vehicles in Phase 3
OC_S^k	Operational cost of the inbound vehicle k in Phase 1
OC_C^k	Operational cost of the outbound vehicle k in Phase 3
SC_i^k	Service cost at supplier i in Phase 1 or customer i in Phase 3 by vehicle k
SC_h^k	Service cost at receiving or shipping door h by vehicle k in Phase 2
A_c	Fixed preparation cost for loading or unloading products in all 3 phases
B_c	Variable shipping cost for loading or unloading a unit of product in all 3 phases
x_{ij}^k	1, if vehicle k travels from supplier (customer) i to supplier (customer) j 0, otherwise

$$\sum_{i \in N} x_{ih}^k \le 1 \qquad \forall k \in V, \ \forall h \in O \qquad ...(2)$$

$$\sum_{i \in N \cup O} \sum_{k \in V} x_{ij}^k = 1 \qquad \forall j \in N \qquad ...(3)$$

$$\sum_{j \in N \cup O} \sum_{k \in V} x_{ij}^k = 1 \qquad \forall i \in N \qquad ...(4)$$

$$x_{ii}^k = 0 \qquad \forall i \in N \cup O, \quad \forall k \in V \qquad ...(5)$$

$$x_{ij}^k + x_{ji}^k \le 1 \quad \forall i, j \in N \cup O, \ \forall k \in V \qquad ...(6)$$

$$\sum_{i \in S} q_i = \sum_{i \in C} q_i \qquad ...(7)$$

$$\sum_{\substack{i \in S \\ j \in S \cup \{o\}}} q_i x_{ij}^k \le Q_S \qquad \forall k \in V_S \qquad \ldots(8)$$

$$\sum_{\substack{i \in C \\ j \in C \cup \{o'\}}} q_i x_{ij}^k \le Q_C \qquad \forall k \in V_C \qquad \ldots(9)$$

Inequalities (1) and (2), respectively, represent the closeness of the Vehicle Routing Problem; at the beginning of any route, vehicles (inbound or outbound) should depart from CDF to suppliers in Phase 1 or customers in Phase 3, and concurrently, all the vehicles (inbound and outbound) should arrive from suppliers in Phase 1 or customers in Phase 3 at the end of their routes. Furthermore, only one vehicle has to arrive at a supplier in Phase 1 or a customer in Phase 3; likewise only one vehicle has to depart from a supplier in Phase 1 or a customer in Phase 3. This is depicted in the equations (3) and (4), respectively. Moreover, equations (5) and (6), respectively, prevent the repeating routes and backward movements in routes. Also equation (7) controls the equilibrium condition of total supply in Phase 1 which must be equal to the total demand in Phase 3. In addition, the inequalities (8) and (9) depict the limitation of the capacities of inbound vehicles in Phase 1 and outbound vehicles in Phase 3, respectively.

The required output

After satisfying the aforementioned constraints, the following required outputs are obtained to calculate the total cost incurred by all three phases described in the previous section.

Required number of inbound vehicles to collect the total supply from all the suppliers:

$$m = \sum_{k \in V_p} \sum_{j \in P} x_{oj}^k$$

Required number of outbound vehicles to distribute the total demand by all the customers:

$$m' = \sum_{k \in V_d} \sum_{j \in D} x_{o'j}^k$$

Cost of transportation at the collecting and distributing processes:

$$TC_P = \sum_{k \in V} \sum_{i,j \in N \cup O} tc_{ij} x_{ij}^k$$

Service cost at the suppliers or customers:

$$SC_P = \sum_{k \in V} \sum_{\substack{i \in N \cup O \\ j \in N}} SC_j^k x_{ij}^k ,$$

where

$$SC_j^k = A_c + B_c \, q_j x_{ij}^k$$

$$\forall i \in N \cup O, \ \forall j \in N, \forall k \in V$$

Service cost (cost of unloading) at the receiving doors of CDF:

$$SC_S = \sum_{k \in V_S} \sum_{i \in N} SC_o^k x_{io}^k ,$$

where $\quad SC_o^k = A_c + B_c \sum_{\substack{i \in N \\ j \in N \cup \{o\}}} q_i x_{ij}^k \qquad \forall k \in V_S$

Service cost (cost of loading) at the shipping doors of CDF:

$$SC_C = \sum_{k \in V_C} \sum_{i \in N} SC_{o'}^k x_{o'i}^k , \text{ where}$$

$$SC_{o'}^k = A_c + B_c \sum_{\substack{i \in N \\ j \in N \cup \{o'\}}} q_i x_{ij}^k \qquad \forall k \in V_C$$

Cost of moving shipments from the receiving doors to the shipping doors of CDF:

$$MC_T = \sum_{k \in V_S} \sum_{\substack{i \in S \\ j \in S \cup \{o\}}} q_i x_{ij}^k$$

Operational cost of required number of inbound and outbound vehicles:

$$OC_P = \sum_{k \in V_S} \sum_{i \in S} OC_S^k x_{io}^k + \sum_{k \in V_C} \sum_{j \in C} OC_C^k x_{o'j}^k$$

The single objective Mixed Integer Linear Programming (MILP) model is developed to minimize the total cost incurred through all three phases from Phase 1 to Phase 3. Therefore, the objective function of the developed MILP model can be articulated as follows:

Minimizing *Total Cost* $= TC_P + SC_P + SC_S + SC_C +$

$$MC_T + OC_P$$

In the following sub-sections, the algorithms to solve the problem VRPCD&MS with the related software are described.

Branch and Bound (BB) Algorithm

The exact solutions to the fifteen small-scale instances (up to 14 suppliers and customers) are obtained using the traditional algorithm known as the Branch and Bound algorithm. Version 18 of *LINGO* optimization software is used in this regard to code the developed Mixed Integer Linear Programming model to obtain the optimal solution. Since the Branch and Bound algorithm always seeks to reach the exact optimal solution, the algorithm is more appropriate to solve small-scale instances and it performs poorly for large-scale instances. Therefore, to obtain near optimal solutions for the large-scale instances, the following meta-heuristic method based on Genetic Algorithm is employed.

Genetic Algorithm (GA)

In 1975, John Holland proposed the Genetic Algorithm (GA) which is based on the Darwinian revolution of 'survival of the fittest' (Holland, 1975), and it was popularized by Goldberg in 1989 (Goldberg, 1989). The Genetic Algorithm is a probabilistic search method which contains genetic operators such as reproduction, crossover, and mutation. In this study, to optimize the total cost, the proposed Genetic Algorithm is divided into three parts, one for each phase defined earlier. It must be emphasized that all these three parts are combined into a single programme. In detail, Part 1 is for the process of pick up the products from suppliers. The internal operations at the cross-dock are considered in Part 2. Part 3 is for the process of delivering the collected products to the customers. There are many combinations of genetic operators used to design a Genetic Algorithm. However, in this study, the Taguchi parameter design method is used to select the best combination of the genetic operators. Accordingly, in this study, the following selection procedures are adapted to design the Genetic Algorithm to solve the VRPCD&MS:

Solution representation

Each solution consists of a set of numbers representing permutation of suppliers and customers in Part 1 and part 3, respectively.

Generation of initial solution

The Genetic Algorithm starts with the initial population based on the random generation method. Since this is one of the best methods to prevent the diversity of the population, the initial population is generated randomly in this proposed Genetic Algorithm. In this case, random permutations are generated based on the number of suppliers or customers as a giant chromosome in the initial population.

Selection procedure

The parent chromosomes are randomly chosen from the initial population based on the tournament selection method to create offspring to the next generation of the population. The minimum value of the chromosome is selected among four randomly chosen chromosomes from the previous generation of the population. To avoid accounting for byes and without loss of generality, the second power of two is selected as the size of the tournament.

Crossover operation

To produce the offspring for the next generation, the order crossover method is applied by randomly selecting two parent chromosomes from the current generation of the population. An offspring is produced by copying the sub-route from the first chromosome into the corresponding positions. Then unfixed positions of the offspring are filled from the second chromosome (the chromosome modified by deleting the genes which are already in the first chromosome) from left to right according to the order of the sequence.

Mutation operation

To find a nearest solution in the search space, the swap mutation is used by selecting a random chromosome from the current generation of the population. The genes of two randomly chosen positions in the chromosome exchange their positions in the chromosome.

Elitism

A set of better solutions in the current generation of the population is transformed to the next generation as it is, so that the better solutions are always preserved.

Operations at the Part 1 and Part 3

Figure 1 given below explains Part 1 and Part 2 in the proposed Genetic Algorithm for the pickup and delivery processes of the VRPCD&MS model:
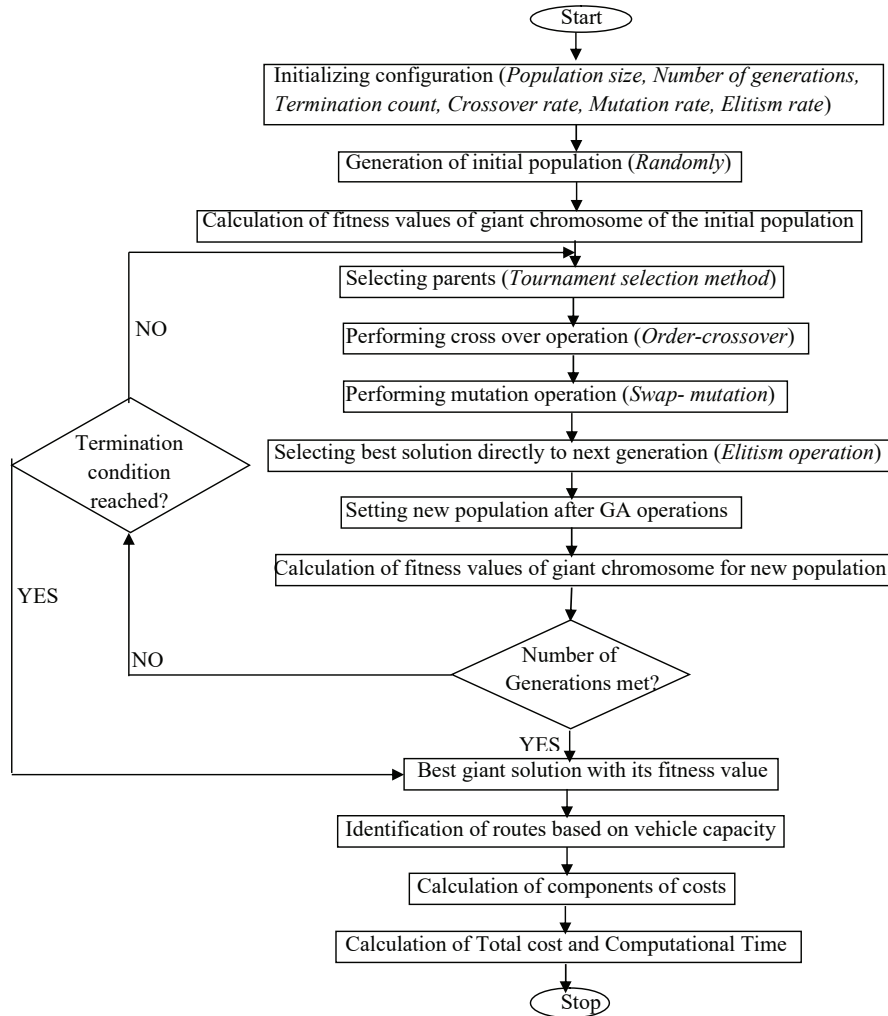
Figure 1:   Flow chart for the part 1 and part 3 of the proposed Genetic Algorithm

It should be emphasized that the very first instruction is applicable only for Part 1. In this, the estimated values of the parameters of the Genetic Algorithm are to be included. Consequently, those parameters are tuned by the Taguchi parameter design method and are reported in Table 3.

Moreover, the very last instruction is applicable only for Part 3 and those calculations are performed based on the formulas described earlier. Furthermore, all the operations of the middle portion (except the first and the last instructions) given in the Flow chart shown in Figure 1 are common to both Part 1 and Part 3 of the proposed Genetic Algorithm. Besides, it can be observed from

Figure 1 that there are two termination criteria to reach the best solution. One criterion is after the execution of 'total number of generations' of new populations. The second criterion is meeting the 'termination count' defined as no improvement in the current solution after a predetermined number of iterations, and the current solution would then be considered as the best near optimal solution to the problem.

Internal operations at the cross-docking facility

The operations inside the CDF of VRPCD&MS are depicted in the Figure 2 below:
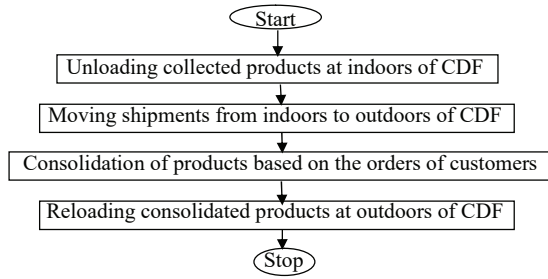
Figure 2: Flow chart for the part 2 of the proposed Genetic Algorithm

The aforementioned Genetic Algorithm is coded in *MATLAB* environment on an Intel Core i5 personal computer with 2.30 GHz CPU and 4 GB RAM. The data are extracted from the benchmark instances (Wen *et al.*, 2009) in the literature of VRPCD, in which the small-scale instances are used to test the compatibility of the developed VRPCD&MS model and to compare

the optimal solutions obtained by the Branch and Bound Algorithm and Genetic Algorithm.

RESULTS AND DISCUSSION

Benchmark instances given by Wen *et al.* (2009) are used to compare the solutions to small-scale instances as well as to large-scale instances of VRPCD&MS.

Parameter values

Table 2 below provides the values, which are chosen arbitrarily, for the problem parameters of the VRPCD&MS: Table 3 below provides the values of the parameters of the Genetic Algorithm for the meta-heuristic method, which are further tuned by the Taguchi method: The same estimated values are fixed in all the cases in the small-scale and large-scale instances considered in this study.

Table 2: Values of the problem parameters of the VRPCD&MS model

Parameter	Value	Parameter	Value
Fixed preparation cost (A_c)	10 cost units	Variable unit shipping cost (B_c)	1 cost unit
Operational cost of inbound vehicle (OC_S^k)	150 cost units	Operational cost of outbound vehicle (OC_C^k)	100 cost units
Inbound vehicle capacity (Q_S)	80 units	Outbound vehicle capacity (Q_C)	50 units

Table 3: Values of the parameters of the Genetic Algorithm

Parameter	Value	Parameter	Value
Population size	50	Mutation rate	0.3
Termination count	50	Crossover rate	0.7
Number of generations	100	Elitism rate	0.1

Results for small-scale instances of VRPCD&MS

The results of the small-scale instances of the VRPCD&MS model obtained from both the Branch and Bound (BB) algorithm and the Genetic Algorithm (GA) are compared in Table 4 below. The instances are described here in terms of number of suppliers and

customers in Phase 1 and Phase 3 respectively. In Table 4, the optimal solutions found for fifteen instances by the method of the Branch and Bound algorithm are compared with the near optimal solutions found by the Genetic Algorithm. In the Genetic Algorithm, the best solution for 10 repetitions of the same instance and the average solution of those 10 solutions are included in Table 4. The average time is the average computational time calculated by executing repeatedly the same instance 10 times under the same conditions. Since the other output values such as the required number of vehicles in Phase 1 and Phase 3 are the same in both methods, it is mainly the solutions in terms of the total cost, and the time required to obtain those results, that are compared in Table 4 below. The GAP value in Table 4 is calculated as follows:

$$GAP = \frac{(Average\ near\ Optimal\ Solution\ by\ GA\ method - Optimal\ Solution\ by\ BB\ method)}{Optimal\ Solution\ by\ BB\ method} \times 100$$

Table 4: Comparison of results between BB algorithm and GA for small-scale instances

Problem no.	Instance		BB algorithm		GA			GAP in %
	No. of suppliers	No. of customers	Optimal solution	Average time (s)	Best solution	Average solution	Average time (s)	
01	02	02	786.76	0.11	786.76	786.76	3.50	0.00
02	02	03	831.76	0.12	831.76	831.76	3.47	0.00
03	02	04	788.28	0.14	788.28	788.28	3.34	0.00
04	03	03	922.38	0.13	922.38	922.38	3.35	0.00
05	03	04	853.90	0.15	853.90	853.90	3.27	0.00
06	03	05	926.02	0.25	926.02	926.02	3.51	0.00
07	04	04	817.88	0.23	817.88	817.87	3.50	0.00
08	04	05	840.00	0.36	840.00	839.99	3.55	0.00
09	04	06	1052.96	2.17	1104.70	1104.70	3.40	4.91
10	05	05	1116.74	1.69	1146.70	1150.18	4.51	2.99
11	05	06	1080.80	2.48	1105.50	1107.78	4.00	2.50
12	05	07	1179.18	4.24	1191.20	1198.94	4.90	1.68
13	06	06	1091.87	3.90	1106.90	1110.20	4.84	1.68
14	06	07	959.92	10.31	1005.06	1005.73	5.47	4.77
15	06	08	1173.37	93.38	1228.40	1228.82	6.40	4.73

When comparing the solutions in terms of total cost exhibited in Table 4, it can be seen that, if the size of the problem is less than 10 (the first 8 instances), then the Genetic Algorithm also gives the same exact optimal solution as is given by the Branch and Bound algorithm. But, it can be observed from problems 10 to 15, when the size of the problem increases, in each and every instance, only a near optimal solution is reached by the Genetic Algorithm with a GAP of nearly 5%.

In the Branch and Bound algorithm, in spite of the average computational time to reach the optimum solution for the first 13 instances being comparatively less, it gradually increases as the size of the problem increases. Also it can be observed that, for the first 8 instances, the averages of the computational time taken by the Genetic Algorithm method are close to the computational time taken by the Branch and Bound algorithm. This occurs mainly as the values of the two parameters (number of generations = 100 and termination count = 50) of the Genetic Algorithm (described in Table 3) are fixed in the *MATLAB* program. However, for the first 8 small-scale instances, if those two particular parameter values are reduced, the same solutions can be obtained with less computational time than that specified in Table 4. Furthermore, it can be seen from Table 4 that in the last two instances, a near optimal solution can be reached in

less computational time by the Genetic Algorithm, than by the Branch and Bound algorithm. Therefore, with respect to the computational time, it can be concluded that to solve the VRPCD&MS model, the proposed Genetic Algorithm is more appropriate.

It can be observed from Table 4 that the average computational time rapidly increases to reach the optimal solution with the increase of the scale of the problem. Also, the study by Gnanapragasam & Daundasekera (2022) showed that the convergence time increased exponentially to reach the optimal solutions for the moderately large-scale instances. It recommends that, for the large-scale instances, a meta-heuristic method is more appropriate. Therefore, in this study, the Genetic Algorithm is used for further analysis for the large-scale instances of VRPCD&MS model and the corresponding results have been reported.

Results obtained by the GA for the large-scale instances of VRPCD&MS

Table 5 shows the number of suppliers and customers in each instance, which is considered as the size of the problem. The required fleets of vehicles in Phase 1 and Phase 3 are indicated as inbound and outbound vehicles respectively. In each instance, the average of the best

optimal solutions obtained in 10 replicates and finally the average computational time of those 10 replicates are exhibited in Table 5. From Table 5, the required number of inbound vehicles in Phase 1 and outbound vehicles in Phase 3 can be seen in each of the fifteen problems. It can be concluded that from the average computational time given in Table 5, a near optimal solution to each problem can be reached in less than 6 seconds even when the size of the problem is 200 in both phases. Since it is relatively a better in performance, this model can be used to schedule the routes of the vehicles at the last moment prior to the start of the time horizon.

Table 5: Results by the Genetic Algorithm for the large-scale instances of VRPCD&MS

Problem no.	No. of suppliers	No. of customers	Inbound vehicles	Outbound vehicles	Best solution	Average solution	Average time (s)
01	10	10	02	03	2741.10	2742.31	4.70
02	10	15	03	04	3778.40	3806.87	4.88
03	20	20	04	06	5569.80	5629.09	4.80
04	20	25	05	07	6700.30	6782.84	5.21
05	30	30	06	08	8278.30	8377.96	5.18
06	30	35	07	10	9383.10	9663.48	5.06
07	40	40	08	11	10987.00	11198.00	5.08
08	40	45	08	12	12319.00	12454.60	5.17
09	50	50	09	14	14146.00	14308.20	5.40
10	50	55	10	15	15100.00	15380.20	5.51
11	60	60	11	17	16392.00	16535.90	5.31
12	70	70	13	19	19285.00	19483.00	5.71
13	80	80	15	22	22362.00	22595.90	5.88
14	90	90	16	25	25605.00	25872.60	5.91
15	100	100	18	28	28443.00	28900.30	5.95

Table 6: Best solution to the problem with 10-suppliers and 10-customers

Phase	Routes	Elements of total cost						Route-wise cost
		TC_P	SC_P	SC_S	MC_T	SC_C	OC_P	
1	CDF - S_2 - S_4 - S_3 - S_1 - S_9 - CDF	211.94	99	59	49	N/A	150	568.94
	CDF - S_{10} - S_8 - S_5 - S_6 - S_7 - CDF	123.64	101	61	51	N/A	150	486.64
3	CDF - C_3 - C_5 - C_1 - C_4 - CDF	337.12	79	N/A	N/A	49	100	565.12
	CDF - C_7 - C_2 - C_6 - C_{10} - CDF	417.40	73	N/A	N/A	43	100	633.40
	CDF - C_8 - C_9 - CDF	301.02	48	N/A	N/A	38	100	487.02

Table 6 above elaborates the best solution to the first problem with 10 suppliers in Phase 1 and 10 customers in Phase 3. Here it should be noted that the calculation of the total cost is explained in a previous section.

As per the best solution reported in Table 6 to the problem with 10 suppliers and 10 customers (the first problem in Table 5), it can be observed that the individual route-wise results in both phases can be obtained from the proposed Genetic Algorithm in an average of 4.7 seconds.

It can be noticed that the costs due to the highlighted elements (SC_S, MC_T and SC_C) in Table 6 are actually

incurred in Phase 2 as they are due to the three internal operations considered in this study. The total cost can be obtained by summing up all the elements of the total cost reported in Table 6 as 2741.12 units. Since there are two routes in Phase 1 and three routes in Phase 3, two inbound and three outbound vehicles are required to complete the task in the specified cost units which is same as the results obtained to the first problem given in Table 5.

CONCLUSIONS AND RECOMMENDATIONS

In this study, the Genetic Algorithm, which is known as a meta-heuristic method, is proposed to solve the VRPCD&MS model. In the developed Mixed Integer Linear Programming model, the cost of internal operations at the Cross Docking Facility (CDF) is added to the total cost. The unloading of the collected products from all the suppliers at the indoors of CDF, moving unloaded shipments from indoors to outdoors at the CDF, and loading the moved shipments onto the outbound vehicles to deliver the shipments to all the customers are the internal operations considered at the CDF. In the case of small-scale instances, the near optimal solutions obtained from the Genetic Algorithm are compared with the exact solutions obtained by the Branch and Bound algorithm. The results obtained for small-scale instances reveal that the GAP between exact solution and the near optimal solution is approximately 5%. Therefore, it can be concluded that, the proposed Genetic Algorithm is a better alternative to solve the VRPCD&MS model. It is observed that the computational time to reach a near optimal solution to a large-scale instance is under six seconds. Hence, it can be recommended that the proposed Genetic Algorithm can be used to schedule the routes of the vehicles at the last moment prior to the start of the time horizon. Since the Genetic Algorithm focuses only on the cost, it is recommended in future studies to take into account the time related constraints including arrival time of vehicles and time windows of each supplier/customer. This study further recommends that to incorporate additional constraints to the model, such as available vehicles to transport products and limitation of temporary storage capacity and other resources at the CDF, to generalize the study under investigation. Moreover, other existing heuristic or meta-heuristic methods can be exploited to investigate the adaptability in solving the VRPCD&MS model.

REFERENCES

Alinaghian M., Rezaei Kalantari M., Bozorgi-Amiri A. & Golghamat Raad N. (2016). A novel mathematical model for cross dock open-close vehicle routing problem with splitting. *International Journal of Mathematical Sciences and Computing* **3**(2): 21–31.
DOI: https://doi.org/10.5815/ijmsc.2016.03.02

Apte U.M. & Viswanathan S. (2000). Effective cross docking for improving distribution efficiencies. *International Journal of Logistics Research and Applications: A Leading Journal of Supply Chain Management* **3**(3): 291–302.
DOI: http://dx.doi.org/10.1080/713682769

Baniamerian A., Bashiri M. & Zabihi F. (2018a). A modified variable neighbourhood search hybridized with genetic algorithm for vehicle routing problems with cross-docking. *Electronic Notes in Discrete Mathematics* **66**: 143–150.
DOI: https://doi.org/10.1016/j.endm.2018.03.019

Baniamerian A., Bashiri M. & Zabihi F. (2018b). Two phase genetic algorithm for vehicle routing and scheduling problem with cross-docking and time windows considering customer satisfaction. *Journal of Industrial Engineering International* **14**(1): 15–30.
DOI: https://doi.org/10.1007/s40092-017-0203-0

Birim Ş. (2016). Vehicle routing problem with cross docking: a simulated annealing approach. *Procedia - Social and Behavioral Sciences* **235**: 149–158.
DOI: https://doi.org/10.1016/j.sbspro.2016.11.010

Buakum D. & Wisittipanich W. (2019). A literature review and further research direction in cross-docking. *Proceedings of the International Conference on Industrial Engineering and Operations Management MAR* 471–481.

Dantzig G. & Ramser J. (1959). The truck dispatching problem. *Management Science* **6**(1): 80–91.
DOI: https://doi.org/10.1287/mnsc.6.1.80

Dondo R. (2013). A branch-and-price method for the vehicle routing problem with cross-docking and time windows. *Iberoamerican Journal of Industrial Engineering* **5**(10): 16–25.
DOI: https://doi.org/10.13084/2175-8018.v05n10a02

Fakhrzad M.B. & Sadri Esfahani A. (2014). Modeling the time windows vehicle routing problem in cross-docking strategy using two meta-heuristic algorithms. *International Journal of Engineering, Transactions A: Basics* **27**(7): 1113–1126.
DOI: https://doi.org/10.5829/idosi.ije.2014.27.07a.13

Gnanapragasam S.R. & Daundasekera W.B. (2022). Optimal solution to the capacitated vehicle routing problem with moving shipment at the cross-docking terminal. *International Journal of Mathematical Sciences and Computing* **8**(4): 60–71.
DOI: https://doi.org/10.5815/ijmsc.2022.04.06

Goldberg D.E. (1989). *Genetic Algorithms in Search Optimization and Machine Learning*. Addison -Wesley, Reading, MA, USA.

Grangier P., Gendreau M., Lehuédé F. & Rousseau L.M. (2017). A matheuristic based on large Neighbourhood search for the vehicle routing problem with cross-docking. *Computers and Operations Research* **84**: 116–126.
DOI: https://doi.org/10.1016/j.cor.2017.03.004

Gunawan A., Widjaja A.T., Vansteenwegen P. & Yu V.F. (2020a). A matheuristic algorithm for solving the vehicle routing problem with cross-docking. *Proceedings of the*

14ᵗʰ Learning and Intelligent Optimization Conference, 12096 LNCS (Lion), pp. 9–15.
DOI: https://doi.org/10.1007/978-3-030-53552-0_2

Gunawan A., Widjaja A.T., Vansteenwegen P. & Yu V.F. (2020b). Adaptive large Neighbourhood search for vehicle routing problem with cross-docking. *2020 IEEE Congress on Evolutionary Computation (CEC)*, 19–24 July.
DOI: https://doi.org/10.1109/CEC48606.2020.9185514

Hasani-Goodarzi A. & Tavakkoli-Moghaddam R. (2012). Capacitated vehicle routing problem for multi-product cross-docking with split deliveries and pickups. *Procedia - Social and Behavioral Sciences* **62**(2010): 1360–1365.
DOI: https://doi.org/10.1016/j.sbspro.2012.09.232

Hasani Goodarzi A., Diabat E., Jabbarzadeh A. & Paquet M. (2022). An M/M/c queue model for vehicle routing problem in multi-door cross-docking environments. *Computers and Operations Research* **138**: 105513.
DOI: https://doi.org/10.1016/j.cor.2021.105513

Hasani Goodarzi A., Nahavandi N. & Zegordi S.H. (2018). A multi-objective imperialist competitive algorithm for vehicle routing problem in cross-docking networks with time windows. *Journal of Industrial and Systems Engineering* **11**(1): 1–23.

Holland J.H. (1975). *Adaptation in Natural and Artificial Systems*. The University of Michigan Press, Ann Arbor, MI, USA.

Ieva M.-K., Nihal S., Figen Y., Shahryar G. & Renata C. (2022). Optimizing multi cross-docking systems with a multi-objective green location routing problem considering carbon emission and energy consumption. *Energies* **15**(1530).
DOI: https://doi.org/10.3390/en15041530

Kargari Esfand Abad H., Vahdani B., Sharifi M. & Etebari F. (2018). A bi-objective model for pickup and delivery pollution-routing problem with integration and consolidation shipments in cross-docking system. *Journal of Cleaner Production* **193**: 784–801.
DOI: https://doi.org/10.1016/j.jclepro.2018.05.046

Larioui S. & Reghioui M. (2017). Resolution of the vehicle routing problem with cross-docking. *Proceedings of the International Conference on Industrial Engineering and Operations Management*, April, pp. 1184–1194.

Lee Y.H., Jung J.W. & Lee K.M. (2006). Vehicle routing scheduling for cross-docking in the supply chain. *Computers and Industrial Engineering* **51**(2): 247–256.
DOI: https://doi.org/10.1016/j.cie.2006.02.006

Liao C.J., Lin Y. & Shih S.C. (2010). Vehicle routing with cross-docking in the supply chain. *Expert Systems with Applications* **37**(10): 6868–6873.
DOI: https://doi.org/10.1016/j.eswa.2010.03.035

Moghadam S.S., Ghomi S.M.T.F. & Karimi B. (2014). Vehicle routing scheduling problem with cross docking and split deliveries. *Computers and Chemical Engineering* **69**: 98–107.
DOI: https://doi.org/10.1016/j.compchemeng.2014.06.015

Morais V.W.C., Mateus G.R. & Noronha T.F. (2014). Iterated local search heuristics for the vehicle routing problem with cross-docking. *Expert Systems with Applications* **41**(16): 7495–7506.
DOI: https://doi.org/10.1016/j.eswa.2014.06.010

Nikolopoulou A.I., Repoussis P.P., Tarantilis C.D. & Zachariadis E.E. (2016). Adaptive memory programming for the many-to-many vehicle routing problem with cross-docking. *International Journal of Operational Research* **19**(1): 1–38.
DOI: https://doi.org/10.1007/s12351-016-0278-1

Santos F.A., Mateus G.R. & Salles Da Cunha A. (2011a). A branch-and-price algorithm for a vehicle routing problem with cross-docking. *Electronic Notes in Discrete Mathematics* **37**(C): 249–254.
DOI: https://doi.org/10.1016/j.endm.2011.05.043

Santos F.A., Mateus G.R. & Salles Da Cunha A. (2011b). A novel column generation algorithm for the vehicle routing problem with cross-docking. *Lecture Notes in Computer Science (Including Subseries Lecture Notes in Artificial Intelligence and Lecture Notes in Bioinformatics)*, *6701 LNCS*, pp. 412–425.
DOI: https://doi.org/10.1007/978-3-642-21527-8_47

Tarantilis C.D. (2013). Adaptive multi-restart Tabu Search algorithm for the vehicle routing problem with cross-docking. *Optimization Letters* **7**(7): 1583–1596.
DOI: https://doi.org/10.1007/s11590-012-0558-5

Vahdani B., Reza T.M., Zandieh M. & Razmi J. (2012). Vehicle routing scheduling using an enhanced hybrid optimization approach. *Journal of Intelligent Manufacturing* **23**(3): 759–774.
DOI: https://doi.org/10.1007/s10845-010-0427-y

Vahdani B. & Zandieh M. (2010). Scheduling trucks in cross-docking systems: Robust meta-heuristics. *Computers and Industrial Engineering* **58**(1): 12–24.
DOI: https://doi.org/10.1016/j.cie.2009.06.006

Van Belle J., Valckenaers P. & Cattrysse D. (2012). Cross-docking: State of the art. *Omega* **40**(6): 827–846.
DOI: https://doi.org/10.1016/j.omega.2012.01.005

Wen M., Larsen J., Clausen J., Cordeau J.F. & Laporte G. (2009). Vehicle routing with cross-docking. *Journal of the Operational Research Society* **60**(12): 1708–1718.
DOI: https://doi.org/10.1057/jors.2008.108

Yin P.Y. & Chuang Y.L. (2016). Adaptive memory artificial bee colony algorithm for green vehicle routing with cross-docking. *Applied Mathematical Modelling* **40**(21–22): 9302–9315.
DOI: https://doi.org/10.1016/j.apm.2016.06.013

Yu V.F., Jewpanya P. & Redi A.A.N.P. (2014). A simulated annealing heuristic for the vehicle routing problem with cross-docking. In: *Logistics Operations, Supply Chain Management and Sustainability*, pp. 15–30. Springer.
DOI: https://doi.org/10.1007/978-3-319-07287-6

Yu V.F., Jewpanya P. & Redi A.A.N.P. (2016). Open vehicle routing problem with cross-docking. *Computers and Industrial Engineering* **94**: 6–17.
DOI: https://doi.org/10.1016/j.cie.2016.01.018

RESEARCH ARTICLE

Agricultural Economics

Impact of climate on tea yield: an empirical investigation from Sri Lanka

JC Edirisinghe[1*], H Ranjan[1], HMLK Herath[1], UK Jayasinghe-Mudalige[1], M Wijeratne[2], V Kuruppu[1], C Jayathilake[3], W Wijesuriya[4], K Somarathna[1], S Karunaratne[5], S Jayawardana[6], D Gunathilaka[7] and D Balasooriya[4]

[1] *Department of Agribusiness Management, Faculty of Agriculture and Plantation Management, Wayamba University of Sri Lanka, Makandura, Gonawila (NWP), Sri Lanka.*

[2] *Tea Research Institute of Sri Lanka, Sri Lanka.*

[3] *Information and Communication Centre, Wayamba University of Sri Lanka, Sri Lanka.*

[4] *Rubber Research Institute of Sri Lanka, Sri Lanka.*

[5] *Commonwealth Scientific and Industrial Research Organization*

[6] *Department of Meteorology, Sri Lanka.*

[7] *Department of Export Agriculture, Uwa Wellassa University of Sri Lanka, Sri Lanka.*

Abstract: Agriculture is heavily climate dependent. Tea cultivation is of no exception. Tea is cultivated in many developing nations around the globe and the climate change impact is to be mostly felt by developing nations in comparison to the developed. In countries such as Sri Lanka, where the major portion of export earning from agriculture comes from the tea industry, the climate change impacts would harm its progress. Hence, understanding how climate has been linked with production would pave the way for development of a country specific policy. To this end, this research attempted to measure the long-run relationship of the climate with the yield per hectare, using monthly data from 2005 to 2019. A panel Autoregressive Distributed Lag model (ARDL) was used to obtain long-run cointegration between minimum and maximum temperatures and the amount of rainfall received. Data on production and input variables were obtained from records kept at 37 large-scale tea estates at monthly intervals. Monthly temperature and rainfall data were obtained from the Meteorological Department of Sri Lanka. Panel cointegration tests indicated that there is a coexisting long-run relationship between climate variables and the tea yield. Maximum temperature had a positive relationship with yield, but minimum temperature shows a long-run negative relationship. Rainfall is positively related. Production inputs show a long-run positive impact. Thus, the possible negative impacts of rising minimum temperature could be overcome if proper management practices are adopted in the long-run.

INTRODUCTION

Climate change is one of the greatest challenges faced in this century. Increasing global temperature and drought are altering agricultural production and productivity in the world (Appiah *et al.*, 2018; Ahsan *et al.*, 2020; Markou *et al.*, 2020). Crop yields across Europe, Sub-Saharan Africa, and Australia have decreased because of climate change (Ray *et al.*, 2019). The effects of climate change are unevenly distributed across the world. Adverse impacts of climate change on agriculture will have undesirable effects on food prices and therefore food security in the future. Predictions are that food prices will rise by 80% by 2050 due to climate change impacts on agriculture (Mbow *et al.*, 2019). Agriculture is the backbone of many countries in the developing world, contributing in larger proportions to their gross domestic product (GDP), and in some cases are the main source of foreign exchange earnings. Therefore, the impacts of climate change need more attention than they

* Corresponding authors (jagathed07@gmail.com; https://orcid.org/0000-0003-4602-9266)

have received over the years, especially on agriculture in the developing world.

Sri Lanka is also an agriculturally based small island where a high proportion (27.1 %) of its population is involved in agricultural activities. Agriculture accounted for 6.9 % of the Sri Lanka's GDP in 2021 (Central Bank of Sri Lanka, 2021). Out of the agricultural products, tea is one of the main export earners of the country and Sri Lankan tea is a major player in the international tea market. At present, Sri Lanka is the third largest exporter of tea while being the fourth largest producer in the world (Sri Lanka Export Development Board, 2020). Sri Lanka has a 150-year history of tea cultivation with its origin in 1867. This industry has traditionally been the largest employment provider. According to estimates, the tea industry provides direct and indirect employment for about 1.5 million people, 11% of labour force of the country (Central Bank of Sri Lanka, 2018). Foreign exchange earnings from tea exports accounted for 11.3% of total exports earning in 2019 which is equivalent to US\$ 1,346 million, the second-largest contributor to the total export earnings of Sri Lanka (Central Bank of Sri Lanka, 2019). Additionally, the tea industry accounts for 0.7% of the Gross Domestic Product (GDP) of Sri Lanka (Central Bank of Sri Lanka, 2020).

Around 4% of land area is covered by tea cultivation in Sri Lanka, which is close to 203,000 hectares (Sri Lanka Export Development Board, 2020). Tea is cultivated at three elevations: low (<600 m), medium (600 m – 1200 m) and high (>1200 m), by large scale tea estates as well as smallholders in lands less than 4 hectares. A temperature range of 20-30 degrees Celsius is desirable for shoot growth in tea (Jayasinghe *et al.*, 2020). Tea needs a higher mean annual rainfall than most other perennial crops (TRI, 2002; Galmés *et al.*, 2007) with an optimum around 2500 mm – 3000 mm (Jayasinghe *et al.*, 2020). Data show that temperature in Sri Lanka is rising and the temperature change with respect to a baseline climatology is given in Figure 1. Hence, the impact of this on the main export crop in the nation needs attention.

MATERIALS AND METHODS

Data

Data were collected from 37 large-scale estates producing tea in three elevations: high, medium, and low. Data were in monthly intervals and related to the period 2005 – 2019. Monthly green leaf production and the extent of cultivation were obtained from each estate and the yield was calculated using those values. Other inputs into production, the labour, fertilizer, and chemicals were recorded as costs. Therefore, these were deflated by using the consumer price index (CPI). All input variables were converted to amounts per unit land area by dividing the relevant value by the cultivation extent. In addition to input and output variables, the GPS locations of all estates were recorded. These points were used to predict temperature and rainfall data obtained from the meteorological stations to exact GPS points of the estates by a Kriging procedure. All variables were converted to their natural logarithm values prior to estimation.

Model

The form of a panel ARDL model can be stated as.

$$YIELD_{it} = \sum_{j=1}^{p} \delta_i YIELD_{i,t-j} + \sum_{j=0}^{q} \beta'_{ij} X_{i,t-j} + \varphi_i + \varepsilon_{it}$$

To obtain the short run and long-run relationships, the model is reparametrized as below:

$$\Delta YIELD_{it} = \theta_i \big(YIELD_{i,t-j} - \lambda'_i X_{it} \big) + \sum_{j=1}^{p-1} \xi_{ij} \Delta YIELD_{i,t-j}$$
$$+ \sum_{j=0}^{q-1} \beta'_{ij} \Delta X_{i,t-j} + \varphi_i + \varepsilon_{it}$$

In this specification, λ_i is the vector of long-run relationships which includes the long-run relationships of all independent variables in the model. The group specific speed of adjustments is given by $\theta_i = -(1 - \delta_i)$ which is expected to be less than zero. If $\theta_i = 0$, then there is no long-run relationship. The term $\big(YIELD_{i,t-j} - \lambda'_i X_{it} \big)$
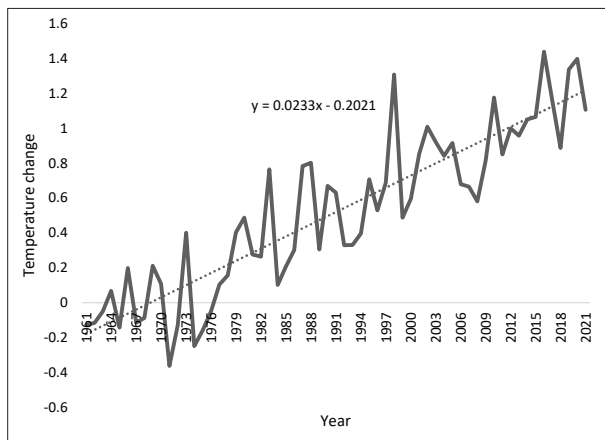

Figure 1: Annual change in temperature in Sri Lanka (Meteorological year). Source: FAO, 2022

denotes the error correction while the $\xi_{ij}, \boldsymbol{\beta}'_{ij}$ are the short run dynamic coefficients. The $\boldsymbol{X}_{it}$, the $k \times 1$ vector is allowed to be purely I (0) or I (1) or cointegrated. This vector included three weather variables, the monthly averages of minimum and maximum temperatures and rainfall. There are many other input variables at play in explaining the variation of the yield. These are included as controls in the model. Thus, most common variables used in tea production, fertilizer and chemicals applied per unit area, and labour use per unit area were included. Because these inputs are recorded in estates as costs, they were deflated using the Consumer Price Index (CPI) to obtain constant values prior to the estimation.

There are several approaches for the estimation of this model. A fixed-effects (FE) estimation approach is suitable if one assumes that the time-series data for each group could be pooled and only the intercepts are permitted to vary across units. In the mean group (MG) estimator proposed by Pesaran & Smith (1995), the simple arithmetic average of coefficients is obtained after the model is fit separately for each group. Additionally, Pesaran *et al*. (1997) proposed a pooled mean group (PMG) estimator, where pooling and averaging carried out in the earlier two models are combined allowing intercept, short-run coefficients, and error variances to differ across the groups, while constraining the long-run coefficients to be equal across units (Blackburne & Frank 2007).

To examine the stationarity level and order of integration of the selected variables, a unit root test was carried out, the 'Im–Pesaran–Shin' (2003) unit root test, which uses mean of individual unit root test statistics to test unit roots of dynamic heterogeneous panels. Additionally, the 'Im–Pesaran–Shin test' reports a standardized t-bar test statistic grounded on the (augmented) Dickey-Fuller statistics averaged across the groups. Conducting such a test is important to ensure that no variable of order 2 is integrated. The optimum lag length of the panel ARDL model described above is selected by running ARDL models for each panel. Optimum lags were selected based on Akaike Information Criteria (AIC) and Bayesian Information Criteria (BIC). The most common lag for each variable was chosen to be used in the panel ARDL model. If cointegration exists, the panel ARDL model is said to have an error correction model interpretation. Therefore, there is better evidence that the long-run estimates are common across all estates under study. The cointegration test derived by Kao (1999) was applied to test cointegration, which assumes a cointegrating vector that is the same across all panels. Finally, the Hausman test was applied to select between MG and PMG estimators.

RESULTS AND DISCUSSION

Table 1 reports the descriptive statistics of the data used.

Table 1: Descriptive Statistics

Variable	Unit	Mean	Std. dev.
Yield	Kgs of green leaf per Ha per month	440.63	278.89
Extent	Hectares	193.22	110.72
Lab	LKR per Ha in constant LKR	17434.98	10722.61
Fert	LKR per Ha constant LKR	2427.43	2680.79
Chem	LKR per Ha constant LKR	498.23	844.94
Min T	Celsius	20.04	3.84
Max T	Celsius	27.80	3.51
RF	Millimeters per month	221.40	135.24

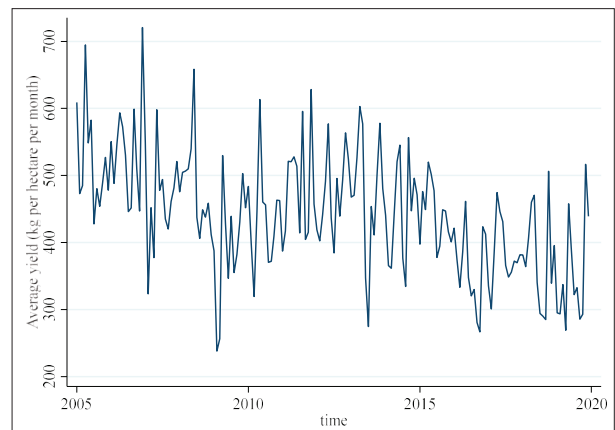Lab: Labour, Fert: Fertilizer, Chem: Chemicals, Min T: Minimum temperature, Max T: Maximum temperature, RF: Rainfall

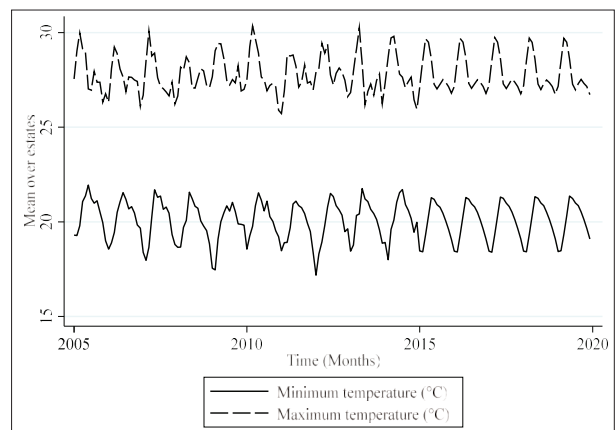**Figure 2:** Average monthly estate yield (kg/ha/month) from 2005–2019

Figure 3: Variation of Minimum and maximum temperature (^{0}C) from 2005–2019 averaged over estates
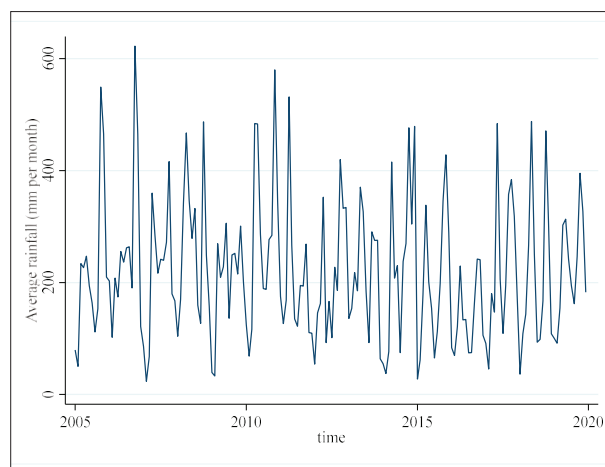
Figure 4: Variation in monthly rainfall 2005–2019 averaged over estates

According to the Figure 2, the estate level yield has declined over the years in the study period. The temperature shows a monthly variation but there is no marked overall trend from 2005-2019 (Figure 3). Rainfall, however, shows a greater variation (Figure 4).

Correlation analysis

The selected variables in the model were first subjected to correlation analysis. The results are presented in Table 2. Results suggested that labour, fertilizer, and chemical use are positively correlated to yield. Out of the climate variables, temperature (both maximum and minimum) shows a negative correlation with yield. However, rainfall show a positive correlation. Maximum and minimum temperatures show high correlation and may create multicollinearity in estimation. However, both variables were retained in the model estimation because of their importance in the model.

Table 2: Correlation analysis of variables in the model

	*ln*Yield	*ln*Lab	*ln*Fert	*ln*Chem	*ln*MinT	ln MaxT	*ln*RF
*ln*Yield	1.000						
*ln*Lab	0.617*	1.000					
*ln*Fert	0.468*	0.492*	1.000				
*ln*Chem	0.240*	0.179*	0.239*	1.000			
*ln*MinT	-0.304*	-0.407*	-0.139*	-0.199*	1.000		
*ln*MaxT	-0.352*	-0.481*	-0.262*	-0.251*	0.867*	1.000	
*ln*RF	0.192*	0.168*	0.264*	0.037*	0.127*	-0.033*	1.000

* Significant at 0.05

Lab: Labour, Fert: Fertilizer, Chem: Chemicals, Min T: Minimum temperature, Max T: Maximum temperature, RF: Rainfall

Table 3: Results of the Im-Pesaran-Shin test

Variable	IPS	IPS with trend
*ln*Yield	-31.725 (0.000)	-34.520 (0.000)
*ln*Lab	-29.066 (0.000)	-32.001 (0.000)
*ln*Fert	-32.774 (0.000)	-33.999 (0.000)
*ln*Chem	-29.202 (0.000)	-30.906 (0.000)
*ln*MinT	-29.599 (0.000)	-29.623 (0.000)
*ln*MaxT	-34.823 (0.000)	-34.833 (0.000)
*ln*RF	-42.894 (0.000)	-43.075 (0.000)

Note: Figures within parentheses are p values
Lab: Labour, Fert: Fertilizer, Chem: Chemicals, Min T: Minimum temperature, Max T: Maximum temperature, RF: Rainfall

Unit Root Test

Time series data are prone to unit roots and hence may be non-stationary. Use of such non-stationary series may create spurious regression outcomes. Therefore, all variables in the model were tested for unit roots. The results of the unit root tests are provided in Table 3. Specifically, the 'Im-Pesaran-Shin' (IPS) test proposed by Im *et al.* (2003) was used. The null hypothesis of IPS test is that all panels contain unit roots, hence a significant result of the test would indicate that data do not contain unit roots. The IPS with and without trend was used and the significance with respect to all variables show that unit roots are absent in them and thus, the data are stationary.

Optimum Lag Length Selection

Selection of optimum lag length is important as ARDL is sensitive to the lag lengths selected (Abbas, 2020). Since panel data were used, lag length selection was carried out for each panel using Akaike Information Criteria (AIC) values to select the lag lengths of each panel and then obtain the most common lag length of each variable selected. The results suggested a lag of one for dependent variable (yield). Of the independent variables, labour reported one lag while the other variables (fertilizer, chemical, minimum temperature, maximum temperature, and the rainfall) reported zero lags (Table 4). Hence, an ARDL (1,1,0,0,0,0,0) model was estimated.

Table 4: Lag lengths of each variable

Variable	Optimal lag length
lnYield	1
lnLab	1
lnFert	0
lnChem	0
lnMinT	0
lnMaxT	0
lnRF	0

Lab: Labour, Fert: Fertilizer, Chem: Chemicals, Min T: Minimum temperature, Max T: Maximum temperature, RF: Rainfall

Cointegration test

The cointegration test was done to see whether data are related in the long-run before the panel ARDL model was estimated. Here, the interest is to see whether there is a long-run relationship of labour, fertilizer, and chemical use, and especially the climate variables with estate level yield. Hence, the cointegration relationship was specified as.

$$lnYield_{it} = \gamma_i + \beta_1 lnLab_{it} + \beta_2 lnFert_{it} + \beta_3 lnChem_{it}$$

$$+ \beta_4 lnMinT_{it} + \beta_5 lnMaxT_{it} + \beta_6 lnRF_{it} + e_{it}$$

A model with panel-specific means without a time trend was used. The null hypothesis of this test is that no panels are cointegrated while the alternative hypothesis is that all panels are cointegrated. Table 5 reports 6 test statistics and their significance levels. The null hypothesis of no cointegration was rejected by all test statistics, favouring the alternative hypothesis that there exists a cointegration relationship between yield and the independent variables defined in the above model.

Table 5: Results of the Kao cointegration test

	Statistic	p-value
Modified Dickey–Fuller t	-20.687	0.0000
Dickey–Fuller t	-18.718	0.0000
Augmented Dickey–Fuller t	-10.415	0.0000
Unadjusted modified Dickey–Fuller t	-100.000	0.0000
Unadjusted Dickey–Fuller t	-35.411	0.0000

Model Checking – Hausman Test

This was carried out to test which estimator best fits the data at hand. Pooled mean group (PMG), mean group (MG), and dynamic fixed effects (DFE) models were estimated and compared using the Hausman test (Hausman, 1978). The results are reported in Table 6. The null hypothesis of these Hausman tests was that there is homogeneity. The probability value for PMG vs. MG is greater than 0.05 and hence, the null hypothesis is rejected; the PMG estimator is more efficient than the MG estimator. The second test compared PMG with DFE, and the resulting probability value is 0.9993. This indicates that best estimator to be used finally is the PMG estimator.

Table 6: Hausman test results of model selection

Model	Chi2	Prob>chi2
PMG Vs. MG	3.12	0.7936
PMG Vs. DFE	0.34	0.9993

The long-run relationship between climate variables and tea yield

The model consisted of three climate related variables: the minimum and maximum temperatures, and the rainfall. All these three variables are significant in at 5% error level. The average maximum temperature or the day temperature has a positive relationship with yield in the long-run. A one percent increase in the temperature would lead to an increase in yield by 1.352 % in the long-run. However, the average minimum temperature shows a negative long-run equilibrium relationship with the yield of tea. A one percent increase in the average minimum temperature would reduce tea yield by 0.81 % (Table 7). Impacts of temperature on tea yields as well as production has been studied in Sri Lanka as well as in other countries. Mallik & Ghosh (2022) reported that increases in summer and monsoon temperatures reduce tea yield in Dooars Region in India. Duncan *et al.* (2016) observed decreasing tea yields with increased monthly average temperatures in Assam, India. They

collect monthly data from 2004 – 2013 from 82 tea gardens and used a panel data regression to estimate the climate effects. However, they have used only average temperature and no distinction between minimum and maximum temperature has been made by them. Wijeratne (1996) also suggest that increase in temperature adversely affect growth and yield of tea. However, from the present dataset, the yield is negatively affected in the long-run (*i.e.*, the climate effect) only when the minimum or the night temperature increases, but not by the increase in day temperature. Maximum temperature has a positive effect. Yan *et al.* (2021) studied the effects of extreme weather events on tea production in China. They have reported that both heat and cold extremes negatively affect tea yields. However, they also predict positive net impacts of climate change on tea yield at both the 1.5 °C and 2.0 °C global warming levels. As tea is a C3 plant, increased CO_2 raises yield, and it can be further amplified by rising temperatures especially at high elevations, although it can be negatively affected in low elevations if increasing temperature reaches the ceiling temperature range. In the present dataset, the average maximum temperature in the study period is 27.8 ± 3.5 °C (Figure 3) and therefore, it does not reach the ceiling temperature range. Han *et al.* (2017) also found that in some regions, an increase in temperature would increase yield. Sitienei *et al.* (2017) found that climatic variables during some months in both the concurrent year and the previous year were positively correlated with the tea yield. Further, Sen *et al.* (1966) also reported that rise in mean temperature during the cold weather period increased tea yield in the Assam valley.

In Table 7, rainfall shows a positive and significant long-run association with the tea yield. A one percent increase in rainfall would increase tea yield by 0.135%. To have a good tea cultivation, a minimum annual rainfall between 1150 mm and 1400 mm is needed. The optimal annual rainfall is around 2500 mm – 3000 mm (Carr, 1999; Jayasinghe *et al.*, 2020). The average annual rainfall in the present data set is 2657 ± 609 mm. The findings suggest that decreasing rainfall would reduce tea yield per hectare. Low moisture content in soil is known to reduce photosynthesis and hence growth of tea plants (Ahmed *et al.*, 2014). Hence, prolonged dry periods would significantly hamper yields of tea. The positive effect of rainfall was also confirmed by Boehm *et al.* (2014), who studied the relationship between rainfall and tea productivity in India. Dutta *et al.* (2011) found that monthly rainfall has a positive effect on tea productivity in Northern India. They used a combined statistical and modelling approach to study the impact factors affecting tea productivity. Numerous studies revealed that uneven distribution of rainfall reduces the tea production in many tea-producing nations, including China (Boehm *et al.*,

2016; Lou *et al.*, 2021), India (Duncan *et al.*, 2016; Biggs *et al.*, 2018; Raj *et al.*, 2019), and Sri Lanka (Wijeratne *et al.*, 2007; Gunathilaka *et al.*, 2017).

Long-run effects of input use in tea yield

In the discussion of climate's impact on tea yields, other key factors that affect the yield need to be controlled, and therefore they were included in the model as covariates. All descriptions of the effects of temperature and rainfall are, therefore, *'ceteris paribus'* explanations. However, as one would recognize, key inputs such as labour, fertilizer, etc. play a vital role in increasing yield. The production input variables used in the study are used per hectare, as the dependent variable is green leaf production per hectare. Results in the Table 7 show that labour, fertilizer, and chemical usage all have a long-term positive relationship with yield. Out of the three inputs, production elasticity with labour is the highest indicating a 0.235 % increase in yield for 1 % increase in labour use. The error correction term, ECT was –0.417 and significant. The ECT give the speed of adjustment from the short-run disequilibrium to the long-run equilibrium. This indicates that 42% of the disequilibrium in tea yield in the short-run is adjusted to equilibrium by the covariates in the model monthly.

Table 7:   Results of the long-run analysis

Variable	Coefficient	Std. errs.	P>z
*ln*MinT	-0.816*	0.119	0.000
*ln*MaxT	1.352*	0.194	0.000
*ln*RF	0.135*	0.015	0.000
L(*ln*Lab)	0.235*	0.021	0.000
L(*ln*Fert)	0.033*	0.008	0.000
*ln*Chem	0.022*	0.009	0.019
ECT	-0.417*	0.039	0.000
Log-likelihood	855.739		
AIC	-1683.48		
BIC	-1596.22		

Lab: Labour, Fert: Fertilizer, Chem: Chemicals, Min T: Minimum temperature, Max T: Maximum temperature, RF: Rainfall

CONCLUSIONS

The research findings unveiled essential insights regarding the enduring relationship between climate variables and tea yields in Sri Lankan tea plantations from 2005 to 2019. Pairwise correlation analysis indicated a negative correlation between tea yield and both minimum and

maximum temperatures, whereas rainfall exhibited a positive correlation with yield.

The analysis derived from the study's models revealed intriguing results. Maximum temperature displayed a long-term positive cointegration relationship with tea yield, while minimum temperature exhibited a negative long-term cointegration relationship. This finding diverges from prior studies, highlighting that the long-term response of tea yield to temperature differs significantly between night time and daytime temperatures. Notably, rising night temperatures predominantly impact tea yield as opposed to daytime temperatures.

Furthermore, the research identified a sustained positive equilibrium relationship between rainfall and tea yield. Consequently, increased rainfall was associated with higher tea yields over the long term, while a decrease in rainfall predicted a reduction in future tea yields. The research also observed a declining trend in the yield of tea estates. However, it noted a long-term positive cointegration relationship between inputs used in tea cultivation and the yield.

Given the context of climate change, the research underscores the critical importance of proper tea land management practices such as timely fertilization, effective pest and disease control, and appropriate pruning. These measures are crucial in mitigating the expected yield losses due to the impact of climate change on tea cultivation.

Conflict of interest statement

There are no conflicts of interests

Acknowledgements

REFERENCES

Abbas S. (2020) Climate change and cotton production: an empirical investigation of Pakistan. *Environmental Science and Pollution* **27**(23): 29580–29588.
  DOI: https://doi.org/10.1007/s11356-020-09222-0

Ahmed S., Stepp J.R., Orians C., Griffin T., Matyas C., Robbat A., Cash S., Xue D., Long C., Unachukwu U. & Buckley S. (2014). Effects of extreme climate events on tea (*Camellia sinensis*) functional quality validate indigenous farmer knowledge and sensory preferences in tropical China. *PloS ONE* **9**(10): e109126.

DOI: https://doi.org/10.1371/journal.pone.0109126

Ahsan F., Chandio A.A. & Fang W. (2020). Climate change impacts on cereal crops production in Pakistan evidence from cointegration analysis. *International Journal of Climate Change Strategies and Management* **12**(2): 257–269.
  DOI: https://doi.org/10.1108/IJCCSM-04-2019-0020

Appiah K., Du J. & Poku J. (2018) Causal relationship between agricultural production and carbon dioxide emissions in selected emerging economies. *Environmental Science and Pollution Research* **25**(25): 24764–24777.
  DOI: https://doi.org/10.1007/s11356-018-2523-z

Biggs E.M., Gupta N., Saikia S.D. & Duncan J. M. (2018). The tea landscape of Assam: Multi-stakeholder insights into sustainable livelihoods under a changing climate. *Environmental Science & Policy* **82**: 9–18.
  DOI: https://doi.org/10.1016/j.envsci.2018.01.003

Blackburne III E.F. & Frank M.W. (2007) Estimation of nonstationary heterogeneous panels. *The Stata Journal* **7**(2): 197–208.
  DOI: https://doi.org/10.1177/1536867X0700700204

Boehm R., Cash S.B., Anderson B.T., Ahmed S., Griffin T.S., Robbat A., Stepp J.R., Han W., Hazel M. & Orians C.M. (2016). Association between empirically estimated monsoon dynamics and other weather factors and historical tea yields in China: results from a yield response model. *Climate* **4**(2): 20.
  DOI: https://doi.org/10.3390/cli4020020

Carr M.K.V. (1999). Evaluating the impact of research for development: tea in Tanzania. *Experimental Agriculture* **35**(3): 247–264.
  DOI: https://doi.org/10.1017/S0014479799003051

Central Bank of Sri Lanka (2018). *Annual Report 2018*. Available at *https://www.cbsl.gov.lk/en/publications/economic-and-financial-reports/annual-reports/annual-report-2018*. Accessed 14 November 2022.

Central Bank of Sri Lanka (2019). *Annual Report 2019*. Available at *https://www.cbsl.gov.lk/en/publications/economic-and-financial-reports/annual-reports/annual-report-2019*. Accessed 14 November 2022.

Central Bank of Sri Lanka (2020). *Annual Report 2020*. Available at *https://www.cbsl.gov.lk/en/publications/economic-and-financial-reports/annual-reports/annual-report-2020*. Accessed 14 November 2022.

Central Bank of Sri Lanka (2021). *Annual Report 2021*. Available at *https://www.cbsl.gov.lk/en/publications/economic-and-financial-reports/annual-reports/annual-report-2021*. Accessed 15 November 2022.

Dutta R., Smaling E.M.A., Bhagat R.M., Tolpekin V.A. & Stein A. (2012). Analysis of factors that determine tea productivity in North-eastern India: A combined statistical and modelling approach. *Experimental Agriculture* **48**(1): 64–84.
  DOI: https://doi.org/10.1017/S0014479711000834

Duncan J.M., Saikia S.D., Gupta N. & Biggs E.M. (2016). Observing climate impacts on tea yield in Assam, India. *Applied Geography* **77**: 64–71. DOI: https://doi.org/10.1016/j.apgeog.2016.10.004

Food and Agriculture Organization (FAO) (2022). FAOSTAT *Statistical Database*. Food and Agriculture Organization of the United Nations, Rome, Italy.

Galmés J., Medrano H. & Flexas J. (2007). Photosynthetic limitations in response to water stress and recovery in Mediterranean plants with different growth forms. *New Phytologist* **175**: 81–93.
DOI: https://doi.org/10.1111/j.1469-8137.2007.02087.x

Gunathilaka R.D., Smart J.C. & Fleming C.M. (2017). The impact of changing climate on perennial crops: The case of tea production in Sri Lanka. *Climatic Change* **140**: 577–592.
DOI: https://doi.org/10.1007/s10584-016-1882-z

Han W.Y., Huang J.G., Li X., Li Z.X., Ahammed G.J., Yan P. & Stepp J.R. (2017). Altitudinal effects on the quality of green tea in east China: a climate change perspective. *European Food Research and Technology* **243**(2): 323–330.
DOI: https://doi.org/10.1007/s00217-016-2746-5

Hausman J.A. (1978). Specification tests in econometrics. *Econometrica* **46**(6): 1251–1271.

Im K.S., Pesaran M.H. & Shin Y. (2003). Testing for unit roots in heterogeneous panels. *Journal of Econometrics* **115**(1): 53–74.
DOI: https://doi.org/10.1016/S0304-4076(03)00092-7

Jayasinghe S.L., Kumar L. & Hasan M.K. (2020). Relationship between environmental covariates and Ceylon tea cultivation in Sri Lanka. *Agronomy* **10**(4): 476.
DOI: https://doi.org/10.3390/agronomy10040476

Kao C. (1999). Spurious regression and residual-based tests for cointegration in panel data. *Journal of Econometrics* **90**(1): 1–44.
DOI: https://doi.org/10.1016/S0304-4076(98)00023-2

Labour Force by sector. *www.statistics.gov.lk*. Accessed 19 February 2021.

Lou W., Sun K., Zhao Y., Deng S. & Zhou Z. (2021). Impact of climate change on inter-annual variation in tea plant output in Zhejiang, China. *International Journal of Climatology* **41**: E479–E490.
DOI: https://doi.org/10.1002/joc.6700

Mallik P. & Ghosh T. (2022). Impact of climate on tea production: a study of the Dooars region in India. *Theoretical and Applied Climatology* **147**:559–573.
DOI: https://doi.org/10.1007/s00704-021-03848-x

Markou M., Moraiti C.A., Stylianou A. & Papadavid G. (2020). Addressing climate change impacts on agriculture: adaptation measures for six crops in Cyprus. *Atmosphere* **11**(5): 483.
DOI: https://doi.org/10.3390/atmos11050483

Mbow C. *et al*. (12 authors) (2019). Food Security. In: *Climate change, the monsoon, and Tea Yields in China* (eds. P.R. Shukla *et al*.). *Proceedings of the Agricultural and Applied Economics Association's Annual Meeting, Minneapolis, USA*, pp. 27–29.

Pesaran M.H. & Smith R. (1995). Estimating long-run relationships from dynamic heterogeneous panels. *Journal of Econometrics* **68**(1): 79–113.
DOI: https://doi.org/10.1016/0304-4076(94)01644-F

Pesaran M.H., Shin Y. & Smith R.P. (1997). Pooled estimating of long-run relationships in dynamic heterogeneous panels. *Cambridge Working Papers in Economics 9721*. Faculty of Economics, University of Cambridge, UK.

Raj E.E., Ramesh K.V. & Rajkumar R. (2019). Modelling the impact of agrometeorological variables on regional tea yield variability in South Indian tea-growing regions: 1981–2015. *Cogent Food & Agriculture* **5**(1): 1581457.
DOI: https://doi.org/10.1080/23311932.2019.1581457

Ray D.K., West P.C, Clark M., Gerber J.S., Prishchepov A.V. & Chatterjee S. (2019). Climate change has likely already affected global food production. *PLoS ONE* **14**(5): e0217148.
DOI: https://doi.org/10.1371/journal.pone.0217148

Sen A.R., Biswas A.K. & Sanyal D.K. (1966). The influence of climatic factors on the yield of tea in the Assam valley. *Journal of Applied Meteorology* (1962–1982) **5**(6): 789–800.
DOI: https://doi.org/10.1175/1520-0450(1966)005<0789: TIOCFO>2.0.CO;2

Sitienei B.J., Juma S.G. & Opere E. (2017). On the use of regression models to predict tea crop yield responses to climate change: A case of Nandi East, sub-county of Nandi County, Kenya. *Climate* **5**(3): 54.
DOI: https://doi.org/10.3390/cli5030054

Sri Lanka Export Development Board (2020). Pure Ceylon Tea: A Beverage, Legacy & Way of Life. Available at *https://www.srilankabusiness.com/tea/about-tea/*, Accessed 12 October 2022.

Tea Research Institute of Sri Lanka (2002). T.R.I. Advisory Circular. *Guidelines on Land Suitability Classification for Tea*, pp. 1–3. Tea Research Institute of Sri Lanka, Talawakelle.

Wijeratne M.A. (1996). Vulnerability of Sri Lanka tea production to global climate change. *Water, Air, and Soil Pollution* **92**(1): 87–94.
DOI: https://doi.org/10.1007/BF00175555

Wijeratne M.A., Anandacoomaraswamy A., Amarathunga M.K.S.L.D., Ratnasiri J., Basnayake B.R.S.B. & Kalra N. (2007). Assessment of impact of climate change on productivity of tea (*Camellia sinensis* L.) plantations in Sri Lanka. *Journal of the National Science Foundation of Sri Lanka* **35**(2): 119–126.
DOI: https://doi.org/10.4038/jnsfsr.v35i2.3676

Yan Y., Sujong J., Park C.-E., Mueller N.D., Shilong P., Hoonyoung P., Jaewon J., Chen X., Wang X. & Liu J. (2021). Effects of extreme temperature on China's tea production. *Environmental Research Letters* **16**(4): 044040.
DOI: https://doi.org/10.1088/1748-9326/abede6

RESEARCH ARTICLE

Acoustics

Determination of noise level and acoustic analysis of toys for children in Sri Lanka market

CM Kalansuriya*, RM Weerasingha, DC Jayaratne and KKN Darshana
Electro Technology Laboratory, Industrial Technology Institute, Colombo 7, Sri Lanka.

Abstract: This study was conducted to determine the existing noise levels and perform acoustic analysis on different toys in the Sri Lankan market. The study was carried out using international references, and the noise level descriptors LpAeq, LpCpeak, and LpAFmax were recorded during measurement. A total of 205 toys were selected, and 1986 measurements were taken for analysis. The study reveals that 59 (28.8%) of the 205 toys in different categories had noise levels that exceeded two parameters, and 35 (17.1%) exceeded one parameter, considering the LpAeq, LpCpeak, and LpAFmax parameter values as described in BS EN 71-1:2011+A3:2014 Safety of toys. Measurements indicate that cap firing, wind, and squeeze toys have higher noise levels than international standards (reference values for cap firing: 125 dB, squeeze and cap firing: 110 dB). The study clearly indicates that when measuring noise levels in the frequency range compared to our normal reference hearing range (150 Hz to 5 kHz), it may affect the hearing levels. The study demonstrates the necessity for awareness, warning signs, and enforcing toy acoustic standards and regulations to improve the situation in Sri Lanka.

Keywords: Noise level, Sri Lanka market, toys noise, toys for children.

INTRODUCTION

Many toys produce noise, and children playing with toys also produce noise. Children are always learning something while playing with toys. Toys play an important role in the mental and physical development of children. They contribute to child development, and play is an essential part of growing up. It helps children to improve certain skills and abilities during their childhood. However, toys must be safe for children to play with. The sounds generated by electronic and mechanical toys should not lead to damage to children's hearing. The maximum impulse and continuous sound levels emitted by toys should be within safe limits.

Most importantly, a child cannot verbally express or identify a hearing loss until at least the age of six (Axelsson, 1996). Exposing children to loud, noisy toys regularly or to one-time explosive toys can cause Noise Induced Hearing Loss (NIHL) in children's hearing. The unsafe incidents that can happen when playing with noisy toys and the effect of noisy toys on children's hearing is a major issue. There are many different kinds of toys all around the world. They can be categorized by considering various factors such as mechanism, size, age limit, and intended play. Toys are identified as one of the sources that can cause NIHL in children (Levey *et al.*, 2012). This is very dangerous because unlike teens and adults, children don't even realize that their hearing has been damaged. Even if they realize it, children under six years old cannot verbally communicate it (Axelsson, 1996). Even though there are safety standards like ISO, EN, and ASTM regarding the sound pressure levels of toys, there are still toys that exceed the recommended sound pressure levels. Also, as of 2021, there are still countries that do not have rules and regulations regarding appropriate sound pressure levels of toys.

* Corresponding authors (channacmkk@gmail.com; https://orcid.org/0000-0003-3450-7275)

There are several studies related to the assessment of different toys around the world. One study was conducted by Yaremchuk *et al.* (1997) who tested 25 toys purchased from a national toy store in the USA in order to check the risk of noise-induced hearing loss in accordance with the Occupational Safety and Health Act (OSHA). The study showed that 13 toys exceeded the OSHA permissible noise level. In 2008, Bittel *et al.*, tested the noise levels of 24 toys in the USA and compared them to the recommended noise levels in the American Society for Testing and Materials International (ASTM International) noise standard in 2003 (Bittel *et al.*, 2008). The noise levels observed in this study revealed that many toys exceeded the recommended levels, which may cause noise-induced hearing loss in children. McLaren *et al.* (2013) evaluated 28 toys that were imported to New Zealand according to the ISO standard, and they showed that 21% of these toys did not meet the acoustic requirements in the ISO standard (AS/NZS ISO 8124.1:2010). Hawks (1998) measured the sound levels emitted by 22 toys that were intended to be used by children aged six months to 5+ years from different distances. From the results of this study, they suggest that the noise emitted by these toys carries a potential risk of high-frequency hearing loss for school-aged children. Sleifer *et al.* (2013) analysed the sound pressure levels emitted by 48 non-certified children's toys available at popular retail stores in Brazil and compared them to Brazilian standards. The authors concluded that the majority of these toys emitted higher sound levels than the recommended values.

The European Commission is considering implementing acoustical requirements in the toys directive. As of March 2001, Standard EN 71-1:1998 divided toys into five main categories. To the best of the authors' knowledge, no systematic measurements have been carried out in Sri Lanka to determine the degree of noise level in toys. In 1995, at the World Health Assembly, it was estimated that there were 120 million people with hearing difficulties worldwide. It has been shown that men and women are equally at risk of noise-induced hearing impairment (Smith, 1998). The importance of high-frequency audibility in the speech and language development of children with hearing loss has been discussed by stetmachowicz *et al.* (2004).

The effects of noise can have various impacts based on daily activities and have been discussed in many research papers. Most studies have focused on industrial, transportation, and community noise, but there are few research papers regarding noise produced by toys.

In Sri Lanka, all kinds of toys are available in the market, with no indication of their sound emission levels. Neither the sound emission limit of the toy nor the permissible distance from the child's ear is not mentioned. Additionally, there is no consideration for protecting children's ears from the noise emitted by toys. The sounds may be continuous, impulsive, or a combination of both in character. Sri Lanka has two noise control regulations related to the environment; however, they do not extend to toys.

MATERIALS AND METHODS

All samples were collected from existing toy shops located in various centres, open markets including individual vendors, and popular retail stores.

The selected toys were evaluated using the following references: ISO 8124-1:2018 Safety of toys - Part 1: Safety aspects related to mechanical and physical properties, and BS EN 71-1:2011+A3:2014 Safety of toys - Mechanical and physical properties. The tested toys were measured for A-weighted equivalent sound pressure level, LpAeq, C-weighted peak sound pressure level, LpCpeak, and A-weighted maximum sound pressure level, LpAFmax. The two internationally standardized weighting networks in common use are the "A" and "C," which have been built to correspond to the frequency response of the human ear for different sound levels.

The measurements were taken according to the toy category using a B & K type 2270 handheld analyser, and the measured data were recorded. Different microphone positions were used for different toy categories. For a selected microphone position in each toy category, noise level readings were taken three times and recorded. Additionally, for each tested toy, the markings or warnings indicated on the packaging of toys were recorded. To ensure proper performance on battery-operated toys, new batteries were used. Each toy was operated as intended for about 15 seconds to measure sound pressure levels, except for cap-firing, wind toys, and pull-along or push toys. Cap-firing and wind toys were operated only once to measure sound pressure levels, while pull-along or push toys were operated at a selected distance to measure sound pressure levels. The following toy categories were selected for testing: table top or floor, hand held, squeeze, percussion, wind, rattles, pull-along or push, and cap firing. A total of 205 toys were tested, and 1986 tests were performed and analysed for the selected toys.

Noise levels were measured using a noise level analyser, Bruel & Kjaer (B & K) Type 2270 (class-1). The noise level meter was calibrated before and after taking the measurements using the noise level calibrator, B & K Type 4231, which is traceable to the primary standard maintained at Brüel & Kjær, The Calibration Laboratory, Denmark.

All noise level data were saved during measurement, and the data were analysed offline by the enhanced sound analysis software, Bruel & Kjaer BZ 7202, which conforms to the International Electrotechnical Commission (IEC) specific standard.

RESULTS AND DISCUSSION

Noise levels analysed with parameters

The results in Table 1 show that 59 (28.8%) of the tested toys' noise levels exceeded two parameters, and 35 (17.1%) of the toys exceeded one parameter out of 205 toys. In total, 94 (45.9%) items exceeded the prescribed noise levels. However, when considering the category of the toys, two parameters were exceeded by all wind toys (13 units), and 9 cap firing toys also exceeded two parameters. Additionally, 36 (63.2%) of squeeze toys exceeded two noise level parameters. Among the table top toys, 67 (94.4%) did not exceed the recommended noise level. Similarly, 9 (81.8%) of the hand-held toys and 5 (100%) of the pull-along or push toys did not exceed the prescribed levels as per the international standard. In the selected toy categories, tabletop or floor, percussion, rattles, and pull-along or push toys were roughly providing better results compared to other toys. However, cap firing, wind-up, and squeeze toys gave higher noise levels compared to the international standard. The summarized results are given in the following Table 1.

Table 1: Summary of analysed measurements

Toys category	Number of tested items	Number of tests	Two parameters exceeded	One parameter exceeded	Not exceeded
Table top or floor	71	984	0	4 (5.6 %)	67 (94.4 %)
Hand held	11	180	1 (9.1 %)	1 (9.1 %)	9 (81.8 %)
Squeeze	57	172	36 (63.2 %)	17 (29.8 %)	4 (7 %)
Percussion	7	111	0	5 (71.4 %)	2 (28.6 %)
Wind	13	195	13 (100 %)	0	0
Rattles	32	99	0	8 (25 %)	24 (75 %)
Pull along or push	5	50	0	0	5 (100 %)
Cap firing	9	195	9 (100 %)	0	0
Total	205	1986	59 (28.8 %)	35 (17.1 %)	111 (54.1 %)

Noise level distribution variations relative to international standard (BS EN 71) limits

The variation of wind toy sound levels (LAeq and LpCpeak) with the number of measurements is shown in Figure 1(a). A total of 195 measurements were taken and analyzed for wind toys. However, 189 noise level measurements exceeded the international standard noise level with an LAeq value of 85 dB(A), and 153 noise level measurements exceeded the recommended noise level with an LpCpeak value of 110 dB(A), as shown in Figure 1(a). Similarly, the sound level variation of squeeze toys with the number of measurements is shown in Figure 1(b). A total of 172 measurements were taken and analysed for squeeze toys. However, 149 noise level measurements exceeded the recommended noise level LAeq values, and 82 noise level measurements exceeded the recommended noise level LpCpeak values. The sound level variations of cap firing toys with the number of measurements are shown in Figure 1(c). A total of 195 measurements were taken and analysed for cap firing, and 190 noise level measurements exceeded the recommended noise level LpCpeak values. In general, a high noise level was observed during the measurement compared to the recommended values. The study clearly indicates that the measured noise level LAeq values and noise peak level LpCpeak values can be above the reference range. It is an unsafe situation that can happen when playing with a toy, and the effect of noisy toys on children's hearing is a major issue.

Noise emission percentage from three categories of toys

By way of contrast, very high noise level parameters were observed during the noise level measurement in the following selected categories of toys. The analysed results are provided in Table 2. According to the cap firing toys, the recommended peak value (LpCpeak) is 125 dB, but 90% of the total number of measurements exceeded
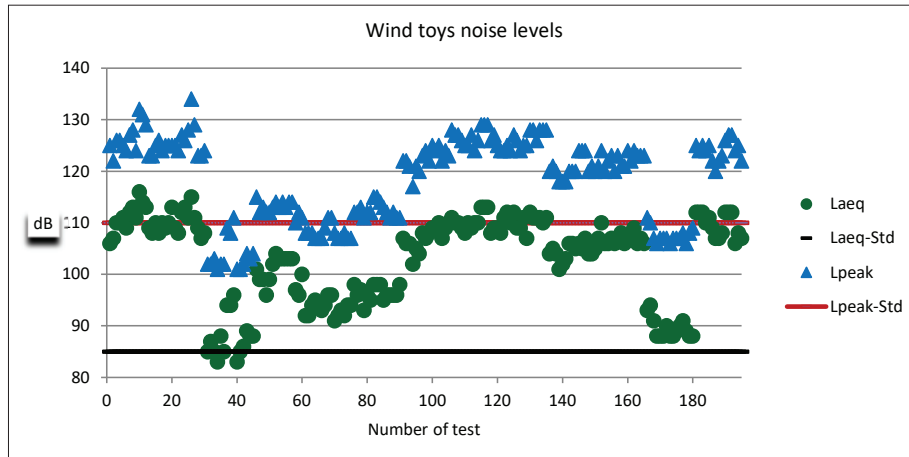
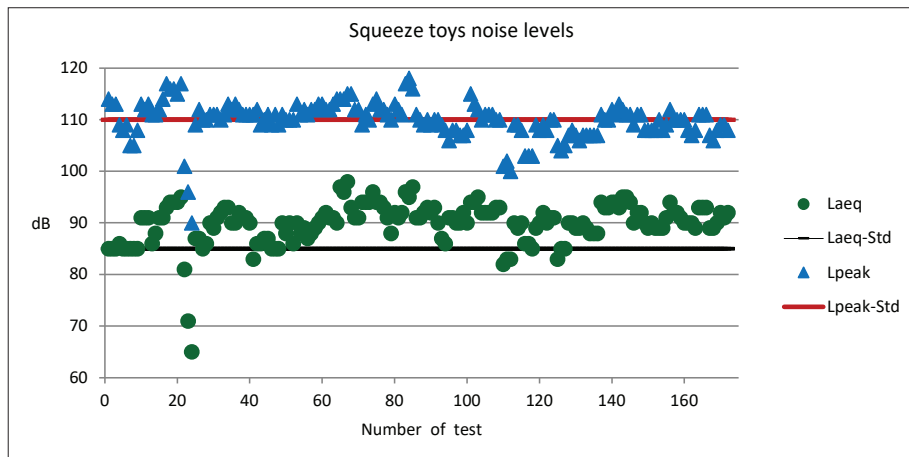**Figure 1(a):**   The variation of wind toys noise levels

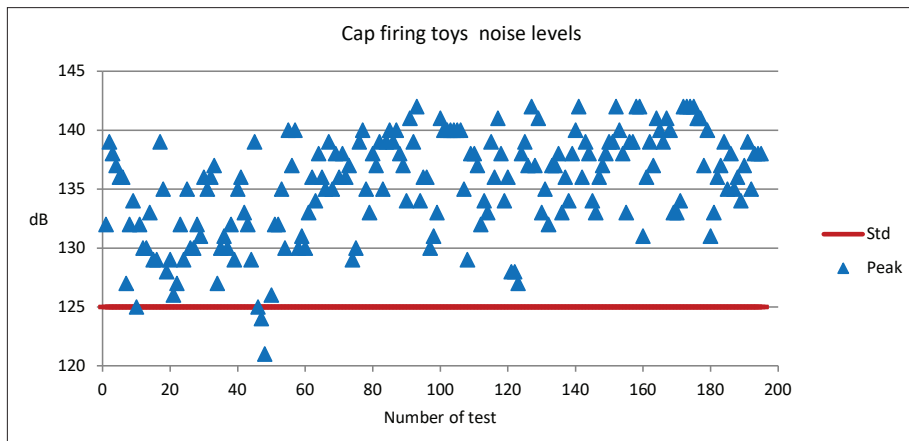**Figure 1(b):**   The variation of squeeze toys noise levels

Figure 1(c):   The variation of wind toys noise levels

129 dB. For squeeze toys, the number of measurements with noise levels exceeding LAeq surpassed 90% of the total number of measurements, and the peak value (LpCpeak) exceeded 90% of the noise level at 107 dB. Over 80% exceeded recommended levels for wind toys' peak values. The peak values exceeded by 50% of cap firing, squeeze, and wind toys were 136 dB, 110 dB, and 122 dB respectively. The LAeq values exceeded by 50% of squeeze toys and wind toys were 90 dB and 106 dB respectively.

Very high noise levels were observed in the following selected categories of toys. The analyzed results are provided in Table 2. According to the standard, the recommended peak noise level for cap firing toys is 125 dB. It was observed that about 90% of the measurements exceeded 129 dB. However, for squeeze toys, 90% of the LpCpeak measurements exceeded 106 dB. Around 80% of the measurements exceeded the recommended peak noise levels for wind toys. This is an unsafe situation, as mentioned before.

Table 2: Noise limits exceed benchmarks for three categories

Number of noise measurement exceed (%)	Cap firing toys		Wind toys		Squeeze toys	
	Lp_{Cpeak}	L_{Aeq}	L_{Aeq}	Lp_{Cpeak}	L_{Aeq}	Lp_{Cpeak}
90%	129	--	89	107	85	106
80%	131	--	94	109	87	108
70%	133	--	98	112	89	109
60%	135	--	103	118	90	110
50%	136	--	106	122	90	110
40%	137	--	107	123	91	111
30%	138	--	109	124	92	111
20%	139	--	110	125	93	112
10%	140	--	112	127	94	113
Recommended Limits*	125 dB		90 dB	110 dB	85 dB	110 dB

Note: Cap-firing toys do not indicate LAeq. The reason is that the measurement time period is very low.

* EN 71-1 Standard. L_{pCpeak} - Peak L_{Aeq} - Equivalent sound pressure level

Pressure level variation with frequencies

The variation of the pressure level of high noise level toys with frequency is discussed in this section.

The variation of C-weighted peak sound pressure level with frequency is shown in following figures. The standard "C" weighted audible frequencies are commonly used for the measurement of Peak Sound Pressure level. Figure 2(a) shows the reference chart for auditory field. Figure 2(b) shows the sound pressure values versus one-third octave band frequency variations for cap firing. Similarly, Figure 2(c) shows the wind toys, and Figure 2(d) shows the squeeze toys. These results clearly indicate that above the 1 kHz frequency range, the peak sound pressure level is 70 dB (C) values. Some values exceeded 100 dB(C) in the above 1 kHz frequency range. According to the figures, it is clear that the selected toys mostly generated higher frequency range

noise levels. The lower frequency values are limited for the toys category selected above. It can be observed that high frequencies are more critical than low frequencies near the measuring location. From Figures 2(b), 2(c), and 2(d), it can be observed that peak sound pressure levels at low frequencies up to about 500 Hz occurred below the loudness level contour, showing that the noise level-induced noise occurred below the human perception level of hearing. But peak sound pressure levels of higher frequencies above 1 kHz occurred above the loudness level contour, showing that noise level-induced noise occurred at higher than the human perception level of hearing.

The study clearly indicates that compared to the reference chart, the noise levels of the toys may affect the human speech range. It is an unsafe situation that can occur when children play with noisy toys, as it can have a major effect on their hearing.
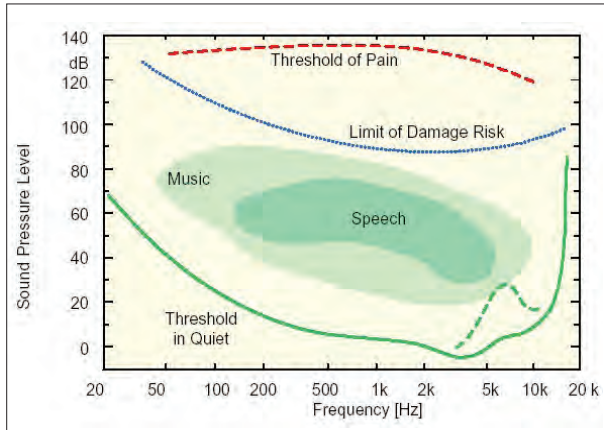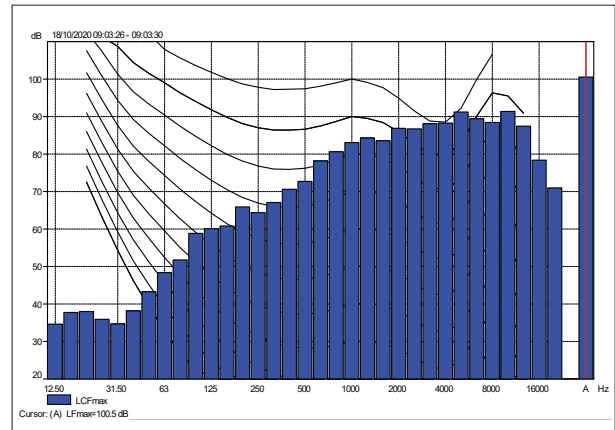
Figure 2(a):   Reference curve

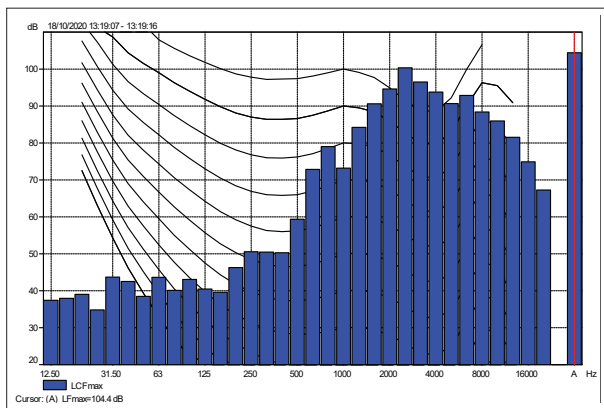**Figure 2(b):**   Frequency analyses- cap firing toys

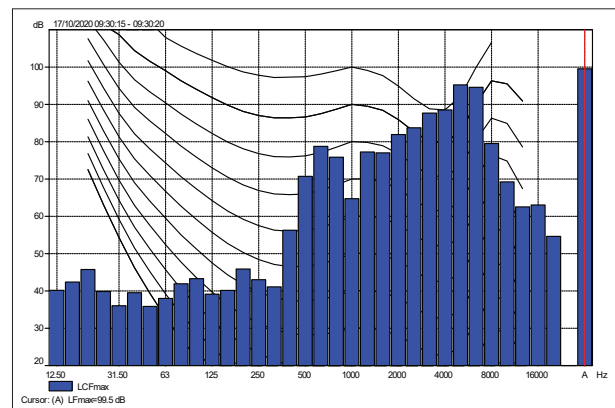**Figure 2(c):**   Frequency analyses- wind toys

Figure 2(d):   Frequency analyses- squeeze toys

CONCLUSIONS

According to the study, most cap firing, wind, and squeeze toys produced higher noise levels compared to international standards. A total of 94 (45.9%) items from the selected toys exceeded prescribed noise levels. The analysis indicates that the peak value (LpCpeak) of cap firing toys exceeded 90% of the noise level (129 dB), squeeze toys exceeded 60% of the noise level (110 dB), and wind toys exceeded 70% of the noise level (110 dB). The 50% exceeded peak values for cap firing, squeeze, and wind toys were 136 dB, 122 dB, and 110 dB, respectively. These toys mostly generate noise levels in the higher frequency range (above 1 kHz), and have limited lower frequency values. The study clearly indicates that compared to reference charts, these toys may influence human speech range, and they are unsafe for children playing with them, as they can have a major effect on the children's hearing.

Thus, it is necessary to raise awareness, include warning signs, and enforce acoustic regulations for toys in the Sri Lankan market.

REFERENCES

Axelsson A. (1996). The risk of sensorineural hearing loss from noisy toys and recreational activities in children and teenagers. *International Journal for Consumer and Product Safety* **3**(3): 137–146.
DOI: https://doi.org/10.1080/09298349608945772

Bittel S.N., Freeman B.A. & Kemker B.E. (2008). Investigation of toy-noise exposure in children. *Seminars in Hearing* **29**(1): 10–18.
DOI: https://doi.org/10.1055/s-2007-1021768

BS EN 71-1:2011+A3:2014 Safety of toys. Mechanical and Physical Properties

Hawks J.W. (1998). Sound levels emitted by children's toys. *Contemporary Issues in Communication Science and Disorders*: 41–44.
DOI: https://doi.org/10.1044/cicsd_25_S_41

ISO 8124-1:2018. Safety of toys - Part 1: Safety Aspects Related to Mechanical and Physical Properties.

Levey S., Fligor B. J., Ginocchi C. & Kagimbi L. (2012). The effects of noise-induced hearing loss on children and young adults. *Contemporary Issues in Communication Science and Disorders* **39**: 76–83.
DOI: https://doi.org/10.1044/cicsd_39_F_76

McLaren S. J., Page W. H., Parker L. & Rushton M. (2013). Noise producing toys and the efficacy of product standard criteria to protect health and education outcomes. *International Journal of Environmental Research and Public Health* **11**(1): 47–66.
DOI: https://doi.org/10.3390/ijerph11010047

Smith A.W. (1998). World Health Organisation and the prevention of deafness and hearing impairment caused by noise. *Noise and Health* **1**: 6–12.

Stelmachowicz P.G. Pittman A.L., Hoover B.M., Lewis D.E. & Moeller M.P. (2004). The importance of high-frequency audibility in the speech and language development of children with hearing loss. *Arch. Otolaryngology-Head Neck Surgery* **130**(5): 556–562.
DOI: https://doi.org/10.1001/archotol.130.5.556

Sleifer P., Gonçalves M.S., Tomasi M. & Gomes E. (2013). Analysis of sound pressure levels emitted by children's toys. *Revista Paulista de Pediatria* **31**(2): 218–222.
DOI: https://doi.org/10.1590/S0103-0582201300020 0013

Yaremchuk K., Dickson L., Burk K. & Shivapuja B.G. (1997). Noise level analysis of commercially available toys. *International Journal of Pediatric Otorhinolaryngology* **41**(2): 187–197.
DOI: https://doi.org/10.1016/S0165-5876(97)00083-9

RESEARCH ARTICLE

Phylogeny

Russell's viper (*Daboia russelii*) in the Jaffna peninsula, Sri Lanka bears signatures of incipient genetic divergence from the South Indian population

ND Abeyaweera[1], A Sivaruban[1], A Murugananthan[2] and KP Amarasinghe[2]*

[1] Department of Zoology, Faculty of Science, University of Jaffna, Sri Lanka.
[2] Department of Parasitology, Faculty of Medicine, University of Jaffna, Adiyapatham Road, Kokuvil West, Kokuvil, Jaffna, Sri Lanka.

Abstract: The Russell's viper (*Daboia russelii*) is a medically important viper found in South Asia, including Sri Lanka. This study focused on the phylogeny of Russell's vipers in the geographically segregated coastal peninsula of Jaffna, Sri Lanka. The study aimed to find out whether the specimens collected in Jaffna are different from previously reported forms since such an investigation has not been carried out so far specifically in this area, and to find out whether geographical segregation has had an impact on it. We obtained mtDNA sequences of samples representing six geographical locations in the Jaffna peninsula for the mitochondrial protein-coding genes *Cytb*(576bp) and *ND2*(270bp). Our molecular analyses recovered two distinct clades: *D. russelii* and *D. siamensis*. The clade of *D. russelii* comprises two sister lineages, Pakistan and India/Sri Lanka. The uncorrected pairwise *Cytb* genetic distance between the species range from 5.0 to 14.5 percent. The current study confirms a sister group relationship between the Indian/Sri Lankan lineage and the Pakistani lineage of the Russell's viper (*D. russelii*). Additionally, it discloses the presence of an incipient genetic divergence between Russell's viper populations in Jaffna and South India.

Keywords: *Daboia russelii*, Jaffna, mitochondrial gene, mtDNA, phylogeny, Viperidae, Viperinae.

INTRODUCTION

Sri Lanka is a tropical island located south of India. It has an explicit variation of topography that favours isolation of populations and directing them towards speciation (Gunatilleke *et al.*, 2017). Home to one of the highest snake bite rates in the world, the island houses about 89 species of inland terrestrial snakes (Pyron *et al.*, 2013b), out of which five species are of medical importance; including the Russell's viper, *Daboia russelii* (Shaw & Nodder, 1797). This reptile is found in South and Southeast Asian countries and classified under the family Viperidae as a true viper (Subfamily: Viperinae) and they lack loreal pits and possess solenoglyphous fangs (Wall, 1921; Smith, 1943). The venom glands that produce a cocktail of venom, coupled with its excellent camouflage, robust body, and defensive behaviour accounts for a higher number of mortalities due to its bite, earning its medically important status (Wüster, 1998). On the other hand, due to the ecological niche that it holds as a carnivore of third or higher trophic levels (Wall, 1921), the snake also contributes to the ecological balance in the environment; especially in the human-made ecosystems of paddy fields where it is generally found, maintaining the populations of fast-growing pests like mice under control (Beaupre & Douglas, 2009; Warrell, 2010; Glaudas, 2021a, 2021b; Martin, 2021).

The current taxonomy of *Daboia russelii* is a result of the integration of morphological studies of several authors including Smith (1917;1943), Deraniyagala (1955) and Wüster *et al.*, (1992), molecular genetic studies including that of Thorpe *et al.*, (2007) and

information on envenomation symptoms (Warrell, 1989). The latest update on its classification includes two species, namely, *Daboia russelii* (West of the Bay of Bengal) to which the Sri Lankan haplotype belongs, and *Daboia siamensis* (East of the Bay of Bengal) (Wüster *et al.*, 1992; Thorpe *et al.*, 2007). Because a synonymous nomen *Daboia pulchella* (Gray, 1842) originating from Sri Lanka is present, Thorpe *et al.*, (2007) rightly included Sri Lankan population sequences too. The sequence was sourced from Gampola, a wet zone place in Sri Lanka known for its biotic distinction from the Indian mainland (Gunawardene *et al.*, 2007). However, the molecular taxonomic analysis process that led to the above classification has not incorporated a sufficient number of samples from Sri Lanka, presumably based on the small geographical area and the fact that the Russell's viper population in Sri Lanka is similar or closely related to the South Indian haplotype (Thorpe *et al.*, 2007). Studies on symptoms of envenomation have also revealed varying patterns, showing distinct symptoms such as neurotoxicity in Sri Lanka, in addition to the most common haemolytic and anticoagulant symptoms shown by both Sri Lankan and Southern Indian populations (Warrell, 1989; Tan *et al.*, 2015). Furthermore, experiments carried out on the protein composition of venom from varying geographical locations have also produced concordant results (Pla *et al.*, 2019).

Records on snake bite envenomation shows that the Russell's viper is abundant in the Wet Zone, Intermediate Zone and mainly in the Dry Zone of Sri Lanka, which includes Jaffna (Kasturiratne *et al.*, 2005; Abyerami & Sivashanthini, 2008). The revised taxonomical work of Russell's viper, as reported by Thorpe *et al.* (2007), included only a sample from the wet zone of Sri Lanka and did not include samples from other climatic areas. Therefore, we aimed to find out whether the specimens collected in Jaffna are different from the *Daboia russelii* population in Tamil Nadu, India. A previous study has also reported that Jaffna experiences the highest incidence of venomous snake bites in agricultural fields, specifically paddy fields, primarily attributed to the Russell's vipers (Ravichandren & Thirunavukarasu, 2016), which further enhanced our interest on this study. During the current study, we examined the morphological characteristics following the literature of Wall (1921), Smith (1917; 1943), Deraniyagala (1955), characteristics of Western subspecies (Wüster, 1998), and notes on the Russell's vipers in Jaffna peninsula (Abyerami & Sivashanthini, 2008) to identify the Jaffna samples in fine scale resolution.

MATERIALS AND METHODS

Daboia russelii specimens were obtained from the Jaffna Teaching Hospital (JTH), which were collected from different locations in Jaffna (9.668°N, 80.029°E) and brought along with the bite victims. A total of eight specimens were collected within the time period from 11 September 2019 to 25 October 2021. After assigning the reference numbers and collecting the preliminary information, we examined the detailed morphological characters to identify the authentic specimens. The ethical clearance for animal handling and obtaining tissue samples, given by the Animal Ethics Review Committee of the University of Jaffna, Sri Lanka, holds the reference number AERC/2021/05.

Laboratory protocols

The liver and spleen tissues of the specimen were obtained by making an incision 2-3 head-lengths behind the head under sterile conditions. Exactly 0.02 g of the frozen tissue samples were used to extract the whole genome of each tissue sample, using the DNeasy® Blood and Tissue Kit. After quantifying its purity, successful extracts (of six individual specimens) were used to amplify partial mitochondrial gene fragments of Cytochrome-b (*Cytb*) and *NADH* dehydrogenase subunit-2 (*ND2*) using the specific primers (Table 1).

Table 1:   Primers used in PCR amplification

Gene	Primer	Sequence (5'-3')	Specific snake	Reference	Amplified size (bp)
Cytb	Forward	TCAAACATCTCAACCTGATGAAA	*Daboia russelii*	(Thorpe *et al.*, 2007)	758
	Reverse	GGCAAATAGGAAGTATCATTCTG	*Daboia russelii*	(Thorpe *et al.*, 2007)	758
ND2	Forward	CCTTGAAGCACTTCTGGGAATCAGA	All snakes	(Hackett, 1996)	363
	Reverse	TATCGGGCCCATACCCCGAAAAT	All snakes	(Hackett, 1996)	363

A standard PCR was carried out for each gene using the master mix, which consisted of 5.0 µL of 5x Buffer, 3.0 µL of MgCl$_2$ (25 µM), and 0.2 µL of *Taq* DNA polymerase. For *Cytb* replicates, the reaction mix included 3.0 µL of DNTP (2 µM), 2.0 µL of forward primer (10 µM), 2.0 µL of reverse primer (10 µM), and 2.0 µL of Template DNA; while for *ND2* replicates, the reaction mix included 4.0 µL of DNTP (2 µM), 2.5 µL of forward primer (10 µM), 2.5 µL of reverse primer (10 µM), and 3.0 µL of Template DNA. Finally, each replicate was topped up to 25µL with nuclease free water, and a total of four replicates were maintained for PCR amplification of each gene from each sample. The PCR conditions for *Cytb* gene consisted of an initial denaturation at 95^{0}C for 3 min, 35 cycles of denaturation at 95^{0}C for 30 s, annealing at 50^{0}C for 45 s, extension at 72^{0}C for 1 min, and a final extension at 72^{0}C for 5 min. The PCR conditions for *ND2* gene consisted of initial denaturation at 95^{0}C for 5 min, 35 cycles of denaturation at 95^{0}C for 45s, annealing at 50^{0}C for 45s, extension at 72^{0}C for 1 min, and a final extension at 72^{0}C for 3 min. The PCR amplified product was detected through agarose gel electrophoresis (1.5%) at 80V for 45minutes (Figure 1). The purity and the size of the product were confirmed with DNA quantifier. The four replicates of each PCR product were pooled together to obtain a higher yield. Finally, all the samples were purified using a DNA purification kit.
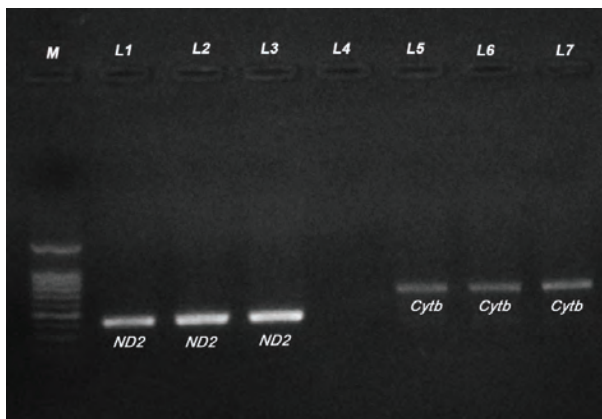

Figure 1: Agarose gel electrophoresis (1.5%) analysis of amplified PCR products from *Cytb* and *ND2* mitochondrial genes. The lane M displays the molecular weight marker 100 bp step ladder (Promega) is positioned in the left corner. Lanes L1-L3 depict the *ND2* marker; Lane L4 serves as the negative control (Nuclease-free water); Lanes L5-L6 display the *Cytb* marker.

Phylogenetic analysis

A dataset with a total of 34 taxa including out-group taxa (576 bp of *Cytb* and 270 bp of *ND2*) was used to carry out the phylogenetic analysis. A list of the 34-taxa dataset included in current study, with their isolate number, geographical location, GeneBank accession number, and reference is presented in Table 2. The nucleotide sequences of the amplified DNA fragments were obtained using Capillary Electrophoresis Sequencing (CES) (Macrogen Inc., Seoul, South Korea). The obtained sequences were double-checked with the ABI chromatogram files and aligned with homologous sequences from the National Centre for Biotechnology Information (NCBI) database using ClustalW (Thompson *et al*., 1994) in MEGA XI® (Tamura *et al*., 2021). Considering the availability of homologous sequences in NCBI, only the isolates with both *Cytb* and *ND2* were concatenated. A total of 33 sequences were used for *Cytb* gene; while 19 concatenated sequences of both *Cytb* and *ND2* were used for available localities to build a further accurate result. *Daboia mauritanica*, which is a sister species of *D. russelii* was used as the outgroup in all cases. The number of parsimony informative sites were determined using DNAsp v6 (Rozas *et al*., 2017). Phylogenetic reconstruction was carried out using maximum likelihood (ML) and Bayesian inference (BI) analysis. The best fit nucleotide substitution model and the partitioning scheme for the BI were determined using the PhyML (Guindon *et al*., 2010) and greedy (Lanfear *et al*., 2012) algorithms via PartitionFinder 2 software (Lanfear *et al*., 2017) under the Corrected Akaike Information Criterion (AICc). A similar software was used to determine the best fit nucleotide substitution models for ML as well. Two phylogenetic trees were constructed for *Cytb* and concatenated *Cytb+ND2* sequences by Bayesian Inference using Markov Chain Monte Carlo (MCMC) randomization in MrBayes 3.2.7 (Ronquist *et al*., 2012). Two parallel runs of four chains (3 heated and 1 cold) were performed for 1 million generations in *Cytb* and 1.5 million generations in *Cytb+ND2* respectively (significant value of the standard deviation of split frequency < 0.01). The runs were sampled at every 500th generation. The point of convergence (burnin) and the average estimated sample size for each parameter were estimated in Tracer v1.7.2 (Rambaut *et al*., 2018). The first 25% generations of burnin were discarded and the consensus trees were calculated from the remaining 75% of the posterior distribution. The Ultrafast bootstrap (BP) with 1,000 iterations (Minh *et al*., 2013) in IQ-TREE and the partitioning scheme obtained from PartitionFinder

2 were used to determine the statistical support in the ML trees (both *Cytb* and *Cytb+ND2* trees). The output consensus trees were viewed using FigTree v1.4.4. The different evolutionary best fit nucleotide substitution models, partitioning scheme, and number of sequences used in the analysis are provided in Supplementary Table S1. The uncorrected pairwise genetic distances for various populations of *Daboia* for the two genes were calculated using MEGA XI®. Finally, the haplotype network reconstruction for *Cytb* gene of various populations of *Daboia russelii* was inferred by Median Joining Network (Bandelt *et al.*, 1999) using PopArt (Leigh & Bryant, 2015). The sequences generated by the current study and the sequences obtained from the GenBank (Supplementary Table 2) were used for this analysis.

Table 2: NCBI accession numbers of the gene sequences used for phylogenetic analysis (NA- not given)

Source	Isolate	Organism	Locality	*Cytb*	*ND2*
NCBI	RA-1961.325, DM02	*Daboia mauritanica*	Morocco	MF140584	MT232999
(Thorpe *et al.*, 2007)	NA	*D. russelii*	Thayur, Tamil Nadu, India	AY165087.1	AY165075.1
(Thorpe *et al.*, 2007)	NA	*D. russelii*	Gampola, Sri Lanka	AY165088.1	AY165076.1
(Thorpe *et al.*, 2007)	NA	*D. russelii*	Pakistan	AJ275723.1	AY165074.1
This Study	RV001	*D. russelii*	Jaffna, Sri Lanka	MW771366.1	MW881135.1
This Study	RV002	*D. russelii*	Jaffna, Sri Lanka	MW771367.1	MW881136.1
This Study	RV003	*D. russelii*	Jaffna, Sri Lanka	MW771368.1	MW881137.1
This Study	RV006	*D. russelii*	Jaffna, Sri Lanka	MW771369.1	MW881138.1
This Study	RV007	*D. russelii*	Jaffna, Sri Lanka	MW771370.1	MW881139.1
This Study	RV008	*D. russelii*	Jaffna, Sri Lanka	MW771371.1	MW881140.1
NCBI	DR11	*D. russelii*	Pakistan	MZ711546.1	-
NCBI	DR18	*D. russelii*	Pakistan	MZ711545.1	-
NCBI	DR15	*D. russelii*	Pakistan	MZ711544.1	-
NCBI	DR20	*D. russelii*	Pakistan	MZ711543.1	-
NCBI	DR4	*D. russelii*	Pakistan	MZ711542.1	-
NCBI	DR3	*D. russelii*	Pakistan	MZ711541.1	-
NCBI	DR1	*D. russelii*	Pakistan	MZ711540.1	-
NCBI	DR2	*D. russelii*	Pakistan	MZ711539.1	-
NCBI	NA	*D. russelii*	Pakistan	HM179463.1	-
NCBI	AIWC 074	*D. russelii*	Tamil Nadu, India	MZ029432.1	-
NCBI	V30	*D. russelii*	Vedenemmeli, Tamil Nadu, India	MG995824.1	-
NCBI	V27	*D. russelii*	Goa, India	MG995821.1	-
(Thorpe *et al.*, 2007)	NA	*D. siamensis*	Fong Shan, Pingtung, Taiwan	AY165089.1	AY165077.1
(Thorpe *et al.*, 2007)	NA	*D. siamensis*	Tuban, W of Gresik, East Java, Indonesia_1	AY165083.1	AY165070.1
(Thorpe *et al.*, 2007)	NA	*D. siamensis*	Tuban, W of Gresik, East Java, Indonesia_2	AY165084.1	AY165071.1
(Thorpe *et al.*, 2007)	NA	*D. siamensis*	Tonggurambang, Mbay, Flores, Indonesia_1	AY165085.1	AY165072.1
(Thorpe *et al.*, 2007)	NA	*D. siamensis*	Tonggurambang, Mbay, Flores, Indonesia_2	AY165086.1	AY165073.1
(Thorpe *et al.*, 2007)	NA	*D. siamensis*	Htauk Kyant, Myanmar	AY165080.1	AY165067.1
(Thorpe *et al.*, 2007)	NA	*D. siamensis*	Thailand (southern central)_1	AY165090.1	AY165078.1
(Thorpe *et al.*, 2007)	NA	*D. siamensis*	Thailand (southern central)_2	AY165091.1	AY165079.1
(Thorpe *et al.*, 2007)	NA	*D. siamensis*	Poipet, Sisophon, Cambodia	AY165081.1	AY165068.1
(Thorpe *et al.*, 2007)	NA	*D. siamensis*	Guangdong, China	AY165082.1	AY165069.1
NCBI	S-05	*D. siamensis*	China	KF913330.1	-
NCBI	S-04	*D. siamensis*	China	KF913329.1	-

RESULTS AND DISCUSSION

Until 2007, the systematics of the Russell's viper species complex was deduced solely based on the utilization of morphological characters and envenomation symptoms. Owing to its discontinuous distribution across the regions of South and Southeast Asia, these populations were designated as discrete subspecies. This designation was prompted by observed divergences in morphology, as well as differences in envenomation patterns. Smith (1943) in his description, identified two distinct colour forms *Vipera russelli russelli* and *V. r. siamensis*. Later, the Russell's viper was reclassified under the genus *Daboia* due to its isolated position under albumin immunology and blood serum electrophoresis (Herrmann *et al.*, 1992).
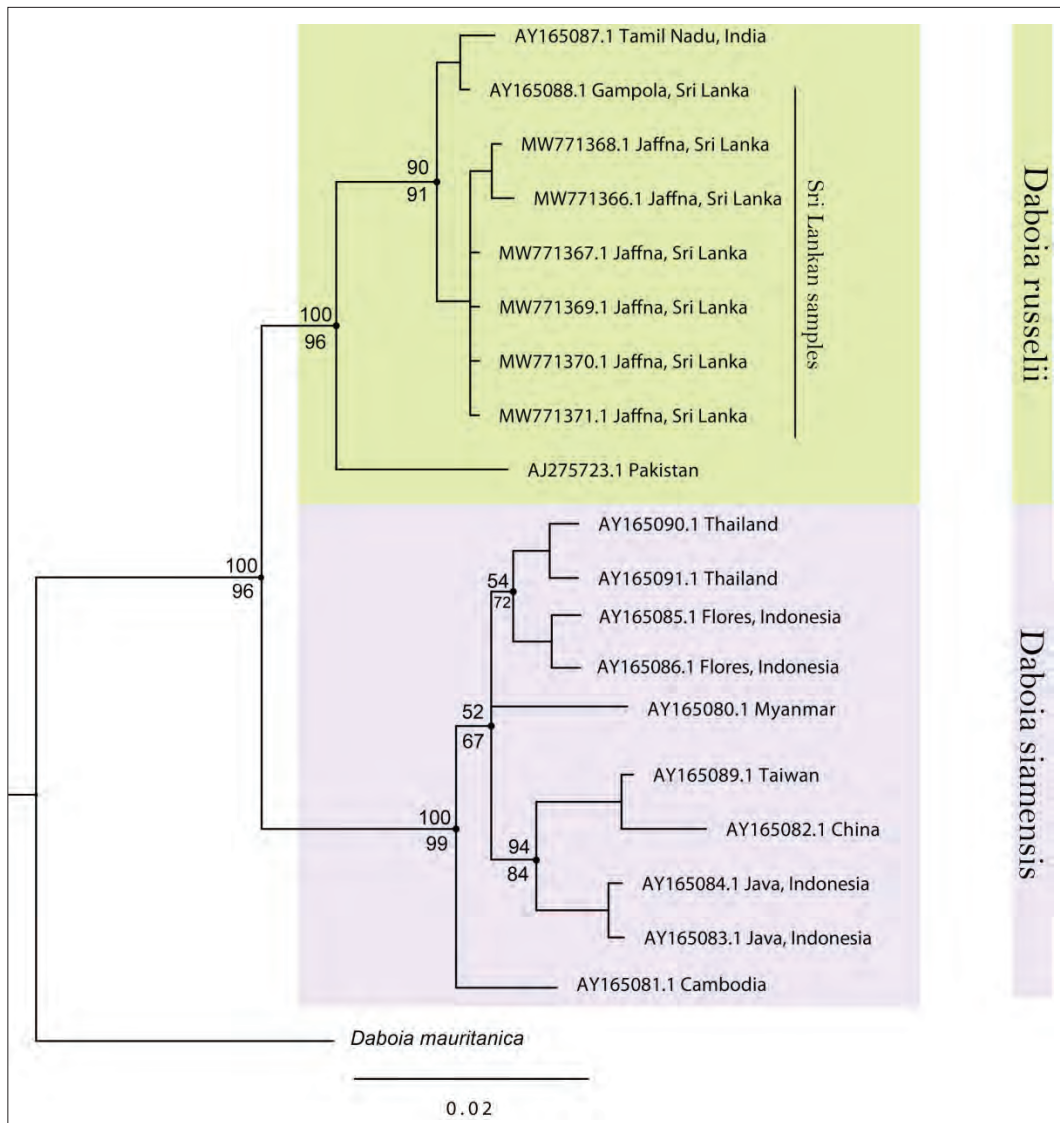

Figure 2: Molecular phylogenetic relationships of Russell's viper, built upon Bayesian inference of the concatenated sequence alignment of the *Cytb + ND2* (846 bp) mitochondrial-gene markers. The numerical values above and below the nodes indicate Bayesian posterior probabilities and maximum likelihood ultrafast bootstrap values respectively. The scale bar corresponds to the number of genetic changes per site. The accession number at the branch tip corresponds to the *Cytb* gene, listed in Table 2.

The work of Wüster *et al*., (1992) showed variation in the Russell's viper taxonomy by performing multivariate analysis of morphological characters only. Later, Thorpe *et al*. (2007), explained the genetic variation of the Russell's viper by studying the phylogeography of the species in relation to its colour pattern and envenomation symptoms and classified them into two species, namely,

Daboia russelii and *Daboia siamensis*. The molecular phylogenetic analysis revealed their distinction at the species level, attributed to significant genetic divergence, as well as discernible morphometric and geographic distinctions (Thorpe *et al*., 2007). This classification remains upheld to the present day (Wallach *et al*., 2014; Boundy, 2020).
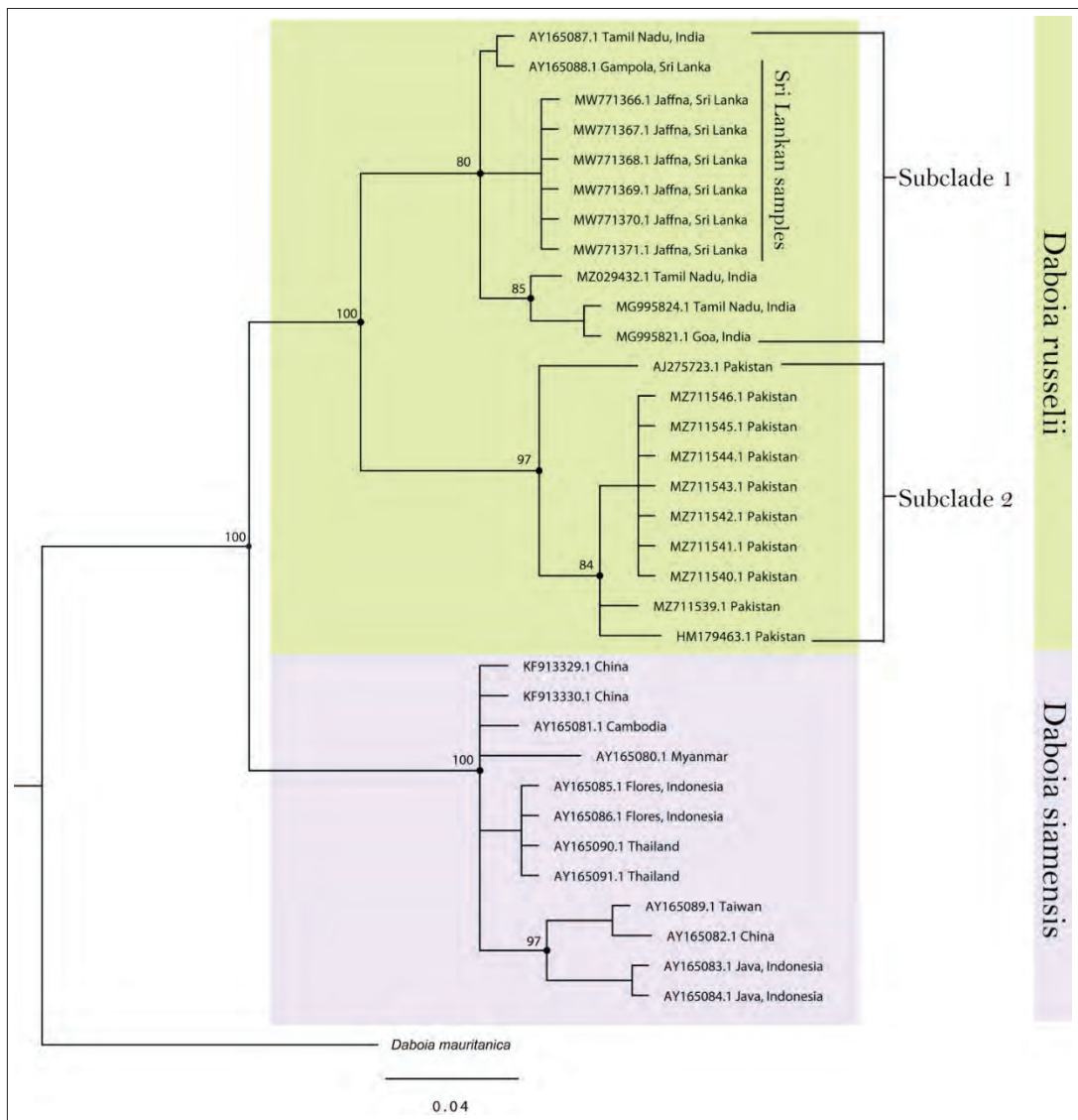

Figure 3: Molecular phylogenetic relationships of Russell's viper, built upon Bayesian inference of the multiple sequence alignment of the *Cytb* (576 bp) mitochondrial-gene markers. The numerical values above the nodes indicate Bayesian posterior probability values. The scale bar corresponds to the number of genetic changes per site. The accession number at the branch tip corresponds to the *Cytb* gene, listed in Table 2.

Above study (Thorpe *et al*., 2007) utilized three mitochondrial genes (cytochrome b, *NADH* dehydrogenase subunit 2 and 4) of Russell's viper from the Southern and South-east Asian countries; in which the position of Sri Lanka has been analyzed with a single specimen, despite the availability of Russell's viper from a range of geographical locations according to the bite records (Kasturiratne *et al*., 2005; Das & Silva, 2016).

In the present study, the final alignment of *Cytb* consisted of 576 base pairs while the concatenated *Cytb*+*ND2* alignment consisted of 846 base pairs (*Cytb*: 576bp and *ND2*: 270bp). The pseudogenes were confirmed to be absent with the absence of indels and stop codons within the coding genes (Zhang & Hewitt, 1996). The maximum parsimony informative sites for the sequences analysed are *Cytb*: 71, *Cytb*+*ND2*: 90. The best evolutionary models for each partition determined by PartitionFinder 2 (Lanfear *et al*., 2017), are given in Supplementary Table S1. The standard deviations of split frequencies in BI analysis for *Cytb* and *Cytb*+*ND2* datasets are 0.007 and 0.003 respectively. The results consist of two BI phylogenetic trees (Figure 2 and 3) and two ML trees (Supplementary Figure S1 and S2). The Bayesian posterior probability (PP) and Ultrafast bootstrap (BP) of each node has been given at the tip of each node. Interspecific and intraspecific uncorrected pairwise genetic distance (p-distance) computed for the *Cytb* and *ND2* genes for the various populations of genus *Daboia* is presented in Table 3 and 4, respectively.

Table 3: Interspecific uncorrected pairwise genetic distances (%), for the *Cytb* and *ND2* genes among *Daboia* species

Cytb *ND2*	*Daboia mauritanica*	*Daboia russelli*
Daboia mauritanica		
Daboia russelii	14.5-10.9 12.2-10.2	
Daboia siamensis	14.3-13.6 12.8-12.5	11.6-5.0 9.9-8.2

The BI (Figure 2 and 3) and ML (Supplementary Figure S1 and S2) analysis retrieved concordant trees with similar topologies. However, the topological differences were observed in the few substructures of the *Daboia siamensis* clade. The major variations were observed between the *Cytb* BI tree (Figure 3) and *Cytb* ML tree

(Supplementary Figure S2). Our phylogenetic analysis retrieved two primary clades, i.e., *D. russelii* clade and *D. siamensis* clade, with strong node support, while *Daboia mauritanica* is recovered as the basal in both the BI and ML trees. Our interspecific uncorrected pairwise distances values (Table 3) also support the aforementioned divergence between the primary clades.

The *D. siamensis* clade consists of four main lineages, viz 1) Cambodia, 2) Myanmar, 3) Thailand / Flores, 4) China / Taiwan / Java. This clade exhibits a "star" phylogeny in all four trees with minor differences (Figure 2, 3 and Supplementary Figure S1, S2), as the aforementioned lineages are recovered with poorly supported nodes, similar to the previous finding of Thorpe *et al*., (2007). This type of phylogeny shows a population expansion event from a common ancestor (the founder lineage) in the recent past. The Cambodian sample is recovered as the basal group in all trees despite the slight changes in BI tree for *Cytb* (Figure 3). A similar finding was also reported by Thorpe *et al*. (2007), although their BI phylogeny retrieved the Myanmar sample as the basal lineage. The *D. russelii* clade includes samples confined to Pakistan, India and Sri Lanka. The Pakistan lineage (subclade 1) is recovered as sister group to the India/ Sri Lanka lineage (subclade 2), with high node support, in both BI (Figure 3) and ML (Supplementary Figure S2) tree for *Cytb*. However, in both the BI tree (Figure 2) and the ML tree for the concatenated sequence (Supplementary Figure S1), the Pakistan group is identified as the basal group within the *D. russelii* clade. This basal position for the Pakistan group within the *D. russelii* clade was also reported in a previous study (Thorpe *et al*., 2007).

The present study represents the first phylogenetic analysis of the Russell's viper from the Jaffna peninsula, Sri Lanka, having used the mitochondrial gene sequences obtained from the specimens of Jaffna, and the sequence data from NCBI (Table 2).The initial intention was to use the fragments of the same genes as Thorpe *et al*. (2007), but due to the lack of amplification yield with the provided *NADH* dehydrogenase subunit 4 (*ND4*) primers, it was decided to proceed with the study using *Cytb* and *ND2* genes only. The present study included six individual samples of Russell's viper from Jaffna; excluding two of the total eight samples due to putrifaction. The primers used for the amplification were identified from the published literature (Table 1). The phylogenetic analysis of the current study utilized mitochondrial gene sequences from 33 different isolates, including the six samples from Jaffna, Sri Lanka, generated by current study (Table 2).

Thirteen isolates were previously reported by Thorpe *et al*. (2007), and the remaining 14 were downloaded from the GeneBank database. These additional fourteen isolates have sequences only for the *Cytb* gene region (Table 2). Therefore, in this study a separate tree has been drawn for the *Cytb* gene (Figure 3) for which the highest number of sequences are available from multiple localities within South Asia. All the trees represent the deviation between *Daboia siamensis* (Node B) and *Daboia russelii* (Node A) with strong node support.

Furthermore, in addition to the results of previous studies, the specimen from Pakistan also shows mild divergence from the South Indian specimen (including Sri Lanka) with strong node support showcased with BI tree for *Cytb* (Figure 3). Sri Lanka shows genetic proximity to the South Indian specimen which is clearly observed in BI tree for *Cytb* (Figure 3), but with poor node support. This is also supported by the results of intraspecific uncorrected pairwise genetic distance analysis (Table 4).

Table 4: Intraspecific uncorrected pairwise genetic distances (%), for the *Cytb* and *ND2* genes among *Daboia russelii* populations from various localities

Cytb ND2	Pakistan	Goa, India	Tamil Nadu, India	Jaffna, Sri Lanka
Pakistan				
Goa, India	2.8 NA			
Tamil Nadu, India	3.3-2.6 2.0	0.9-0.4 NA		
Jaffna, Sri Lanka	3.1-2.2 1.7	1.0 NA	1.0-0.8 0.7	
Gampola, Sri Lanka	2.9-2.4 1.6	0.7 NA	0.7-0.2 0.3	0.6-0.5 0.6

The haplotype network generated for *Cytb* gene (Figure 4) also resembles this shallow divergence between the Pakistan and India/Sri Lanka lineages (Figure 4B), while demonstrating the genetic proximity between Indian samples and Sri Lankan samples. However, a contradiction arises with the specimen from Gampola, Sri Lanka which has been clustered together with Tamil Nadu specimen (*Cytb* p-distance: 0.7 - 0.2, *ND2* p-distance: 0.3) and not with the specimen from Jaffna, Sri Lanka (*Cytb* p-distance: 0.6 - 0.5, *ND2* p-distance: 0.6) in all four phylogenetic trees. This is a completely opposite outcome from what we expected to observe.

The Sri Lankan affinity to the South Indian fauna has also been published in previous studies (Bossuyt *et al*., 2004; Crusz, 1973; Gunatilleke *et al*., 2017). The Western Ghats and Sri Lanka display considerable diversity in both landscape and climate, which gives rise to a rich variety of plant life and distinct animal communities. However, Sri Lanka's wet zone has a more pronounced wet and seasonal climate. The evergreen forests in both regions boast unique animal species, many of which

belong to specific, localized groups. In contrast, the lowland dry forests show more similarities in terms of the plants and animals they host. This difference might be due to the possibility that connections between wet zones were less frequent during ice ages compared to the connections between dry zones (Gunawardene *et al*., 2007). However, the expected genetic proximity between South India and the dry-zone in Sri Lanka (Jaffna) was not observed in the outcome of our phylogenetic analysis. However, this underscores the necessity for a study to be conducted using authentically collected samples that represent all the geographical locations in South Asia where the population of Russell's viper is abundant. Furthermore, incorporating an additional number of genes (both mitochondrial and nuclear) may influence the accuracy of the phylogenetic analysis outcomes (Rokas & Carroll, 2005). This approach has been successfully implemented in a previous study as well (Pyron *et al*., 2013a; 2013b). Therefore, it could be helpful in resolving the unresolved phylogenetic relationship of the India/Sri Lanka subclade within the *Daboia russelii* clade. Under the current availability of data, a regional comparison for both areas of the mitochondrial genome

is impossible due to the lack of adequate sequences. Of all two genes, Cytochrome b (*Cytb*) can be proposed as the most effective barcode to construct the phylogeny for its availability of sequences. Also, this study could not completely address the variations in envenomation symptoms and the composition of venom to fully evaluate the status of the Jaffna population. Therefore, as a future suggestion, such analysis would be helpful to discuss the results of our phylogenetic analysis.
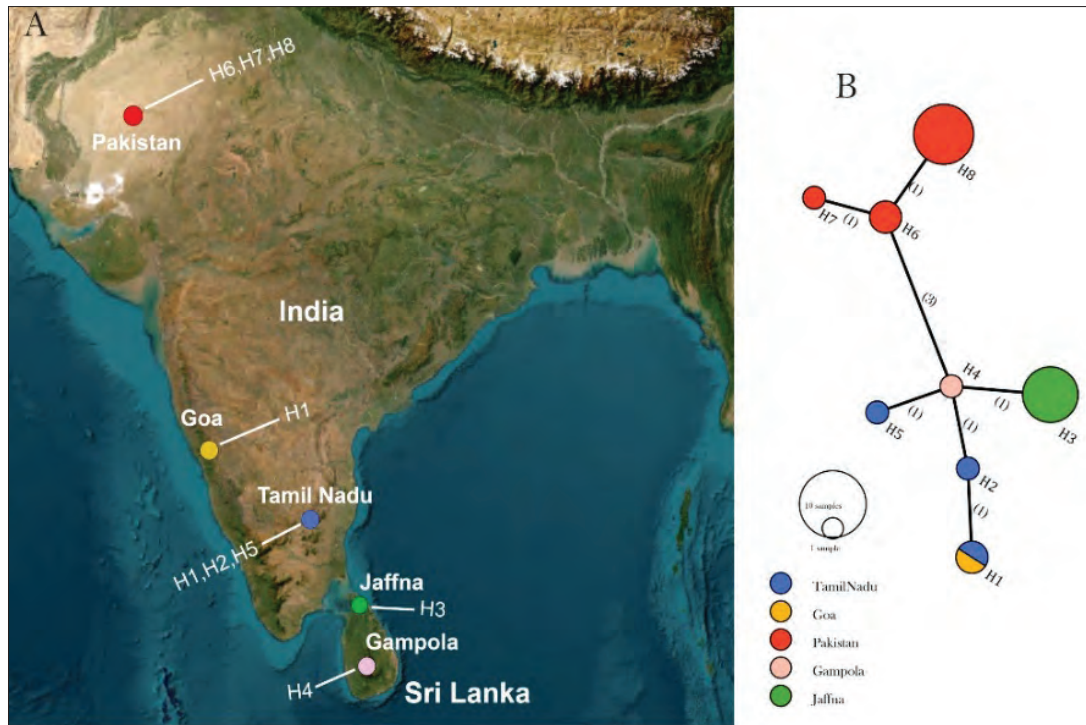

Figure 4: The haplotype network using PopART v1.7, for *Cytb* mitochondrial-gene markers of *Daboia russelii*. (A) A map represents the sample localities. (B) Median joining haplotype network for the 576 bp fragment of the *Cytb* gene marker. The mutational steps are shown in parentheses.

Discussion

Sri Lanka is a continental island connected to the Indian subcontinent under the seabed (Crusz, 1973). In the Pleistocene glacial ages, Sri Lanka and mainland India periodically connected until around 10,000 years ago due to rising sea levels. Comparing faunal components across the Palk Strait reveals morphological similarities, suggesting a recent exchange of plant and animal life with Southern India (Bossuyt *et al.*, 2004). However, evergreen forests in Sri Lanka and the Western Ghats hold unique animal species, many specific to localized groups. This distinction may arise due to wet zones having fewer connections during ice ages (Bossuyt *et al.*, 2004; Gunawardene *et al.*, 2007). While the differentiation between the primary subclade of *D. russelii* in Pakistan and India/Sri Lanka is clear, the phylogenetic relationship within the India/Sri Lanka subclade remains unresolved. This is evidenced by the BI tree, ML tree, and p-distance analysis. The current phylogenetic analysis recovered the Russell's viper population in Sri Lanka (Gampola and Jaffna) as a paraphyletic group in all analyses. Although we expect the genetic affinity of the Jaffna population to be more towards Tamil Nadu, the Gampola population shows more proximal genetic relatedness to the Tamil Nadu population than Jaffna.

Fluctuating sea levels have separated the island from the Indian sub-continent, creating a narrow strip of sea known as the "Palk Strait" (Arasaratnam & Peiris, 1999), which limits the migration of terrestrial animals between the two landmasses. Thus, geographical isolation of organisms has driven the way to allopatric speciation (Cabej, 2012) creating new species and subspecies of

reptiles and other terrestrial animals of Sri Lanka. This underscores the necessity for a study to be conducted using authentically collected samples that represent all the geographical locations in South Asia where the population of Russell's viper is abundant. Incorporating more taxa and more gene markers (nuclear + mitochondrial) to the phylogenetic study may improve the resolution among the phylogenetic analysis, and a reliable outcome can be expected (Rokas & Carroll, 2005).

Russell's viper can be considered as a keystone species due to its ecological contributions in maintaining the ecological balance and controlling populations of pests such as rodents (Beaupre & Douglas, 2009; Glaudas, 2021a; Martin, 2021). Although it has been listed as a least concerned (LC) species in the national red list of Sri Lankan fauna and flora (MOE, 2012), its survival is threatened by deforestation and intentional killing by humans out of fear. Therefore, understanding its exact phylogenetic position and relationships is critically important. This understanding will not only help resolve uncertainties related to evolutionary biology but also aid in assessing the conservation status of *D. russelii* in Sri Lanka, laying a platform for which future conservation efforts may be initiated.

CONCLUSION

The current study confirms a sister group relationship between the Indian/Sri Lankan lineage and the Pakistani lineage of the Russell's viper (*D. russelii*). Additionally, it discloses the presence of an incipient genetic divergence between Russell's viper populations in Jaffna and South India.

Acknowledgements

REFERENCES

Abyerami S. & Sivashanthini K. (2008). Diversity of snakes from the Jaffna Peninsula, Sri Lanka. *Pakistan Journal of Biological Sciences* **11**(16): 1969–1978.
DOI: https://doi.org/10.3923/pjbs.2008.1969.1978

Arasaratnam S. & Peiris G.H. (1999). History of Sri Lanka. Available at *https://www.britannica.com/place/Sri-Lanka/History*, Accessed 30 September 2021.

Bandelt H.J., Forster P. & Röhl A. (1999). Median-joining networks for inferring intraspecific phylogenies. *Molecular Biology and Evolution* **16**(1): 37–48.
DOI: https://doi.org/10.1093/oxfordjournals.molbev.a026036

Beaupre S.J. & Douglas L.E. (2009). Snakes as indicators and monitors of ecosystem properties. In: *Snakes: Ecology and Conservation* (eds. S.J. Mullin & R.A. Seigel), pp. 244–261. Cornell University Press, USA.
DOI: https://doi.org/10.7591/9780801459092-013

Bossuyt F. *et al*., (14 authors) (2004). Local endemism within the Western Ghats-Sri Lanka biodiversity hotspot. *Science* **306**(5695): 479–481.
DOI: https://doi.org/10.1126/science.1100167

Boundy J. (2020). *Snakes of the World: A Supplement* (1st edition). CRC Press, USA.
DOI: https://doi.org/10.1201/9780429461354

Cabej N.R. (2012). Species and allopatric speciation. In: *Epigenetic Principles of Evolution*, 1st edition, pp. 707–723. Elsevier, Netherlands.

Crusz H. (1973). Nature conservation in Sri Lanka (Ceylon). *Biological Conservation* **5**(3): 199–208.
DOI: https://doi.org/10.1016/0006-3207(73)90012-8

Das I. & de Silva A. (2016). *A Photographic Guide to Snakes and Other Reptiles of Sri Lanka*, 2nd edition. New Holland Publishers.

Deraniyagala P.E.P. (1955). *A Coloured Atlas of Some Vertebrates from Ceylon (Serpentoid, Reptilia)*, 1st edition. Ceylon National Museum's Publication, Ceylon.

Glaudas X. (2021a). Natural history of a highly medically important snake, Russell's Viper (*Daboia russelii*), in a human-dominated Indian rural landscape. *Journal of Herpetology* **55**(2): 151–159.
DOI: https://doi.org/10.1670/20-042

Glaudas X. (2021b). Proximity between humans and a highly medically significant snake, Russell's viper, in a tropical rural community. *Ecological Applications* **31**(4): 1–8.
DOI: https://doi.org/10.1002/eap.2330

Guindon S., Dufayard J.-F., Lefort V., Anisimova M., Hordijk W. & Gascuel O. (2010). New algorithms and methods to estimate maximum-likelihood phylogenies: assessing the performance of PhyML 3.0. *Systematic Biology* **59**(3): 307–321.
DOI: https://doi.org/10.1093/sysbio/syq010

Gunatilleke N., Pethiyagoda R. & Gunatilleke S. (2017). Biodiversity of Sri Lanka. *Journal of the National Science Foundation of Sri Lanka* **36**(1): 25–62.
DOI: https://doi.org/10.4038/jnsfsr.v36i0.8047

Gunawardene N.R. *et al*. (11 authors) (2007). A brief overview of the Western Ghats - Sri Lanka biodiversity hotspot. *Current Science* **93**(11): 1567–1572.

Hackett S J. (1996). Molecular phylogenetics and biogeography of tangers in the genus *Ramphocelus* (Aves). *Molecular Phylogenetics and Evolution* **5**(2): 368–382.
DOI: https://doi.org/10.1006/mpev.1996.0032

Herrmann H.-W., Joger U. & Nilson G. (1992). Phylogeny and systematics of viperine snakes. III: resurrection of the genus *Macrovipera* (Reuss, 1927) as suggested by biochemical evidence. *Amphibia-Reptilia* **13**(4): 375–392.
DOI: https://doi.org/10.1163/156853892X00076

Kasturiratne A., Pathmeswaran A., Fonseka M.M.D., Lalloo D.G., Brooker S. & de Silva H.J. (2005). Estimates of disease burden due to land-snake bite in Sri Lankan hospitals. *The Southeast Asian Journal of Tropical Medicine and Public Health* **36**(3): 733–740.

Lanfear R., Calcott B., Ho S.Y.W. & Guindon S. (2012). PartitionFinder: Combined selection of partitioning schemes and substitution models for phylogenetic analyses. *Molecular Biology and Evolution* **29**(6): 1695–1701.
DOI: https://doi.org/10.1093/molbev/mss020

Lanfear R., Frandsen P.B., Wright A.M., Senfeld T. & Calcott B. (2017). PartitionFinder 2: New methods for selecting partitioned models of evolution for molecular and morphological phylogenetic analyses. *Molecular Biology and Evolution* **34**(3): 772–773.
DOI: https://doi.org/10.1093/molbev/msw260

Leigh J.W. & Bryant D. (2015). POPART : full-feature software for haplotype network construction. *Methods in Ecology and Evolution* **6**(9): 1110–1116.
DOI: https://doi.org/10.1111/2041-210X.12410

Martin G. (2021). Russell's vipers: Predators of the undergrowth. Available at *https://roundglasssustain.com/species/russells-vipers*. Accessed 30 September 2021.

Minh B.Q., Nguyen M.A.T. & von Haeseler A. (2013). Ultrafast approximation for phylogenetic bootstrap. *Molecular Biology and Evolution* **30**(5): 1188–1195.
DOI: https://doi.org/10.1093/molbev/mst024

MOE (2012). *The National Red List 2012 of Sri Lanka; Conservation Status of the Fauna and Flora*. Ministry of Environment, Colombo, Sri Lanka.

Pla D. *et al*. (11 authors) (2019). Phylovenomics of *Daboia russelii* across the Indian subcontinent. Bioactivities and comparative in vivo neutralization and in vitro third-generation antivenomics of antivenoms against venoms from India, Bangladesh and Sri Lanka. *Journal of Proteomics* **207**: 103443.
DOI: https://doi.org/10.1016/j.jprot.2019.103443

Pyron R.A., Burbrink F.T. ,& Wiens J.J. (2013a). A phylogeny and revised classification of Squamata, including 4161 species of lizards and snakes. *BMC Evolutionary Biology* **13**(93): 13–93.

Pyron R.A., Kandambi H.K.D., Hendry C.R., Pushpamal V., Burbrink F.T. & Somaweera R. (2013b). Genus-level phylogeny of snakes reveals the origins of species richness in Sri Lanka. *Molecular Phylogenetics and Evolution* **66**(3): 969–978.
DOI: https://doi.org/10.1016/j.ympev.2012.12.004

Rambaut A., Drummond A.J., Xie D., Baele G. & Suchard M.A. (2018). Posterior summarization in Bayesian phylogenetics using Tracer 1.7. *Systematic Biology* **67**(5): 901–904.
DOI: https://doi.org/10.1093/sysbio/syy032

Ravichandren S. & Thirunavukarasu K. (2016). A study on epidemiological and clinical profile of victims of snake bite admitted to Teaching Hospital Jaffna, Sri Lanka. *International Journal of Medical Microbiology and Tropical Diseases* **2**(4): 118–124.
DOI: https://doi.org/10.18231/2455-6807.2016.0001

Rokas A. & Carroll S.B. (2005). More genes or more taxa? The relative contribution of gene number and taxon number to phylogenetic accuracy. *Molecular Biology and Evolution* **22**(5): 1337–1344.
DOI: https://doi.org/https://doi.org/10.1093/molbev/msi121

Ronquist F. *et al*. (2012). MrBayes 3.2: Efficient Bayesian phylogenetic inference and model choice across a large model space. *Systematic Biology* **61**(3): 539–542.
DOI: https://doi.org/10.1093/sysbio/sys029

Rozas J., Ferrer-Mata A., Sánchez-DelBarrio J.C., Guirao-Rico S., Librado P., Ramos-Onsins S.E. & Sánchez-Gracia A. (2017). DnaSP 6: DNA sequence polymorphism analysis of large data sets. *Molecular Biology and Evolution* **34**(12): 3299–3302.
DOI: https://doi.org/10.1093/molbev/msx248

Smith M. (1943). *The Fauna of British India, Ceylon and Burma*, volume III- Serpentes. Today & Tomorrow's Printers and Publishers, India.

Smith M.A. (1917). Descriptions of new reptiles and a new batrachian from Siam. *The Journal of the Natural History Society of Siam* **2**: 221–225.

Tamura K., Stecher G. & Kumar S. (2021). MEGA11: molecular evolutionary genetics analysis version 11. *Molecular Biology and Evolution* **38**(7): 3022–3027.
DOI: https://doi.org/10.1093/molbev/msab120

Tan N.H., Fung S.Y., Tan K.Y., Yap M.K.K., Gnanathasan C.A. & Tan C.H. (2015). Functional venomics of the Sri Lankan Russell's viper (*Daboia russelii*) and its toxinological correlations. *Journal of Proteomics* **128**: 403–423.
DOI: https://doi.org/10.1016/j.jprot.2015.08.017

Thompson J.D., Higgins D.G. & Gibson T.J. (1994). CLUSTAL W: improving the sensitivity of progressive multiple sequence alignment through sequence weighting, position-specific gap penalties and weight matrix choice. *Nucleic Acids Research* **22**(22): 4673–4680.
DOI: https://doi.org/10.1093/nar/22.22.4673

Thorpe R.S., Pook C.E. & Malhotra A. (2007). Phylogeography of the Russell's viper (*Daboia russelii*) complex in relation to variation in the colour pattern and symptoms of envenoming. *The Herpetological Journal* **17** 209–218.

Wall F.C. (1921). *Ophidia Taprobanica or the Snakes of Ceylon*. H.R. Cottle, Government Printer, Ceylon.

Wallach V., Williams K.L. & Boundy J. (2014). *Snakes of the World: a Catalogue of Living and Extinct Species*, 1ˢᵗ edition. CRC Press.

Warrell D.A. (1989). Snake venoms in science and clinical medicine. 1. Russell's viper: biology, venom and treatment of bites. *Transactions of the Royal Society of Tropical Medicine and Hygiene* **83**(6): 732–740.
DOI: https://doi.org/10.1016/0035-9203(89)90311-8

Warrell D.A. (2010). Snake bite. *The Lancet* **375**(9708): 77–88.
DOI: https://doi.org/10.1016/S0140-6736(09)61754-2

Wüster W. (1998). The genus *Daboia* (Serpentes: Viperidae): Russell's viper. *Hamadryad* **23**(1): 33–40.

Wüster W., Otsuka S., Malhotra A. & Thorpe R.S. (1992). Population systematics of Russell's viper: a multivariate study. *Biological Journal of the Linnean Society* **47**(1): 97–113.
DOI: https://doi.org/10.1111/j.1095-8312.1992.tb00658.x

Zhang D.-X. & Hewitt G.M. (1996). Nuclear integrations: challenges for mitochondrial DNA markers. *Trends in Ecology & Evolution* **11**(6): 247–251.
DOI: https://doi.org/10.1016/0169-5347(96)10031-8

SUPPLEMENTARY MATERIALS

Supplementary Table S1: The best-fit nucleotide substation model and the partitioning schemes used for the phylogenetic inference analysis as determined by PartitionFinder 2

| Subsequent Analysis	Genes (Number of Taxa)	Number of partitions (Subsets)	Partitions	The best model
Bayesian inference using MrBayes	Cytb (34)	1	Cytb cp1	SYM
		2	Cytb cp2	HKY
		3	Cytb cp3	GTR
	Cytb + ND2 (18)	1	Cytb cp1	SYM
		2	Cytb cp2	HKY
		3	Cytb cp3	GTR
		4	ND2 cp1	HKY+G
		5	ND2 cp2	HKY+I
		6	ND2 cp3	HKY+G
Maximum likelihood inference using IQ-TREE	Cytb (34)	1, 2, 3	Cytb cp1, Cytb cp2, Cytb cp3	TRN
	Cytb + ND2 (18)	1, 2, 3	Cytb cp1, Cytb cp2, Cytb cp3	TRN
		4	ND2 cp1	K81UF+G
		5	ND2 cp2	HKY+I
		6	ND2 cp3	TRN

cp, codon position

Supplementary Table S2: Details of the samples considered for construction of haplotype network in PopART v1.7, including localities, voucher reference, and GeneBank accession numbers.

Sample/Isolate	Organism	Locality	*Cytb*	Haplotype
NA	*D. russelii*	Thayur, Tamil Nadu, India	AY165087.1	H5
NA	*D. russelii*	Gampola, Sri Lanka	AY165088.1	H4
NA	*D. russelii*	Pakistan	AJ275723.1	H7
RV001	*D. russelii*	Jaffna, Sri Lanka	MW771366.1	H3
RV002	*D. russelii*	Jaffna, Sri Lanka	MW771367.1	H3
RV003	*D. russelii*	Jaffna, Sri Lanka	MW771368.1	H3
RV006	*D. russelii*	Jaffna, Sri Lanka	MW771369.1	H3
RV007	*D. russelii*	Jaffna, Sri Lanka	MW771370.1	H3
RV008	*D. russelii*	Jaffna, Sri Lanka	MW771371.1	H3
DR11	*D. russelii*	Pakistan	MZ711546.1	H8
DR18	*D. russelii*	Pakistan	MZ711545.1	H8
DR15	*D. russelii*	Pakistan	MZ711544.1	H8
DR20	*D. russelii*	Pakistan	MZ711543.1	H8
DR4	*D. russelii*	Pakistan	MZ711542.1	H8
DR3	*D. russelii*	Pakistan	MZ711541.1	H8
DR1	*D. russelii*	Pakistan	MZ711540.1	H8
DR2	*D. russelii*	Pakistan	MZ711539.1	H6
NA	*D. russelii*	Pakistan	HM179463.1	H6
AIWC 074	*D. russelii*	Tamil Nadu, India	MZ029432.1	H2
V30	*D. russelii*	Vedenemmeli, Tamil Nadu, India	MG995824.1	H1
V27	*D. russelii*	Goa, India	MG995821.1	H1
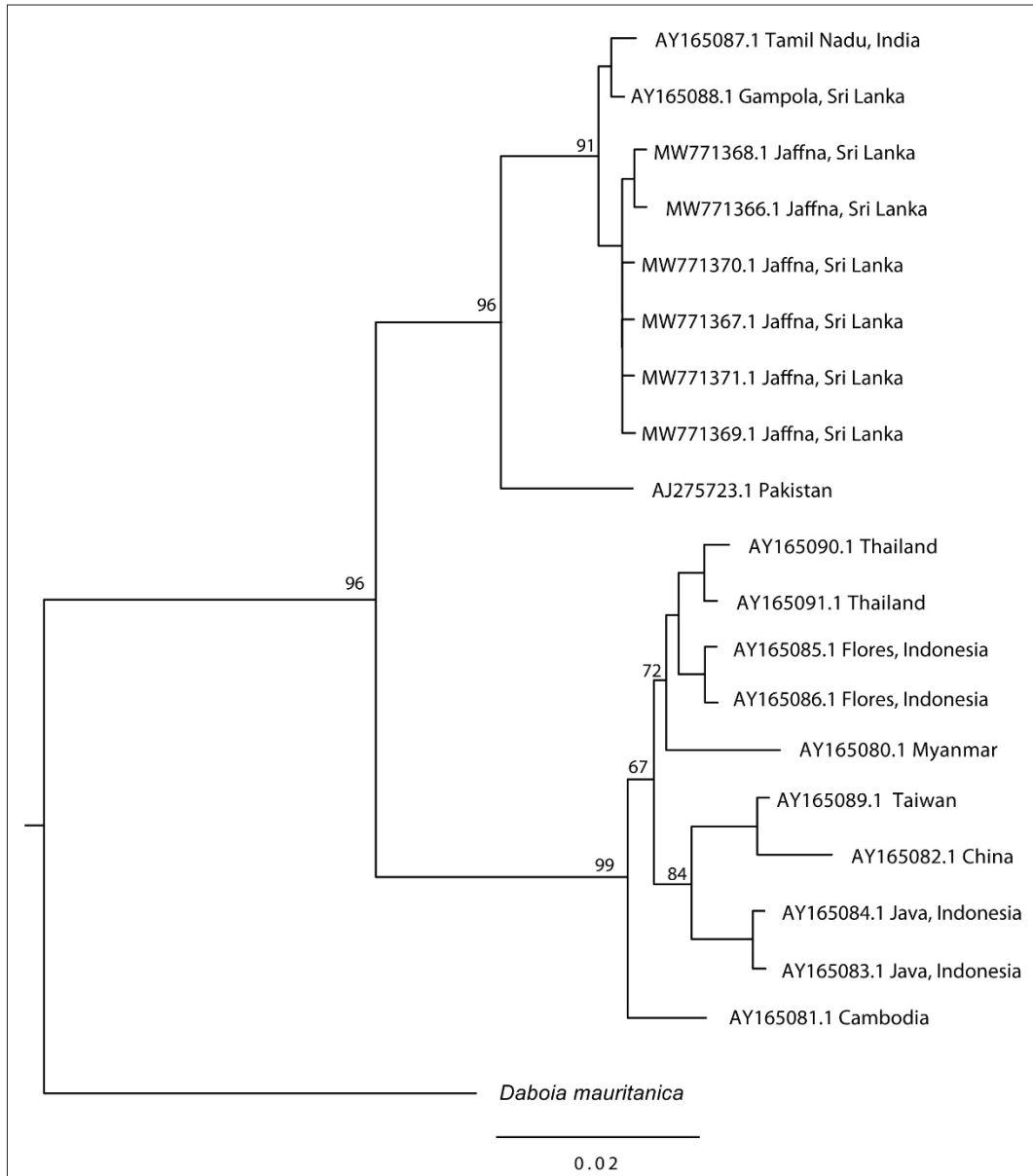
Supplementary Figure S1: Molecular phylogenetic relationships of Russell's viper, built upon maximum likelihood method of the concatenated sequence alignment of the Cytb + ND2 (846 bp) mitochondrial-gene markers. The numerical values above and below nodes indicate maximum likelihood ultrafast bootstrap values. The scale bar corresponds to the number of genetic changes per site. The accession number at the branch tip corresponds to the Cytb gene, listed in Table 2.
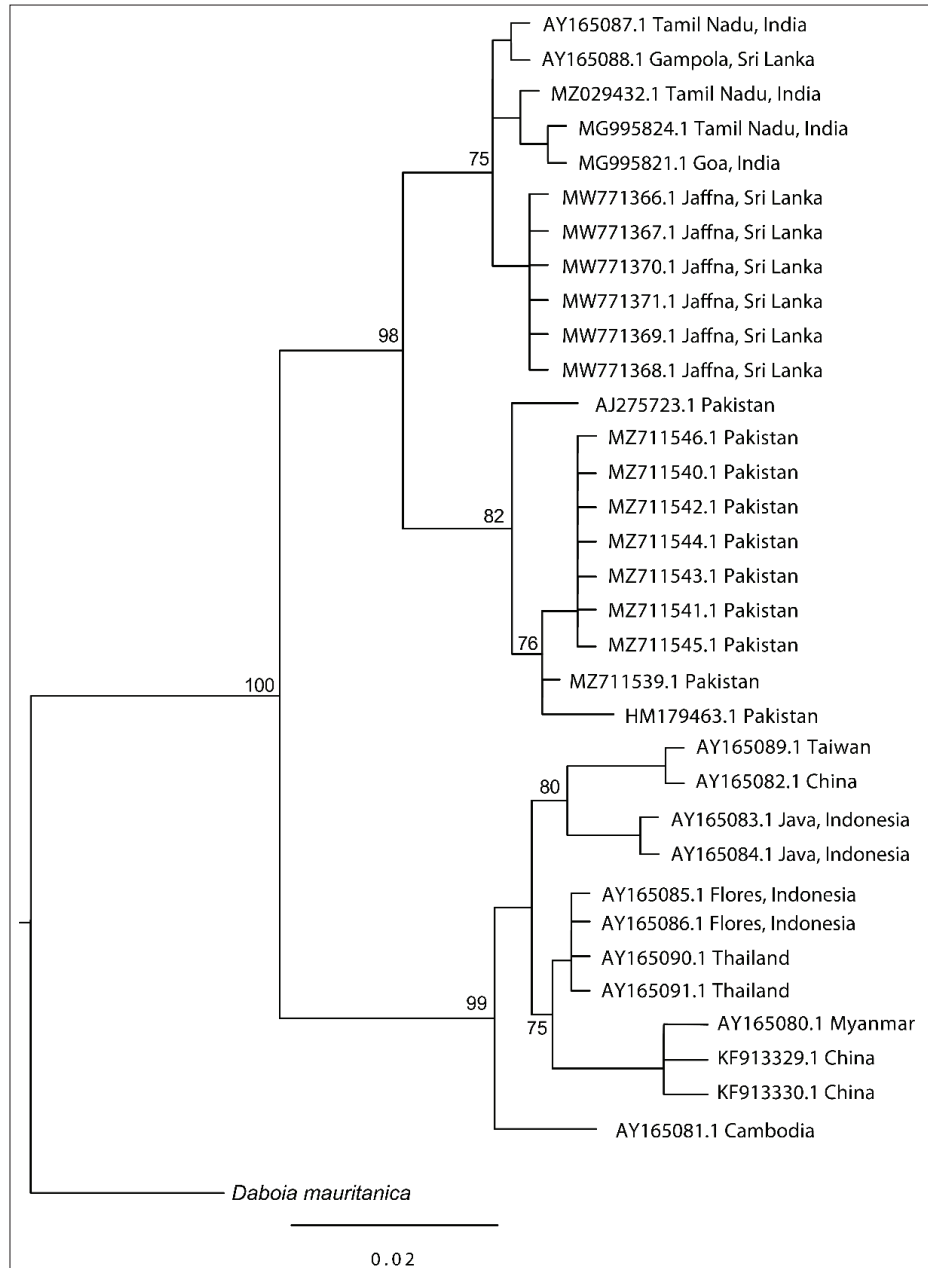
Supplementary Figure S2: Molecular phylogenetic relationships of Russell's viper, built upon maximum likelihood method of the multiple sequence alignment of the Cytb (576 bp) mitochondrial-gene markers. The numerical values above nodes indicate ultrafast bootstrap values. The scale bar corresponds to the number of genetic changes per site. The accession number at the branch tip corresponds to the Cytb gene, listed in Table 2.

RESEARCH ARTICLE

Plant Genetics

Genetic diversity analysis of traditional and improved rice genotypes in Sri Lanka using SSR markers

AL Ranawake[1*] and HAPA Shyamalee[2]

[1] *Department of Agricultural Biology, Faculty of Agriculture, University of Ruhuna, Mapalana, Kamburupitiya, Sri Lanka*
[2] *Faculty of graduate studies, University of Ruhuna, Mapalana, Kamburupitiya, Sri Lanka.*

Abstract: The objective of the present study was to find the genetic diversity of eight improved varieties and eighty-four traditional accessions of rice using nine polymorphic simple sequence repeat (SSR) markers. The SSR markers detected 32 alleles ranging from 2 to 5, with an average of 3.55 alleles per locus, indicating a high genetic diversity. The number of effective alleles (ne) ranged from 1.85 (*RM208*) to 3.84 (*RM493*), with an average of 2.64 alleles per locus, which reconfirms an existing broad genetic diversity. Nei's genetic diversity index was very high (0.5955), indicating a high mean expected heterozygosity (HE). *RM493* recorded the maximum polymorphism information content (PIC) value (0.8814). The mean PIC value was 0.5955 for the used SSR markers. Out of nine SSR markers, seven scored more than 0.5 PIC values, proving their potential to be used as genetic markers. Shannon's information index (I) ranged from 0.65 (*RM208*) to 1.36 (*RM493*), with a mean value of 1.00. All genetic diversity indicators, na, ne, HE, PIC and I reflect the high genetic differentiation in representative sample of rice genotypes. According to the unweighted pair group method with arithmetic mean dendrogram and Nei's genetic distance, the ninety-two rice genotypes were classified into seven groups at an ~85 level of similarity with additional sub-clusters within each group. Rice genotypes with significant genetic divergence can be chosen for upcoming breeding programmes by assessing their positions within the dendrogram. In the dendrogram, genotypes sharing the same name were not clustered together, indicating their distinct genetic backgrounds despite them sharing the same name. The traditional rice accessions clustered together in the dendrogram can be further analysed using more polymorphic SSR markers.

INTRODUCTION

The availability of breeding materials with sufficient genetic variation is essential for developing improved new varieties (Temesgen, 2021). Local institutes in several countries, such as the International Rice Research Institute (IRRI), maintain rice gene banks, and IRRI conserves more than 106,800 rice accessions. Germplasm collection, maintenance, conservation, and evaluation are carried out in gene banks (Priyanka *et al.*, 2021). Morphological, physiological, cytological (Jiang, 2013), and molecular marker-based methods are used for diversity analysis in germplasm evaluation (Nakayama, 2005).

Dissection of diversity in genetic materials is essential for plant breeders to select desirable characteristics (Jiang, 2013). Morphological characterization is the simplest method broadly used to analyze germplasm collections (Maji, 2012). Many studies have used phenotypic traits to assess the genetic diversity of rice (Krishnamurthy *et al.*, 2014; Gaballah *et al.*, 2021a). Conventional breeding relies on morphological characterization, though it is time-consuming, labour-consuming, and needs a large population and infrastructure to manage

* Corresponding author (lankaranawake@hotmail.com; [iD] https://orcid.org/0000-0003-0517-9911)

the replicated trials. However, phenotypic evaluation may not be accurate due to the environmental effect on phenotype, and molecular-based analysis is required to validate the morphological characterization (Ray *et al.*, 2013). Different molecular markers are used for this (Bhanu, 2017). Molecular markers accelerate breeding programmes with greater accuracy (Lema, 2018). Genotypic diversity has been effectively assessed using agronomical traits (Kocaman *et al.*, 2020), physiological characteristics (Sanghamitra *et al.*, 2021; Ril *et al.*, 2022) and quality characteristics (Utami *et al.*, 2017). SSR markers are DNA sequences linked with a specific known location. About 2500 SSR primer pairs were developed for rice (McCouch *et al.*, 2002). The copy number changing with the individuals is the source of polymorphism in SSR markers (Schrider & Hahn, 2010). The superiority of SSR markers over other molecular markers is due to their technical simplicity in assessing co-dominant inheritance and the requirement of a small amount of DNA to initiate PCR reactions. Further, SSR markers are relatively low-cost, time-saving, hypervariable, guarantee extensive genomic coverage, and provide high genomic resolution (Ijaz, 2011; Kocaman *et al.*, 2020; Ril *et al.*, 2022).

The diversity of rice germplasm collections has been studied using SSR markers in different collections: wild rice (Getachew *et al.*, 2018; Ngangkham *et al.,* 2019), upland rice (Roy *et al.*, 2016), weedy rice (Hanafiah *et al.*, 2022), traditional rice (Dahanayaka *et al.*, 2015; Hemachandra, 2018; Manatunga *et al.*, 2018; Weerakoon & Somaratne, 2021; Koodalugodaarachchi *et al.*, 2022), *Japonica* and *indica* rice types (Yogi *et al.*, 2021), Ethiopian rice genotypes (Getachew *et al.*, 2018), Thai rice genotypes (Pathaichindachote *et al.*, 2019), and landraces in China (Yang *et al.*, 2022).

Sri Lankan traditional rice accessions have been evaluated using SSR markers for different purposes: drought tolerance (Munasunghe *et al.*, 2017), development of conventional rice co-collection accessions (Weerakoon & Somaratne, 2021), detection of amylose content (Kottearachchi *et al.*, 2014) and flowering time (Ranawake & Mori, 2014).

Several sets of traditional rice accessions with the same names and improved rice varieties were included in the present study. The objectives of the present study were to analyse the genetic diversity among a selection of improved and traditional rice genotypes from Sri Lanka, investigate genetic resemblances among accessions sharing the same name, explore genetic relationships using SSR markers, and identify genetically distant genotypes. The overlap

between *Murungakayan3490* accession was found in the present study and study conducted by Manathunga *et al.*, (2018). Additionally, a pair of *Kaluheenati* accessions (*5191, 7802*) was previously studied by Siriwardhana *et al.*, (2016). No overlapping accessions were identified among the *Suwandal* accessions examined by Gunasena *et al.* (2016), or the *Suduheenati* accessions studied by Tharmarajan *et al.* (2018). The specificity in this study is discrimination between accessions, accuracy of clustering, or phylogenetic analysis and utility in breeding programs.

MATERIALS AND METHODS

Plant materials

Ninety-two rice genotypes, including eighty-four traditional and eight improved varieties of Sri Lankan origin, were collected from the Plant Genetic Resources Centre, Gannoruwa, Sri Lanka (PGRC, 1999). These accessions had been assigned unique accession numbers as part of the documentation process. The farmers used the provided names when referring to them as they were grown in various locations across Sri Lanka. The names/numbers were as follows:

Dahanala5386, Kalubalawee3976, Mawee3618, Ratawee3525, Dahanala6739, Kalubalawee3172, Mawee855, Ratawee3466, Dahanala3917, Kalubalawee3158, Mawee5384, Rathuwee3905, Dahanala3304, Kalubalawee5480, Murungakayan6285, Rathuwee3473, Dikwee4927, Kaluheenati7802, Murungakayan6263, Rathuheenati6249, Dikwee3741, Kaluheenati5191, Murungakayan3921, Rathuheenati5486, Dikwee3504, Kaluheenati4991, Murungakayan3900, Rathuheenati4992, Dikwee3444, Kaluheenati, Murungakayan3809, Suduheenati4932, Dikwee2203, Kaluheenati4621, Murungakayan3495, Suduheenati7799, Elwee3578, Kaluheenati3851, Murungakayan3492, Suduheenati5670, Heenati6402, Kaluheenati3471, Murungakayan3490, Suduheenati3932, Heenati4935, Kuruwee4679, Murungakayan3489, Sudurusamba4362, Heenati4618, Kuruwee3982, PodiweeA8-3109, Sudurusamba3671, Heenati4524, Kuruwee3898, Pokkali3922, Sudurusamba2202, Heenati3998, Kuruwee3552, Pokkali3881, Sudurusamba4363, Heenati3936, Kuruwee3465, Pokkali3701, Heenati3707, Mawee8552, Pokkali3573, Kaluwee4624, Mawee8497, Pokkali3567, Kaluwee3876, Mawee5531, Pokkali3562, Kaluwee3728, Mawee5384, Polayal3661, Kaluwee3212, Mawee4145, Polayal3639, Kalubalawee5481, Mawee3704, Ratawee4580, Kalubalawee5479, Mawee3683, Ratawee3655, Bg250, Bg251, Bg300, Bg350, Bg352, Bg359, Bg360, Bg369

DNA extraction

Dormancy broke (50°C for five days) rice seeds were germinated under dark conditions and grown for two weeks. Genomic DNA was extracted from two weeks old whole seedlings using the cetyl trimethyl ammonium bromide (CTAB) method (Murray & Thompson, 1980).

The concentration of each sample was observed by visual assessment of the band intensity compared to the lambda DNA of known concentrations, using 1% agarose gel. DNA was amplified using nine polymorphic SSR markers (Temnykh *et al*., 2001; McCouch *et al*., 2002) (Table 1).

Table 1: The sequences of the polymorphic SSR primers used for the diversity analysis in rice

Marker	Chromosome no	Forward sequence	Reverse sequence
RM208	2	5′ TCTGCAAGCCTTGTCTGATG 3′	5′ TCTGCAAGCCTTGTCTGATG 3′
RM277	12	5′ CGGTCAAATCATCACCTGAC 3′	5′ CAAGGCTTGCAAGGGAAG
RM248	7	5′ TCCTTGTGAAATCTGGTCCC 3′	5′ GTAGCCTAGCATGGTGCATG
RM464A	9	5′ AACGGGCACATTCTGTCTTC 3′	5′ TGGAAGACCTGATCGTTTCC
RM493	1	5′ TAGCTCCAACAGGATCGACC 3′	5′ GTACGTAAACGCGGAAGGTG
RM589	6	5′ ATCATGGTCGGTGGCTTAAC 3′	5′ CAGGTTCCAACCAGACACTG
RM271	10	5′ TCAGATCTACAATTCCATCC 3′	5′ TCGGTGAGACCTAGAGAGCC
RM122	5	5′ CTTCTTCCGCTTCCTCCCTTCC 3′	5′ TGTACCAGTGCACCGAGAGTTGG 3′
RM280	4	5′ ACACGATCCACTTTGCGC 3′	5′ TGTGTCTTGAGCAGCCAGG 3′

PCR was done in a 20 µL reaction mixture using around 50 ng template DNA, 125 U Taq DNA polymerase, 1.0 mM dNTPs, polymerase buffer (Mg^{2+} plus) (Promega), and ten µM primer in Applied Biosystems GeneAmp 9700 (2012) PCR System (USA). The PCR program was 95°C for 5 min, followed by 25 cycles of 95°C for 1 min, 55°C for 1 min, and 72°C for 2 min, with a final extension at 72°C for 7 min. The PCR products were run on a 1.0% poly acrylamide gel using 1x TBE buffer. Gel plates were silver stained for visualization. Banding profiles generated by each set of markers were compiled into a co-dominant data matrix by manual scoring according to Wu & Tanksley (1993). Tabulated scored data were analyzed using Popgene 1.31 (Yeh *et al*., 1999).

RESULTS AND DISCUSSION

Applying SSR markers in high-resolution genetic studies is critical for obtaining insights into the genome-wide distribution of genetic variation. Though using a limited set of nine polymorphic SSR markers may not directly elaborate the genetic parameters extensively, the derived values and advanced analytical methods can facilitate a nuanced comprehension of the underlying genetic dynamics.

Allelic polymorphism (na)

Allelic polymorphism is defined as the existence of more than one allele at a locus at a frequency greater than 5% in the population (Nei, 1984). SSR markers are highly polymorphic, even in closely related genotypes (Ellis & Burke, 2007). In the present study, nine polymorphic SSR markers identified thirty-two alleles across ninety-two genotypes. Out of nine polymorphic alleles, the maximum number of alleles (5) was generated by *RM277* and *RM464A*, followed by *RM493*, *RM589*, and *RM280* (4 alleles each). The minimum number of alleles was generated by *RM208* and *RM248* (3 alleles each). The average number of alleles per polymorphic locus was 3.55 (Table 2).

A study that used 41 rice genotypes and 15 SSR markers reported 68 total alleles, and the number of alleles detected by a marker ranged from 2 to 8 (Freeg & Anis, 2016). The number of alleles per locus ranged from 2 to 5 with an average value of 3.7 in the study carried out by Tripathi *et al*. (2020), and the average number of alleles per locus ranged from 1.20 to 4.30 with an average value of 2.45 according to Gaballah *et al*. (2021a). Similar results were also reported by Donde

et al. (2019), who investigated the genetic variability of sixteen rice landraces using sixty-three primers where alleles per locus ranged from 1 to 3 with an average value

of 1.5. Allelic polymorphism ranged from 2 to 47 alleles per locus in different studies that used SSR markers in rice diversity analysis (Table 2).

Table 2:   Genetic parameters as revealed by polymorphic SSR markers

Locus	na	ne	Nei	HE	PIC	I
RM208	2.0000	1.8506	0.4596	0.4623	0.4279	0.6522
RM277	5.0000	3.3741	0.7036	0.7090	0.5346	1.3413
RM248	2.0000	1.9656	0.4912	0.4949	0.3489	0.6844
RM464A	5.0000	2.2484	0.5552	0.5594	0.7076	0.9306
RM493	4.0000	3.8352	0.7393	0.7444	0.8814	1.3651
RM589	4.0000	3.3153	0.6984	0.7039	0.7448	1.2777
RM271	3.0000	2.0436	0.5107	0.5135	0.5108	0.7462
RM122	3.0000	2.1851	0.5424	0.5465	0.5444	0.8465
RM280	4.0000	2.9310	0.6588	0.6639	0.6589	1.1617
Mean	3.5556	2.6388	0.5955	0.5997	0.5955	1.0006
SD	1.1304	0.7333	0.1048	0.1058	0.1670	0.2886

na = observed number of alleles, ne = effective number of alleles, HE = expected heterozygosity computed using Levene (1949), Nei = Nei's (1973) gene diversity, PIC = polymorphism information content

Nei's (1973) expected heterozygosity, I = Shannon's Information index [Lewontin (1972)]

The number of effective alleles (ne)

The number of effective alleles (ne) is the number of alleles that can exist in a population (IPGRI and Cornell University, 2003). The number of effective alleles per locus ranged from 1.8506 (*RM208*) to 3.8352 (*RM493*), with an average of 2.6388 in the present study (Table 2). In contrast to the effective allele count presented by Getachew *et al*. (2018), which was derived from an analysis of 426 distinct genotypes (Table 4), the findings of the present study highlight a notably higher level of genetic diversity within the examined rice genotypes (*Supplementary table 1*). The number of effective alleles in the present study was greater compared to that reported by Getachew *et al*. (2018) which used 426 different genotypes (Table 4), which indicates an existing greater genetic diversity in the studied rice genotypes.

Nei's genetic diversity

Nei's genetic diversity shows the genetic variance within specific populations (Nei, 1973). In the present study, Nei's genetic diversity ranged from 0.4596 to 0.7393, indicating a significant genetic variation among

genotypes. The recorded Nei's genetic diversity index is more remarkable than reported in previous studies (Jasim *et al*., 2018; Dao *et al*., 2018; Verma *et al*., 2019; Razak *et al*., 2020) and less than the Nei's genetic diversity index reported by Sarif . (2020). The maximum Nei's genetic index (0.7393) recorded in the present study is almost similar to the reported value of 0.744 by Koodalugodaarachchi *et al*. (2022) for Sri Lankan rice genotypes, while Dahanayaka *et al*. (2015) reported 0.8078 as the maximum Nei's genetic index for a separate Sri Lankan rice genotype.

Expected heterozygosity (HE)

The expected heterozygosity (HE) is the probability that two alleles chosen randomly from a population differ (Nei, 1973). RM493 recorded the highest HE value (0.7444), and the average HE value was 0.5997, emphasizing the heterozygous nature of the studied genotypes. The HE values ranged from 0 to 0.94 in different diversity studies in rice (Supplementary Table 1). Compared to most of them, 0.7444 is a higher HE value for diversity analysis in rice.

Polymorphism information content (PIC)

PIC processes the ability of a marker to identify polymorphisms and therefore decides the utility of the specific SSR marker as a suitable genetic marker (Serrote *et al.*, 2020). Other than *RM208* and *RM248*, all seven remaining markers showed more than 0.5 PIC values, suggesting they could be used as genetic markers. Markers with high PIC values indicate greater genetic diversity within the population for those alleles. Genetic diversity is essential for plant breeding programmes as it provides a broader range of traits and characteristics that breeders can select from to develop improved cultivars. Further, higher PIC values suggest that the markers capture variations in traits that interest breeders, such as disease resistance, yield, quality, or environmental adaptability. These markers could lead to the identification of plants with desirable traits.

Moreover, markers with high PIC values are more informative, as they can distinguish between many different genotypes. This efficiency allows breeders to make more accurate selections in a shorter period. When markers have higher PIC values, they are more likely to be linked to genes that significantly impact the traits of interest. This means that selecting plants based on these markers has a higher chance of resulting in the desired traits in the next generation. Markers with higher PIC values are more likely to be spread across the genome, reducing the likelihood of "linkage drag," where unwanted traits are inadvertently transferred along with the desired trait during breeding. *RM493* and *RM248* reported the maximum (0.8814) and minimum (0.3489) PIC values, respectively, and the average PIC value was 0.5955. Different ranges of PIC values have been recorded, such as 0.4824–0.8078 (Dahanayaka *et al.*, 2015), 0.36–0.98 (Kumar *et al.*, 2012), 0.41–0.89 (Hue *et al.*, 2018) in rice diversity analysis studies, indicating a long history of domestication leading to trait evolution and selection.

Shannon's Information Index (I)

Shannon's Information index is a mathematical explanation of originally developed species diversity in a particular community based on the number of species present and individuals per species. The increasing number of species results in higher diversity. When Shannon's diversity index was applied to the diversity of the rice genotypes in a study, the values ranged from 0 to 5, and 1.5 to 3.5 is the typical range (CNR-University of Idaho, 2009). Shannon's index in the present study ranged from 0.6522 *(RM208)* to 1.3653 *(RM493)*,

averaging 1.0006. The average of Shannon's indices of two previous studies were reported as 0.58 (Jasim *et al.*, 2018) and 2.8 (Sarif *et al.*, 2020). The comparison of the genetic parameters of the present study with other similar studies carried out on rice in the near past shows the broad genetic diversity of Sri Lankan rice genotypes (*Supplementary table 1*).

Analysis of genetic relationships among ninety-two Sri Lankan rice genotypes

Using Nei's genetic distance and the UPGMA method of clustering, ninety-four rice genotypes were clustered into seven distinct groups at 85% similarity (Nei's genetic distance) (Figure 1). Nei's genetic identity was automatically calculated based on bootstrap analysis in Popgene. In the UPGMA dendrogram, a group I consisted of 22 rice genotypes, including one improved rice variety, *Bg360*. Among traditional accessions in group I, there were three *Dahanala (5386, 6739, 3304)*, three *Kuruwee (3982, 3552, 4679)*, three *Mawee (5531, 8497, 3704)*, and two *Pokkali (3881, 3922)* accessions. The other accessions in group I were *Heenati4618, Kaluheenati3471, Murungakayan6263, Dikwee4927, Polayal3639, Suduheenati7799, Rathuheenati4992, Rathuwee3473, Ratawee3655,* and *Kalubalawee3172*. Group one was divided into four subgroups at the Nei's genetic distance of 74%, and improved variety *Bg360* was separated from the other traditional rice accessions to make a separate subgroup. The largest subgroup of group I consisted of seventeen traditional rice accessions, with three *Mawee* and three *Kuruwee* rice accessions. In this group, most genotypes take more than 100 days for flowering, including improved variety *Bg360* (*unpublished data*).

Group II contained sixteen genotypes including improved varieties *Bg250* and *Bg251*. It was divided into four subgroups at the Nei's genetic distance of 70%. Group II-a had ten different traditional rice accessions. Group II-b consisted of two *Murungakayan* accessions (*3921, 3809*), and group II-c was separated with two improved rice varieties, *Bg250* and *Bg251*. Manathunga *et al.* (2018) identified *Murungakayan3490* as a representative accession, among others, namely *5378, 5614, 6279, 12824, 3329, 3491*, and *5611*, that possessed true-to-type characteristics in their study. Among these accessions, only *Murungakayan3490* was studied in the present research. The present results revealed that *Murungakayan3490* clustered with *Murungakayan3921* and *Murungakayan3809*, demonstrating their genetic similarities (Figure 1). Group III was the largest group, containing thirty-one rice genotypes. Five improved rice

varieties (*Bg300, Bg350, Bg352, Bg359,* and *Bg369*) out of eight were clustered in this group. In addition, some traditional rice accessions with the same name, *i.e.*, *Rathuheenati (6249, 5486), Dikwee (3504, 3741), Pokkali (3562, 3573, 3701), Heenati (4524, 3998, 6402, 4935, 3707), Kalubalawee (5481, 5479, 3158), Suduheenati (5670, 3932), Sudurusamba (3671, 4362), Kaluheenati (4621, 4991),* and *Ratawee (4580, 3466)* were in group III.

Group IV comprised two *Murungakayan (3900, 3495)* and two *Sudurusamba (2202, 4363)* accessions. Group V contained eight traditional rice

accessions: *Kaluwee (4624, 3728), Kaluheenati (5191, 7802), Mawee3683, Murungakayan6285, Ratawee3525,* and *Elwee3578.* The study of Siriwardhana *et al. (2016)* has reported nine genetically related accessions *(4089, 5191, 5385, 7802, 4087, 6713, 12932, 12926,* and *4091)* as a representative set for the pure line of *Kaluheenati.* Interestingly, the present study confirmed the genetic similarities of the Kaluheenati 5191 and 7802 accessions by clustering them together in Group V.

Group VI was the smallest group with four traditional rice accessions, including *Kaluheenati (4090, 3851), Mawee8552,* and *Kalubalawee5480.*
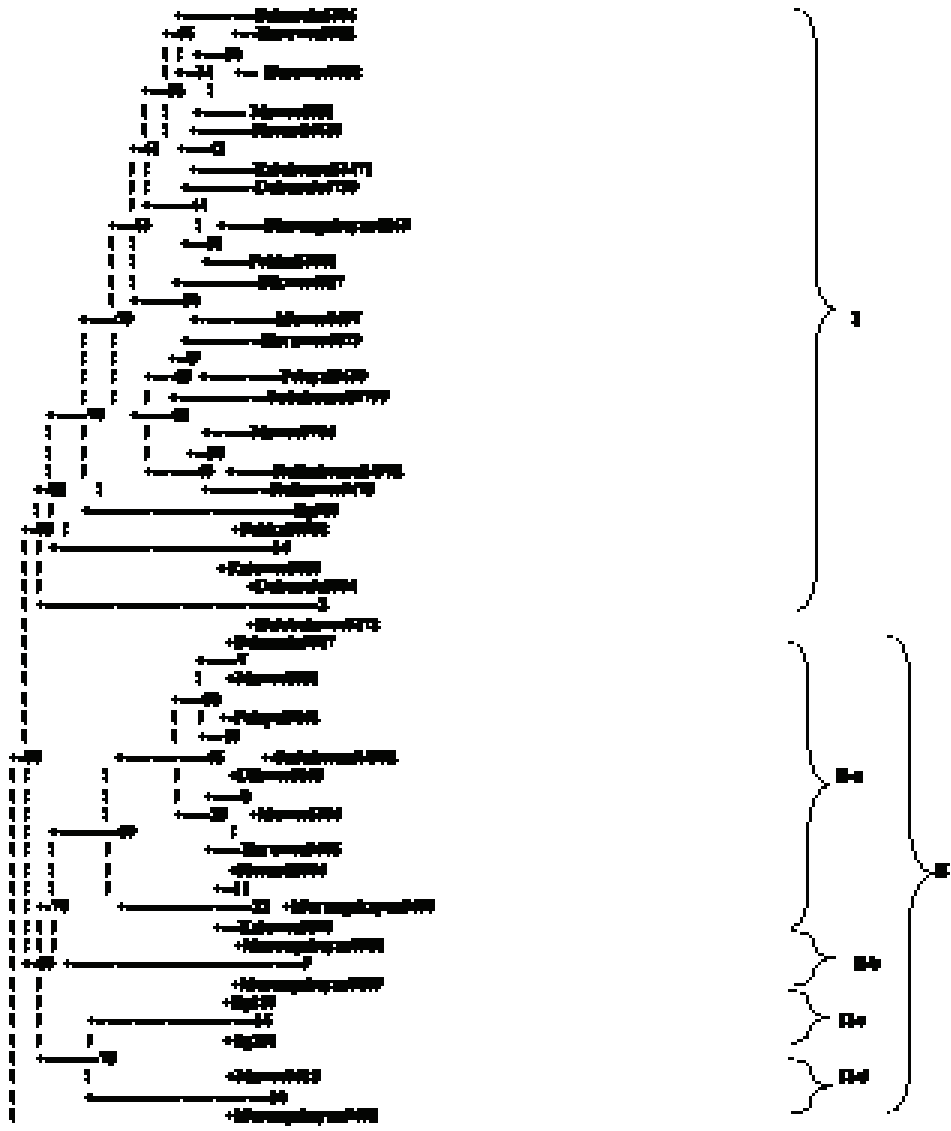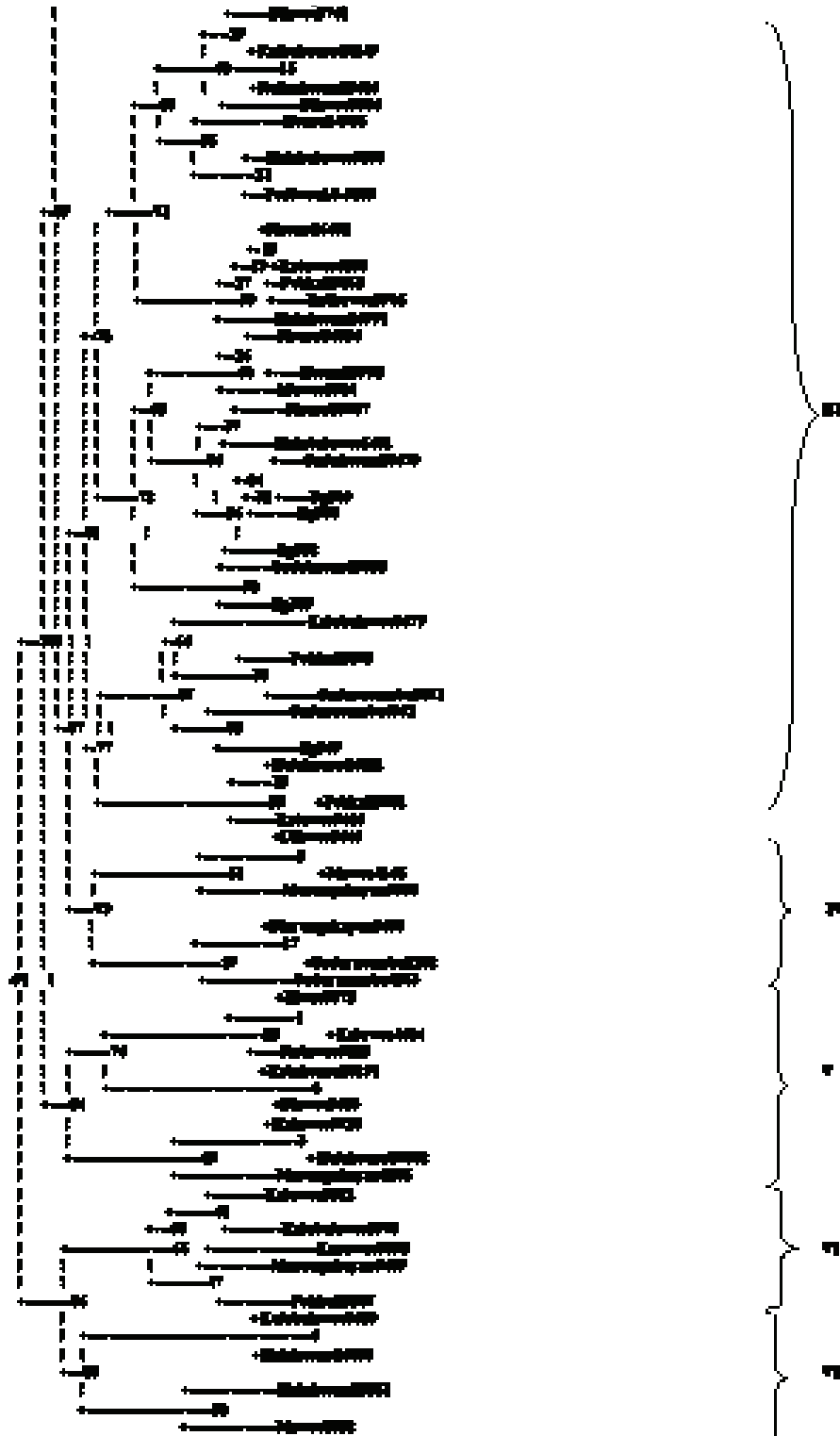
Figure 1: UPGMA Dendrogram based on Nei's (1978) genetic distance among ninety-two rice genotypes

A similar result has been reported in a diversity analysis where a UPGMA dendrogram of 24 rice cultivars based on a combination of SSR and sequence-tagged site (STS) markers resulted in five clusters at a genetic similarity coefficient value of 0.84 (Mosab-bin *et al.*, 2022). Another study that analysed thirty genotypes using thirty-five SSR markers resulted in five distinct clusters at a genetic similarity level of 66% (Seetharam *et al.*, 2009), whose cluster diversity is narrower than the present study's diversity. Nine clusters were reported in a study that used sixty-two rice genotypes with a comparatively low dissimilarity coefficient of 0.40 in Malaysia (Anisuzzaman *et al.*, 2022). Despite using 151 SSR markers for 24 Philippine rice genotypes, the dendrogram created three distinct clusters at a 40% similarity level (Lapitan *et al.*, 2007). Two *Kaluheenati* accessions *(4090, 3851)* were clustered in a previous diversity analysis using SSR markers (Siriwardana *et al.*, 2016). The genetic diversity of Sri Lankan traditional rice accessions with the same name, including *Suwandal* (Gunasena *et al.*, 2016), *Murungakayan (*Manathunga *et al.*, 2018), Kaluheenati* (Siriwardhana *et al.*, 2016), and *Suduheenati* (Tharmarajan *et al.*, 2018) was studied using SSR markers. According to Gunasena *et al.* (2016), there were no duplicate accessions in the studied *Suwandal* accessions. Manathunga *et al.* (2018) revealed four sets of *Murungakayan* duplicates, and Siriwardhana *et al.* (2016) identified nine true-to-type *Kaluheenati* accessions. Out of nineteen *Suduheenati* accessions,

nine accessions were identified as representatives of *Suduheenati* accessions by Tharmarajan *et al.* (2018).

The well-spanned dendrogram constructed using the UPGMA method and Nei's genetic distance emphasizes the usefulness of SSR markers dissecting genetic diversity in rice. Accessions clustered into one group are supposed to have high genetic similarity, while those clustered away from others are considered divergent.

The dendrogram helps assess the genetic diversity present in different rice germplasm collections. This information is essential for identifying unique and diverse genetic resources that can be conserved to ensure a wide range of traits and adaptations for future breeding efforts.

SSR markers allow for accurate and reliable characterization of rice germplasm. They help distinguish between different rice genotypes, ensuring that the correct genetic material is conserved. Further, the dendrogram depicts the genetic relationships among different rice genotypes. This information guides the selection of diverse parents for breeding programs and assists in avoiding redundancy in conservation efforts. Future repetition or regular monitoring of rice germplasm using SSR markers helps detect any loss of genetic diversity over time for identifying vulnerable or endangered accessions that require immediate conservation actions.

Table 5:   Cluster groups of rice genotypes with the same name by UPGMA Dendrogram

Group	Traditional rice genotypes	Improved rice accessions
I	*Dahanala5386, Dahanala6739, Dahanala3304, Kuruwee3982, Kuruwee3552, Kuruwee4679, Mawee5531, Mawee8497, Mawee3704, Pokkali3881, Pokkali3922*	*Bg360*
II	*Mawee8551, Mawee3618, Mawee5384, Murungakayan3921, Murungakayan3809, Murungakayan3490, Murungakayan3492*	*Bg250, Bg251*
III	*Rathuheenati6249, Rathuheenati5486, Dikwee3504, Dikwee3741, Pokkali3562, Pokkali3573, Pokkali3701, Heenati4524, Heenati3998, Heenati6402, Heenati4935, Heenati3707, Kalubalawee5481, Kalubalawee5479, Kalubalawee3158, Suduheenati5670, Suduheenati3932, Sudurusamba3671, Sudurusamba4362, Kaluheenati4621, Kaluheenati4991, Ratawee4580, Ratawee3466*	*Bg300, Bg350, Bg352, Bg359, Bg369*
IV	*Murungakayan3900, Murungakayan3495, Sudurusamba2202, Sudurusamba4363*	
V	*Kaluwee4624, Kaluwee3728, Kaluheenati5191, Kaluheenati7802*	
VI	*Kaluwee3212, Kalubalawee3976,*	
VII	*Kaluheenati4090, Kaluheenati3851, Kalubalawee5480*	

Though the outcome of the present study is limited due to the small number of SSR markers used, the output of this type of study facilitates the exchange of rice germplasm between different gene banks and research institutions; accurate genetic characterization ensures that exchanged materials are true to their original identity and maintain their genetic integrity. Furthermore, genotype position in the dendrogram can be considered for selecting appropriate parental lines for rice breeding programs, promoting the incorporation of diverse and desirable traits into new varieties while avoiding genetic bottlenecks.

Clustering traditional rice accessions with the same name but different accession numbers into one cluster gives evidence to consider them as duplicated collections (Table 5). However, the strength of conclusions drawn from diversity analysis studies regarding genetic similarities and dissimilarities is positively correlated with the increased number of SSR markers that span across all twelve chromosomes in rice.

CONCLUSIONS

The present study revealed a broad genetic diversity in ninety-two rice accessions. SSR markers found high genetic diversity with an average of 3.55 alleles per locus, effective alleles ranged from 1.85 to 3.84 per locus, and Nei's genetic diversity index was 0.5955. *RM493* had the highest PIC value (0.8814) among the markers used. *RM 277, RM464A, RM473, RM589, RM271, RM122,* and *RM280* SSR markers that scored more than 0.5 PIC values are promising genetic markers for future breeding programmes. Rice varieties exhibiting a significant genetic variation may be selected for forthcoming breeding endeavours by evaluating their placement within the dendrogram. This study confirmed the presence of genetically distinct genotypes among various accessions sharing identical names (*e.g.*, *Murungakayan, Mawee, Kaluwee, Sudurusamba, Kalubalawee,* etc.). Increasing the number of polymorphic SSR markers in future studies will effectively address the unsolved genetic dissimilarities among rice genotypes clustered together at lower cluster distances. Such studies will contribute to establishing a co-collection within Sri Lanka's traditional rice germplasm.

Acknowledgements

REFERENCES

Anisuzzaman M., Islam M.R., Khatun H., Haque M. A., Islam M. S. & Ahsan M. S. (2022). Molecular diversity of rice (*Oryza sativa* L.) genotypes in Malaysia based on SSR markers. *Acta Agriculturae Slovenica* **118**(4): 1–13.
DOI: https://doi.org/10.14720/aas.2022.118.4.2500

Beşer N. & Mutafçilar Z.Ç. (2020). Identification of SSR markers for differentiating rice (*Oryza sativa* L.) varieties marketed in Turkey. *Journal of Agricultural Sciences* **26**: 357–362.
DOI: https://doi.org/10.15832/ankutbd.518276

Bhanu A.N. (2017). Assessment of genetic diversity in crop plants - An Overview. *Advance Plants and Agricultural Research* **7**: 279–286.
DOI: https://doi.org/10.15406/apar.2017.07.00255

CNR-University of Idaho (2009). Estimates of Biodiversity.

Dahanayaka B.A., Gimhani D.R., Kottearachchi N.S. & Samarasinghe W.L.G. (2015). Assessment of salinity tolerance and analysis of SSR markers linked with Saltol QTL in Sri Lankan rice (*Oryza sativa*) genotypes. *American Journal of Experimental Agriculture* **9**: 1–10.
DOI**:** https://doi.org/10.9734/AJEA/2015/20255

Dao S., Timbine H., Goita O. & Traore D. (2018). Genetic variability assessment in irrigated rice (*Oryza sativa* and *Oryza glaberrima*) by PCR-SSR in Mali **6**: 22–29.
DOI: https://doi.org/10.11648/j.ijgg.20180602.11

Donde R., Kumar J., Gouda G., Gupta M.K., Mukherjee M., Baksh S.Y., Mahadani P., Sahoo K.K., Behera L.B. & Dash S.K. (2019). Assessment of genetic diversity of drought tolerant and susceptible rice genotypes using microsatellite markers. *Rice Science* **26**: 239–247.
DOI: https://doi.org/10.1016/j.rsci.2019.01.004

Ellis J.R. & Burke J.M. (2007). EST-SSRs as a resource for population genetic analyses. *Heredity* **99**: 125–132.
DOI: https://doi.org/10.1038/sj.hdy.6801001

Farahzadi F., Ebrahimi A., Zarrinnia V. & Azizinezhad R. (2020). Evaluation of genetic diversity in Iranian rice (*Oryza sativa*) cultivars for resistance to blast disease using microsatellite (SSR) markers. *Agricultural Research* **9**: 460–468.
DOI: https://doi.org/10.1007/s40003-019-00447-1

Freeg H.A. & Anis G.B. (2016). Genetic diversity among some rice genotypes with different drought tolerant based on SSR markers. *Cercetări Agronomice în Moldova* **XLIX**: 39–50.
DOI: https://doi.org/10.1515/cerce-2016-0024

Gaballah M.M., Fiaz S., Wang X., Younas A., Khan S.A., Wattoo F.M. & Shafiq M.R. (2021). Identification of genetic diversity among some promising lines of rice under drought stress using SSR markers. *Journal of Taibah University for Science* **15**: 468–478.

DOI: https://doi.org/10.1080/16583655.2021.1989738

Getachew M., Shilai Z. & Teklehaymanot H. (2018). Comparative evaluation of rice SSR markers on different *Oryza Species*. *Journal of Rice Research and Development* **1**: 38–48.
DOI: https://doi.org/10.36959/973/418

Gunasena P.G.S.D., Wasala S.K. & Sumanasingha V.A. (2016). Molecular characterization of accessions from a traditional rice cultivar, Suwandel conserved at plant genetic resources centre, Sri Lanka. *Tropical Agricultural Research* **27**(1): 103–109.
DOI: https://doi.org/10.4038/tar.v27i1.8158.

Hanafiah N.M., Cheng A., Lim P., Sethuraman G., Zain N.A.M., Baisakh N. & Mispan M.S. (2022). Novel PCR-based multiplex assays for detecting major quality and biotic stress in commercial and weedy rice. *Life* **12**(10): 1542.
DOI: https://doi.org/10.3390/life12101542

Hemachandra P.V. (2018). Evaluation of new rice lines derived through induced mutation of traditional variety: *Suduru samba*. *Journal of Agriculture and Value Addition* **1**(2): 67–72.

Hue H.T., Nghia L.T., Minh H.T., Anh L.H., Trang L.T.T. & Khanh T.D. (2018). Evaluation of genetic diversity of local-colored rice landraces using SSR Markers. *International Letters of Natural Sciences* **67**: 24–34.
DOI: https://doi.org/10.18052/www.scipress.com/ilns.67.24

Ijaz S. (2011). Microsatellite markers: An important fingerprinting tool for characterization of crop plants. *African Journal of Biotechnology* **10**(40): 7723–7726.
DOI: https://doi.org/10.5897/ajbx10.021

IPGRI and Cornell University (2003). Measures of genetic diversity. In: *Genetic Diversity Analysis with Molecular Marker Data: Learning Module*, pp. 1–71.

Jasim A.S., Rafii M.Y., Latif M.A., Sakimin S.Z., Arolu I.W. & Miah G. (2018). Genetic diversity of aromatic rice germplasm revealed by SSR markers. *Biomedical Research International* **2018**: Article ID 7658032.
DOI: https://doi.org/10.1155/2018/7658032

Jiang G.L. (2013). Plant marker-assisted breeding and conventional breeding: challenges and perspectives. *Advance Crop Science Technology* **1**: 1–2.

Kocaman B., Toy S. & Marakli S. (2020). Application of different molecular markers in biotechnology. *International Journal of Science Letters* **2**: 98–113.
DOI: https://doi.org/10.38058/ijsl.770081

Koodalugodaarachchi V., Kekulandara D.S. & Gimhani D.R. (2022). Genetic diversity of *Oryza sativa* 'Dahanala' traditional red rice and molecular markers associated with trichome density on adaxial surfaces. *Genetic Resource* **3**(5): 10–23.
DOI: https://doi.org/10.46265/genresj.AVEO9374

Kottearachchi N.S., Peiris R.K. & Rebeira S. (2014). Application of DNA markers for the detection of amylose content in Sri Lankan rice (*Oryza sativa* L.) varieties. *Asian Journal of Agricultural Biology* **2**: 44–50.

Krishnamurthy S.L., Sharma S.K., Kumar V., Tiwari S., Batra V. & Singh N.K. (2014). Assessment of genetic diversity in rice genotypes for salinity tolerance using Saltol markers of Chromosome 1. *Indian Journal of Genetics and Plant Breeding* **74**: 243–247.
DOI: https://doi.org/10.5958/0975-6906.2014.00167.9

Kumar R., Kumar Singh A. & Kumar A. (2012). Evaluation of genetic diversity in rice using simple sequence repeats (SSR) markers. *African Journal of Biotechnology* **11**: 14956–14995.
DOI: https://doi.org/10.5897/AJB12.215

Lapitan V.C., Brar D.S., Abe T. & Redoña, E.D. (2007). Assessment of genetic diversity of Philippine rice cultivars carrying good quality traits using SSR markers. *Breeding Science* **57**: 263–270.
DOI: https://doi.org/10.1270/jsbbs.57.263

Lema M. (2018). Marker assisted selection in comparison to conventional plant breeding: *Agricultural Research & Technology* **14**: 1–10.
DOI: https://doi.org/10.19080/artoaj.2018.14.555914

Lewontin R.C. (1972). The apportionment of human diversity. *Evolution Biology* **6**: 381–398.

Maji A.T. (2012). Application of principal component analysis for rice germplasm characterization and evaluation. *Journal of Plant Breeding & Crop Science* **4**: 87–93.
DOI: https://doi.org/10.5897/jpbcs11.093

Manatunga M.M.S.L., Wasala S.K., Sumanasinghe V.A. & Ubeysekara N.M. (2018). Genetic diversity analysis of "Murungakayan" rice accessions based on seed morphology and molecular characterization. *Tropical Agriculture Research* **30**: 65.
DOI: https://doi.org/10.4038/tar.v30i2.8310

McCouch *et al*. (19 authors)(2002). Development and mapping of 2240 new SSR markers for rice (*Oryza sativa* L.). *DNA Research* **9**: 199–207.
DOI: https://doi.org/10.1093/dnares/9.6.199

Mishra S.S., Behera P.K., Kumar V., Lenka S.K. & Panda D. (2018). Physiological characterization and allelic diversity of selected drought tolerant traditional rice (*Oryza sativa* L.) landraces of Koraput, India. *Physiology and Molecular Biology of Plants* **24**(6): 1035–1046.
DOI: https://doi.org/10.1007/s12298-018-0606-4

Munasinghe S.P., Somaratne S. & Weerakoon S.R. (2017) Screening of Sri Lankan rice (*Oryza sativa* L.) landraces for drought tolerance. *Tropical Agricultural Research* **28**(2): 183–191.

Murray M.G. & Thompson W.F. (1980). Rapid isolation of high molecular weight plant DNA. *Nucleic Acids Research* **8**(19): 4321–4326.
DOI: https://doi.org/10.1093/nar/8.19.4321

Mosab-bin A., Kamruzzaman M., Reflinur R. & Nahar N. (2022). Morpho-molecular diversity study of rice cultivars in Bangladesh. *Czech Journal of Genetics and Plant Breeding* **58**(2): 64–72.
DOI: https://doi.org/10.17221/69/2021-CJGPB

Nakayama S. (2005). Molecular cytological diversity in cultivated rice *Oryza sativa subspecies japonica* and *indica*. *Breeding Science* **55**: 425–430.
DOI: https://doi.org/10.1270/jsbbs.55.425

Nei M. (1984). Genetic Polymorphism and Neomutationism. In: *Evolutionary Dynamics of Genetic Diversity* (ed. G.S. Mani), Lecture Notes in Biomathematics, volume 53, pp. 214–241. Springer, Berlin, Heidelberg.
DOI: https://doi.org/10.1007/978-3-642-51588-0_3

Nei M. (1973). Analysis of gene diversity in subdivided populations. *Proceedings of the National Academy of Sciences USA* **70**: 3321–3323.
DOI: https://doi.org/10.1073/pnas.70.12.3321

Ngangkham U., Dash S., Parida M., Samantaray S., Nongthombam D., Yadav M.K., Kumar A., Chidambaranathan P., Katara J.L., Patra B.C. & Bose L.K. (2019). The potentiality of rice microsatellite markers in assessment of cross-species transferability and genetic diversity of rice and its wild relatives. *Biotechnology* **9**: 1–19.
DOI: https://doi.org/10.1007/s13205-019-1757-x

Pathaichindachote W., Panyawut N., Sikaewtung K., Patarapuwadol S. & Muangprom A. (2019). Genetic diversity and allelic frequency of selected Thai and exotic rice germplasm using SSR Markers. *Rice Science* **26**: 393–403.
DOI: https://doi.org/10.1016/j.rsci.2018.11.002

PGRC (1999). *Characterization Catalogue on Rice (Oryza sativa L.) Germplasm*. Plant Genetic Resources Centre, Sri Lanka.

Priyanka V., Kumar R., Dhaliwal I. & Kaushik P. (2021). Germplasm conservation: Instrumental in agricultural biodiversity. *Sustainable* **13**:1–18.
DOI: https://doi.org/10.3390/su13126743

Ranawake A.L. & Mori N. (2014). Study on flowering time SSR marker RM 248 in traditional rice accessions in Sri Lanka. *Breeding & Biotechnology Journal* **4**: 1165–1174.
DOI: https://doi.org/10.9734/bbj/2014/12569

Ray A., Deb D., Ray R. & Chattopadhayay B. (2013). Phenotypic characters of rice landraces reveal independent lineages of short-grain aromatic indica rice. *AOB Plants* **5**: 1–9.
DOI: https://doi.org/10.1093/aobpla/plt032

Razak S.A., Azman N.H.E.N., Kamaruzaman R., Saidon S.A., Yusof M.F.M., Ismail S.N., Jaafar M.A. & Abdullah N. (2020). Genetic diversity of released Malaysian rice varieties based on single nucleotide polymorphism markers. *Czech Journal Genetic & Plant Breeding* **56**: 62–70.
DOI: https://doi.org/10.17221/58/2019-CJGPB

Ril S., Shuhu, G., Gan L. & Huan, L. (2022). Phenotypic Variation and Molecular Marker Network Expression of Some Agronomic Traits in Rice (*Oryza sativa* L.). *Agronomy* **12**(12): 2980.
DOI: https://doi.org/10.3390/agronomy12122980

Roy S., Marndi B.C., Mawkhlieng B., Banerjee A., Yadav R.M., Misra A.K. & Bansal K.C. (2016). Genetic diversity and structure in hill rice (*Oryza sativa* L.) landraces from the North-Eastern Himalayas of India. *BMC Genetics* **17**: 1–15.
DOI: https://doi.org/10.1186/s12863-016-0414-1

Sanghamitra P., Nanda N., Barik S.R., Sahoo S., Pandit E., Bastia R., Bagchi T.B. & Pradhan S.K. (2021). Genetic structure and molecular markers-trait association for physiological traits related to seed vigour in rice. *Plant Gene* **28**: 100338.
DOI: https://doi.org/10.1016/j.plgene.2021.100338

Sarif H.M., Rafii M.Y., Ramli A., Oladosu Y., Musa H.M., Rahim H.A., Zuki Z.M. & Chukwu S.C. (2020). Genetic diversity and variability among pigmented rice germplasm using molecular marker and morphological traits *Biotechnology & Biotechnological Equipment* **34**: 747–762.
DOI: https://doi.org/10.1080/13102818.2020.1804451

Schrider D.R. & Hahn M.W. (2010). Gene copy-number polymorphism in nature. *Proceedings of the Royal Society B: Biological Sciences* **277**(1698): 3213–3221.
DOI: https://doi.org/10.1098/rspb.2010.1180

Seetharam K., Thirumeni S. & Paramasivam K. (2009). Estimation of genetic diversity in rice (*Oryza sativa* L.) genotypes using SSR markers and morphological characters. *African Journal of Biotechnology* **8**: 2050–2059.

Serrote C.M.L., Reiniger L.R.S., Silva K.B., Rabaiolli S.M. dos S. & Stefanel C.M. (2020). Determining the Polymorphism Information Content of a molecular marker. *Gene* **726**: 144175.
DOI: https://doi.org/10.1016/j.gene.2019.144175

Siriwardana, S.M.T.T., Samarasinghe W.L.G. & Gimhani D.R. (2016). Molecular characterization of a traditional rice variety Kaluheenati (*Oryza sativa* L.) using simple sequence repeats markers. *Proceedings of 15th Agricultural Research Symposium*, Wayamba University of Sri Lanka, pp. 135-139.

Temesgen B. (2021). Role and economic importance of crop genetic diversity in food security. *International Journal of Agricultural Science & Food Technology* **7**(1): 164–169.
DOI: https://doi.org/10.17352/2455-815x.000104

Temnykh S., De Clerck G., Lukashova A., Lipovich L., Cartinhour S. & McCouch S. (2001). Computational and experimental analysis of microsatellites in rice (*Oryza sativa* L.): frequency, length variation, transposon associations, and genetic marker potential. *Genome Research* **11**(8): 1441–1452.
DOI: https://doi.org/10.1101/gr.184001

Tharmarajan M., Wasala S.K. & Ranawake A.L. (2018). Genetic diversity analysis of traditional rice Suda Heenati (*Oryza sativa*) based on seed morphology and Simple Sequence Repeat (SSR) markers. *4th International Research Symposium*, Rajarata University of Sri Lanka.

Tripathi S., Singh S.K., Srivashtav V., Khaire A.R., Vennela P. & Singh D.K. (2020). Molecular diversity analysis in rice (*Oryza sativa* L.) using SSR markers **11**: 776–782.

Utami S., Widyastuti U., Utami D., Rosdianti I. & Lestari P. (2017). Molecular marker-assisted selection of rice grain quality on rice (*Oryza sativa* L.) lines tolerant to Fe toxicity stress. *Journal of Tropical Life Science* **7**: 268–276.
DOI: https://doi.org/10.11594/jtls.07.03.13

Verma H., Borah J.L. & Sarma R.N. (2019). Variability assessment for root and drought tolerance traits and genetic diversity analysis of rice germplasm using SSR Markers. *Science Report* **9**: 1–19.

DOI: https://doi.org/10.1038/s41598-019-52884-1

Weerakoon S. & Somaratne S. (2021). Development of a core collection from Sri Lankan traditional rice (*Oryza sativa*) varieties for phenotypic and genetic diversity. *Nusantara Bioscience* **13**: 61–67.
DOI: https://doi.org/10.13057/nusbiosci/n130109g201u

Wu K.S. & Tanksley S.D. (1993). Abundance, polymorphism and genetic mapping of microsatellites in rice. *Molecular Genetics and Genomics* **241**(1-2): 225–235.
DOI: https://doi.org/10.1007/BF00280220

Yang N., He P., Chen K., Zhang W., Li Y., Yang Q., Wang Y., Wang Z. & Han G. (2022). Genetic diversity and population structure of Yunnan rice landraces and disease resistance assessment 1–19.
DOI: ttps://doi.org/10.21203/rs.3.rs-1219478/v1

Yeh F., Rong-cai Y. & Boyle T. (1999). Popgene version 1.31 Microsoft Window-based Freeware for Population Genetic Analysis, Quick user guide. University of Alberta Centre. *International Research Edmonton*, pp. 1–29.

Yogi R., Kumar N., Kumar R. & Jain R.K. (2021). Genetic diversity analysis among important rice (*Oryza sativa* L.) genotypes using SSR markers. *Advances in Biological Research* **11**(2): 68–74
DOI: https://doi.org/10.15515/abr.0976-4585.11.2.6874

Supplementary Table 1: Comparison of the genetic parameters of the present study with other similar studies carried out in rice

Genotypes	Markers	Allele range /locus	Total na	ne	Nei	HE	PIC	I	Reference
92	9	2 to 5 (Avg 3.555)	32	1.85 to 3.83 (Avg 2.64)	0.4596 to 0.7393 (Avg 0.5955)	0.4623 to 0.7444 (Avg 0.5997)	0.3489 to 0.8814 (Avg 0.5955)	0.65 to 1.27 (Avg 1.00)	Present study
32	31	6 to 0.303	124		0.169- 0.744		0-161-0.697		(Koodalugodaarachchi *et al.*, 2022)
32	6	3 to 7	23				0.4824-0.8078		(Dahanayaka *et al.*, 2015)
54	59	2 to 9 (Avg 4.24)	250		0.4325		0.0688-0.8854 (Avg 0.3940)		(Dao *et al.*, 2018)
27	12	3 to 5 (Avg 3.7)	40				0.38-0.65 (Avg 0.56)		(Tripathi *et al.*, 2020)
32	34	11 to 38 (Avg 20.76)	706		28.17	0.94	0.86-0.97 (Avg 0.92)	2.8	(Sarif *et al.*, 2020)
46	1536 SNP	1.944 to 2.000			0.268		0.173-0.259 (Avg 0.213)		(Razak *et al.*, 2020)
64	20	1 to 10	467				0.36-0.98		(Kumar *et al.*, 2012)
5	9		74						(Sari *et al.*, 2021)
462	264	2 to 47 (Avg 12.88)	3361				0-0.93		(Chen *et al.*, 2021)
15	10	2 to 13 (Avg 7.20)	72	1.20 to 4.30 (Avg 2.45)		0.94-1.00 (Avg 0.98)	0.83-0.99 (Avg 0.94)		(Gaballah *et al.*, 2021a)
60	50	6, 2.	279	23 (Avg 2.3)					(Beşer and Mutafçilar, 2020)
30	10	28 (Avg 2.8)		23 (Avg 2.21)			0.60-0.081 (Avg 0.42)		(Farahzadi *et al.*, 2020)
426	67	2 to 19 (Avg 6.49)	440	0.85 - 2.3 (Avg 1.54)		0.06-0.48 (Avg 0.27)	0.09-0.72		(Getachew *et al.*, 2018)
90	40	3 to 12 (Avg 7.1)	184				0.41-0.89 (Avg 0.74)		(Hue *et al.*, 2018)
50	32			0.36	0.05-0.98 (Avg 0.36)	0.60	0.25-0.98 (Avg 64)	0.22-0.91 (Avg 0.58)	(Jasim Aljumaili *et al.*, 2018)
130	19	2.6	50			0.0-0.767	0.0-0.718		(Mishra *et al.*, 2018)
114	65	2.26	147		0.118-0658 (Avg 0.334)		0.51		(Verma *et al.*, 2019)
16	63	1-3 (Avg 1.5)							(Donde *et al.*, 2019)

na = observed number of alleles, ne = effective number of alleles, HE = expected heterozygosity computed using Levene (1949), Nei = Nei's (1973) genetic diversity, PIC = polymorphism information content

RESEARCH ARTICLE

Construction Engineering

Thermal performance of glass facade under fire loading: a numerical approach

RGSS Perera, JHA Ruwanmali, T Thevega, JASC Jayasinghe*, CS Bandara and AJ Dammika
Department of Civil Engineering, Faculty of Engineering, University of Peradeniya, Peradeniya, Sri Lanka.

Abstract: Non-structural internal and external walls play a crucial role in high-rise buildings. Exterior walls contribute to the building's aesthetic appearance and create a comfortable indoor environment against thermal and wind effects. Interior walls divide the space and minimize sound distractions while maintaining desired conditions. External walls are particularly important as the presence of combustible materials can pose a significant fire hazard. Hence, it is crucial to use materials with high thermal performance to mitigate risks. Glass is a commonly used material for external walls due to its transparency, affordability, availability, and sustainability. However, glass panels are susceptible to failure when exposed to heat due to their brittleness. Therefore, this study aims to assess the thermal performance of glass panels under fire by analyzing single, laminated, and insulated glass panels using *ABAQUS* finite element software. Through a parametric study using validated numerical models, the study identifies the optimal configuration for glass panels. The findings indicate that increasing the thickness of a single glass panel by 2 mm resulted in a temperature decrease of approximately 13.5%. Additionally, the impact of shape on thermal performance is studied by evaluating crack initiation time and temperature for various shapes with equal areas. The results show that rectangular panels exhibit the poorest thermal performance. Furthermore, the type of glass panel significantly influences thermal performance compared to shape and thickness. Insulated glass panels demonstrate superior performance compared to single and laminated glass panels. When investigating different insulation materials, krypton outperforms argon and air in terms of thermal performance. This study contributes to the advancement of fire-safety solutions in buildings by using a validated numerical model to identify critical parameters affecting the thermal performance of glass facades across various types and configurations.

Keywords: Finite element analysis, glass facades, insulated glass panel, laminated glass panel, thermal loads.

INTRODUCTION

There are two main types of building elements: structural and non-structural elements. Structural elements, including slabs, columns, beams, and foundations, are load-bearing and support the weight of the building. Non-structural elements, such as ceilings, windows, doors, and wall panels, do not bear the dead and live loads but should withstand the impact and environmental loads. This study focuses specifically on non-load-bearing wall panels, which are essential components in high-rise buildings. Wall panels can be categorized as either interior or exterior. Interior wall panels are used to partition the building into rooms and must be able to withstand fire, seismic load, and self-weight. Exterior wall panels, on the other hand, must be able to withstand wind, seismic load, fire, and self-weight. Additionally, they must enhance the building's exterior appearance and protect occupants from external loads such as wind and fire. Fire is considered one of the most devastating hazards that buildings and other structures can face (Kodur, 2014; SFPE series, 2022). Structural fire damage results in numerous fatalities, injuries, and millions in property damage worldwide on an annual basis (Brushlinsky

* Corresponding author (supunj@eng.pdn.ac.lk; https://orcid.org/0000-0003-1054-9358)

et al., 2007; Kodur *et al*., 2020). According to data from the Centre of Fire Statistics (CTIF, 2018), approximately 510,000 structural fire incidents are reported each year, indicating that a structural fire occurs somewhere in the world every 62 seconds.

Wall panels can be manufactured in various shapes and sizes to meet different design requirements.

In modern construction, the most popular types of exterior wall panels include lightweight concrete precast sandwich panels, lightweight steel gauge framed panels, and curtain wall panels. According to Moutassem & Alamara (2021), lightweight concrete precast sandwich panels are typically composed of facing, core, and connector materials. The facing materials provide structural integrity and durability, while the core material provides fire resistance. Connectors are used to join the materials together (O'Hegarty & Kinnane, 2020). The advantages of these wall panels are that they are environmentally friendly, durable, fire and impact-resistant, economical, lightweight, and can be rapidly installed. However, the disadvantages include a lack of strength and more segregation (Fayez & Kadhim, 2021). Lightweight steel gauge framed (LSF) wall panels are made up of a steel frame, sheathing panel, cavity insulation, and an external thermal insulation composite (ETIC) system (Kesawan & Mahendran, 2017; Santos *et al*., 2019). Steel studs have higher thermal conductivity, which increases the heat transfer speed even in a normal fire. Due to the increased heat transfer of steel studs, there is a thermal bridge effect. This effect caused a decrease in the thermal resistance of the wall panel. Thermal break strips can be used to mitigate this effect (Santos & Mateus, 2020). The advantages of these wall panels are that they are economical, lightweight, require less maintenance, and can be rapidly installed. However, the main disadvantage is that they have high thermal conductivity. Vacuum insulation panel (VIP) is good as an insulation material for both LSF and concrete precast sandwich panels (Rajanaygam *et al*., 2021). Curtain walls typically consist of metal frames and infill materials (No *et al*., 2008; Lu *et al*., 2016; Oh *et al*., 2016). Metals such as aluminium and steel can be used as frame materials. The infill materials play a crucial role in providing a modern and aesthetically pleasing appearance while protecting the occupants and reducing environmental impacts.

The mechanical performance of wall panels is typically considered during the design, but thermal performance is often overlooked. This has led to major fire incidents in buildings in the past, with wall panel types being the primary factor for fire spread (Guillaume *et al*., 2018). In recent times, curtain wall panels have become more popular due to their numerous advantages over other wall panel types. These panels can be categorized based on their infill material as either combustible or non-combustible. Non-combustible materials are preferable due to their lower fire-spreading risk in large panel areas (Bonner & Rein, 2018; Yuen *et al*., 2021). Glass is frequently utilized as a non-combustible material in curtain walls because of its lightweight, transparent, and eco-friendly characteristics, along with its positive aspects in terms of daylighting and views. Nevertheless, glass is susceptible to sudden failure under thermal and mechanical stresses due to its high brittleness and weakness in tension. The non-flammable glass material is identified as weak under heat loadings (Shields *et al*., 2001, 2002; Wang *et al*., 2016; Wang *et al*., 2018). Therefore, critical consideration of the breaking temperature of a glass facade and the impact parameters is essential, as beyond this point, the glass is incapable of bearing any load and necessitates replacement.

Glass can be classified based on the manufacturing process, including float annealed glass (AN), heat-strengthened glass (HS), and fully tempered glass (FT). AN glass is produced using the float manufacturing process (Nodehi, 2016), which offers the advantages of low cost, wide availability, good quality, and the ability to produce large panes of glass. It is the most economical but has lower strength compared to the other two types (Bedon *et al*., 2018). HS glass is produced by heating the float glass and cooling it at a lower rate. This glass is about two times stronger than AN glass because of residual surface compression resulting from thermal strain compatibility through the glass thickness during the heating and cooling processes (Bedon *et al*., 2018). FT glass is made by heating AN glass to above 700°C and then force-cooling it, providing substantially higher surface compression compared to HS glass. This makes FT glass four to five times stronger than AN glass, with very high tensile strength (Bedon *et al*., 2018).

Single, laminated, and insulated glass panels are popular choices for curtain wall panels at present. A single glass panel consists of a single glass plate. Glass plates are commonly fused together to create laminated glass components using interlayer polymers such as polyvinyl butyral (PVB) and Ethyl vinyl acetate (EVA) that generate adhesion forces during lamination (Santarsiero *et al*., 2018). The inter-layer moderates the impact energy and modifies the brittle fracture (Vedrtnam & Pawar, 2017). The designed fracture of laminated glass is contingent on the type of glass as well as the

type and thickness of interlayer used. Generally, the PVB interlayer is not fully bonded to the glass, and the impact resistance of the laminated glass plate is higher than that of a glass plate of the same thickness. However, the impact fracture behaviour of laminated glass is complicated due to the combined influence of large deformation and delamination strength. The brittle nature of glass, the nonlinear characteristics of PVB, and the adhesive bonding make the impact damage behaviours of laminated glass much more complicated (Keller *et al.*, 1999). Insulating glass is a building material that is used to reduce heat loss within a building. It consists of two or more glass panes and a gas-filled gap (Cuce, 2018). The gas within the gap acts as a barrier against heat and sound, with gases such as argon and krypton that are commonly used. However, according to Wang *et al.* (2017), this is better for insulation, but it is easily subjected to fire. The thermal performance of insulated glass panels mainly depends on the cavity thickness and cavity gas type (Erdem, 2018). This type of glass panel can significantly reduce air conditioning costs, noise penetration, and UV transmission.

Most researchers were concerned about the thermal performance of float glass with rectangular and square shapes. Wang analyzed the thermal performance of laminated and insulated glass with variations in cavity thickness and insulation material (Wang *et al.*, 2017, 2017a). As experimental tests are expensive, consume more time, and negatively affect the environment, numerical analysis is preferred for a large amount of analysis. Also, numerical modelling offers a cost-effective, flexible, and efficient approach to studying complex systems. Especially for parametric studies with a large number of parameters and repeated processes, developed numerical technology gives great support. In recent years, modelling heat transfer effects has become increasingly critical in product design, including fields such as electronics, automotive, and medical industries. By utilizing computer simulations, engineers and researchers can optimize process efficiency and explore new designs while also reducing the need for costly experimental trials.

The aim of this study is to evaluate the thermal performance of glass facades under fire loadings using numerical analysis. The thermal performances of single, laminated, and insulated glass panels are investigated numerically using *ABAQUS* finite element software. First, numerical models of these panels are validated based on past experimental results. Then parametric study is conducted on the thermal effects by varying the shape, thickness, and type of glass panels. This analysis

was done using float glass with thicknesses of 6 mm, 8 mm, and 10 mm and square, rectangular, and triangular shapes. The effect of heating on single glass panels is evaluated by measuring the temperature variation and breaking temperature when changing thickness and shape. After that, the thermal behaviour of laminated and insulated glass panels is obtained by measuring only the temperature variation when changing interlayer thickness and cavity thickness, respectively. Finally, the improvement in the thermal response of insulated glass panels is observed with different insulation materials such as air, argon, and krypton. These analyses give a clear overview of the usage of different types of glass panels in different geometric configurations under various conditions.

MATERIALS AND METHODS

Modelling methodology

The thermal analysis of the glass wall panel is numerically carried out in *ABAQUS* software using a past study (Wang *et al.*, 2017). *ABAQUS* is a commercially available finite element software capable of performing simple linear analysis of the most complex non-linear simulations, as described by the SIMULIA User Assistance (2021).

To model the behaviour of a single glass panel, a laminated glass panel, and an insulated glass panel, 3D deformable solid parts were created and partitioned into exposed and covered regions for heat analysis. Material data from Table 1 was assigned to the glass section, and a heat transfer step in the transient state was used to obtain temperature variation results from the non-heated side to the heat, as described by Wang *et al.* (2017). The modelling utilized initial and heat transfer boundary conditions. As shown in Figure 1, the ENCASTRE (U1 = U2 = U3 = UR1 = UR2 = UR3 = 0) initial boundary condition was applied to the four partitioning edges of both the exposed and non-exposed surfaces as a fixed boundary condition. The heat transfer boundary condition was applied to the average temperature in the exposed and covered areas at each time obtained from experimental results. Heat can be transferred via conduction, convection, and radiation, all of which require a temperature difference and occur from high-temperature to low-temperature mediums. Conduction, convection, and radiation occurred through the glass, cavity gas, and exposed area, respectively, to the environment. The heat transfer step used an initial temperature of 280 K as a predefined field and the Stefan Boltzmann constant of 5.67×10^{-8} W/m^{2}K^4. Figure 2(a) illustrates the geometry of a 6 mm thick, single-coated float glass panel.

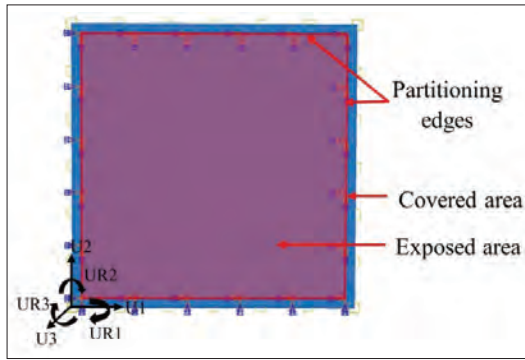**Figure 1:** Assigned boundary conditions of the wall for numerical analysis

Table 1: Material properties (Wang *et al.*, 2017)

Properties	Symbol	Value
Glass		
Density (kg/m³)	ρ	2,500
Modulus of elasticity (Pa)	E	7.3×10^{10}
Poisson ratio	v	0.17
Thermal expansion coefficient (1/K)	β	8.46×10^{-6}
Reference temperature (K)	T_R	280
Specific heat capacity (J/(kg.K))	C	820
Thermal conductivity (W/(m.K))	K	0.94
Emissivity	ε	0.85
PVB		
Density (kg/m³)	ρ_{PVB}	1,070
Specific heat capacity (J/(kg.K))	c_{PVB}	1,100
Thermal conductivity (W/(m.K))	k_{PVB}	0.221
Air		
Density (kg/m³)	ρ_{air}	1.16
Specific heat capacity (J/(kg.K))	c_{air}	1,007
Thermal conductivity (W/(m.K))	k_{air}	0.0263

In addition, as glass is a brittle material, the brittle crack model in *ABAQUS* software was used to investigate the breaking behaviour of the single glass panel. The material properties of the brittle cracking model can be found in Table 2 (Khan *et al.*, 2016). The dynamic analysis was used to obtain the breaking behaviour of the single glass panel in a temperature-displacement explicit step.

Table 2: Brittle material properties (Khan *et al.*, 2016)

	Direct stress after cracking (MPa)	Direct cracking strain
Brittle cracking	36.8	0
	34.1	0.000333
	21.1	0.000667
Direct cracking failure strain	1×10^{-6}	
Brittle shear	Shear retention factor	Crack opening strain
	1	0
	0.5	0.001
	0.25	0.002
	0.125	0.003

Next to the single glass panel, the model for the laminated glass panel, consisting of two 6 mm single-coated float glass panels with a 0.38 mm interlayer of polyvinyl butyral (PVB) film, is depicted in Figure 2(b). The model for the insulated glass panel, as shown in Figure 2(c), was created using two 6 mm single-coated float glass panels and a 6 mm thick air cavity. In the numerical model, the air gap was assumed to be stagnant, and heat was transferred through the air via conduction. Despite the dominance of convection in facilitating higher heat transfer rates, the effective thermal conductivity for air was specifically used to analyze heat transfer through conduction. The effective thermal conductivity (K_{eff}) of the air is calculated using equations from Cengel *et al.* (2012).

RESULTS AND DISCUSSION

Validation

Numerical models for single-coated float glass panels, laminated glass panels, and insulated glass panels were developed using past data from Wang *et al.* (2017), and the variation of temperature was validated with experimental results. Initially, the temperature variation model for the single glass panel was validated by obtaining temperature outputs on the exposed surface of the non-heated side, using a finite element analysis with a $4 \times 4 \times 3$ mesh (size). Figure 3 illustrates a comparison between the numerical and experimental results of the single glass panel.
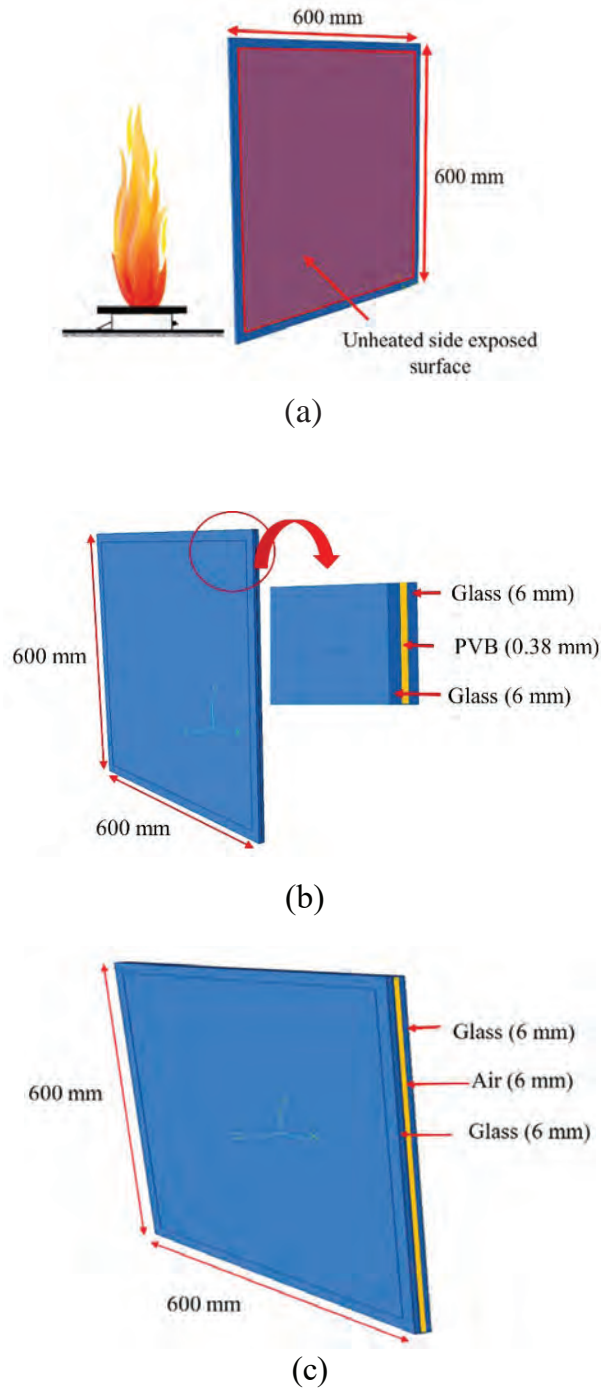
(a)

(b)

(c)

Figure 2: Geometric configuration of models: (a) Single; (b) Laminated, and (c) Insulated glass panel
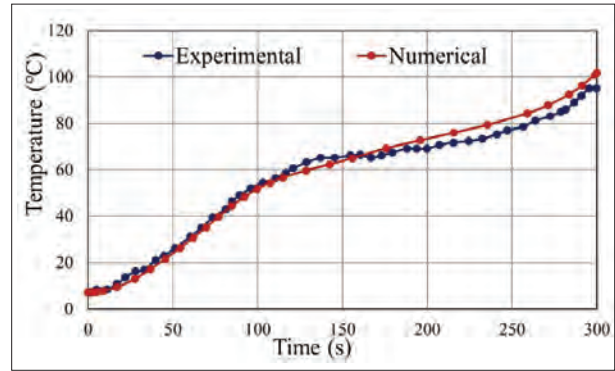

Figure 3: Comparison of experimental and numerical temperature variation results of single glass panel

The error between numerical and experimental results can be calculated by mean absolute deviation (MAD) as mentioned in equation 1. The MAD value for the single glass panel was calculated as 3.55, indicating a strong agreement between the experimental and numerical results. This suggests that the numerical model is reliable and can be used for further analysis and to investigate results.

$$MAD = \frac{\sum_{t=1}^{n}|y_t - \hat{y}|}{n} \quad ...(01)$$

where y_t is the experimental temperature, $\hat{y}$ is the numerical temperature, and *n* is the number of results.

The breaking temperature of the single glass panel was then analyzed. According to the experimental results of Wang *et al.,* (2017), numerical results of heat exposed side are investigated as the crack firstly occurs on the side of the glass panel to which heat is applied. As shown in Figure 4, cracks are initiated at the four corners of the heated side exposed area. When comparing the experimental and numerical results using absolute percentage error, the value was found to be 4.53%, indicating good agreement between both results. However, predicting the time of glass breakage remains a challenging task, as it is highly unpredictable. Experimental research is a useful approach to examining this issue, as suggested by Wang *et al*. (2014). Figure 5 shows the variation of maximum principal stress at the node where the crack was initiated (one corner).
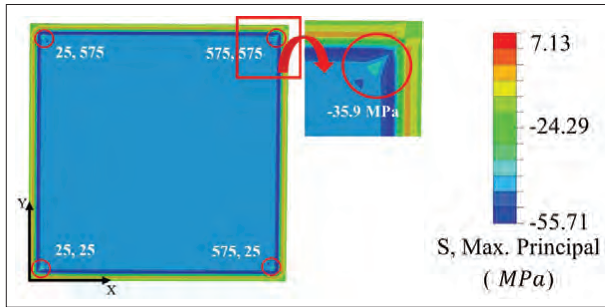
Figure 4:   Variation of maximum principal stress and crack initiation points
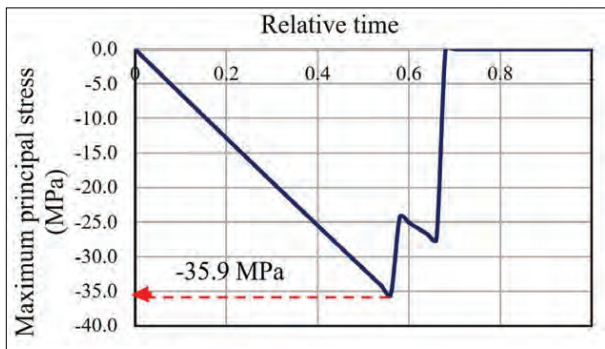
Figure 5:   Variation of maximum principal stress at crack initiation node (at one corner)
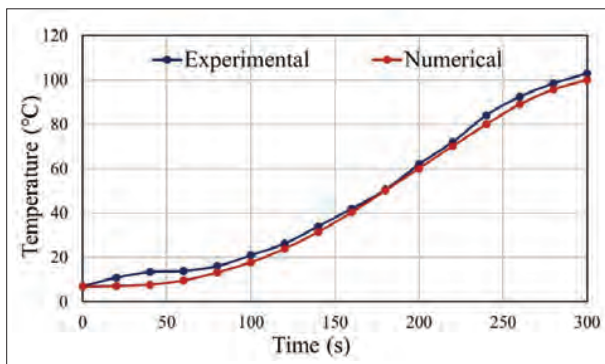
Figure 6:   Comparison of experimental and numerical temperature variation results of laminated glass panel
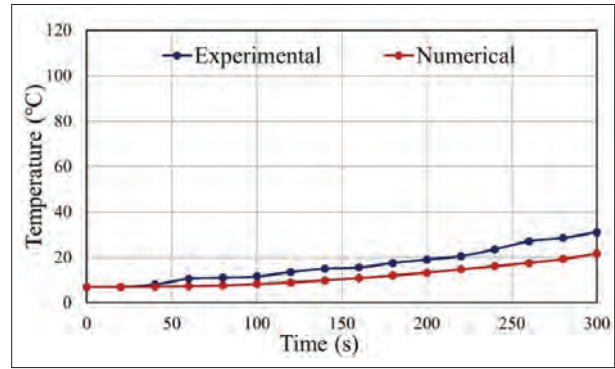

Figure 7:   Comparison of experimental and numerical temperature variation results of insulated glass panel

After analyzing the thermal performance of a single panel, the temperature variations of the laminated glass panel and insulated glass panel were evaluated, and the results are shown in Figure 6 and Figure 7, respectively. The deviation between the experimental and numerical temperature values on the non-heated side of the exposed surface of the laminated glass is less than 3%, indicating good agreement between the two sets of data. The insulated glass model was created using air as cavity gas, assuming stagnancy. Based on Cengel *et al*. (2012), the effective thermal conductivity of air was calculated to reduce the effect of the stagnancy assumption. The MAD value for the insulated glass panel is 4.11, which can be expected due to the assumption of stagnant air.

Parametric study of the glass panel

The effect of different parameters, namely shape, thickness, and type, on the thermal performance of glass facades is analyzed while heating. The temperature variation of a single glass panel was investigated by changing the thickness with the same shape, and the breaking temperature was evaluated by changing the shape with the same cross-sectional area and the same thickness of glass panels. The thermal performance of square, rectangular, and triangular glass shapes with 6 mm, 8 mm, and 10 mm thicknesses were analyzed under fixed boundary conditions, as shown in Table 3. The effect on temperature variation was also studied for laminated glass panels with varying polyvinyl butyral

(PVB) film thicknesses of 0.38 mm, 0.76 mm, 1.14 mm, and 1.52 mm (Wang & Hu, 2019), as well as for insulated glass panels with varying cavity gas thicknesses of 8 mm, 16 mm, 24 mm, and 32 mm. Table 4 presents all the parametric study models of laminated and insulated glass panels. Finally, the variation of temperature for different glass panels, such as single, laminated, and insulated glass panels, was performed while considering the same volume of glass material.

Table 3:   Models of a single glass panel

Shape	Thickness (mm)	Investigation factor
Square	6	
Square	8	Temperature variation
Square	10	
Square	8	
Rectangular	8	Crack behaviour
Triangular	8	

Table 4:   Models of laminated and insulated glass panels

Glass type	PVB film / cavity thickness (mm)
	0.38
Laminated	0.76
	1.14
	1.52
	8
Insulated	16
	24
	32

Effects of thickness of glass

The temperature variation of a square-shaped single glass panel was investigated with varying thickness, as shown in Figure 8. Figure 9 presents the non-heated side exposed area temperature values for different thicknesses at 300 seconds. It is noticeable that increasing the thickness of the single glass panel by 2 mm results in a temperature drop of approximately 13.5%, indicating a linear variation.
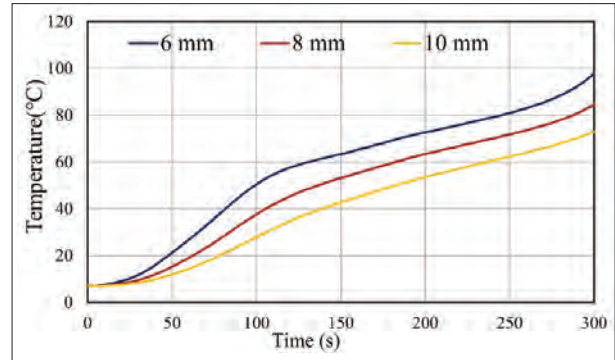
Figure 8:   Comparison of temperature variation with glass thickness

Increasing the thickness of a glass panel makes it better at controlling temperature, as thicker glass provides improved insulation by resisting heat transfer more effectively. However, this comes with the major drawback of increasing the weight of the wall panel. To address this issue, an effective glass thickness of 8 mm was selected for further studies. Additionally, an increase in thickness leads to higher breaking stress and breaking time (Xie *et al*., 2011). To investigate the breaking temperature, the
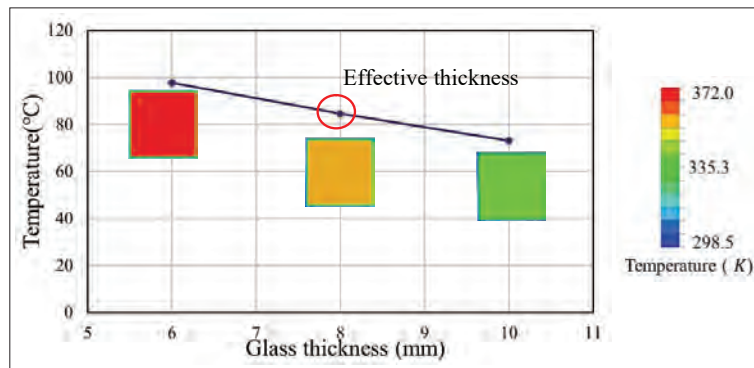

Figure 9:   Comparison of the exposed surface of the non-heated side temperature values with glass thickness at 300 s

thickness was kept constant at 8 mm, and the thermal performance was analyzed by varying only the shape.

Effects of the shape of the glass

In Table 5, the breaking temperature and time of a single glass panel with an 8 mm thickness were analyzed under fixed boundary conditions while varying the shape. The volume of the glass panel was kept constant to maintain the constant weight of the glass panel. Aspect ratios

for rectangular and triangular shapes are 1 and 2.25, respectively. As observed in the experimental results, fracture is firstly observed at the corners of each shape due to the constraint stresses. The breaking behaviour results indicate that the rectangular shape is the worst shape for thermal performance. Due to the impact of the symmetric restraint condition on stress distribution, the square-shaped panel demonstrates enhanced performance in comparison to both rectangular and triangular panels.

Table 5:   Maximum principal stress variation at crack initiate time

Shape of the glass panel (mm)	Breaking temperature (K)	Breaking time (s)
Rectangular	375.00	212.5
Triangular	378.66	228.1
Square	392.25	265.6

Effects of type of glass

The thickness of the glass greatly affects the thermal performance of a single glass panel. While increasing the thickness can enhance the performance significantly, it is not necessarily the optimum solution for the construction industry. Therefore, alternative methods must be explored to enhance the thermal performance of single-glass facades. In this regard, the temperature variation of the non-heated side exposed area of a square-shaped fixed-supported laminated glass panel was investigated by varying the PVB thickness, as shown in Figure 10. The laminated glass panel comprised two 8mm thickness single glass panels and a PVB layer. Figure 11 shows that the temperature drop between 0.38 mm and 0.76 mm

PVB thickness is 8.83%, while between 0.76 mm and 1.14 mm PVB thickness, it is 13.74%, and between 1.14 mm and 1.52 mm PVB thickness, it is 2.74%. While a greater thickness in the insulation material enhances heat resistance, improvements become less significant beyond a certain point. Therefore, the suggested optimal solution, considering both cost and total weight, is the laminated glass panel with a 1.14 mm PVB thickness.

Figure 12 shows the temperature variation at the exposed surface of the non-heated side of the insulated glass panel with an 8 mm thickness of each single glass panel by creating cavity thicknesses of 8 mm, 16 mm, 24 mm, and 32 mm. Here, krypton is used as the cavity gas in the insulated glass panel. As depicted in Figure 13, the temperature drop between an 8 mm and 16 mm cavity thickness is 14.67%, between a 16 mm and 24 mm cavity thickness is 5.62%, and between a 24 mm and 32 mm cavity thickness is 3.20%. It is evident that as the cavity thickness increases, the transferring rate of temperature decreases, but the volume of gas increases, leading to an increase in the total weight (weight increase is negligible if it is only glass) and the cost of the glass panel. As per the technical code for glass curtain wall engineering, 2003, the cavity thickness is typically between 12 mm to 20 mm. Within this range, the thickness does substantially impact the insulating properties, with smaller cavity thickness having greater heat conduction through the cavity gas, and larger gaps allowing more convection within the space, leading to higher convective heat loss. As such, a 16 mm cavity thickness is often selected as the optimum thickness for insulated glass panels.
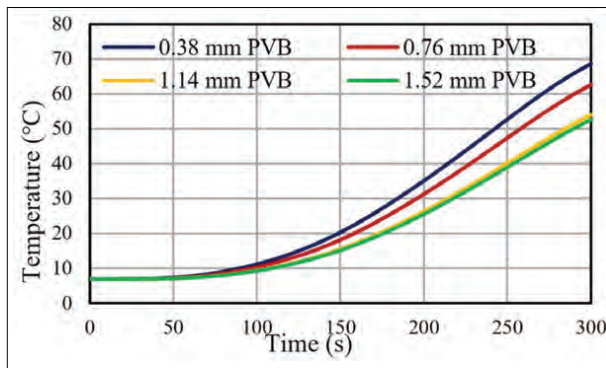

Figure 10: The variation of temperature with time for different PVB thicknesses of laminated glass panels
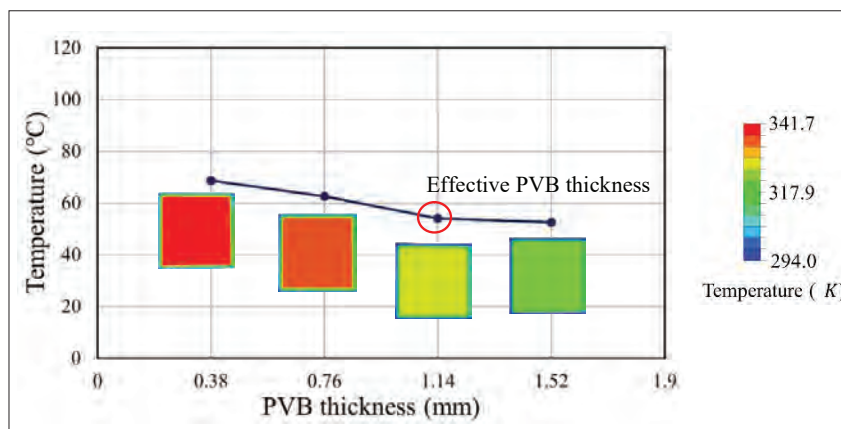

Figure 11: Comparison of the exposed surface of the non-heated side temperature values with different PVB thicknesses of laminated glass panels at 300 s
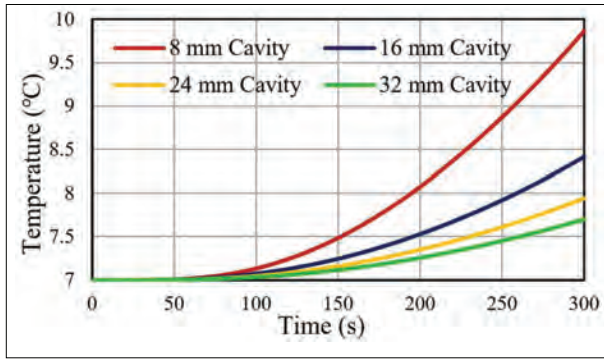
Figure 12: The variation of temperature with time for different cavity thicknesses of insulated glass panels (the cavity is filled with krypton)

To compare the effect of different types of glass panels, single, laminated and insulated glass panels were selected with the same weight of glass material. A 16 mm single glass panel, a laminated glass panel with two 8 mm glass panels and 1.14 mm PVB thickness, and an insulated glass panel with two 8 mm glass panels and 16 mm cavity thickness were modelled and analyzed under the same thermal loading, as shown in Figure 14. The variation of exposed surface temperature at the non-heated side with time for different glass panels is shown in Figure 15. At 300 seconds, the temperature drops between the single glass panel and the laminated glass panel (1.14 mm PVB thickness) is 28.13%, and between the single glass panel and the insulated glass panel (16 mm cavity thickness) is 81.51%. Hence, the order of the temperature increase rate on the non-heated
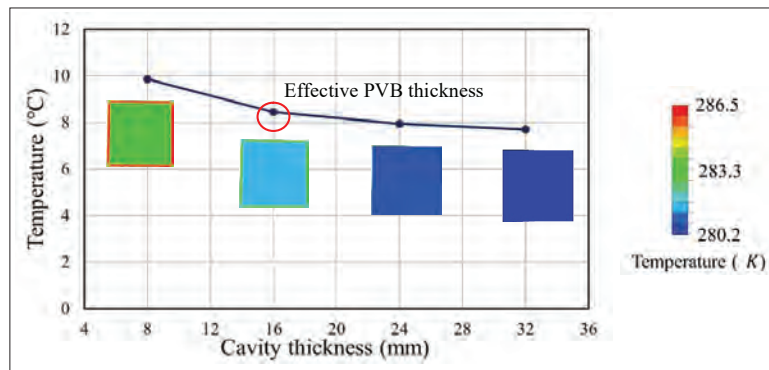
Figure 13: Comparison temperature with cavity thickness of insulated glass panel at 300 s (krypton)
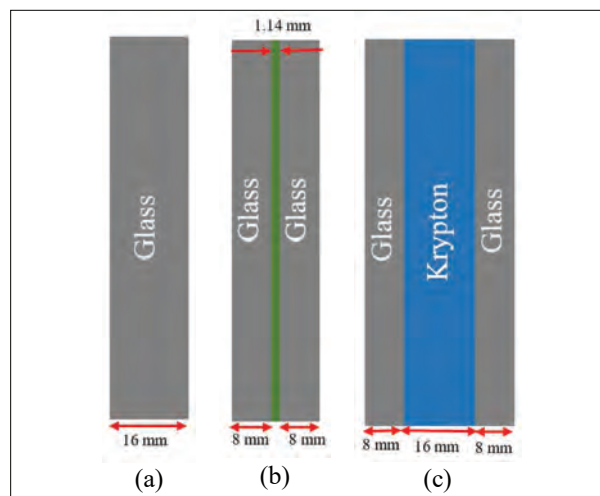
Figure 14: Geometric arrangement: (a) single; (b) laminated, and (c) insulated glass panels

side exposed surface is as follows: single > laminated > insulated. Among them, as the conductivity of gas is less than the solid material, the heat transfer in the insulated panel is less than the laminated panel. Figure 16 displays the temperature variation along the thickness of the glass panels at 300 seconds. Owing to the symmetry of temperature variation, Figure 16 depicts the top half of the wall panel.
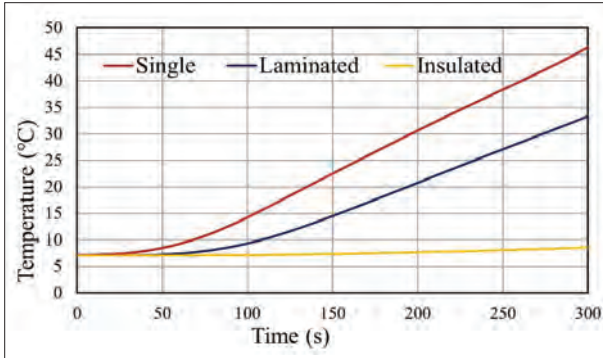

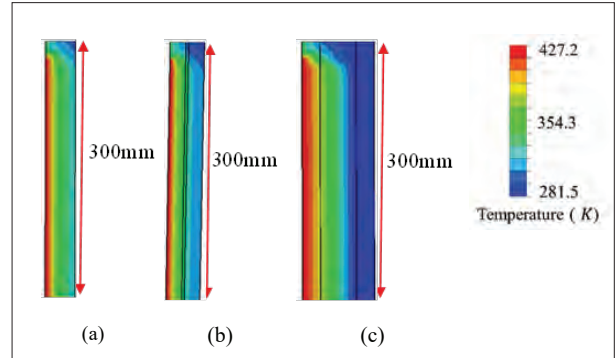**Figure 15:** Comparison of temperature variation with different glass panels

Figure 16: Comparison of temperature variation with different glass panels along thickness at 300 s: (a) Single; (b) Laminated, and (c) Insulated glass panels
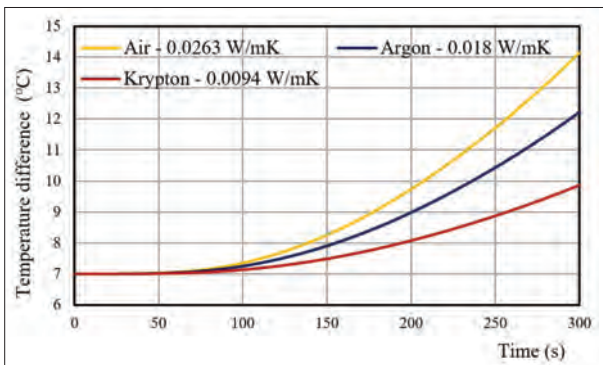
Figure 17: Comparison of temperature variation with different insulation materials of insulated glass panel

Insulated glass panel with different insulation materials

The thermal performance of these insulated glass panels mainly depends on the cavity thickness and the cavity gas type (Cuce, 2018). In this study, three different cavity gases, namely air, argon, and krypton, were investigated to determine their impact on the thermal performance of square-shaped insulated glass panels with fixed support. The glass panels consisted of two 8 mm single glass panels with an 8 mm cavity. The thermal conductivity of the glass panel plays a critical role in determining its thermal performance. Materials with lower thermal conductivity tend to have better thermal performance since they conduct less heat energy (Buck & Rudtsch, 2006). Krypton, with a thermal conductivity of 0.0094 W/m.K (Kralj *et al.*, 2011), has a lower thermal conductivity than both air and argon, resulting in better thermal performance than the other two gases. Figure 17 shows a comparison of temperature variation results on the non-heated side exposed area with varying insulation materials.

CONCLUSION

In this study, numerical analysis was carried out to evaluate the thermal performance of float glass facades of different types and different geometric configurations under fire loadings using *ABAQUS* software. The study investigated the temperature variation on the non-heated side of single, laminated, and insulated glass panels. Furthermore, the study examined the temperature and time at which cracks were initiated in single glass panels. Based on the findings, the following conclusions are drawn:

* As experimental tests are not supportive of all the analyses, the thermal performance of glass facades can be investigated by analyzing the heat-transferring process using finite element numerical simulations.
* In single glass panels, surface temperature varies with thickness; it is reduced by around 13.5% when increasing the thickness by 2 mm. The crack-initiating temperature and crack-initiating time depend on the

shape of the glass, and the worst shape for the given fixed boundary condition is a rectangular shape (Aspect ratios for rectangular and triangular shapes were used 1 and 2.25, respectively).

- The laminated glass panel analysis proved that increasing the PVB layer thickness can further reduce temperature. Specifically, at 300 seconds, the temperature drop between PVB thickness of 0.38 mm and 0.76 mm is 8.83%, while the temperature drop between 0.76 mm and 1.14 mm is 13.74%. Additionally, the temperature drop between 1.14 mm and 1.52 mm is 2.74%.

- The non-heated side temperature of the insulated glass panel can be reduced by increasing the cavity thickness. Specifically, at 300 seconds, the temperature drop between 8 mm and 16 mm cavity thickness is 14.67%, while the temperature drop between 16 mm and 24 mm is 5.62%. Furthermore, the temperature drop between 24 mm and 32 mm thickness is 3.20%.

- From the study of different glass panels at 300 seconds, the temperature drop between single and laminated glass panels is 36.15%, and between single and insulated glass panels is 90.04%. As a result, the order of the temperature increase rate on the non-heated side exposed surface is single > laminated > insulated.

- According to the insulated glass model results, it can be concluded that at 300 seconds, the temperature drop between air and krypton is 30.32%, while the temperature drop between air and argon is 13.75%. Therefore, krypton is a more effective insulator than both air and argon.

REFERENCES

Bedon C., Zhang X., Santos F., Honfi D., Kozłowski M., Arrigoni M., Figuli L. & Lange D. (2018). Performance of structural glass facades under extreme loads - Design methods, existing research, current issues and trends. *Construction and Building Materials* **163**: 921–937.
  DOI: https://doi.org/10.1016/j.conbuildmat.2017.12.153

Bonner M. & Rein G. (2018). Flammability and multi-objective performance of building facades: Towards optimum design. *International Journal of High-Rise Buildings* **7**(4): 363–374.
  DOI: https://doi.org/10.21022/IJHRB.2018.7.4.363

Brushlinsky N., Ahrens M., Sokolov S. & Wagner P. (2007). *World Fire Statistics*. International Association of Fire and Rescue Services.

Buck W. & Rudtsch S. (2006). Thermal properties. In: *Springer Handbook of Materials Measurement Methods* (eds H. Czichos, T. Saito & L. Smith). Springer Handbooks. Springer, Berlin, Heidelberg.

Cengel Y.A., Cimbala J.M. & Turner R.H. (2012). Fundamentals of Thermal fluid sciences, chapter 19 & 20. McGraw Hill.

CTIF. (2018). *World Fire Statistics*. Center for Fire Statistics of CTIF.

Cuce E. (2018). Accurate and reliable U-value assessment of argon-filled double-glazed windows: A numerical and experimental investigation. *Energy and Buildings* **171**: 100–106.
  DOI: https://doi.org/10.1016/j.enbuild.2018.04.036

Guillaume E., Fateh T., Schillinger R., Chiva R. & Ukleja S. (2018). Study of fire behaviour of facade mock-ups equipped with aluminium composite material-based claddings, using intermediate-scale test method. *Fire and Materials* **42**(5): 561–577.
  DOI: https://doi.org/10.1002/fam.2635

Keller U. & Mortelmans H. (1999). June. Adhesion in laminated safety glass – what makes it work. *Glass Processing Days* **8**: 353–356.

Keshawan S. & Mahendran M.A. (2017). Review of parameters influencing the fire performance of light gauge steel frame walls. *Fire Technology* **54**: 3–35.
  DOI: https://doi.org/10.1007/s10694-017-0669-8

Khan A.J., Iqbal N., Saeed H.A. & Tarar W.A. (2016). Development of material model for assessment of brittle cracking behavior of plexiglas. *IOP Conference Series: Materials Science and Engineering* **146**(1).
  DOI: https://doi.org/10.1088/1757-899X/146/1/012008

Kodur V. (2014). Properties of concrete at elevated temperatures. *ISRN Civil Engineering* **2**: 1–15.
  DOI: https://doi.org/10.1155/2014/468510

Kodur V., Kumar P. & Rafi M.M. (2020). Fire hazard in buildings: review, assessment and strategies for improving fire safety. *PSU Research Review* **4**(1): 1–23.

Kralj A., Znidarsic M., Fir M.J. & Remec C. (2011). Gas-filled panels as a high insulation alternative for 21st century building envelopes. *World Engineers' Convention:* 9.

Lu W., Huang B., Mosalam K.M. & Chen S. (2016). Experimental evaluation of a glass curtain wall of a tall building. *Earthquake Engineering & Structural Dynamics* **45**: 1185–1205.

Moutassem F. & Alamara K. (2021). Design and production of sustainable lightweight concrete precast sandwich panels for non-load bearing partition walls. *Cogent Engineering* **8**(1): 1–15.
  DOI: https://doi.org/10.1080/23311916.2021.1993565

No S., Kim K. & Jung J. (2008). Simulation and mock-up tests of the thermal performance of curtain walls. *Energy and Buildings* **40**: 1135–1144.
  DOI: http://doi:10.1016/j.enbuild.2007.10.004

Nodehi Z. (2016). Behaviour of structural glass at high temperatures. *Masters thesis*, Delft University of Technology, Netherlands.

Oh J.H., Yoo H.J. & Kim S.S. (2016). Evaluation of strategies to improve the thermal performance of steel frames in curtain wall systems. *Energies* **9**(12): 1055.
  DOI: https://doi.org/10.3390/en9121055

O'Hegarty R. & Kinnane O. (2020). Review of precast concrete sandwich panels and their innovations. *Construction and Building Materials* **233**: 117145.
DOI: https://doi.org/10.1016/j.conbuildmat.2019.117145

Rajanayagam H., Upasiri I., Poologanathan K., Gatheeshgar P., Sherlock P., Konthesingha C., Nagaratnam B. & Perera D. (2021). Thermal performance of LSF wall systems with vacuum insulation panels. *Buildings* **11**(12): 621.
DOI: https://doi.org/10.3390/buildings11120621

Santarsiero M., Bedon C. & Louter C. (2018). Experimental and numerical analysis of thick embedded laminated glass connections. *Composite Structures* **188**: 242–256.
DOI: https://doi.org/10.1016/j.compstruct.2018.01.002

Santos P., Lemes G. & Mateus D. (2019). Thermal transmittance of internal partition and external facade LSF walls: a parametric study. *Energies* **12**(14): 2671.
DOI: https://doi.org/10.3390/en12142671

Santos P. & Mateus D. (2020). Experimental assessment of thermal break strips performance in load-bearing and non-load bearing LSF walls. *Journal of Building Engineering* **32**: 101693.
DOI: https://doi.org/10.1016/j.jobe.2020.101693

Shields T.J., Silcock G.W.H. & Flood M.F. (2001). Performance of a single glazing assembly exposed to enclosure corner fires of increasing severity. *Fire and Materials* **25**: 123–152.
DOI: https://doi.org/10.1002/fam.764

Shields T.J., Silcock G.W.H. & Flood M.F. (2005). Behaviour of double glazing in corner Fires *Fire Technology* **41**: 37–65.

SIMULIA User Assistance (2021).

SFPE series (2022). *Fire Safety for Very Tall Buildings*. Springer.

China Architecture & Building Press (2003). *Technical Code for Glass Curtain Wall Engineering*. Ministry of Construction of the People's Republic of China.

Vedrtnam A. & Pawar S.J. (2017). Laminated plate theories and fracture of laminated glass plate A review. *Engineering Fracture Mechanics* **186**: 316–330.
DOI: https://doi.org/10.1016/j.engfracmech.2017.10.020

Wang Y. & Hu J. (2019). Performance of laminated glazing under fire conditions. *Composite Structures* **223**: 110903.
DOI: https://doi.org/10.1016/j.compstruct.2019.110903

Wang Y., Wang Q., Shao G., Chen H., Su Y., Sun J., He L. & Liew K.M. (2014). Fracture behavior of a four-point fixed glass curtain wall under fire conditions. *Fire Safety Journal* **67**: 24–34.
DOI: https://doi.org/10.1016/j.firesaf.2014.05.002

Wang Y., Wang Q., Sun J., He L. & Liew K.M. (2016). Influence of fire location on the thermal performance of glass façades. *Applied Thermal Engineering* **106**: 438–442.
DOI: http://dx.doi.org/10.1016/j.applthermaleng.2016.06.057

Wang Y., Wang Q., Wen J.X., Sun J. & Liew K.M. (2017). Investigation of thermal breakage and heat transfer in single, insulated and laminated glazing under fire conditions. *Applied Thermal Engineering* **125**: 662–672.
DOI: https://doi.org/10.1016/j.applthermaleng.2017.07.019

Wang Y., Wang Q., Su Y., Sun J., He L., and Liew K.M. (2017a). Experimental study on fire response of double-glazed panels in curtain walls. *Fire Safety Journal* **92**: 53–63.
DOI: https://doi.org/10.1016/j.firesaf.2017.05.016

Wang Y., Zhang Y., Wang Q., Yang Y. & Sun J. (2018). The effect of glass panel dimension on the fire response of glass façades. *Construction and Building Materials* **181**: 588–597.
DOI: https://doi.org/10.1016/j.conbuildmat.2018.06.088

Xie Q., Zhang H. & Si D. (2011). Experimental study on critical breakage stress of float glass with different thicknesses under conditions with temperatures of 25 and 200 C. *Fire and Materials* **35**(5): 275–283.
DOI: https://doi.org/10.1002/fam.1052

Yuen A.C.Y., Chen T.B.Y., Li A., De Cachinho Cordeiro I.M., Liu L., Liu H., Lo A.L.P., Chan Q.N. & Yeoh G.H. (2021). Evaluating the fire risk associated with cladding panels: An overview of fire incidents, policies, and future perspective in fire standards. *Fire and Materials* **45**(5): 663–689.
DOI: https://doi.org/10.1002/fam.2973 s

RESEARCH ARTICLE

Rock Mechanics

Quantifying the relationship between uniaxial compressive strength and slake durability index in gneiss rocks: an experimental approach

G Kanagasundaram[*], ABN Dassanayake, CL Jayawardena and SP Chaminda
Department of Earth Resources Engineering, Faculty of Engineering, University of Moratuwa, Moratuwa 10400, Sri Lanka.

Abstract: This study investigated the relationship between Uniaxial Compressive Strength (UCS) and slake durability index (SDI) in gneiss rocks collected from two aggregate quarry sites. The analysis revealed varying correlations between these two parameters depending on the grouping and categorisation of the data. Initially, a moderate correlation was observed between experimental and estimated UCS values when considering all the data together. However, further examination of the data by dividing it into two categories based on UCS values greater than or equal to 40 MPa and less than 40 MPa yielded insightful results. Within these divided categories, a robust correlation was found between experimental and estimated UCS values for cycles two and four of SDI. Moreover, this study reveals that fresh rock samples from the quarry locations maintained a durability of over 98% through four cycles of the slake durability test. Nonetheless, these same samples exhibited decreased strength, which can be attributed to their mineral composition and internal structural arrangements of the rock samples tested. Therefore, this study incorporated complementary testing methods such as Ultrasonic Pulse Wave Velocity (UPV) and Scanning Electron Microscope/Energy Dispersive X-ray Spectroscopy (SEM/EDX). These tests served as valuable tools for validating the results and enhancing the understanding of micro-scale changes within the gneiss rock samples. The comparison of test values and the exploration of underlying factors confirmed the reliability and usefulness of UPV and SEM/EDX as supporting tools for this study. The study also recommended that the developed equations can be useful for engineers and researchers in estimating rock strength quickly and inexpensively by replacing the laborious tasks involved in traditional laboratory testing.

INTRODUCTION

Engineering practices related to rocks involve studying their properties and behaviour to use them effectively in construction projects. Two critical tasks in this field are the characterisation of the strength of rocks and their appropriate application for various construction activities. The strength of rocks plays a crucial role in the stability and performance of structures built with them, both in the short and long term (Frenelus *et al*., 2021). Short-term stability refers to the ability of a structure to withstand the loads and stresses it is subjected to during construction, while long-term stability refers to its ability to maintain its integrity and performance over time (Frenelus *et al*., 2021). The uniaxial compressive strength (UCS) test is a commonly used method to determine the strength of rocks. This test involves applying a compressive force to a cylindrical rock sample until it fails. The maximum force the rock can withstand before it fails is its uniaxial compressive strength (Arman, 2021). The UCS test is used because it provides a relatively simple and standardised way to measure rock strength, which is important for designing structures that can withstand the expected loads and stresses. The strength of rocks also affects their behaviour under different loading conditions, such

* Corresponding author (gamsavi@gmail.com; https://orcid.org/0009-0002-2266-3908)

as tension, bending, or shear. Therefore, understanding the UCS value of rocks helps select the appropriate type of rock for a specific construction project and design structures that can withstand the expected loads and stresses.

The uniaxial compressive strength (UCS) test is a reasonably straightforward but costly and time-consuming method of assessing rock strength. The test involves preparing cylindrical rock samples of a specific size and shape, which must be carefully cut and prepared to ensure their accuracy and consistency (Kahraman *et al*., 2017). To obtain a typical strength value for a rock material, it is necessary to test multiple samples to obtain an average strength value. This is because rock strength can vary due to factors such as the geological composition, mineralogy, and structural features of the rock (Yılmaz & Sendır, 2002; Heidari *et al*., 2012; Kurtulus *et al*., 2018; Arman *et al*., 2019; Arman, 2021). This has led to the development of alternate tests and analytical/empirical correlations for calculating their strength characteristics. These methods are often used as supplements to the UCS test or when it is impossible to conduct the test due to practical or logistical reasons. In such cases, the slake durability index (SDI) test can be used as an alternative. This test is relatively easy and inexpensive to prepare and conduct (Arman, 2021). The Slake Durability Index (SDI) test was first developed by Franklin and Chandra (Franklin & Chandra, 1972) and then standardised by ISRM and ASTM standards. Some researchers have suggested that the index values at the end of the fourth cycle of the SDI test should be taken as a basis for estimating the strength parameters of the rock. This is because the first three cycles are considered primarily related to surface effects and do not necessarily provide an accurate representation of the internal strength of the rock. By the fourth cycle, the effects of weathering and erosion are supposed to have penetrated deeper into the rock, providing a more representative measure of its strength (Ulusay *et al*., 1995; Gökceoglu *et al*., 2000).

However, it is important to note that the use of the fourth-cycle SDI values as a basis for estimating rock strength is not universally accepted or standardised. Researchers have conducted various studies to establish analytical and empirical relationships between the slake durability index (SDI) and other properties of rocks, such as strength, weathering, and mineralogical-petrographical properties. These relationships can provide a means of estimating the strength parameters of rocks based on their SDI values or vice versa (Dhakal *et al*., 2002; Sharma & Singh, 2008; Sharma *et al*., 2011; Yagiz, 2011; Altindag, 2012; Sarkar *et al*., 2012).

In order to develop an estimation equation for UCS based on SDI, several researchers additionally looked into the relationship between the uniaxial compressive strength (UCS) and slake durability index (SDI) values of rocks. The goal of this approach is to provide a means of estimating the strength parameters of rocks based on the more easily measurable SDI values. (Cargill & Shakoor, 1990; Koncagül & Santi, 1999; Gökceoğlu *et al*., 2000; Dinçer *et al*., 2008; Yagiz, 2011; Yagiz *et al*., 2012; Kahraman *et al*., 2017; Arman, 2021). Consequently, it is possible to estimate the uniaxial compressive strength (UCS) values of rocks using a simple, fast, and inexpensive slake durability index (SDI) test. This can be achieved by applying an empirical equation that relates SDI values to UCS values.

In the context of Sri Lanka, there are only a few studies that have examined the relationship between uniaxial compressive strength (UCS) and slake durability index (SDI) for gneiss rocks. To address this gap, the current study aims to investigate the correlation between UCS and SDI for gneiss rocks from two quarry sites located around the Colombo area. The selected sites were identified based on their homogeneous geological traits, located within both the Highland and Wanni complexes, characterized by high-grade metamorphic rock primarily consisting of biotite gneiss or garnet-bearing biotite gneiss. This uniformity in geological composition facilitates a more precise examination of the correlation between Uniaxial Compressive Strength (UCS) and Slake Durability Index (SDI), specifically for gneiss rocks.

Existing correlations of UCS and SDI

Researchers have investigated the relationship between UCS and SDI to develop an estimation equation for UCS based on SDI, which will be described below in periodical order. The idea is to use SDI as a surrogate measure for UCS when direct measurement of UCS is not possible or practical. The exploration of the correlation between Uniaxial Compressive Strength (UCS) and Slake Durability Index (SDI) has been a focal point of research within the geotechnical field, especially concerning the mechanical properties of different rock types.

Cargill & Shakoor (1990) investigated various sedimentary rocks, analyzing the UCS-SDI relationship and contributing to the burgeoning body of empirical knowledge. The late 1990s saw further advancements, with studies specifically targeting the Breathitt shale in 1999 (Koncagül & Santi, 1999), aiming to establish a predictive model for UCS based on SDI measurements.

The turn of the millennium marked a continued exploration into this domain, with a 2000 study delving into the impact of mineralogy and mechanical strength on the durability of an array of weak and clay-bearing rocks in Turkey (Gökceoğlu *et al.*, 2000). Despite challenges in identifying a universal correlation across all examined rock types, a focused analysis on marls yielded a promising equation for UCS prediction from SDI values.

The year 2008 witnessed the development of estimation formulas for UCS and Young's modulus, particularly for Quaternary caliche deposits, utilizing a variety of model types, including linear, logarithmic, power, and exponential correlations (Dinçer *et al.*, 2008). This innovative approach underscored the potential for diverse modelling strategies in understanding UCS-SDI relationships.

Subsequent research in 2011 further reinforced the significance of these relationships within the context of carbonate rocks, uncovering a strong and direct correlation between UCS and SDI (Yagiz, 2011). This period also introduced more sophisticated analytical techniques, with

a 2012 study employing both Artificial Neural Networks (ANN) and nonlinear multiple regression analysis to predict UCS values for different rock materials based on SDI values from both the second and fourth cycles of testing (Yagiz *et al.*, 2012).

More recent investigations have continued to build on this foundation, with a 2017 study focusing on the UCS determination of pyroclastic rocks from fourth-cycle SDI values. This research underscored the nature of UCS-SDI relationships, generating separate predictive equations for data points below and above 20 MPa (Kahraman *et al.*, 2017). Furthermore, a study conducted in 2021 aimed at empirically estimating UCS values of evaporitic rocks based on second-cycle SDI values (Arman, 2021) highlights the ongoing efforts to refine and expand empirical models for predicting rock strength and durability.

Table 1 presents the empirical equations relating to Uniaxial Compressive Strength (UCS) and Slake Durability Index (SDI) as derived by the aforementioned researchers, showcasing the evolution of predictive modeling across various rock types.

Table 1: Summary of the existing correlations of UCS and SDI

Year	Primary rock type	Types of Rocks	Equations		References
1990	Sedimentary and metamorphic rock	Sandstone Limestone Dolomite Marble Syenitic gneiss	$UCS = 60.34 Id_2 - 5822$	$r = 0.74$	(Cargill & Shakoor, 1990)
1999	Sedimentary rock	Breathitt shale	$UCS = 0.658 Id_2 + 9.081$	$r = 0.63$	(Koncagül & Santi, 1999)
2000	Sedimentary, volcano- sedimentary and metamorphic rock	Clay bearing rocks	$UCS = 2.54 Id_4 - 202$	$r = 0.70$	(Gökceoğlu *et al.*, 2000)
2008	Sedimentary rock	Quaternary caliche deposits	$UCS = 0.211 Id_2 - 13.815$ $UCS = 13.636 ln Id_2 - 69.552$ $UCS = 4.9 \times 10^{-7} Id_2{}^{3.578}$ $UCS = 0.084 e^{0.45 Id2}$	$r = 0.68$ $r = 0.65$ $r = 0.74$ $r = 0.76$	(Dinçer *et al.*, 2008)
2011	Sedimentary rock	Carbonate rocks	$UCS = 29.63 Id_4 - 2858$	$r = 0.94$	(Yagiz, 2011)
2012	Sedimentary rock	Carbonate rocks	$UCS = 0.7183 Id_2 - 0.0886$ $UCS = 0.7233 Id_2 - 0.0889$ $UCS = 0.7856 Id_2 - 0.1171$ $UCS = 0.531 Id_4{}^{1.454}$ $UCS = 0.7454 Id_4 - 0.1122$ $UCS = 0.6341 Id_4 - 0.0753$	$r = 0.63$ $r = 0.66$ $r = 0.71$ $r = 0.66$ $r = 0.67$ $r = 0.60$	(Yagiz *et al.*, 2012)
2017	Volcanic rock	Pyroclastic rocks	$UCS = 0.047 e^{0.065 Id_4}$ $UCS = 0.453 Id_4 - 26.22$ $UCS = 7.75 Id_4 - 711.4$	$r = 0.92$ $r = 0.82$ $r = 0.93$	(Kahraman *et al.*, 2017)
2021	Sedimentary rock	Evaporitic rocks	$UCS = 17.792 e^{0.0083 Id_2}$	$r = 0.62$	(Arman, 2021)

UCS - dry uniaxial compressive strength (MPa); Id_2 - second-cycle SDI (%); r - the correlation coefficient; Id_4 - fourth-cycle SDI (%)

This body of work illustrates a progressive enhancement in the understanding and prediction of UCS from SDI values across a diverse array of rock types, reflecting both the complexity of these properties and the evolving methodologies employed in their study.

While numerous studies have explored the relationship between the Slake Durability Index (SDI) and Uniaxial Compressive Strength (UCS) across a variety of rock types, metamorphic rocks have largely been overlooked in this research domain. Consequently, the primary objective of this study is to fill this gap by investigating the potential of predicting the strength parameter (UCS) of metamorphic rocks using the more accessible SDI test, which benefits from a simplified sample preparation process.

MATERIALS AND METHODS

Samples of gneiss rocks were collected from two different locations, Kaduwela and Kudayala, in the Colombo area, Sri Lanka. Strength and durability values were tested for those collected samples. Moreover, SEM, EDX, and ultrasonic pulse wave velocity were done to analyse the surface texture, elements present, and travel velocity, respectively.

Uniaxial compressive strength (UCS)

The specimens were transported to the laboratory, where they were cored to prepare NX-size samples to measure the UCS following the guidelines outlined by ASTM standards (ASTM D 2938, 2002). To maintain consistency and to reduce the influence of anisotropy, samples were cored in the direction perpendicular to the foliation planes because planes will easily slide over if the load is given parallel to the foliation plane and provides a minimal value of strength. To ensure accurate and reliable results, all core specimens intended for UCS testing underwent a thorough visual inspection and ultrasonic pulse wave velocity (UPV) measurements before testing. The inspection was conducted to detect any surface failures, such as macro cracks, fissures, or veins, that could impact the measurement results. Once the core specimens passed the inspection, nine rock core samples were selected for UCS testing. These samples were prepared by flattening their ends to ensure smooth and parallel surfaces that were normal to the long core axis. While maintaining the 2:1 length-to-diameter ratio of the samples, the end faces of the specimens were ground with a parallelism of 2/100. Subsequently, the UCS tests for the nine samples were performed under a constant loading rate of 40 kN/min, carefully controlled to ensure consistency across all measurements. This loading rate is typically determined based on the expected strength of the rock samples and the capabilities of the testing equipment being used. The results obtained from these tests were then used to determine the UCS of the rock samples being tested.

Slake durability index (SDI)

Following the guidelines outlined in the ASTM standard, slake durability tests were conducted using ten rounded rock lumps that were taken from the same boulder which was used to prepare the core samples, each with a mass ranging between 40 and 60 g (ASTM D 4644, 2004). The slake durability tests were conducted by taking the oven-dried rock lumps and placing them in a standard test drum that was then filled with tap water at a temperature of approximately 20°C. The drum was then rotated 200 times over 10 minutes. Following the test, the rock fragments inside the drum were carefully taken out and dried in an oven for 24 hours at 110°C. Once the rock pieces were completely dried, they were cooled to room temperature and weighed. To obtain a reliable measure of the slake durability of the rock samples, the process was repeated for four cycles, with the samples being subjected to the same conditions in each cycle. The four-cycle (I_{d4}) slake durability index was then calculated by dividing the weight of the rock pieces retained in the drum after the four cycles by the initial dry weight of the rock samples used in the test. The equation for the second cycle (I_{d2}) is given below;

$$Id_2 = [(WF - C)/(B - C)] \times 100 \qquad ...(1)$$

where:

Id_2 = Slake durability index (second cycle)
B   = mass of drum plus oven-dried specimen before the first cycle (g)
WF = mass of drum plus oven-dried specimen retained after the second cycle (g)
C   = mass of drum (g)

Ultrasonic pulse wave velocity

This typical laboratory method for characterising rock materials can be achieved non-destructively. The test involves sending ultrasonic waves through the rock aggregate and measuring the velocity of the waves as they travel through the material. The test measures the UPV value of the rock core, calculated based on the ratio of the distance between the two transducers to the time the ultrasonic waves travel between them (Chawre, 2018).

The results of the UPV test can also be used to detect defects or anomalies within the aggregate, such as cracks, voids, or inclusions, which may affect its elastic properties (Chai *et al.*, 2011). These defects can cause stress concentrations within the aggregate, leading to localised failure and potentially compromising the overall strength and stability of the structure. Experimental readings of sonic velocity are typically lower than theoretical values, but it remains a sensitive parameter that correlates with other characteristics within the same rock type, making it valuable for standalone analysis or obtaining information about more complex parameters (ASTM D 2845, 2000). Since it is a non-destructive test, samples prepared for UCS testing were used for this analysis.

Table 2: Sample Identifier and Laboratory Testing Results

Sample No.	Sample Name	Location	Fresh/ Weathered	Image	Rock Description	Composition (EDX)	UCS (MPa)	Id_2 (%)	Id_4 (%)	UPV (m/s)
1	KW-FBG1	Kaduwela	Fresh		Biotite Gneiss	49.02% O, 32.06% Si, 8.84% Al, 5.00% K, 2.55% Na, 1.59% Ca, 0.48% Mg, 0.46% Fe	36.32	99.38	99.06	5925.72
2	KW-FBG2	Kaduwela	Fresh		Biotite Gneiss	45.85% O, 31.32% Si, 8.94% Al, 4.34% Fe, 2.84% K, 2.82% Na 2.11% Ca, 1.76% Mg, 0.02% C	31.45	99.78	99.58	5812.06
3	KW-FBG3	Kaduwela	Fresh		Biotite Gneiss	45.04% O, 28.40% Si, 9.45% Al, 6.01% Fe, 4.06% K, 2.81% Na, 2.47% Mg, 1.77% Ca	69.19	99.30	98.96	5114.24
4	KW-WBG1	Kaduwela	Weathered		Biotite Gneiss	47.70% O, 30.95% Si, 11.16% Al, 3.94% K, 2.97% Na, 1.71% Ca, 1.58% Fe	31.47	97.77	95.26	3398.75

Continued -

Sample No.	Sample Name	Location	Fresh/ Weathered	Image	Rock Description	Composition (EDX)	UCS (MPa)	Id_2 (%)	Id_4 (%)	UPV (m/s)
5	KY-FGBG1	Kudayala	Fresh		Garnet-bearing biotite gneiss	46.10% O, 29.33% Si, 8.62% Al, 5.43% Fe 4.12% K, , 2.02% Na, 1.89% Mg, 1.68% Ca, 0.80% Ti	90.50	99.66	99.08	5067.90
6	KY-FGBG2	Kudayala	Fresh		Garnet-bearing biotite gneiss	44.28% O, 31.07% Si, 10.50% Al, 7.50% K, 2.26% Na, 2.02% Fe, 1.75% Ca, 0.62% Mg	30.41	99.66	99.04	5075.62
7	KY-FGBG3	Kudayala	Fresh		Garnet-bearing biotite gneiss	51.62% O, 40.43% Si, 3.77% Al, 1.61% K, 0.90% Ca, 0.83% Na, 0.46% Fe, 0.38% Mg	52.99	99.40	98.76	4013.38
8	KY-WGBG1	Kudayala	Weathered		Garnet-bearing biotite gneiss	48.15% O, 23.69% Si, 10.94% C, 8.87% Al, 3.00% K, 2.58% Fe, 1.45% Na, 0.69% Ca, 0.63% Mg	16.54	94.39	85.02	1836.14
9	KY-WGBG2	Kudayala	Weathered		Garnet-bearing biotite gneiss	47.90% O, 27.38% Si, 12.89% Al, 6.39% K, 1.79% Na, 1.67% Fe, 0.77% Mg, 0.37% Ca, 0.29% Ti	18.51	91.73	82.71	3369.34

SEM and EDX

Scanning electron microscopy (SEM) is an imaging technique that employs an electron beam to scan the surface of a sample and generate high-quality images with exceptional resolution. SEM can be utilised to investigate various physical attributes, such as the surface morphology of a sample, and can be combined with elemental analysis using energy-dispersive X-ray spectroscopy (EDX) (Senarathna *et al.*, 2021). This technology was instrumental in observing the micro crack system's evolution during scanning cycles. EDX, by identifying the components present in a sample and determining their relative concentrations, is an indispensable tool for material characterisation and analysis (Abd El Aal & Kahraman, 2017). The process involves first preparing the rock sample by hammering and removing dust on the surface. The sample is then loaded into the SEM chamber, where it is bombarded with a beam of electrons, generating high-resolution images of the sample's surface. During this process, the EDX detector collects and analyses X-rays emitted by the sample, providing information about its elemental composition.

Correlation analysis

Finally, the study analysed the correlation between SDI values obtained at the end of the second and fourth cycles and the measured UCS values. This also compared the experimental UCS values with the UCS values estimated from the developed empirical models. The results were further validated by SEM/EDX and Ultrasonic pulse wave velocity test results.

RESULTS AND DISCUSSION

UCS-SDI Regression Analysis

Table 2 represents the range of UCS and SDI values obtained from the tested rock samples. UCS values ranged from 16.54 to 90.50 MPa, indicating a wide range of rock strengths. The UCS value increased tremendously, especially with a high presence of quartz and feldspar, since their hardness is high, with 69.19 MPa in Kaduwela and 90.10 in Kudayala. SDI values ranged from 91.73% to 99.78% for the second cycle and from 82.71% to 99.58% for the fourth cycle. These values indicate the percentage of rock material broken down during the slake durability test. The higher the SDI value, the more durable the rock is. The range of SDI values suggests that the tested rocks have varying degrees of durability under slaking conditions.

The least squares regression method is used to fit a line or curve through a set of data points. This study employs a linear curve due to the limited number of data points. This study used the method to analyse the relationship between the second cycle SDI values and UCS values (Figure 1). The moderate level of correlation indicates a relationship between the two variables, but the strength of the relationship is not very strong. The linear function that was found shows that as the SDI values increase, the UCS values also tend to increase, but the relationship is not perfect. In other words, the UCS values are influenced by factors other than the SDI values, but there is a measurable correlation between the two. The equation of the curve is as follows;

$$UCS = 4.92\ Id_2 - 439.36 \qquad r = 0.58 \qquad ...(2)$$
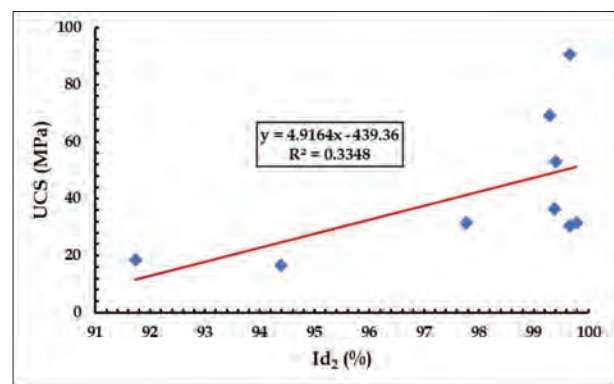

Figure 1: Correlation between UCS and Id_2

Figure 1 illustrates a common pattern of UCS values rising as SDI values increase. However, the data has some scatter, and the correlation coefficient is only moderate. This means that while there is a relationship between SDI and UCS, it is not a very strong one.

To assess the precision of the UCS prediction method using SDI values, Figure 2 displays a graph comparing the projected UCS with the actual UCS. The data points appear to be evenly spread around the diagonal line positioned below the UCS values of 40 MPa. This indicates that the estimated values for UCS are quite precise for rocks with lower strength. Nonetheless, when the UCS values exceed 40 MPa, the data points move away from the diagonal line and exhibit a different pattern. This indicates that the UCS-SDI correlation may not be as accurate for higher-strength gneiss rocks, and further testing may be needed to understand this relationship better.
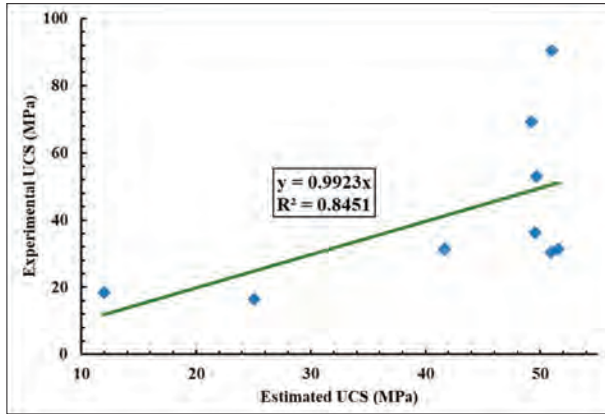
Figure 2:   Correlation between experimental and estimated UCS for
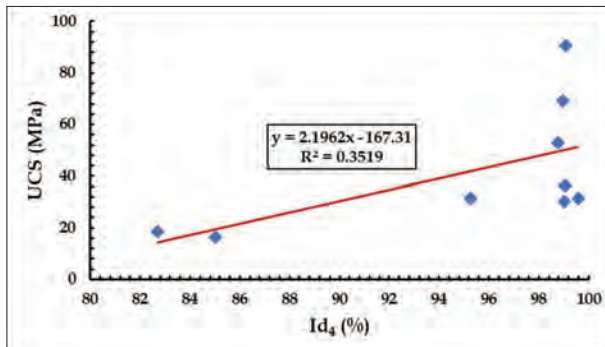the Second cycle

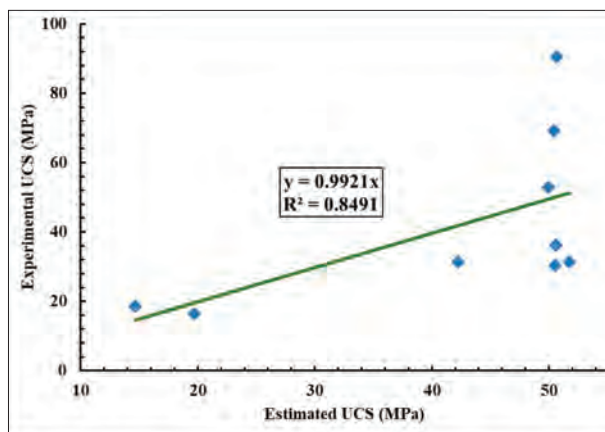**Figure 3:**   Correlation between UCS and Id_4

Figure 4:   Correlation between experimental and estimated UCS for
the Fourth Cycle

Moreover, the analysis was also conducted on the fourth cycle of SDI and UCS values, exhibiting a similar pattern to the second cycle (Figure 3 and Figure 4).

As a result of the different trends observed in the UCS-SDI correlation for gneiss rocks below and above the UCS values of 40 MPa, separate correlation plots were created for cycles two (Figure 5) and four (Figure 6). This 40 MPa was selected as the threshold for segmenting the data into two subsets based on its role as a statistically significant breakpoint. These plots were then used to derive equations for the two observed trends. The resulting equations are presented below;

For the second cycle of SDI and UCS,

$$UCS = 75.41Id_2 - 7428.80 \qquad r = 0.75 \qquad \ldots(3)$$
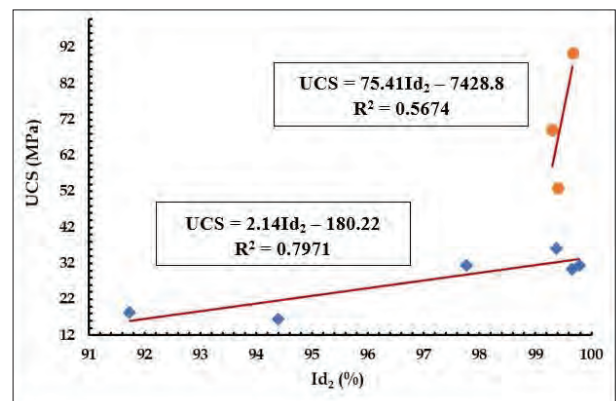
$$UCS = 2.14Id_2 - 180.22 \qquad r = 0.89 \qquad \ldots(4)$$

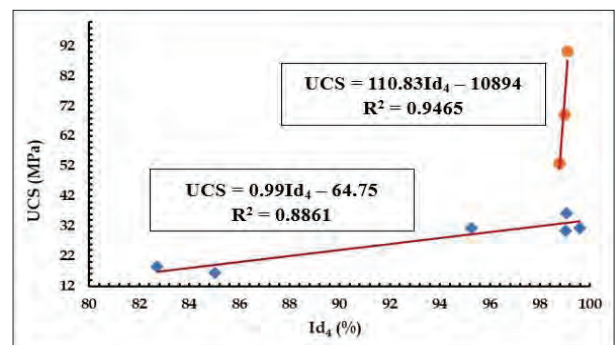**Figure 5:**   Correlation between UCS and Id_2

Figure 6:   Correlation between UCS and Id_4

For the fourth cycle of SDI and UCS,

$$UCS = 110.83Id_4 - 10894 \qquad r = 0.97 \qquad ...(5)$$

$$UCS = 0.99Id_4 - 64.75 \qquad r = 0.94 \qquad ...(6)$$

This analysis showed different trends in the relationship between SDI and UCS depending on the UCS values. Therefore, the authors derived separate regression equations for UCS values above and below 40 MPa for cycles two and four. The strength of the correlation coefficients for the equations was significant, ranging from strong to very strong. This suggests that there is a positive relationship between SDI and UCS values. Kahraman *et al*. (2017) also found that by dividing the dataset into groups with UCS values above and below 20 MPa, the data points showed less scatter and exhibited a strong correlation as well.

It was observed that the inclinations of the regression lines were significantly dissimilar. When UCS values were analysed separately above and below 40 MPa, a robust connection between the experimental and estimated values was evident in cycle two (as illustrated in Figure 7) and cycle four (as shown in Figure 8). This indicates a high correlation between the predicted and estimated UCS values. This approach proved more effective than considering all the data points at once for this specific data points. This will improve the predictive accuracy and will help to understand the material behaviour under different threshold values.
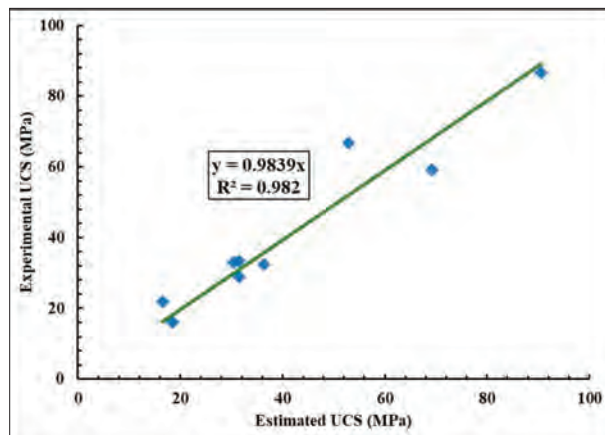

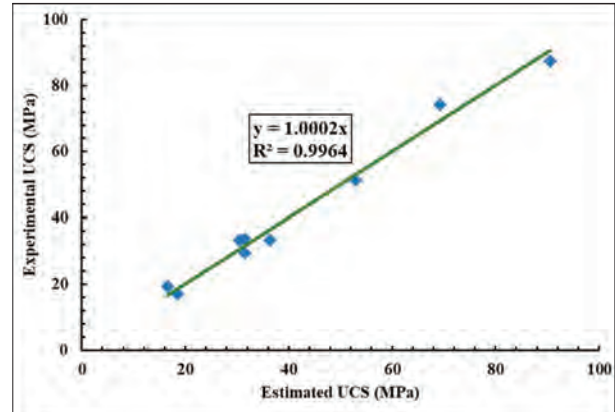**Figure 7:** Correlation between Experimental and Estimated UCS for the Second cycle

Figure 8: Correlation between Experimental and Estimated UCS for the Fourth cycle

Analysis of ultrasonic pulse wave velocity (UPV) results

The Ultrasonic pulse wave velocity results validated the estimated UCS results. For each lower value of UCS, especially below 30 MPa, the velocity was reduced except for sample Number KY-FGBG2 since it is a fresh rock sample and should contain fewer cracks and less porosity than weathered samples. Therefore, UPV is inversely proportional to the rock's strength. As the rock strength decreases, it becomes less resistant to deformation, leading to a slower propagation of ultrasonic waves. This decrease in strength can be caused by factors such as increased porosity, the presence of fractures or cracks, weathering, or alteration of mineral composition. With these factors, the estimated UCS values are in an acceptable condition.

Analysis of SEM / EDX results

The SEM/EDX analysis was conducted on the specimens listed in Table 2, with one sample, KY-WGBG1, being chosen for an in-depth explanation. The analysis was done by visual interpretation and based on the given information in Table 2 under the subheading "compositions (EDX)". The weight percentage of elements in the considered gneissic rock sample follows the order: Silicon (Si) > Aluminum (Al) > Potassium (K) > Iron (Fe) > Sodium (Na) > Calcium (Ca) > Magnesium (Mg). The focus is on assessing the effect of different elements on the rock's weathering behaviour (degradation of strength). Carbon (C) and oxygen (O) are present in the environment,

and gold (Au) coating is done before conducting SEM/ EDX analysis. Therefore, the weight percentages of C, O, and Au can be assumed to have minimal impact on assessing the effect of elements in weathering. Silicon (Si) is the most abundant element in the sample. It is a major component of many minerals in the gneissic rock, such as quartz, feldspar, and mica (Glover *et al*., 2012). Silicon-rich minerals are generally weather-resistant and can withstand environmental conditions, making them relatively stable (Velbel, 1999). However, with the presence of other elements such as Aluminium (Al), Iron (Fe), Calcium (Ca), Sodium (Na) and Magnesium (Mg), the rock sample is prone to weathering because Al compounds are susceptible to weathering, particularly through processes like hydrolysis (Coleman, 1962), which can result in the formation of secondary minerals like clays, while Fe (II) can undergo oxidation reactions when exposed to oxygen and water, leading to the formation of iron oxides or hydroxides (Bernal *et al*., 1959), which are commonly known as rust. This process can contribute to the weathering of the rock. Calcium-rich minerals can be susceptible to chemical weathering, particularly through processes like dissolution (Prestrud Anderson *et al*., 1997), and Na can be susceptible to weathering through processes like ion exchange and leaching (Guicharnaud & Paton, 2006). However, the overall impact of sodium on the weathering behaviour of the rock may be relatively lower than other elements. Mg in primary minerals is released during chemical weathering. This breaks the Mg-O bond in rock to form soluble Mg (Zhao *et al*., 2022).
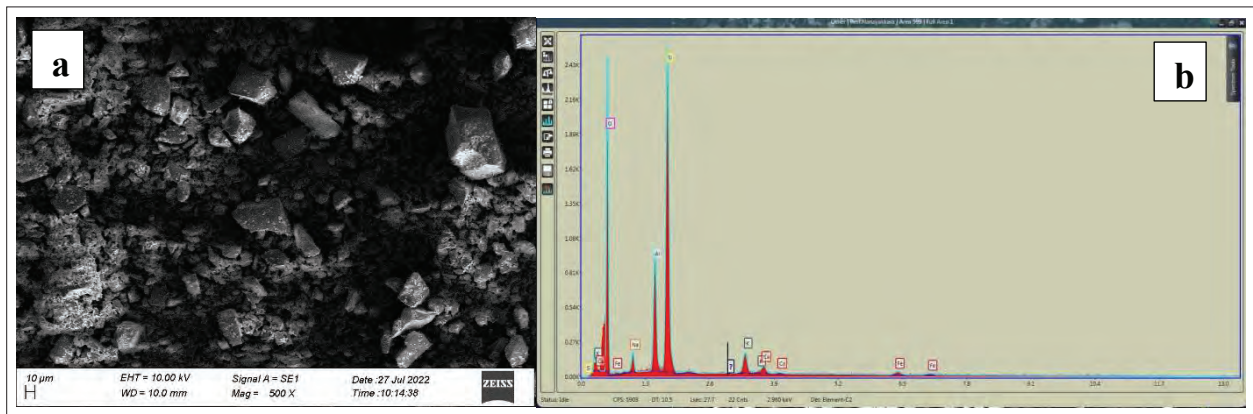

Figure 8: (a) SEM image (b) EDX elemental graph for the sample KY-WGBG1

The data highlighted in Table 2 distinctly show a variation in the weight percentages of elements like iron (Fe) and magnesium (Mg) between fresh and weathered rock samples. In this EDX experiment, chip samples from the UCS-tested specimens were analyzed to investigate the cause of strength parameter variations, which appeared to be linked to internal microstructures. This was pursued particularly because, despite satisfactory Slake Durability Index results, UCS values were not aligning. The findings revealed that the oxidation of Fe (II) to Fe (III) and Mg to Mg (II), indicative of weathering, significantly affects the rock's strength properties. This is evident as the weight percentages of Fe and Mg in weathered rocks are consistently lower due to the onset of weathering processes especially when they exposed to oxygen. Intriguingly, some fresh rock samples also exhibited lower values of Fe and Mg, signalling internal weathering, which consequently leads to a decrease in rock strength.

Even though it is a small-scale interpretation, it can be used as a secondary tool to further understand the changes in rock strength properties due to internal weathering and the validity of the results derived from the proposed equation. Furthermore, using the elemental distribution map, which can be derived during this analysis, and was utilised to examine element partitioning, the results can be further validated by assessing the elemental removal from the eroded areas. Since Sri Lanka is a tropical country with two monsoonal periods, the influence of especially chemical weathering will always be there in every field due to such elemental presence in the rock samples,

which will induce weathering. So, EDX analysis is an important tool for assessing such elemental presence and distribution. Since this analysis was done by taking the sample from UCS-tested samples, these results helped to further confirm the variations of the derived UCS results due to different elemental variations. The information described above, which was based on Table 2, was further validated by overlaying the elemental distribution map onto the SEM image. This approach was used to gain a deeper understanding of the underlying mechanisms.

CONCLUSION

The proposed empirical equation to estimate UCS values from Id_2 and Id_4 values is more accurate for gneiss rocks with UCS values less than or greater than 40 MPa, as opposed to all UCS values combined. This approach will increase the prediction accuracy of UCS values. Therefore, it is concluded that the use of empirical equations (23), (24), (25) and (26) to estimate the uniaxial compressive strength (UCS) of gneiss rocks based on Id_2 and Id_4 is both affordable and straightforward. These equations will predict the maximum strength value a core specimen can provide since the equation was tested for the samples cored perpendicular to the foliation plane. However, it is recommended to use these equations with caution and only within the accuracy level limited to similar rocks at the preliminary analysis stage. The UPV and SEM/EDX tests provided valuable insights into micro-scale changes, thus enhancing the understanding of the sample characteristics and reinforcing the validity of the derived results. To ensure the generalizability and applicability of the findings, extending the investigation to encompass a broader range of rock types is recommended.

Conflict of interest statement

All authors disclose that they have no competing interests.

Acknowledgements

REFERENCES

Abd El Aal A. & Kahraman S. (2017). Indirect methods to predict the abrasion resistance and slake durability of marbles. *Journal of Molecular and Engineering Materials* **5**(02): 1750007.
DOI: https://doi.org/10.1142/S2251237317500071

Altindag R. (2012). Correlation between P-wave velocity and some mechanical properties for sedimentary rocks. *Journal of the Southern African Institute of Mining and Metallurgy* **112**(3): 229–237.

Arman H. (2021). Correlation of uniaxial compressive strength with indirect tensile strength (Brazilian) and 2nd cycle of slake durability index for evaporitic rocks. *Geotechnical and Geological Engineering* **39**(2): 1583–1590.
DOI: https://doi.org/10.1007/s10706-020-01578-x

Arman H., Abdelghany O., Saima M.A., Aldahan A., Mahmoud B., Hussein S., Fowler A.-R. & AlRashdi S. (2019). Strength estimation of evaporitic rocks using different testing methods. *Arabian Journal of Geosciences* **12**: 1–9.
DOI: https://doi.org/10.1007/s12517-019-4916-9

ASTM (2000). *Standard Test Method for Laboratory Determination of Pulse Velocities and Ultrasonic Elastic Constants of Rock- ASTM D 2845 – 00*. ASTM International West Conshohocken, PA, USA.

ASTM (2002). *Standard Test Method for Unconfined Compressive Strength of Intact Rock Core Specimens- ASTM D2938-95*. ASTM International West Conshohocken, PA, USA.

ASTM (2004). *Standard Test Method for Slake Durability of Shales and Similar Weak Rocks- ASTM D 4644-04*. ASTM International West Conshohocken, PA, USA.

Bernal J.D., Dasgupta D.R. & Mackay A.L. (1959). The oxides and hydroxides of iron and their structural inter-relationships. *Clay Minerals Bulletin* **4**(21): 15–30.
DOI: https://doi.org/10.1180/claymin.1959.004.21.02

Cargill J.S. & Shakoor A. (1990). Evaluation of empirical methods for measuring the uniaxial compressive strength of rock. *International Journal of Rock Mechanics and Mining Sciences & Geomechanics Abstracts* **27**(6): 495–503.
DOI:https://doi.org/10.1016/0148-9062(90)91001-N

Chai H.K., Momoki S., Kobayashi Y., Aggelis D.G. & Shiotani T. (2011). Tomographic reconstruction for concrete using attenuation of ultrasound. *Ndt & E International* **44**(2): 206–215.
DOI: https://doi.org/10.1016/j.ndteint.2010.11.003

Chawre B. (2018). Correlations between ultrasonic pulse

wave velocities and rock properties of quartz-mica schist. *Journal of Rock Mechanics and Geotechnical Engineering* **10**(3): 594–602.
DOI: https://doi.org/10.1016/j.jrmge.2018.01.006

Coleman N.T. (1962). Decomposition of clays and the fate of aluminum. *Economic Geology* **57**(8): 1207–1218.
DOI: https://doi.org/10.2113/gsecongeo.57.8.1207

Dhakal G., Yoneda T., Kato M. & Kaneko K. (2002). Slake durability and mineralogical properties of some pyroclastic and sedimentary rocks. *Engineering Geology* **65**(1): 31–45.
DOI: https://doi.org/10.1016/S0013-7952(01)00101-6

Dinçer İ., Acar A. & Ural S. (2008). Estimation of strength and deformation properties of Quaternary caliche deposits. *Bulletin of Engineering Geology and the Environment* **67**: 353–366.
DOI: https://doi.org/10.1007/s10064-008-0146-1

Franklin J.A. & Chandra R. (1972). The slake-durability test. *International Journal of Rock Mechanics and Mining Sciences & Geomechanics Abstracts* **9**(3): 325–328.
DOI: https://doi.org/10.1016/0148-9062(72)90001-0

Frenelus W., Peng H. & Zhang J. (2021). Long-term degradation, damage and fracture in deep rock tunnels: A review on the effect of excavation methods. *Frattura Ed Integrità Strutturale*, **15**(58): 128–150.
DOI: https://doi.org/10.3221/IGF-ESIS.58.10

Glover A.S., Rogers W.Z. & Barton J.E. (2012). Granitic pegmatites: Storehouses of industrial minerals. *Elements* **8**(4): 269–273.
DOI: https://doi.org/10.2113/gselements.8.4.269

Gökceoglu C., Ulusay R. & Sönmez H. (2000). Factors affecting the durability of selected weak and clay-bearing rocks from Turkey, with particular emphasis on the influence of the number of drying and wetting cycles. *Engineering Geology* **57**(3–4): 215–237.
DOI: https://doi.org/10.1016/S0013-7952(00)00031-4

Guicharnaud R. & Paton G.I. (2006). An evaluation of acid deposition on cation leaching and weathering rates of an Andosol and a Cambisol. *Journal of Geochemical Exploration* **88**(1–3): 279–283.
DOI: https://doi.org/10.1016/j.gexplo.2005.08.056

Heidari M., Khanlari G.R., Torabi Kaveh M. & Kargarian S. (2012). Predicting the uniaxial compressive and tensile strengths of gypsum rock by point load testing. *Rock Mechanics and Rock Engineering* **45**: 265–273.
DOI: https://doi.org/10.1007/s00603-011-0196-8

Kahraman S., Fener M. & Gunaydin O. (2017). Estimating the uniaxial compressive strength of pyroclastic rocks from the slake durability index. *Bulletin of Engineering Geology and the Environment* **76**: 1107–1115.
DOI: https://doi.org/10.1007/s10064-016-0893-3

Koncagül E.C. & Santi P.M. (1999). Predicting the unconfined compressive strength of the Breathitt shale using slake durability, Shore hardness and rock structural properties. *International Journal of Rock Mechanics and Mining Sciences* **36**(2): 139–153.
DOI: https://doi.org/10.1016/S0148-9062(98)00174-0

Kurtulus C., Sertcelik F. & Sertcelik I. (2018). Estimation of unconfined uniaxial compressive strength using Schmidt hardness and ultrasonic pulse velocity. *Tehnički Vjesnik* **25**(5): 1569–1574.
DOI: https://doi.org/10.17559/TV-20170217110722

Prestrud Anderson S., Drever J.I. & Humphrey N.F. (1997). Chemical weathering in glacial environments. *Geology* **25**(5): 399–402.
DOI: https://doi.org/10.1130/0091-7613(1997)025< 0399: CWIGE>2.3.CO;2

Sarkar K., Vishal V. & Singh T.N. (2012). An empirical correlation of index geomechanical parameters with the compressional wave velocity. *Geotechnical and Geological Engineering* **30**(2): 469–479.
DOI: https://doi.org/10.1007/s10706-011-9481-2

Senarathna T.M.B., Janith S., Dassanayake A.B.N., Chaminda S.P. & Jayawardena C.L. (2021). Correlations between durability, mineralogy and strength properties of limestone. In: *Proceedings of International Symposium on Earth Resources Management & Environment 2021* (eds. D.M.D.O.K. Dissanayake & C.L. Jayawardena), Department of Earth Resources Engineering, University of Moratuwa, pp. 26–30.

Sharma P.K., Khandelwal M. & Singh T.N. (2011). A correlation between Schmidt hammer rebound numbers with impact strength index, slake durability index and P-wave velocity. *International Journal of Earth Sciences* **100**(1): 189–195.
DOI: https://doi.org/10.1007/s00531-009-0506-5

Sharma P.K. & Singh T.N. (2008). A correlation between P-wave velocity, impact strength index, slake durability index and uniaxial compressive strength. *Bulletin of Engineering Geology and the Environment* **67**(1): 17–22.
DOI: https://doi.org/10.1007/s10064-007-0109-y

Ulusay R., Arikan F., Yoleri M.F. & Çağlan D. (1995). Engineering geological characterisation of coal mine waste material and an evaluation in the context of back-analysis of spoil pile instabilities in a strip mine, SW Turkey. *Engineering Geology* **40**(1–2): 77–101.
DOI: https://doi.org/10.1016/0013-7952(95)00042-9

Velbel M.A. (1999). Bond strength and the relative weathering rates of simple orthosilicates. *American Journal of Science* **299**(7–9): 679–696.
DOI: https://doi.org/10.2475/ajs.299.7-9.679

Yagiz S. (2011). Correlation between slake durability and rock properties for some carbonate rocks. *Bulletin of Engineering Geology and the Environment* **70**(3): 377–383.
DOI: https://doi.org/10.1007/s10064-010-0317-8

Yagiz S., Sezer E.A. & Gokceoglu C. (2012). Artificial neural networks and nonlinear regression techniques to assess the influence of slake durability cycles on the prediction of uniaxial compressive strength and modulus of elasticity for carbonate rocks. *International Journal for Numerical and Analytical Methods in Geomechanic*s **36**(14): 1636–1650.
DOI: https://doi.org/10.1002/nag.1066

Yılmaz I. & Sendır H. (2002). Correlation of Schmidt hardness with unconfined compressive strength and Young's modulus in gypsum from Sivas (Turkey). *Engineering*

Geology **66**(3–4): 211–219.
DOI: https://doi.org/10.1016/S0013-7952(02)00041-8

Zhao T., Liu W. & Xu Z. (2022). Magnesium isotope fractionation during silicate weathering: Constrains from riverine Mg isotopic composition in the southeastern coastal region of China. *Geochemistry, Geophysics, Geosystems* **23**(4): e2021GC010100.
DOI: https://doi.org/10.1029/2021GC010100

RESEARCH ARTICLE

Biomechanics

Ergonomic assessment and gait analysis of a knee joint model with an active spring-reinforced centrally-rollable knee bypass support system

P Ponram[1*], C Mythili[1], NC Selvakumar[2] and A Selwyn J Kumar[3]

[1] *Department of Electrical and Electronics Engineering, University College of Engineering Nagercoil, Konam, Kanyakumari District, Tamil Nadu, India.*

[2] *Government Primary Health Centre, Thadikaara Konam, Kanyakumari District, Tamil Nadu, India.*

[3] *Kanyakumari Government Medical College, Asaripallam, Kanyakumari District, Tamil Nadu, India.*

Abstract: Musculoskeletal issues can lead to severe immobility problems when not identified and addressed early. An ergonomic assessment and gait analysis of a novel knee joint model featuring an innovative active spring-reinforced centrally-rollable knee bypass support system was conducted in this work. The study employed computer simulations using human knee joint models integrated with the proposed knee support system. Gait parameters, joint angles, and muscle activations were assessed to evaluate the system's effects on knee joint stability, impact forces, and gait mechanics during various activities. The knee support system notably improved knee joint alignment, lessened joint forces, and optimized muscle activation patterns. The knee bypass support system facilitated a natural knee roll during walking and running, ultimately enhancing gait efficiency and reducing joint stress. The study's findings showcase improved biomechanics, which hold promising implications for injury prevention, rehabilitation, and overall performance enhancement. With the support system, dynamic changes in tendon forces during activity enhanced the knee joint stability and coordination, which will improve performance and injury prevention. Balance of forces during different activities also encompassed the joint stability. The knee support system demonstrates its potential to address musculoskeletal issues by enhancing knee joint stability and optimizing gait mechanics. This innovation could significantly contribute to minimizing immobility concerns and improving individuals' quality of life.

Keywords: Biomechanics, ergonomic assessment, gait analysis, knee joint model, knee support system.

INTRODUCTION

Musculoskeletal knee issues are a common problem that affects people of all ages, from athletes to the elderly. The knee joint is made up of bones, ligaments, tendons, and cartilage, and is vulnerable to a variety of injuries and conditions. Some of the most common causes of knee pain include overuse injuries, such as tendinitis and bursitis, as well as ligament and cartilage injuries, such as anterior cruciate ligament (ACL) tears and meniscus tears. Osteoarthritis, a degenerative joint disease, is another common cause of knee pain, especially in older adults. Other contributing factors to knee pain include obesity, genetic predisposition, and certain medical conditions, such as rheumatoid arthritis. Proper diagnosis and treatment of knee issues are important in preventing further damage and improving overall quality of life (Barr, 2007).

Musculoskeletal knee issues are often linked to lifestyle factors such as physical activity, diet, and weight management. Individuals who engage in high-impact sports or repetitive motions, such as running or jumping, may be at increased risk for knee injuries such as sprains, strains, or tears (Hunt, 2003). Being overweight or obese can also put added stress on the knee joint, increasing the risk of developing conditions such as osteoarthritis.

* Corresponding author (ponraam@gmail.com; (iD) https://orcid.org/0000-0002-5489-3436)

On the other hand, a healthy diet and regular exercise can help improve joint health and reduce the risk of knee issues (Messier *et al*., 2006). Adopting a healthy lifestyle can play an important role in preventing and managing musculoskeletal knee issues (Bliddal *et al*., 2014).

Musculoskeletal issues can be a significant source of discomfort and can limit one's ability to perform everyday activities. Knee support braces can be a helpful aid in managing knee pain by providing additional support and stability to the knee joint (Valachi & Valachi, 2003). These braces are designed to fit securely around the knee and can help reduce pressure on the joint, providing relief from pain and discomfort. While knee braces are not a cure for musculoskeletal issues, they can be a useful tool in managing symptoms and improving quality of life (Quinlivan *et al*., 2015).

Active knee support braces are currently explored to offer dynamic knee load support and distribution (Alluhydan *et al*., 2023). Spring based braces provide dynamic changes to muscle forces ensuring optimal function and comfort (Dereshgi *et al*., 2023).

Current trends in musculoskeletal knee brace support involve the use of advanced materials and design features to provide maximum comfort and effectiveness. One trend is the use of neoprene and other lightweight materials that offer a snug, yet breathable fit, reducing discomfort and irritation (Zhao *et al*., 2022). Another trend is the use of adjustable straps and hinges that allow for a customized fit and targeted support to specific areas of the knee (Ultich *et al*., 2007*)*. Additionally, many knee braces now incorporate compression technology, which provides targeted compression to reduce swelling and promote healing. In terms of design, some knee braces feature an open patella design, which helps to relieve pressure on the knee cap and reduce pain. Others feature a closed patella design, which provides additional support and stabilization to the knee joint. Finally, many knee braces now incorporate smart technology, such as sensors or tracking software, to monitor the user's activity levels and provide real-time feedback on performance and progress (Kraemer *et al*., 2004). Overall, the latest trends in musculoskeletal knee brace support reflect a focus on comfort, customization, and advanced technology to provide effective support and management of knee issues.

A number of studies were made in the area of prevention of knee injuries. Study of treatment therapies, support systems and life style change to prevent knee musculoskeletal disorders are widely reported.

In recent research, Hunte *et al*. (2020) introduced an assist-as-needed control strategy for a soft knee assistive device, utilizing a custom-built device and a muscle synergy-based walking model. Saccares *et al*. (2017) proposed an innovative method for estimating knee joint torques for assistive devices with reduced sensor requirements, enabling a wearable setup. Zhang *et al*. (2019) discussed advancements in knee assistive devices, covering mechanical design, sensing, control systems, and performance evaluation. Kim *et al*. (2020) developed a joint apparatus with flexures supporting a bar extension, while Osinga *et al*. (2020) designed an apparatus for degenerative joint conditions with elastic buffering mechanisms. Yang *et al*. outlined a challenging treatment concept for knee periprosthetic joint infection and extensor apparatus deficiency. Comer *et al*. devised a joint sensor assembly for screed applications, controlled by a valve signal. Zhao *et al*. described effective management of multiple knee ligament injuries and extensor apparatus rupture. Malone *et al*. patented rehabilitation apparatus for knee flexibility post-surgery, and Wang *et al*. introduced a wearable exoskeleton seat with thigh, knee, and shank mechanisms. Finally, Hsu *et al*. patented a knee massage apparatus with an L-shape structure and integrated massage devices, controlled by a CPU and PCB**.**

Cernohorsky *et al*. (2018) focused on developing a special knee brace for intensive rehabilitation that can also be used daily. They utilized modern drive control systems and status information from drives for sensor-less diagnostics. The brace's design integrated 3D scanning and printing for construction, while the mechatronic system emphasized energy efficiency and lightweight design. Reanaree *et al*. (2018) aimed to assist patients with paralysis through an exoskeleton suit supporting body movement for improved functioning, incorporating a microcontroller-driven system and movement mechanism. Auberger *et al*. (2018) introduced an orthotic system for lower limb paralysis support, featuring a computer-controlled knee joint unit with sensors, hydraulics, and a lever mechanism for controlled motion. Hafizah Amer *et al*. (2020) explored a novel knee support design using a controllable damper unit with magneto-rheological technology to absorb impact, considering its damping characteristics and magnetic damper's behaviour.

Johnson *et al.* (2023) validated the clinical application of a spring loaded knee support system for dynamic unloading during gait. The proof of concept was based on fluidic actuator elements devoid of electronic controls.

Despite advances in musculoskeletal knee brace support technology, there are still some research gaps that need to be addressed. One area that requires further investigation is the long-term effectiveness of knee braces in preventing or managing knee pain and injury. While some studies have shown positive results, more research is needed to determine whether knee braces can provide sustained benefits over time. Additionally, there is a need for further research on the optimal design and fit of knee braces, as not all knee braces may be equally effective for all individuals or types of knee issues. Another area for further investigation is the potential side effects of knee brace use, particularly over extended periods of time. While knee braces are generally considered safe, there is a need for more research on potential risks, such as skin irritation or reduced muscle strength due to prolonged use. Finally, there is a need for more research on the cost-effectiveness of knee braces, as they can be expensive and may not be covered by insurance in all cases. Overall, further research is needed to better understand the effectiveness, safety, and cost-benefit of musculoskeletal knee brace support systems.

MATERIALS AND METHODS

The objective of the project is to design a knee by-passing apparatus used for elderly and obese persons for knee load distribution. The proposed project intended to prevent knee joint disorders such as overlap and joint pains for aged and obese peoples. Knee joint disorders are prevalent in aged persons due to wear of knee joints and overlap due to aging. This will cause mobility disorders and knee joint problems such as severe pain. By reducing the net load over knee joints, by an external load by-passing apparatus across knee joints, the overlap of joints will be reduced. This will ultimately prevent elders from undergoing knee replacement surgeries and getting immobility disorders.

Other than preventive care, this apparatus will also be a supportive mechanism for knees of aged persons who have knee joint issues. The design must be validated for ergonomic compatibility of the design with computer simulations. Validation and analysis of load distribution efficiency through computer simulation needs to be done.

The components of the knee joint apparatus such as the circular roller and side beads are the innovative components of the work. The circular roller part is able to hold the upper and lower load bearing side beads, and simultaneously provides for knee movement. Further it will be able to pass the load from the upper side to the lower side through a bypass arrangement. The entire system in terms of design and way of work is novel and innovative.

Rapid tools like 3D printing enable rapid prototyping and customization of knee support braces, allowing for quick iterations and adjustments based on user feedback. 3D scanning facilitates precise measurement and modelling of individual anatomies, ensuring optimal fit and comfort of the brace. These technologies streamline the design and development process, reducing time-to-market and costs associated with traditional manufacturing methods. Additionally, they offer the flexibility to incorporate complex geometries and materials for enhanced performance and support. Overall, leveraging 3D printing and scanning accelerates innovation and improves the effectiveness of knee support brace solutions.

Knee joints models were created by three dimensional scanning of knees of different age groups with EinScan Pro 2X scanner having scanning accuracy of 0.045 mm and scanning speed 10 fps, 3,000,000 points/s. The models were processed with i7 Intel Processor and NVDIA GTX 1080 Graphic processor with 4GB RAM.

The portable 3D scanning enables creation of models of knee joint anatomy and also provides for universalisation of sizes. This incorporates a number different size and shaped knee joint models to be evaluated in this study.

The models were fitted with a custom designed knee-bypass support system having a spring-reinforced and centrally rollable mechanism. The spring reinforcement enables effective load transfer between upper and lower thighs bypassing the knee joint. The central roll mechanism enables hassle free movement of the knee while fitting the support system. Support frames were drawn from the upper thigh region laterally to accumulate at the centre of the knee joint point, which was further drawn back to the lower thigh laterally from the converging central point.

The central converging points for upper and lower thighs are interconnected by rollable and spring reinforced mechanism, the support system is fitted to the knee joint models also by effecting various upper and mobility load points to stimulate the load analysis over the knee and support system.

Musculoskeletal geometry refers to the study of the structure and arrangement of muscles and bones in the human body. In the current model, the musculoskeletal geometry of knee joint bone and muscles was evaluated for the working of forces of muscle and bone. The movement of knee area is simulated in 400 frames for a body mass index of 86. The normal forces of muscle and joints were pre loaded. The movement of the knee joint for a standard jump is simulated. The muscle and joint forces were calculated. The level of activity of muscle elements is represented in colour, in which red represents more activity.

Forces in hip musculature, knee musculature, ankle musculature, joint contact forces, and peak joint contract forces were simulated in this work.

The activities simulated were bottom of the counter movement, middle of propulsive phase, and take off. The analysis encompasses the physical and mathematical analysis of the geometry of joints, muscles, and bones to better understand their function and movement. This analysis is a crucial one in developing models of human movement, design of knee support braces, and designing prosthetics and orthotics. It is crucial to ensure that these designs are anatomically correct, ergonomically useful and that the materials used mimic the natural musculoskeletal system to ensure maximum functionality. A thorough understanding of knee musculoskeletal geometry is necessary for effective rehabilitation, injury prevention, and overall physical health.

The position of muscle and bone segments, position of patella and patellar tendon, centres of joints, rotation, and tibio-femoral joint contact points were measured during resting and activity.

The knee joint is a complex joint that allows for movement in multiple planes. Kinematics, the study of motion without consideration of forces, is an important aspect of understanding the knee joint's function. The knee joint is composed of two main bones, the femur and the tibia, which articulate with each other. The patella, or kneecap, is also part of the joint and helps to stabilize it.

During flexion and extension of the knee joint, the femur rolls and glides on the tibia. This movement is necessary for the knee joint to bend and straighten. The amount of motion that occurs during flexion and extension depends on the individual and can be influenced by factors such as muscle strength, ligamentous laxity, and previous injuries.

The knee joint also has some degree of rotational motion, which occurs during activities such as pivoting or twisting. This rotation is facilitated by the shape of the femoral condyles, which allow for slight internal and external rotation of the tibia.

In addition to the rolling and gliding motion of the femur on the tibia, there is also some degree of translation that occurs during knee joint motion. This translation refers to the anterior and posterior movement of the tibia relative to the femur. During knee extension, the tibia moves anteriorly, and during knee flexion, the tibia moves posteriorly.

The kinematics of the knee joint are complex and multifaceted. Understanding the various types of motion that occur at the knee joint is essential for diagnosing and treating knee injuries and conditions.

The dynamics of the knee joint refer to the study of the forces that act on the joint during movement. These forces are generated by the muscles, ligaments, and bones that make up the knee joint.

During activities such as walking, running, and jumping, the knee joint is subjected to high forces. These forces are distributed across the joint and are necessary for generating movement. However, if the forces are not distributed evenly or if they exceed the joint's capacity, injuries can occur.

The knee joint is stabilized by a variety of structures, including the ligaments, menisci, and muscles. These structures work together to maintain the joint's stability and prevent excessive motion or displacement.

The quadriceps and hamstrings muscles are particularly important in the dynamics of the knee joint. The quadriceps are responsible for extending the knee, while the hamstrings are responsible for flexing the knee. These muscles work together to control the forces that act on the knee joint and ensure that the joint moves in a controlled and safe manner.

Mathematical model of the knee joint dynamics

The following mathematical models provide a comprehensive framework for designing a knee joint support apparatus. The Knee Joint Stability Model formulates an equation that accounts for various forces acting on the knee joint, including those from muscles, ligaments, gravity, and the support system itself, to

ensure equilibrium. Incorporating equations for specific muscles and ligaments based on their activation levels and mechanical properties enhances the model's accuracy. The Gait Mechanics Model describes the relationship between knee and hip joint angles during walking or running, considering muscle activations and biomechanical principles. The Knee Roll Mechanism Model delineates the dynamics of the knee roll mechanism, crucial for understanding how the support system interacts with knee movement. The Impact Reduction Model quantifies the support system's effectiveness in reducing impact on the knee joint during activities, providing a measurable outcome for performance evaluation. Finally, the Optimal Spring Stiffness Model aims to identify the optimal stiffness for the support system by minimizing an objective function considering factors like joint stability, energy efficiency, and user comfort. By considering both muscle and ligament dynamics, these models provide a holistic approach to designing a knee support apparatus that ensures stability, functionality, and user satisfaction. Additionally, understanding the roles of specific ligaments further informs the design process, emphasizing the importance of comprehensive biomechanical considerations in developing effective knee support solutions.

Knee joint stability model

Let F_muscles represent the forces exerted by muscles around the knee joint, F_ligaments be the forces from the ligaments, F_gravity is the gravitational force, F_support represents the force from the active spring-reinforced knee bypass support system, and F_reaction is the joint reaction force.

The equation for knee joint stability can be formulated as:

$$\text{F\_reaction} = \text{F\_muscles} + \text{F\_ligaments} + \text{F\_gravity} + \text{F\_support}$$

This equation represents the equilibrium of forces acting on the knee joint. The model should also include the equations that describe the forces from specific muscles and ligaments based on their activation levels and mechanical properties.

Gait mechanics model

The gait mechanics model can include the equations for joint angles and muscle activations during walking or running. Let θ_knee represent the knee joint angle, θ_hip be the hip joint angle, and A_muscles denote the activation levels of muscles around the knee and hip.

The equations for gait mechanics can be expressed as:

$$\theta\text{\_knee} = f(\theta\text{\_hip, A\_muscles})$$

$$\theta\text{\_hip} = g(\theta\text{\_knee, A\_muscles})$$

These equations describe the reciprocal relationship between knee and hip joint angles during gait. The model should also include equations for muscle activations based on biomechanical principles and muscle recruitment patterns during different phases of the gait cycle.

Knee roll mechanism model

Let θ_roll represent the knee roll angle, k_spring be the spring stiffness, b_damping denote the damping coefficient, and τ_torque be the torque applied by the spring-reinforced knee bypass support system.

The equations for the knee roll mechanism can be defined as:

$$\tau\text{\_torque} = \text{k\_spring} * \theta\text{\_roll} + \text{b\_damping} * (d\theta\text{\_roll}/dt)$$

These equations describe the dynamics of the knee roll mechanism, where the torque from the support system is a function of the knee roll angle and its angular velocity.

Impact reduction model

To assess the impact reduction capabilities, let F_knee_without_support and F_knee_with_support represent the forces transmitted through the knee joint during activities without and with the knee support system, respectively.

The equation for impact reduction can be given as:

$$\text{Impact\_Reduction} = (\text{F\_knee\_without\_support} - \text{F\_knee\_with\_support}) / \text{F\_knee\_without\_support} * 100$$

This equation calculates the percentage of impact reduction provided by the support system compared to the forces experienced without the support system.

Optimal spring stiffness model

Let k_optimal represent the optimal spring stiffness for the knee support system, and J is an objective function that quantifies the effectiveness of the support system. The objective function J can include factors such as joint stability, energy efficiency, and user comfort.

The equation for the optimal spring stiffness can be defined as:

k_optimal = argmin J(k_spring)

This equation finds the spring stiffness that minimizes the objective function J, indicating the optimal stiffness that achieves the desired level of knee support and overall performance of the support system.

In addition to the muscles, the ligaments of the knee joint also play a crucial role in the joint's dynamics. The medial and lateral collateral ligaments help to prevent excessive side-to-side motion, while the anterior and posterior cruciate ligaments help to control the forward and backward motion of the knee joint.

Overall, the dynamics of the knee joint are complex and involve a variety of structures and forces. Understanding these dynamics is essential for preventing and treating knee injuries and conditions.

RESULTS AND DISCUSSION

The geometry of knee joint muscle forces during active phase is given in the Figures 1, 2, 3, and 4. The figures provide a multilateral point of view in which various muscle forces are simulated against time during the knee joint action (like jumping or walking). The different muscle forces were colour coded with respect to the intensity of force. Dark red representing the most intense force, it can be seen that the patella and meniscus are exerting maximum force reaction during the activity. The simulation was done with and without brace support and the numerical difference in force at these two muscles (patella and meniscus) in focus were recorded.

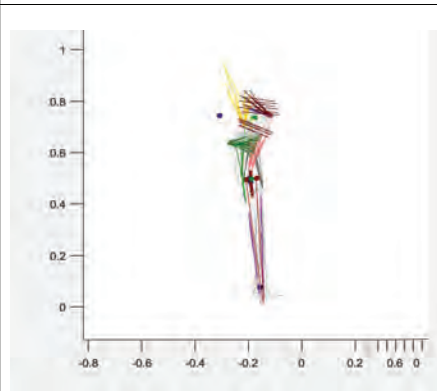Geometry of Knee Joint Muscle Forces during Active Phase

Figure 1:   Front view of knee joint forces
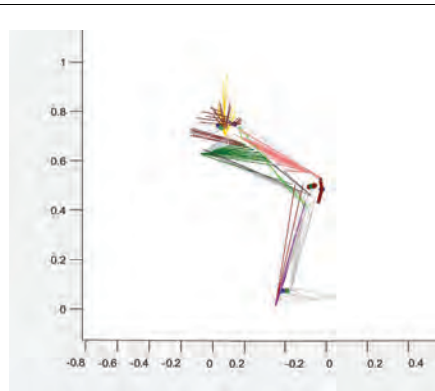
Figure 2:   Lateral (Right) of knee joint forces

Figure 3:   Top view of knee joint forces

Figure 4:   Lateral (Left) of knee joint forces

Load distribution on the knee joint with and without support brace attached at various distance from knee joint

Figure 5: Load distribution on the knee joint with and without braces placed at various distance from knee joint
(a) Brace placed near to Knee (b) Brace placed at a distance of 50 mm (c) Brace placed at 100 mm

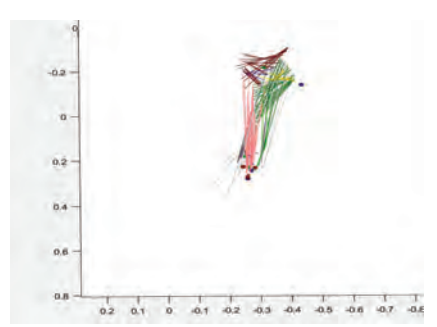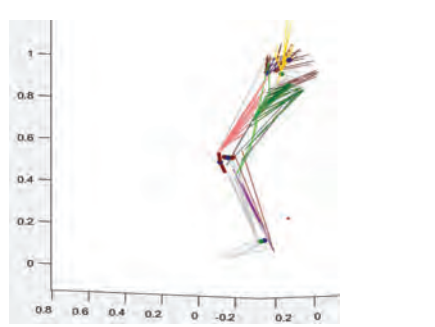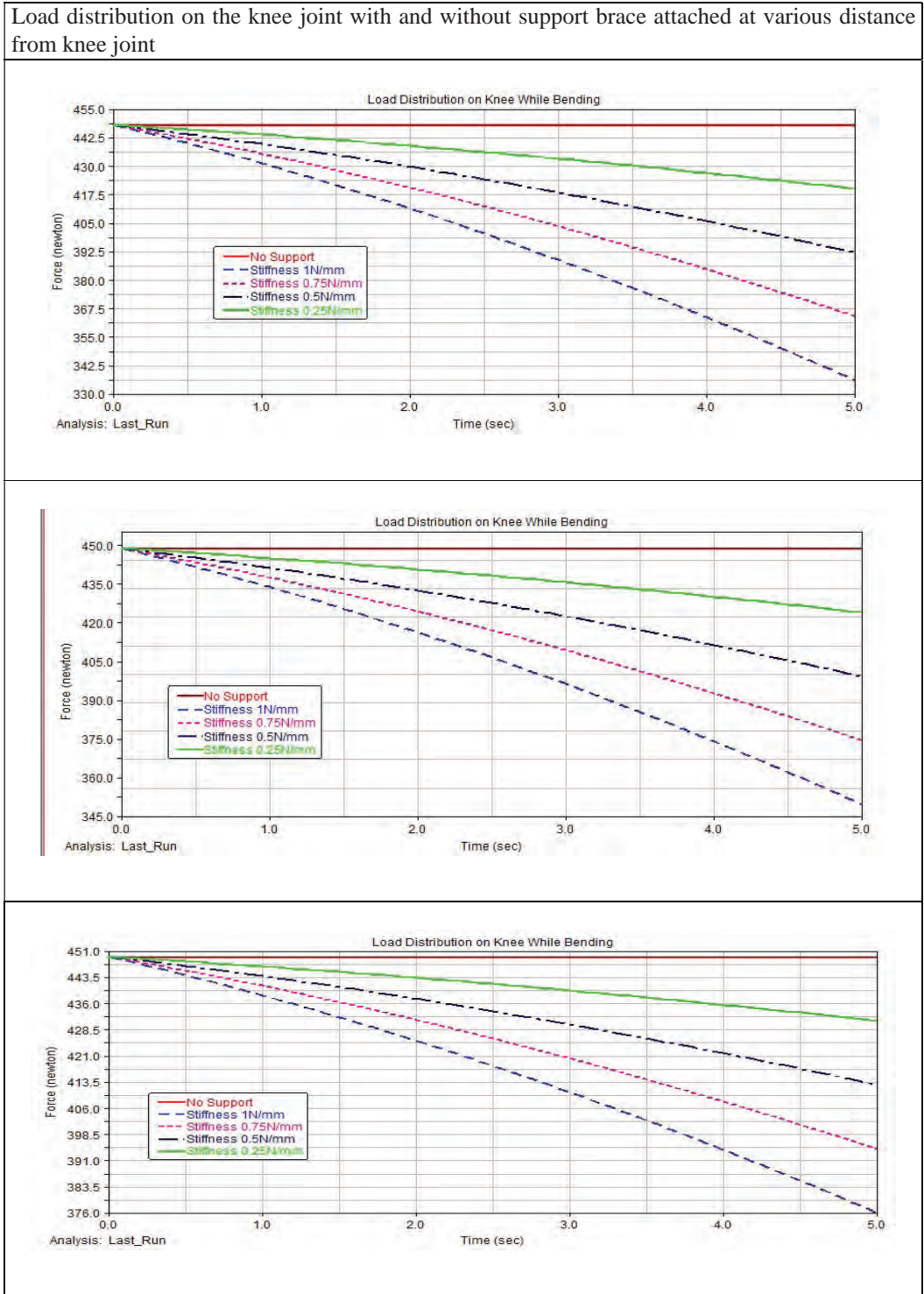A knee joint model with and without brace support was simulated and the results were given in Figure 5. It can be seen that no load distribution occurs when no support brace was placed. The load was applied over the femur and transferred to the tibia through the knee joint. The stiffness of the spring used in the brace was adjusted as 0.25 N/mm, 0.5 N/mm, 0.75 N/mm and 1 N/mm. It can be interpreted from Figure 5 that irrespective of the placement of the support brace over the knee, the spring with maximum stiffness provides effective load distribution. Also, load distribution was more effective when the braces were placed at farther contact points from the knee than closer to the knee joint. However placement of the brace at a farther point beyond the optimum comfort zone of the user may be ineffective when comes to ergonomic usability and knee mobility when the braces were placed.

The knee-joint was modelled in CREO software and the simulation by application of forces were done using the ADAMS.

Knee joint forces in action during movement

In this section the simulated knee joint forces with respect to knee joint movement is discussed. Figure 6 represents the plot of forces in hip musculature against time during a motion, where ADD represents Adductors and GL represents Gluteus Maximus.
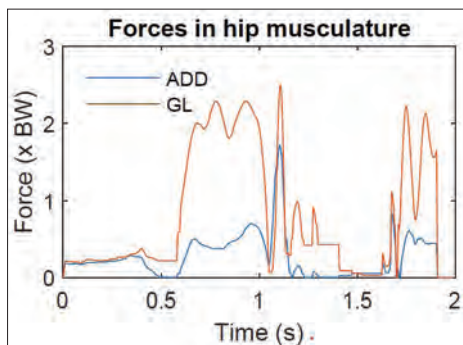

Figure 6: Hip Muscle Forces During

At 0.5 seconds, the Adductors decrease their force to zero, while the Gluteus Maximus maintains its force. This suggests that the Adductors' contribution reduces, possibly as the movement transitions from one phase to another, while the Gluteus Maximus continues to stabilize the hip. At 0.6 seconds, the Adductors start activating again, suggesting their involvement in the movement.

The Gluteus Maximus exhibits a sudden peak in force, indicating a dominant role in generating force during this phase.

The plot describes the forces generated by these muscles relative to time, and different phases and patterns can indicate various muscle actions and contributions. The plot suggests a complex interplay between the Adductors and Gluteus Maximus during the movement. The Adductors seem to play a significant role in generating force at specific moments, while the Gluteus Maximus exhibits both dominant and cyclical force patterns. This pattern of activation and coordination between the muscles is likely tailored to the specific demands of the activity or exercise being performed, such as walking, running, or a specific hip exercise. The plot highlights the dynamic nature of hip muscle function during the movement and showcases their ability to work together to stabilize and produce force throughout different phases

The graph represents the forces exerted by various knee musculature (RF - Rectus Femoris, VAS - Vastus, BIH - Biceps Femoris, and PT - Popliteus) over time during a specific activity or movement.
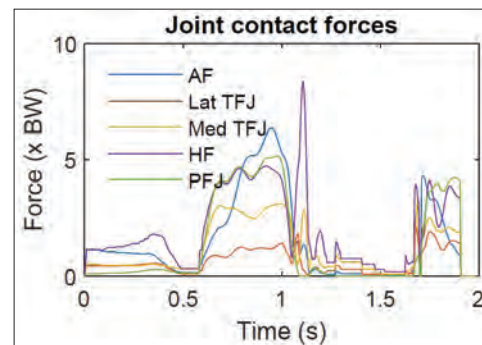
Figure 7: Knee muscle forces during action

The graph illustrates the temporal pattern of muscle activation and relaxation during the specified activity, likely involving knee movements. The initial gradual rise and subsequent sharp increases and decreases in forces suggest specific phases of muscle activation and coordination. Further context and information on the nature of the activity or movement would be required to provide a more detailed and comprehensive interpretation of the results.

The proposed system improves the gait symmetry which implies that the user shall be able to Gair was

appeared to be in symmetry with the knee support brace. The outcome was consistent with similar studies, which validates the gait performance but with different types of knee braces (Li *et al.*, 2023).

The implications of the muscle forces depicted in the graph can provide valuable insights into the functionality and coordination of the knee musculature during the specified activity. Here are some possible implications based on the patterns observed:

1. Gradual Activation and Coordinated Increase: The initial gradual rise in muscle forces (RF, VAS, and BIH) indicates a synchronized activation of these muscles at the beginning of the activity. This coordinated increase suggests that these muscles work together to initiate and support the movement, ensuring stability and control during the early phase.
2. Steady State and Sustained Activation: The period between 0.4 seconds and 0.5 seconds, during which all the forces maintain a constant level of 0.2 force, indicates a steady state of muscle activation. This sustained activation might be related to maintaining a specific posture or holding a position during the activity.
3. Sharp Increase in Forces: The sharp increase in forces at 0.6 seconds, particularly for VAS, BIH, PT, and VAS RESPECTIVELY, suggests a rapid and intense activation of these muscles. This sudden surge in forces could be associated with a more demanding phase of the movement, such as a quick change in direction, jumping, or landing.
4. Differential Muscle Activity: The differences in the timing of force reduction and relaxation among the muscles have implications for their roles during the activity. For instance, the delayed reduction of force in BIH compared to other muscles (at 1.2 seconds) indicates that BIH may be involved in providing ongoing support or stability even after other muscles have ceased their activity.
5. Fluctuating Forces: The fluctuation of forces between 0 force and 0.3 force between 1.2 seconds and 1.7 seconds suggests a transitional or stabilizing phase of the activity. These fluctuations could be related to fine-tuning movements or accommodating changes in the task's demands.
6. Specific Roles of RF and PT: The drop in forces to zero for RF and PT at 2 seconds suggests that these muscles might not be as critical during the later phase of the activity. This could imply that other muscles or mechanisms take over to complete the movement or stabilize the knee joint.

The implications on the muscles suggest a complex and coordinated interplay of different muscle groups during the specified activity. The muscle activation patterns indicate how the knee musculature adapts to varying demands and plays specific roles in supporting movement, stability, and control. Understanding these implications can be crucial in designing targeted rehabilitation programs, optimizing athletic performance, or addressing knee-related issues in elderly and obese populations. However, it is essential to interpret the results in the context of the specific activity and consider other factors that may influence muscle behaviour, such as individual differences and external conditions.
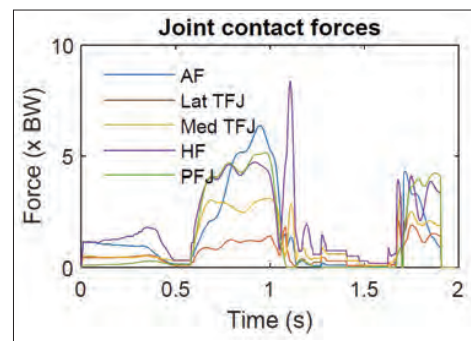

Figure 8: Contact forces at knee joint

The plot demonstrates the dynamic changes in joint contact forces over time during the specific activity or exercise. There are distinct phases of force development and changes in loading patterns across the different joint regions (Medial and Lateral Tibiofemoral Joints, Hip Joint, Patellofemoral Joint, and Ankle Joint). The force values provide valuable insights into the loading and force distribution across the various joints, which can be important for understanding joint mechanics, muscle activation, and potential implications for joint health and performance during the analyzed activity.

The joint contact forces described in the plot provide valuable information about how different joints are loaded and experience forces during a specific activity or exercise. Understanding joint contact forces is essential for assessing the biomechanics of the musculoskeletal system and gaining insights into the stress and load distribution across various joints. Here's what the plot means for joint contacts:

1. Joint loading patterns: The plot shows the time-dependent changes in joint contact forces for several

key joints, including the medial tibiofemoral joint (Med TFJ), lateral tibiofemoral joint (Lat TFJ), hip joint (HF), patellofemoral joint (PFJ), and ankle joint (AF). The pattern of force changes over time indicates how these joints experience loading during the activity.

2. Force magnitude: The peak force values reached by each joint during specific phases of the activity indicate the maximum load they bear. For example, the HF reaches a peak force of 9 BW, suggesting that the hip joint is subjected to relatively high forces during certain phases of the activity. On the other hand, the PFJ reaches a peak force of 5 BW, indicating the magnitude of forces experienced by the patellofemoral joint.

3. Phase-specific behaviour: The plot shows distinct phases in force development and behaviour for different joints. For example, there is an initial burst of force generation around 0.5 seconds, followed by a period of relative stability with slightly elevated forces. This may indicate the different phases of movement during the analyzed activity.

4. Force distribution: By comparing the forces at different joints, we can understand the distribution of forces across the lower extremity and its impact on joint mechanics. For instance, the Lat TFJ may experience higher forces than the PFJ and AF during specific phases, indicating the importance of lateral stability during certain movements.

5. Joint health implications: Joint contact forces are crucial for assessing joint health and potential risks of overloading or joint injuries. High peak forces, particularly at the hip and knee joints, may indicate increased stress on these joints, which can be relevant for athletes, individuals with certain activities or exercises, or patients with certain conditions.

6. Biomechanical insights: Analyzing joint contact forces helps researchers and clinicians understand the biomechanics of movement and the interplay between muscles, bones, and joints. This knowledge can inform the development of rehabilitation protocols, injury prevention strategies, and optimized movement patterns.

In summary, the joint contact forces in the plot provide valuable information about how the forces are distributed across various joints during the activity. This information can be crucial for understanding joint mechanics, optimizing movement patterns, assessing joint health, and designing targeted interventions to improve performance and prevent injuries.
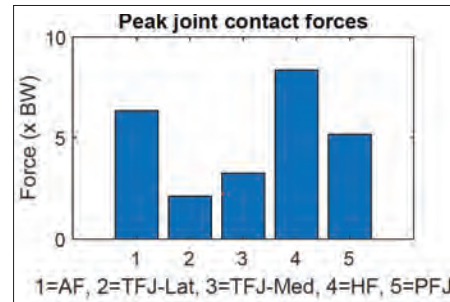

Figure 10: Peak joint contact forces

1. TF (total force) = 6 BW:
   The total force (TF) experienced by the joint system is 6 times the body weight. This includes the combined forces acting on all joint regions (lateral tibiofemoral, medial tibiofemoral, hip, and patellofemoral joints). A total force of 6 BW indicates the overall loading on the entire joint system during the specific activity or exercise being studied.

2. TFJ-LAT (total force at lateral tibiofemoral joint) = 2 BW:
   The total force at the lateral tibiofemoral joint is 2 times the body weight. This specific force value represents the load experienced at the lateral side of the knee joint during the activity. It indicates the contribution of forces acting on the lateral aspect of the tibiofemoral joint, which is crucial for lateral stability during movements such as cutting or side-stepping.

3. TFJ-MED (total force at medial tibiofemoral joint) = 3 BW:
   The total force at the medial tibiofemoral joint is 3 times the body weight. This value represents the load experienced at the medial side of the knee joint. The medial tibiofemoral joint plays a critical role in weight-bearing and shock absorption during activities like walking, running, and jumping.

4. HF (force at hip joint) = 9 BW:
   The force at the hip joint is 9 times the body weight. This value indicates the significant loading experienced at the hip joint during the activity. The hip joint is responsible for transmitting forces from the lower body to the trunk and upper body, making it crucial for overall movement and stability.

5. PFJ (force at patellofemoral joint) = 5 BW:
   The force at the patellofemoral joint is 5 times the body weight. This value represents the load experienced at the knee joint between the patella

(kneecap) and femur (thigh bone). The patellofemoral joint is involved in various knee movements, such as knee flexion and extension, and plays a vital role in knee joint stability.

The interpretation of the results suggests that during the peak joint contact forces in this specific activity or exercise, the hip joint experiences the highest force (9 BW), followed by the total force (6 BW) acting on the entire joint system. The lateral tibiofemoral joint experiences the lowest force (2 BW) among the joint regions. The specific force values provide valuable insights into the distribution of forces across different joint regions, helping to understand the loading patterns and potential implications for joint health and performance during the activity.
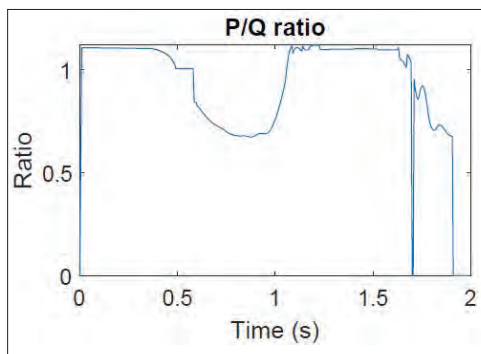

Figure 11: Simulated ratio of patellar tendon to quadriceps tendon force with respect to time from resting state to activity state.

The PQ ratio vs. time plot demonstrates dynamic changes in the balance of forces between the patellar and quadriceps tendons during different phases of the activity. The variations in the ratio indicate how the tendons work together to stabilize the knee joint and control movements throughout the activity. The ratio values and patterns can provide valuable information about the functional efficiency of the knee joint and the coordination between the patellar and quadriceps tendons during the specific activity being analysed.

Ergonomic optimization:

The results outline that key parameters to achieve the ergonomic compatibility in the knee joint support apparatus are load distribution, joint stability, customization, apparatus dimensions, material selection and dynamic balance. The parameters have interlinked relation to actively control the ergonomic factor.

1. Load distribution: Ensuring that forces at critical joints like the hip (9 BW) and patellofemoral joint (5 BW) are appropriately managed to prevent excessive stress and potential injury.
2. Joint stability: Designing the brace to provide adequate support to stabilize the knee joint, particularly during movements such as flexion and extension, to mitigate instability and enhance overall joint function.
3. Customization: Utilizing 3D scanning technology to tailor the brace to individual anatomies, ensuring optimal fit and comfort while maintaining effectiveness in supporting joint mechanics.
4. Material selection: Choosing materials with appropriate stiffness and flexibility characteristics to provide support while allowing for natural movement, thus minimizing discomfort and maximizing user compliance.
5. Apparatus dimensions: Appropriate customized component dimensions improve ergonomics to the user.
6. Dynamic balance: Considering the dynamic balance of forces between the patellar and quadriceps tendons, as indicated by the PQ ratio over time, to optimize functional efficiency and coordination during various phases of activity.

The results of this study provide valuable insights into the biomechanics of the knee joint and hip muscles during specific activities. The analysis of knee joint forces reveals dynamic changes in force distribution and loading patterns across different joint regions, including the medial and lateral tibiofemoral joints, hip joint, and patellofemoral joint. The observed peaks and fluctuations in joint contact forces highlight the importance of joint stabilization and the potential implications for joint health and performance. Additionally, the investigation of the patellar tendon to quadriceps tendon force ratio sheds light on the dynamic balance of forces between these tendons during different phases of activity, providing valuable information about the knee joint's functional efficiency. Understanding these muscle forces and joint contact dynamics is crucial for designing effective rehabilitation protocols, injury prevention strategies, and optimizing movement patterns for improved performance and reduced risk of joint injuries. The function of a spring supported knee support brace on knee joint muscles in movement stabilization and performance improvement, relevant to a clinical setting, was validated by Dzidotor *et al*. (2023). The outcome of the present work, which specifically focuses on spring loaded active knee braces, is in coherence with the findings of Dzidotor *et al.* (2023) on general unloader spring supported knee braces.

The clinical application of these findings lies in informing rehabilitation protocols and injury prevention strategies tailored to specific activities. Understanding the distribution of forces across different joint regions, particularly at the patellofemoral joints, aids in designing interventions to mitigate potential joint overloading and instability. Furthermore, insights into the dynamic balance of forces between the patellar and quadriceps tendons during activity guide the development of targeted approaches for enhancing knee joint stability and functional efficiency. Further research and clinical applications based on these findings can enhance our understanding of the musculoskeletal system's intricacies and inform targeted interventions for individuals engaging in various physical activities.

CONCLUSION

The assessment of ergonomics and gait analysis of the knee joint model validates the usability of the system for effectively supporting the load on the human knee mechanism. The support system can be further validated through clinical trials to assess its viability for use in clinical scenarios for the prevention and management of musculoskeletal diseases.

In conclusion, the findings from the study present a comprehensive analysis of knee joint forces and hip muscle activations during specific activities. The plots of joint contact forces over time reveal the dynamic nature of force distribution across various joint regions, providing valuable insights into loading patterns and potential implications for joint health. The patellar tendon to quadriceps tendon force ratio analysis sheds light on the balance of forces between these tendons during different phases of activity, offering valuable information about knee joint stability. The results contribute to our understanding of the biomechanics of the musculoskeletal system and can guide the development of targeted interventions for optimizing movement patterns and reducing the risk of joint injuries. Further research and clinical applications based on these findings hold the potential to improve rehabilitation protocols, injury prevention strategies, and overall performance for individuals engaged in physical activities.

Conflict of interest

The authors have no conflict of interest to declare.

Ethical approval

There are no animals or humans involved in this study. Hence ethical approval is not applicable.

REFERENCES

Auberger R., Breuer-Ruesch C., Fuchs F., Wismer N., & Riener R. (2018). Smart passive exoskeleton for everyday use with lower limb paralysis: Design and first results of knee joint kinetics. *7th IEEE International Conference on Biomedical Robotics and Biomechatronics (Biorob)*, pp. 1109–1114.
DOI: https://doi.org/10.1109/BIOROB.2018.8488119

Alluhydan K., Siddiqui I.H., & Hesham E. (2023). Functionality and comfort design of lower-limb prosthetics: a review. *Journal of Disability Research* **2**(3): 10–23.
DOI: https://doi.org/10.57197/JDR-2023-0031

Barr K.P. (2007). Review of upper and lower extremity musculoskeletal pain problems. *Physical Medicine and Rehabilitation Clinics of North America* **18**(4): 747–760.
DOI: https://doi.org/10.1016/j.pmr.2007.07.009

Bliddal H., Leeds A.R., & Christensen R. (2014). Osteoarthritis, obesity and weight loss: evidence, hypotheses and horizons – a scoping review. *Obesity Reviews* **15**(7): 578–586.
DOI: https://doi.org/10.1111/obr.12173

Cernohorsky J., Richter A., & Horak M. (2018). Mechatronic design of rehabilitation brace. *2018 IEEE 20th International Conference on e-Health Networking, Applications and Services* (Healthcom), pp. 1–4.
DOI: https://doi.org/10.1109/HealthCom.2018.8531093

Cheng C.Y., Okamoto S., Li P., Akiyama Y., Qiu C., & Yamada Y. (2020). Encouragement of squat-lifting: feasibility study of a highly usable passive knee assistive device. *2020 IEEE/SICE International Symposium on System Integration (SII)*, pp. 504–508.
DOI: https://doi.org/10.1109/SII46433.2020.9025902

Dereshgi H.A., Ersin G.Ö.S.E., Demïr D., & Ghannam H. (2023). Restoring mobility and independence: evaluating the impact of knee exoskeletons in real-world scenarios. *Journal of Smart Systems Research* **4**(1): 61–71.
DOI: https://doi.org/10.58769/joinssr.1308638

Dzidotor G.K., Moorhead J.B. Jr., Ude C.C., Ogueri K.S., Ghosh D., & Laurencin C.T. (2023). Functions and effectiveness of unloader, patellofemoral, and knee sleeve orthoses: a review. *Regenerative Engineering and Translational Medicine* **2023**: 1–25.
DOI: https://doi.org/10.1007/s40883-023-00313-1

Hunt A. (2003). Musculoskeletal fitness: the keystone in overall well-being and injury prevention. *Clinical Orthopaedics and Related Research* **409**: 96–105.
DOI: https://doi.org/10.1097/01.blo.0000057787.10364.4e

Hunte K., Chen S., Yi J., & Su H. (2020). Assist-as-needed control of a wearable lightweight knee robotic device. *2020 IEEE/ASME International Conference on Advanced Intelligent Mechatronics (AIM)*, pp. 1477–1482.
DOI: https://doi.org/10.1109/AIM43001.2020.9159021

Johnson A., Gao R.Z., Marriott K., Dickerson C.R., Maly M., & Ren C. (2023). Electronics-free soft robotic knee brace for dynamic unloading during gait for knee osteoarthritis: a proof-of-concept study. *Journal of Medical Devices* **17**(4): 041004.
DOI: https://doi.org/10.1115/1.4064249

Kraemer W.J., French D.N., & Spiering B.A. (2004).

Compression in the treatment of acute muscle injuries in sport. *International SportMed Journal* **5**(3): 200–208.

Kuan J.Y., Pasch K.A., & Herr H.M. (2014). Design of a knee joint mechanism that adapts to individual physiology. *2014 36th Annual International Conference of the IEEE Engineering in Medicine and Biology Society*, pp. 2061–2064.

Li J., Shen B., Chew C.-M., Teo C.L., & Poo A.N. (2016). Novel functional task-based gait assistance control of lower extremity assistive device for level walking. *IEEE Transactions on Industrial Electronics* **63**(2): 1096–1106.
DOI: https://doi.org/10.1109/TIE.2015.2477347

Li Z., Han Y., Liu C., Xiu H., Wei G., & Ren L. (2023). Design, manufacture, and experimental validation of a hydraulic semi-active knee prosthesis. *IEEE Transactions on Neural Systems and Rehabilitation Engineering* **31**: 1394–1404.
DOI: https://doi.org/10.1109/TNSRE.2023.3246071

Messier S.P., Gutekunst D.J., Davis C., & DeVita P. (2005). Weight loss reduces knee-joint loads in overweight and obese older adults with knee osteoarthritis. *Arthritis and Rheumatism* **52**(7): 2026–2032.
DOI: https://doi.org/10.1002/art.21139

Quinlivan B., Asbeck A., Wagner D., Ranzani T., Russo S., & Walsh C. (2015). *ASME 2015 International Design Engineering Technical Conferences & Computers and Information in Engineering Conference (IDETC/CIE 2015)*, Boston, MA, USA.

Reanaree P. & Pintavirooj C. (2018). Exoskeleton Suit Supports the Movement. *2018 11th Biomedical Engineering International Conference (BMEiCON),* pp. 1–4.
DOI: https://doi.org/10.1109/BMEiCON.2018.8609990

Saccares L., Brygo A., Sarakoglou I., & Tsagarakis N.G. (2017). A novel human effort estimation method for knee assistive exoskeletons. *2017 International Conference on Rehabilitation Robotics (ICORR)*, pp. 1266–1272.

DOI: https://doi.org/10.1109/ICORR.2017.8009423

Shamaei K., Cenciarini M., Adams A.A., Gregorczyk K.N., Schiffman J.M., & Dollar A.M. (2015). Biomechanical effects of stiffness in parallel with the knee joint during walking. *IEEE Transactions on Biomedical Engineering* **62**(10): 2389–2401.
DOI: https://doi.org/10.1109/TBME.2015.2428636

Shen B., Li J., Bai F., & Chew C.M. (2013). Development and control of a lower extremity assistive device (LEAD) for gait rehabilitation. *2013 IEEE 13th International Conference on Rehabilitation Robotics (ICORR)*, pp. 1–6.

Trkov M., Shanqiang W., Kuo C., Jingang Y., Tao L., & Qijie Z. (2017). Design of a robotic knee assistive device (ROKAD) for slip-induced fall prevention during walking. *IFAC-PapersOnLine* **50**(1): 9802–9807.
DOI: https://doi.org/10.1016/j.ifacol.2017.08.887

Ulrich S.D., Bhave A., Marker D.R., Seyler T.M., & Mont M.A. (2007). Focused rehabilitation treatment of poorly functioning total knee arthroplasties. *Clinical Orthopaedics and Related Research (1976–2007)* **464**: 138–145.
DOI: https://doi.org/10.1097/BLO.0b013e3181560d99

Valachi B. & Valachi K. (2003). Mechanisms leading to musculoskeletal disorders in dentistry. *The Journal of the American Dental Association* **134**(10): 1344–1350.
DOI: https://doi.org/10.14219/jada.archive.2003.0048

Zhang L., Liu G., Han B., Wang Z., Li H., & Jiao Y. (2020). Assistive devices of human knee joint: A review. *Robotics and Autonomous Systems* **125**: 103394.
DOI: https://doi.org/10.1016/j.robot.2019.103394

Zhao D.Y., Mazzone B., Yoder A.J., Esposito E.R., Kang T.H., Loh K.J., & Farrokhi S. (2022). Ankle sprain bracing solutions and future design consideration for civilian and military use. *Expert Review of Medical Devices* **19**(2): 113–122.
DOI: https://doi.org/10.1080/17434440.2022.2039622

RESEARCH ARTICLE

Biomaterial Composites

Synthesis and characterization of biocomposite of bovine bone-based hydroxyapatite-poly(lactic acid)-maleic anhydride

J Keerthana, KHIK Hewavitharana[*] and KB Wijesekara
Department of Biosystems Technology, Faculty of Technological Studies, Uva Wellassa University, Passara Road, Badulla, Sri Lanka.

Abstract: Human bone is a composite material of hydroxyapatite (HA) and collagen. HA ($Ca_{10}(PO_4)_6(OH)_2$) is a biomaterial with the calcium to phosphorus ratio being similar to the natural bone composition. In this study, composite materials were prepared by using poly(lactic acid) (PLA) as a polymer matrix, maleic anhydride (MAH) as a compatibilizer, and natural HA extracted from cow bone (BHA) as a suitable mechanical support filler with positive surface properties. Composites with varying HA (10-30 wt. %), PLA, and with or without MAH (0.5–8 wt. %) were prepared by a thermal decomposition method at 900 °C. In comparison to commercial HA (CHA), the effect of the PLA and MAH contribution on morphological, thermal, and mechanical properties of BHA were analyzed by X-ray diffraction (XRD), Fourier transform infrared (FTIR) spectroscopy, thermogravimetric analysis (TGA), scanning electron microscopy (SEM) and tensile strength measurements. As per the results, the HA30/PLA/4MAH composite with 30 wt. % HA, 66 wt. % PLA and 4 wt. % MAH offer the maximum mean tensile strength of 307.71 MPa. The overall results confirm the contribution of MAH compatibilizer in HA/PLA/MAH composite materials for bone tissue engineering from a mechanical point of view.

Keywords: Biocomposite, biomaterials, bone tissue engineering, compatibilizer, hydroxyapatite, poly(lactic acid), maleic anhydride.

INTRODUCTION

Biomaterials are substances that can be engineered to replace a part or a function of the body in a safe, reliable, economical, and physiologically acceptable way. Biomaterials are used in prostheses, scaffolds, hydrogels with cells, and growth factors to treat bone loss due to fracture, osteoporosis, osteoarthritis, and neoplasms (Ramesh *et al.*, 2018). The implant material should be biodegradable, biocompatible, non-toxic, non-mutagenic, and non-immunogenic, with suitable mechanical support and positive surface properties, such as facilitating adhesion, proliferation, and differentiation of cells (Asghari *et al.*, 2017). Human bone is a composite material of 70% HA, a high modulus filler, in a collagen matrix (Liao *et al.*, 2013). HA ($Ca_{10}(PO_4)_6(OH)_2$) is considered an implant material possessing biocompatibility, good corrosion resistance, bioactivity, high osteoconductivity, nontoxicity, and displaying non-inflammatory and non-immunogenic behaviour, due to its calcium to phosphorus ratio being similar to the natural bone composition. It also has some drawbacks, such as brittleness, low fracture strength, low mechanical reliability, lack of resilience, debris formation, and relatively difficult fabrication. To overcome these drawbacks, biocomposites are designed to achieve a combination of the best properties of two or more materials to fulfill various mechanical and biological needs. In this case, polymer matrix composites are commonly considered due to similarity in composition and structure of natural tissue, good biocompatibility, moulding capabilities into desirable shapes and sizes, and controllability over mechanical properties and degradation characteristics (Liao *et al.*,

* Corresponding author (indika.h@uwu.ac.lk; https://orcid.org/0009-0006-1734-9139)

2013; 2014). Petrochemical-based polymers such as polyetheretherketone (PEEK), polysulphone (PSU), and polypropylene (PP) have been reported as good candidates for matrices (Wang *et al.*, 2001; Converse *et al.*, 2007; Liao *et al.*, 2013; 2014; Stubinger *et al.*, 2016) However, biodegradable polymers such as polylactic acid (PLA), polyglycolic acid (PGA), polycaprolactone (PCL), and polyhydroxyalkanoates (PHAs) are more reliable in reducing inflammatory reactions, nontoxic, biodegradable, absorbable and can easily change into different 3D matrix structures (Fabbri *et al.*, 2010; Gao *et al.*, 2016; Lu *et al.*, 2019). PLA is a biodegradable, bioadsorbable, thermoplastic aliphatic polyester, that can be derived from renewable resources (Wang *et al.*, 2001; Converse *et al.*, 2007; Liao *et al.*, 2013; 2014; Stubinger *et al.*, 2016; Asghari *et al.*, 2017; Lu *et al.*, 2019). PLA/HA biocomposite materials are designed both as scaffold materials and as carriers to supply drugs and other proteins to the host. However, the HA percentage in the PLA/HA biocomposites and the temperature influence in the mechanical properties of the composite (Sun *et al.*, 2011; Ramesh *et al.*, 2018). Tazibt *et al.* (2023) have shown the effect of hydroxyapatite (HA) on the morphology and properties of composites based on poly(lactic acid) (PLA) at various filler content ratios (5, 10, and 15 wt.%) using the solvent casting method, followed by thermo-compression. The properties of PLA can be enhanced by blending, copolymerization, cross-linking, and grafting methods (Meng *et al.*, 2023).

Most bio-fillers such as HA do not easily disperse in thermoplastic polymers because of strong intermolecular hydrogen bonding between biofillers and agglomerate during the compounding process with the polymer matrix. Therefore, the improvement of interfacial adhesion between bio-fillers and polymer matrix is very important for the application of composites. Currently, different methods have been studied to improve the interfacial adhesion of composites by modifying the biofiller surface (Prabhu *et al.*, 2016; Moja *et al.*, 2020; Tariq *et al.*, 2021), for example, the construction of a stereo-complexation between poly(d-lactide) grafted hydroxyapatite and poly(l-lactide) via selective laser sintering (SLS) (Shuai *et al.*, 2022) and the application of silane coupling agents to enhance the interfacial features between bioceramic and biopolymer composite (Shuai *et al.*, 2020). In comparison to the above-discussed crosslinkers, maleic anhydride (MAH) is a low toxic, chemically active compound with a low potential to polymerize itself under free radical grafting conditions (Zhang *et al.*; 2004; Nainar *et al.*, 2012; Sumathra

et al., 2020). This study focuses on the development of a cost-effective, biocomposite material using natural hydroxyapatite (HA) which is extracted from waste cow bone by a thermal decomposition method, and a biodegradable polymer (PLA). The enhancement of interfacial coupling in hydroxyapatite and polylactic acid was achieved by incorporating maleic anhydride (MAH) as a compatibilizer toward a bioactive composite (HA/PLA/MAH) with enhanced interfacial bonding. The effect of MAH compatibilizer content on the formation, morphology, and physical properties of hydroxyapatite-poly(lactic acid)-maleic anhydride composites are further studied. Finally, the characteristics of the composites with and without compatibilizer (MAH) are compared.

METHODS AND MATERIALS

Preparation of hydroxyapatite composites

A fresh cow bone sample was cleaned by boiling in water for 4 hours, followed by drying in an oven at 180 °C for 1 hour. The cleaned and dried bones were then ground to a fine powder (<450 μm) using an agate mortar and pestle. The ground bone particles were treated with sodium hydroxide solution for 1 hour. Then the bone sample was neutralized with distilled water, dried in an oven at 180 °C for 4 hours, and sintered in a furnace at 900 °C for 3 hours. The resulting bone sample was crushed in a ball mill for 1 hour at 800 rpm to produce bone powder and sieved to obtain the particle sizes below 125 μm. The powdered sample was oven-dried at 120 °C for 1 hour to prepare composites.

Table 1: Preparation of HA/PLA composite without compatibilizer

Sample ID	BHA wt.%	PLA wt.%
HA10/PLA	10	90
HA20/PLA	20	80
HA30/PLA	30	70

To prepare composites according to Table 1 compositions, PLA pellets were melted in a stainless-steel container on a hot plate at 200 °C. After the melting, BHA powder was slowly added to the melted polymer while continuously stirring using a mechanical stirrer for 1 hour. Thereafter, the mixture was poured into the created wooden mould which was prepared for the tensile test.

Table 2: Preparation of HA/PLA/MAH composite

Sample ID	BHA wt.%	PLA wt.%	MAH wt.%
HA30/PLA/0.5MAH	30	69.5	0.5
HA30/PLA/1MAH		69.0	1.0
HA30/PLA/2MAH		68.0	2.0
HA30/PLA/4MAH		66.0	4.0
HA30/PLA/8MAH		62.0	8.0

To prepare composites according to Table 2 compositions, PLA pellets were melted in a stainless-steel container on a hot plate at 200 °C. After the melting, MAH powder was slowly added to the melted polymer while continuously stirring followed by BHA addition to the PLA/MAH mixture while continuously stirring for 1 hour. Thereafter, the mixture was poured into the created wooden mould for the tensile test.

Characterization techniques

Commercial hydroxyapatite (CHA), prepared HA from cow bone (BHA), and selected HA/PLA and HA/PLA/MAH composites were characterized using fourier transform infrared spectroscopy (Alpha Platinum AKR, FTIR), X-ray diffractometry (Rigaku-Ultima 1V X-Ray diffractometer1, XRD), scanning electron microscopy (LEO-1420P, SEM), and thermogravimetric analysis (SDT Q600, TGA with N_2 environment); the tensile was tested on a JTM-S1000 universal tensile testing machine using a load cell of 98.5 kN.

RESULTS AND DISCUSSION

Bovine bones were first boiled in hot water, and then immersed in a sodium hydroxide solution to remove collagen, fat, and organic substances. Deproteinized white-coloured cow bone pieces (Figure 1A) were ball-milled to make HA powder (BHA) (Figure 1B). The bones were washed with distilled water, dried, and sintered at 900 °C for 3 h to transform to fully crystallized hydroxyapatite. To form composites, BHA was mixed with PLA polymer and moulded into cylindrical shapes using a trial bone plate (Figure 1C) with and without MAH compatibilizer (Figure 2 and 3) to test tensile strength. The highest HA weight percentage containing HA30/PLA composition was selected to continue the study which is more compatible with human bone composition (HA : organic : water = 70:25:5; Rakmae *et al.*, 2011).

Figure 1: Hydroxyapatite A) Raw bone pieces; B) Bone hydroxyapatite; C) Trial bone plate
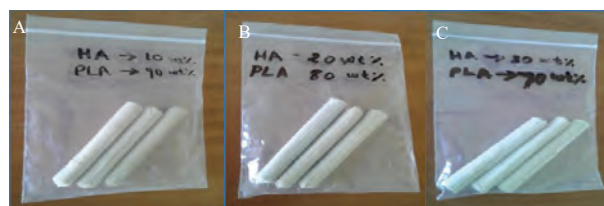

Figure 2: HA/PLA Biocomposites A) HA10/PLA; B) HA20/PLA; C) HA30/PLA

Figure 3: HA/PLA/MAH Biocomposites A) HA30/PLA/0.5MAH; B) HA30/PLA/1MAH; C) HA30/PLA/2MAH; D) HA30/PLA/4MAH; E) HA30/PLA/8MAH
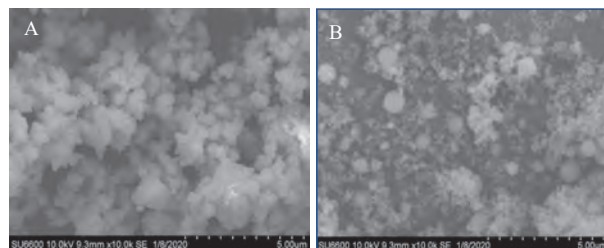

Figure 4: SEM images of HA powder A) BHA, B) CHA

SEM Analysis

According to the SEM images of BHA (Figure 4A) and CHA (Figure 4B), HA particles have an irregular sphere shape and mostly consist of agglomerated big particles with a size of ~1-5 μm, due to the strong intermolecular bonding of HA particles to each other. Agglomeration of HA powder particles will reduce the important surface properties, correlation, and performance of the composites. In the SEM images of the HA30/PLA/4MAH composite (Figure 5), HA was detected on the polymer matrix in a closely packed form, and dark holes were observed in the surface matrix as in Figure 5A and 5B. The appearance of micropores in samples as dark holes would improve surface topographical features for the osteoconductivity of bioceramics and proper porosity is a desirable factor

for cell growth through the channels of the scaffold (Chan *et al*., 2012; Baier *et al*., 2019; Mishchenko *et al*., 2023). Normally HA biofiller does not easily disperse in biodegradable polymers such as PLA because of strong intermolecular hydrogen bonding between HA particles, and they agglomerate during the compounding process with the polymer matrix. However, less pullout of HA powder and less agglomeration of HA powder were observed in the PLA polymer matrix (Figure 5C and 5D). The results indicated that modifying the HA surface with MAH compatibilizer would result in better interfacial adhesion between the HA powder and PLA matrix and would enhance the dispersion properties of the composite (Rakmae *et al*., 2011; Hapuhinna *et al*., 2017; 2018).
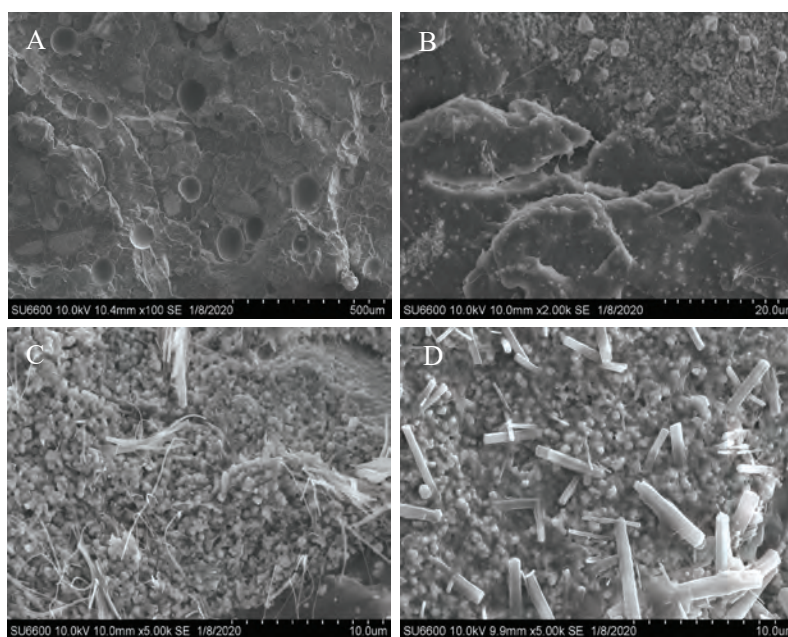

Figure 5:   SEM images of HA30/PLA/4MAH biocomposite

XRD Analysis

The XRD peak positions of BHA (Figure 6B) and CHA (Figure 6C), are overlapped with characteristic peaks related to the crystallographic planes of HA at (002), (210), (211), (112), (300), (202), (310), (222), (213), and (004). Phase analysis according to the standard JCPDS 00-009-0432 revealed that all major peaks of HA present in both BHA and CHA powders are in good agreement with hexagonal HA in reference material (Mondal *et al*., 2014). Data further shows the purity of the prepared HA

from cow bone waste and the crystallinity behaviour of BHA during the sintering process. It indicated that the sintering temperature influences the phase stability, densification behaviour, and hardness of HA ceramics. BHA shows sharp peaks in the XRD pattern due to the higher degree of crystallinity of planes after the sintering process at 900 °C (Figure 6B). The absence of other peaks corresponding to impurities indicates that a pure phase of HA has been synthesized during the procedure (Ferri *et al*., 2017; Hapuhinna *et al*., 2017).
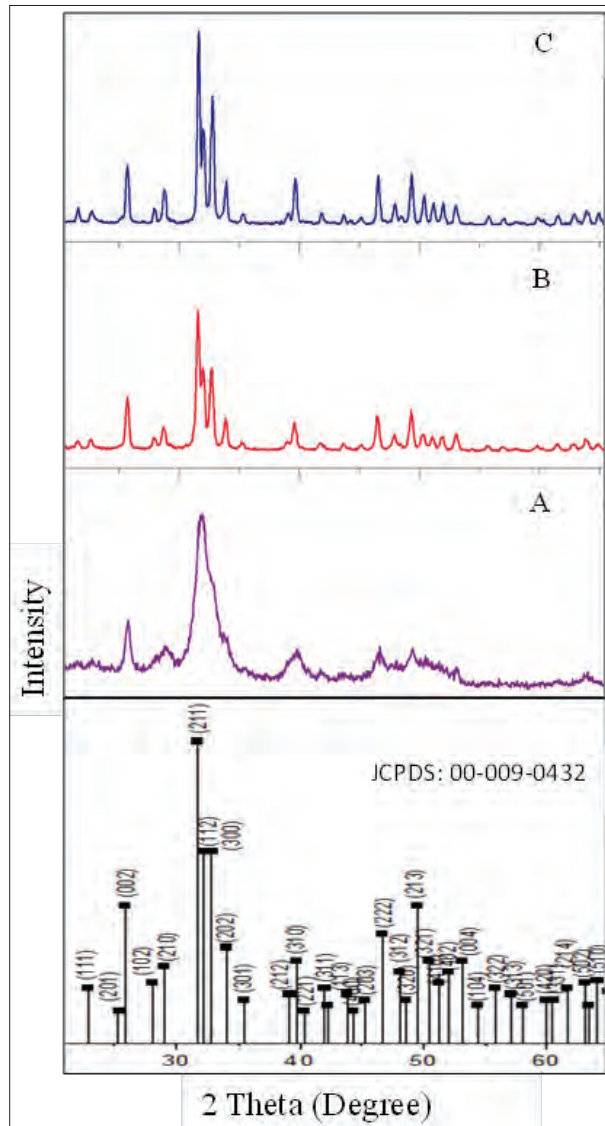
Figure 6: XRD patterns of A) Raw bone HA, B) Sintered bone HA and C) Commercial HA samples.

FTIR Analysis

The representative FTIR spectrum in Figure 7, confirms the presence of phosphate groups (PO_4^{3-}) for all raw bone HA, BHA, and CHA. FTIR peaks at 475, 560 – 601, 640, 963, 1023, and 1090 cm^{-1} were assigned to different vibration modes of phosphate groups. The peaks at 475 cm^{-1} correspond to V_4 of PO_4^{3-} modes, 560 - 601 cm^{-1} relate to V_4 of the bending modes of P-O bonds, 640 cm^{-1} and 963 cm^{-1} to V_1, and the stretching vibrations of PO_4^{3-} of V_3 appear at 1023 and 1090 cm^{-1}. It confirms the presence of the HA phase in BHA

(Hapuhinna *et al*., 2017; 2018). The characteristic peak for OH$^-$/hydroxyapatite appeared nearly at 3572 cm^{-1} in CHA and BHA. Stretching and bending vibrations of OH groups in HA powder were observed at 631 and 3542 cm^{-1} (Rakmae *et al*., 2011; Ferri *et al*., 2017; Hapuhinna *et al*., 2017). The characteristic band of the vibrational mode of structural OH can be seen at 631 cm^{-1}. The stretching vibration band of OH (3542 cm^{-1}) was invisible for raw bone HA due to absorbed water. The peaks at frequencies of ~875 cm^{-1} and ~1450 cm^{-1} resulted from a small amount of carbonate absorbed as CO_2 from the atmosphere during the synthesis process. It is common for biological apatite to allow substitution of other ions, such as carbonate, fluoride, and chloride substitution of either OH$^-$ or PO_4^{3-} groups. Raw bone HA powder shows the presence of amide groups (1660 cm^{-1}, 1547 cm^{-1}, 1244 cm^{-1}) due to collagen and other organic compounds present in the bone (Paschalis *et al*., 2011; Rana *et al*., 2017). However, after the heat treatment at 900 °C, BHA becomes more compatible with CHA (Hapuhinna *et al*., 2017; 2018).
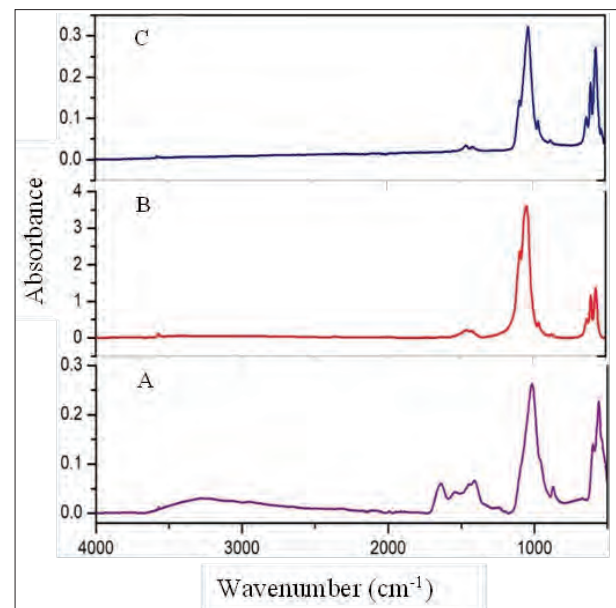

Figure 7: FTIR results of A) Raw bone HA, B) Sintered bone HA and C) Commercial hydroxyapatite samples

TGA Analysis

As shown in Figure 8, BHA and CHA samples were subjected to TGA analysis. The first significant weight loss of BHA occurs at nearly at 200 °C, corresponding to the dehydration of the sample. Thereafter, the TGA

curves of BHA and CHA samples showed weight reduction at a low rate close to 650 °C, due to the removal of bone structure collagen remains (Rakmae *et al.*, 2011; Ferri *et al.*, 2017; Hapuhinna *et al.*, 2017). In addition, a fine TGA descending slope was observed in the temperature range 700 – 1000 °C, with weight loss corresponding to the decomposition of HPO_4^{2-} (2 HPO_4 $\rightarrow P_2O_7^{4-} + H_2O$ and $P_2O_7^{4-} + 2\ OH^- \rightarrow 2PO_4^{2-} + H_2O$) and gaseous compound elimination. Weight loss patterns have shown relatively similar patterns above 500 °C due to composition similarities (Rakmae *et al.*, 2011; Ferri *et al.*, 2017; Hapuhinna *et al.*, 2017).
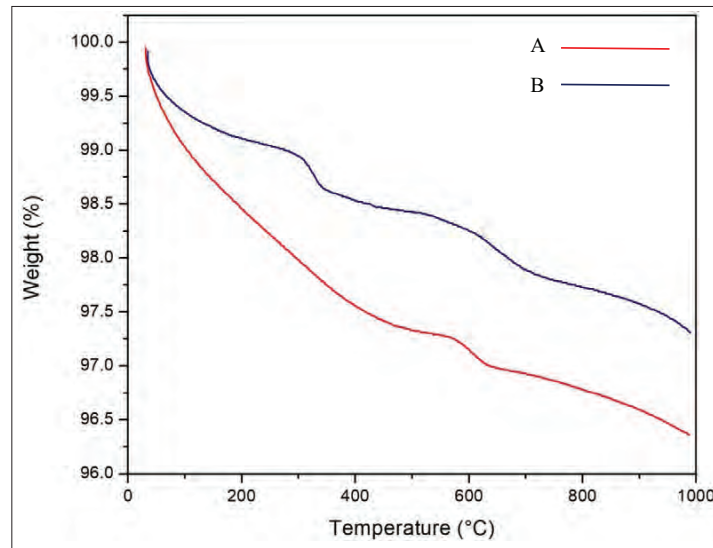

Figure 8: TGA analysis of A) Sintered bone HA and B) Commercial hydroxyapatite samples
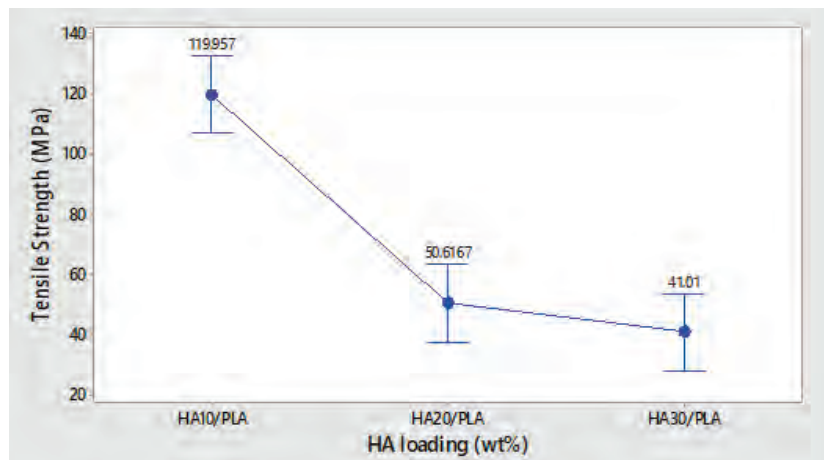

Figure 9: Plot of Tensile strength of HA/PLA composite without compatibilizer
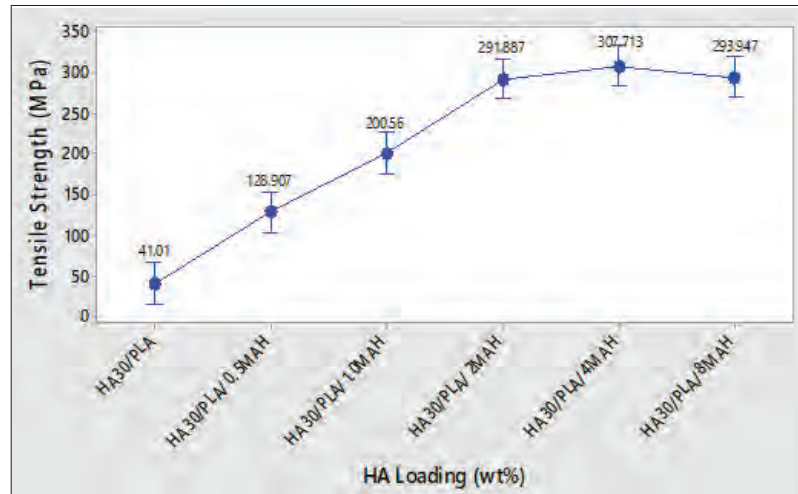
Figure 10: Plot of Tensile strength of HA/PLA composite with MAH compatibilizer

Tensile strength test

The mechanical properties of the HA/PLA without and with MAH are illustrated in Figures 9 and 10 respectively. According to Figure 9 plot, the evolution of tensile strength as a function of the wt. % of hydroxyapatite without compatibilizer, HA10/PLA shows the maximum mean tensile strength of 119.96 ± 8.01 MPa. The Tukey multiple comparison test was run at 95% confidence to get the highest strength. As seen in the results, the tensile strength of the HA/PLA composites decreased with increasing HA loading because of poor dispersion of the filler material in the polymer matrix, detachment of HA from the matrix, weak interfacial adhesion, and low compatibility between the hydrophilic HA and hydrophobic PLA (Kim *et al*., 2007; Gong *et al*., 2017). With HA loading, agglomeration of HA powder particles in the PLA matrix would reduce the surface contact area and create physical voids and defects in the composites which are eventually responsible for inefficient transferring of loading stress between PLA matrix and HA powder particles (Vainio *et al*., 1998: Hong *et al*., 2005). The tensile strength of a particulate HA/polymer composite depends on a uniform filler distribution and the effective interfacial adhesion in the polymer matrix (Rakmae *et al*., 2011; Ferri *et al*., 2017; Hapuhinna *et al*., 2017).

As shown in Figure 10, in comparison to the tensile strength of HA/PLA composites, HA/PLA composite material with MAH compatibilizer results in higher tensile strength (307.71 ± 1.91 MPa in HA30/PLA/4MAH composite) (Rakmae *et al*., 2011; Ferri *et al*., 2017). The tensile strength of the HA/PLA composite increases with increasing amount of compatibilizer up to 4 wt. % of MAH. The composite obtained from HA and PLA with MAH shows better mechanical properties due to the improvement of interfacial adhesion between HA and PLA and effective filler dispersion in the polymer matrix (Vainio *et al*., 1998; Hong *et al*., 2005). The anhydride groups present in MAH could enhance the dispersion of the filler material in the composite by making crosslinks between HA and PLA. Thereby, MAH compatibilizer would result in better interfacial adhesion between the HA powder and PLA matrix and would enhance the mechanical properties of the biocomposite (Rakmae *et al*., 2011; Ferri *et al*., 2017; Hapuhinna *et al*., 2017).

CONCLUSION

XRD and FTIR analysis reveals the similarity of commercial hydroxyapatite and hexagonal hydroxyapatite produced using cow bone waste by the thermal decomposition method at 900 °C as a cost-effective method. The hydroxyapatite (HA) and poly(lactic acid) (PLA) polymer matrix were prepared with and without maleic anhydride (MAH) compatibilizer and mechanical properties were assessed. The mechanical properties of HA/PLA composites with MAH compatibilizer were found to be improved in comparison to HA/PLA

composites. MAH incorporation has shown a significant increase in tensile strength due to the ease of dispersion of HA in PLA polymer matrix and enhanced interfacial adhesion between filler and matrix material. Hence, HA/PLA/MAH composite demonstrates the usefulness from a mechanical point of view for bone tissue engineering.

REFERENCES

Asghari F., Samiei M., Adibkia K., Akbarzadeh A. & Davaran S. (2017). Biodegradable and biocompatible polymers for tissue engineering application: a review. *Artificial Cells, Nanomedicine, and Biotechnology* **45**(2): 185–192.
DOI: https://doi.org/10.3109/21691401.2016.1146731

Baier R., Wijnhoven I., Valle V., Giovanetti C. & Vivanco J. (2019). Microporosity clustering assessment in calcium phosphate bioceramic particles. *Frontiers in Bioengineering and Biotechnology* **7**: 281.
DOI: https://doi.org/10.3389/fbioe.2019.00281

Chan O., Coathup M., Nesbitt A., Ho C-Y., Hing K., Buckland T., Campion C. & Blunn G. (2012). The effects of microporosity on osteoinduction of calcium phosphate bone graft substitute biomaterials. *Acta Biomaterialia*. **8**: 2788–2794.
DOI: https://doi.org/10.1016/j.actbio.2012.03.038

Converse G.L., Yue W. & Roeder R.K. (2007). Processing and tensile properties of hydroxyapatite-whisker-reinforced polyetheretherketone. *Biomaterials* **28**(6): 927–935.
DOI: https://doi.org/10.1016/j.biomaterials.2006.10.031

Fabbri P., Bondioli F., Messori M., Bartoli C., Dinucci D. & Chiellini F. (2010). Porous scaffolds of polycaprolactone reinforced with in situ generated hydroxyapatite for bone tissue engineering. *Journal of Materials Science: Materials in Medicine* **21**(1): 343–351.
DOI: https://doi.org/10.1007/s10856-009-3839-5

Ferri J., Jordá J., Montanes N., Gimeno O. & Balart R. (2017). Manufacturing and characterization of poly(lactic acid) composites with hydroxyapatite. *Journal of Thermoplastic Composite Materials* **31**: 089270571772901.
DOI: https://doi.org/10.1177/0892705717729014

Gao X. *et al.* (11 authors) (2016). Polydopamine-templated hydroxyapatite reinforced polycaprolactone composite nanofibers with enhanced cytocompatibility and osteogenesis for bone tissue engineering. *ACS Applied Materials & Interfaces* **8** (5): 3499–3515.
DOI: https://doi.org/10.1021/acsami.5b12413

Gong M., Zhao Q., Dai L., Li Y. & Jiang T. (2017). Fabrication of polylactic acid/hydroxyapatite/graphene oxide composite and their thermal stability, hydrophobic and mechanical properties. *Journal of Asian Ceramic Societies* **5**(2): 160–168.
DOI: https://doi.org/10.1016/j.jascer.2017.04.001

Hapuhinna K., Gunaratne R. & Pitawala J. (2018). Development of a Biomaterial from Naturally Occurring Chloroapatite Mineral for Biomedical Applications. *International Scholarly and Scientific Research & Innovation* **12**(8).

Hapuhinna K., Gunaratne R., Pitawala J., Wijesekara K. & Ekanayake K. (2017). Synthesis and characterization of hydroxyapatite from Eppawala Rock Phosphate for biomedical applications as a value added product, p. 178. Available at http://www.dr.lib.sjp.ac.lk/handle/123456789/7056.

Hong Z., Zhang P., He C., Qiu X., Liu A., Chen L., Chen X. & Jing X. (2005). Nano-composite of poly(L-lactide) and surface grafted hydroxyapatite: mechanical properties and biocompatibility. *Biomaterials* **26**(32): 6296–6304.
DOI: https://doi.org/10.1016/j.biomaterials.2005.04.018

Kim H.S., Lee B.H., Choi S.W., Kim S. & Kim H.J. (2007). The effect of types of maleic anhydride-grafted polypropylene (MAPP) on the interfacial adhesion properties of bio-flour-filled polypropylene composites. *Composites Part A: Applied Science and Manufacturing* **38**(6): 1473–1482.
DOI: https://doi.org/10.1016/j.compositesa.2007.01.004

Liao C.Z., Li K., Wong H.M., Tong W.Y., Yeung K.W. & Tjong S.C. (2013). Novel polypropylene biocomposites reinforced with carbon nanotubes and hydroxyapatite nanorods for bone replacements. *Materials Science & Engineering C, Materials for Biological Applications* **33**(3): 1380–1388.
DOI: https://doi.org/10.1016/j.msec.2012.12.039

Liao C.Z., Wong H.M., Yeung K.W. & Tjong S.C. (2014). The development, fabrication, and material characterization of polypropylene composites reinforced with carbon nanofiber and hydroxyapatite nanorod hybrid fillers. *International Journal of Nanomedicine* **11**(9): 1299–1310.
DOI: https://doi.org/10.2147/IJN.S58332

Lu J. *et al.* (13 authors) (2019). Properties of polylactic acid reinforced by hydroxyapatite modified nanocellulose. *Polymers* **11**(6): 1009.
DOI: https://doi.org/10.3390/polym11061009

Meng M., Wang S., Xiao M. & Meng Y. (2023). Recent progress in modification and preparations of the promising biodegradable plastics: polylactide and poly(butylene adipate-co-terephthalate). *Sustainable Polymer and Energy* **1**: 1–43.
DOI: https://doi.org/10.35534/spe.2023.10006

Mishchenko O., Yanovska A., Kosinov O., Maksymov D., Moskalenko R., Ramanavicius A. & Pogorielov M. (2023) Synthetic calcium–phosphate materials for bone grafting. *Polymers* **15**: 3822.
DOI: https://doi.org/10.3390/polym15183822

Moja T.N., Bunekar N., Mishra S.B., Tsai T.Y., Hwang S.S. & Mishra A.K. (2020). Melt processing of polypropylene-grafted-maleic anhydride/chitosan polymer blend functionalized with montmorillonite for the removal of lead ions from aqueous solutions. *Scientific Reports* **10**(1): 217.
DOI: https://doi.org/10.1038/s41598-019-57079-2

Mondal S., Mondal A., Mandal N., Mondal B., Mukhopadhyay S.S., Dey A. & Singh S. (2014). Physico-chemical characterization and biological response of *Labeo rohita*-derived hydroxyapatite scaffold. *Bioprocess and Biosystems Engineering* **37**(7): 1233–1240.
DOI: https://doi.org/10.1007/s00449-013-1095-z

Nainar S.M., Begum S., Hasan Z., Ansari M.N.M. & Anuar H. (2012). Influence of maleic anhydride on mechanical

properties and morphology of hydroxyapatite/poly-(lactic acid) composites. *Regenerative Research* **1**(2): 32–38.

Paschalis E.P., Mendelsohn R. & Boskey A.L. (2011). Infrared assessment of bone quality. *Clinical Orthopaedics and Related Research* **469**: 2170–2178.

Prabhu K.N., Macko T., Brull R., Remerie K., Tacx J., Garg P. & Ginzburg A. (2016). Separation of maleic anhydride grafted polypropylene using multidimensional high-temperature liquid chromatography. *Journal of Chromatography A* **1441**: 96–105.
DOI: https://doi.org/10.1016/j.chroma.2016.02.081

Rakmae S., Ruksakulpiwat Y., Sutapun W. & Suppakarn N. (2011). Physical properties and cytotoxicity of surface-modified bovine bone-based hydroxyapatite/poly(lactic acid) composites. *Journal of Composite Materials* **45**(12): 1259–1269.
DOI: https://doi.org/10.1177/0021998310377934

Ramesh N., Moratti S.C. & Dias G.J. (2018). Hydroxyapatite-polymer biocomposites for bone regeneration: A review of current trends. *Journal of Biomedical Materials Research Part B: Applied Biomaterials* **106** (5): 2046–2057.
DOI: https://doi.org/10.1002/jbm.b.33950

Rana M., Akhtar N., Rahman S., Jamil H.M. & Asaduzzaman S.M. (2017). Extraction of hydroxyapatite from bovine and human cortical bone by thermal decomposition and effect of gamma radiation: A comparative study. *Complementary and Alternative Medicine* **8**(3): 00263– 00273.

Shuai C., Yu L., Feng P., Gao C. & Peng S. (2020) Interfacial reinforcement in bioceramic/biopolymer composite bone scaffold: The role of coupling agent. *Colloids and Surfaces B: Biointerfaces* **193**: 111083.
DOI: https://doi.org/10.1016/j.colsurfb.2020.111083

Shuai C., Yu L., Feng P., Peng S., Pan H. & Bai X. (2022) Construction of a stereocomplex between poly(d-lactide) grafted hydroxyapatite and poly(l-lactide): toward a bioactive composite scaffold with enhanced interfacial bonding. *Journal of Materials Chemistry B* **10**(2): 214–223.
DOI: http://dx.doi.org/10.1039/D1TB02111G

Stubinger S., Drechsler A., Burki A., Klein K., Kronen P. & Von Rechenberg B. (2016). Titanium and hydroxyapatite coating of polyetheretherketone and carbon fiber-reinforced polyetheretherketone: A pilot study in sheep. *Journal of Biomedical Materials Research Part B: Applied Biomaterials* **104**(6): 1182–1191.
DOI: https://doi.org/10.1002/jbm.b.33471

Sumathra M., Rajan M., Amarnath Praphakar R., Marraiki N. & Elgorban A.M. (2020). In vivo assessment of a hydroxyapatite/κ-carrageenan-maleic anhydride-casein/doxorubicin composite-coated titanium bone implant. *ACS Biomaterials Science and Engineering* **6**(3): 1650–1662.
DOI: https://doi.org/10.1021/acsbiomaterials.9b01750

Sun F., Zhou H. & Lee J. (2011). Various preparation methods of highly porous hydroxyapatite/polymer nanoscale biocomposites for bone regeneration. *Acta Biomaterialia* **7**(11): 3813–3828.
DOI: https://doi.org/10.1016/j.actbio.2011.07.002

Tariq A., Ahmad N.M., Abbas M.A., Shakir M.F., Khaliq Z., Rafiq S., Ali Z. & Elaissari A. (2021). Reactive extrusion of maleic-anhydride-grafted polypropylene by torque rheometer and its application as compatibilizer. *Polymers* **13**(4): 495.
DOI: https://doi.org/10.3390/polym13040495

Tazibt N., Kaci M., Dehouche N., Ragoubi M. & Atanase L.I. (2023). Effect of filler content on the morphology and physical properties of poly(lactic acid)-hydroxyapatite composites. *Materials* **16**(2): 809.
DOI: https://doi.org/10.3390/ma16020809

Vainio M.H., Heino M. & Seppala J.V. (1998). Reinforcement of biodegradable poly(ester-urethane) with fillers. *Polymer* **39**(4): 865–872.

Wang M., Yue C.Y. & Chua B. (2001). Production and evaluation of hydroxyapatite reinforced polysulfone for tissue replacement. *Journal of Materials Science: Materials in Medicine* **12**(9): 821–826.
DOI: https://doi.org/10.1023/a:1017933220894

Zhang J.F. & Sun X. (2004). Mechanical properties of poly(lactic acid)/starch composites compatibilized by maleic anhydride. *Biomacromolecules* **5**(4): 1446–1451.
DOI: https://doi.org/10.1021/bm0400022

JOURNAL OF THE NATIONAL SCIENCE FOUNDATION OF SRI LANKA

GUIDANCE TO CONTRIBUTORS

GENERAL INFORMATION

Scope

The Journal of the National Science Foundation of Sri Lanka publishes the results of research in all aspects of Science and Technology. It is open for publication of Research Articles, Reviews, Research Communications and Correspondence.

IT related and other non-empirical articles

The JNSF is a journal primarily devoted to natural sciences. It also considers for publication significant and novel contributions from formal sciences. Authors of emerging sub-disciplines of Computing and related areas such as Machine Learning, Artificial Intelligence and Data Sciences are requested to carefully adhere to the following guidelines when submitting manuscripts for this journal.

- Clear formulation of outcome-oriented **Research Objective/s** for targeted knowledge (sub)domain/s or (sub)discipline/s.
- Selection and comprehensive summarization of **appropriate Research Method/s** adopted to achieve the stated Research Objective/s.
- Reporting a sound **(Empirical) Evaluation** of the research finding/s thereby arguing reliability, validity, and generalizability of research claim/s.

Categories of manuscripts

Research Articles: Research Articles are papers that present complete descriptions of original research. Research Articles should include an Abstract, Keywords, Introduction, Methodology, Results and Discussion, Conclusion and Recommendations where relevant. References should be prepared according to the "Guidelines for the preparation of manuscripts". Maximum length of the article should be limited to 25 pages with a word count of 10,000 including references, figures and tables. Any articles above this limit will be returned.

Reviews: Reviews are critical presentations on selected topics of Science or Technology. They should be well focused and organized and avoid general "textbook" style. As reviews are intended to be critical presentations on selected topics, reviewers need to have had substantial leadership in research supported by a publication track record in the areas covered by the review. A person/s wishing to submit a Review Article should obtain prior approval from the Editorial Board by submitting a concise summary of the intended article, along with a list of the author's publications in the related area (jnsf@nsf.gov.lk). Maximum length of the article should be limited to 40 pages with a word count of 12,000 including references, figures and tables. Any articles above this limit will be returned.

Research Communications: Research Communications are intended to communicate important new findings in a specific area of limited scope that are worthy of rapid dissemination among the scientific community. Authors are required to provide a statement justifying the suitability of the submission for a Research Communication. The article should include an Abstract, Keywords, Introduction, Methodology, Results & Discussion, Conclusion and References. Maximum length of the article should be limited to 10 pages with a word count of 2,500 including references, figures and tables. Any articles above this limit will be returned.

Correspondence: Correspondence will be accepted regarding one or more articles in the preceding four issues of the Journal, as well as Letters to the Editor. Articles covering important scientific events or any other news of interest to scientists, reviews of books of scientific nature, articles presenting views on issues related to science and scientific activity will also be considered. Publication will be made at the discretion of the Editor-in Chief. Maximum length of the article should be limited to 05 pages with a word count of 1,500 including references, figures and tables. Any articles above this limit will be returned.

SUBMISSION OF MANUSCRIPT

Authors submitting articles to the JNSF should first create an account in the Sri Lanka Journals Online System (https://jnsfsl.sljol.info/). All manuscripts in MS Word format must be electronically submitted to the journal's online platform at https://jnsfsl.sljol.info/submit/start/. Submissions *via* emails are not encouraged. Please make sure that no author information is mentioned in the article submitted. The names and details of affiliations of all authors and contact information of the corresponding author must be fed into the system during the online submission process. Authors (at least the corresponding author) are required to provide their personal, validated ORCID ID (by obtaining an ORCID ID from https://orcid.org/) when submitting the manuscript. No change to the authors or order of authors will be accepted after the submission. All those who have made significant contributions should be listed as co-authors. The corresponding author should ensure that all contributing co-authors are included in the author list and have approved the final version of the paper and have agreed to its submission for publication.

All submissions should be in English. If the manuscript conforms to the guidelines specified, the date received will be the date that the manuscript was submitted to the online system.

Submissions are accepted for processing on the understanding that they will be reviewed and that they have not been submitted for publication elsewhere (including publication as a full paper or extended abstract as a part of Conference Proceedings). The JNSF does not accept manuscripts that have already been submitted to pre-print servers.

Suggesting potential reviewers by authors

The authors may suggest up to three names of referees when submitting their manuscript, in the Cover Letter space provided at the bottom of the page in the first stage of online submission. Referees should not be from the institution where the work was carried out and should not have been co-authors in previous publications. The address, institutional affiliation and e-mail of the suggested referees should be supplied. Please note that the JNSF is not bound to select all or any of the suggested referees for sending the manuscript for reviewing

Authorship

All authors designated as authors should be eligible for authorship. Those who have made a substantial contribution to the concept or design of the work; or acquisition, analysis or interpretation of data are recognized as Authors.

The corresponding author should be prompt and ensure adherence to timelines when responding to requests, queries and recommendation of reviewers conveyed by or on behalf of the Editor-in Chief and Editorial Board.

Supplementary materials

Any experimental data necessary to evaluate the claims made in the paper but not included in the paper should be provided as supplementary materials. Supplementary materials will be sent to the reviewers and published online with the manuscript if accepted. The supplementary materials should conform to Journal guidelines and should be uploaded as separate files. Authors should number Supplementary Tables and Figures as, for example, 'Supplementary Table S1'. Refer to each piece of supplementary material at the appropriate point(s) in the main article. Supplementary Materials may include description of the materials and methods, controls, or tabulated data presented in Tables or Figures, and programming codes.

Peer review

The manuscripts submitted to the JNSF will initially be screened by the Editorial Board and, if suitable, will be referred to at least two subject experts in the relevant field. The peer-review process of the JNSF is double-blind.

When revision of a manuscript has been requested, the revised manuscript should be submitted on or before the stated deadline. If the revised manuscript is not received on time, the manuscript will not be processed further. The authors' response to the comments of referees should be tabulated with the comment, response and the line number/s for reference. The decision of the Editorial Board shall be final.

Accepted papers are subject to editing. The date of acceptance will be the date when the Editorial Board has decided it to be acceptable for publication.

Article publication fee

A total of US$ 250 will be levied for each accepted manuscript for publication, except when the corresponding author is affiliated to a Sri Lankan Institute, in two stages as explained below.

- A processing fee of US$ 20 will be levied for each manuscript at peer-review stage and the remaining US$ 230 will be charged for accepted manuscripts at the time of publication.

Payments can be made online via NSF Payment Portal (http://pg.nsf.gov.lk/)

Authors' declaration

When an article is accepted for publication, the authors are required to submit the Authors' Declaration signed by all the authors.

Copyright

Articles in JNSF are published under the Creative Commons License CC-BY-ND. This license permits use, distribution and reproduction of articles for commercial and non-commercial purposes, provided that the original work is properly cited and is not changed in anyway. The copyright of the article is with the National Science Foundation of Sri Lanka. Therefore, authors are requested to check with institution's copyright and publication policy before submitting an article to the JNSF. Authors secure the right to reproduce any material that has already been published or copyrighted elsewhere. When an article is accepted for publication, the authors are required to submit the Transfer of Copyright document signed by all the authors.

Post-publication corrections

The Editorial Board reserves the right to take action on publishing an erratum or corrigendum. If serious errors are identified in a published article, the Journal may consider a retraction or publishing a correction.

STRUCTURE OF MANUSCRIPT

Manuscript

The manuscript should be free of errors and prepared in single column, using double-spaced text of Times New Roman 12 font throughout with line numbers, leaving at least 2 cm margins on both sides, and liberal spacing at the top and bottom of each page. Pages should be numbered consecutively.

a. Style

The paper should be written clearly and concisely. The style of writing should conform to scholarly writing. Slang, jargon, unauthorized abbreviations, abbreviated phrasings should not be used. In general, the impersonal form should be used. Poor usage of language will result in rejection of the manuscript during initial screening.

b. Layout

Manuscripts other than review articles should be generally organized as follows: Title, Abstract, Keywords, Introduction, Methodology, Results and Discussion, Conclusions and Recommendations (where relevant), Acknowledgements and References. Pages should be arranged in the following order:

Title page should include the title of manuscript, and no author information should be mentioned in the title page. If a major part of the research has been published as an abstract in conference proceedings, it should be cited as a footnote on the title page. Authors must also indicate the **general and specific research area** of the manuscript in the title page. In order to highlight the significance of the manuscript, authors are required to provide the following highlights in brief. (1) Why was this study conducted? (2) What are the new findings? (3) Possible applications of the findings. Please limit your answers to 25-30 words for each.

Title: Should accurately and concisely reflect the contents of the article.

Running title: Should be a shortened title (limited to a maximum of 50 characters) that could be printed at the top of every other page of the Journal article.

Abstract: Should be between 200 - 250 words for full length articles and written as a single paragraph. It should not contain any references and should be able to stand on its own. It should outline objectives and methodology together with important results and conclusions. A Review Article should carry a summary of not more than 300 words.

Keywords: Include a maximum of six keywords, which may include the names of organisms (common or scientific), methods or other important words or phrases relevant to the study.

Introduction: This should state the reasons for performing the work with a brief review of related research studies in the context of the work described in the paper. Objectives of the study should be clearly stated.

Materials and Methods: This section should give the details of how you conducted your study. New methods may be described in detail with an indication of their limitations. Established methods can be mentioned with appropriate references. Sufficient details should be included to allow direct repetition of the work by others. Where human subjects are involved, they should be referred to by numbers or fictitious names. A paper reporting the results of investigations on human subjects or on animals must include a statement to the effect that the relevant national or other administrative and ethical guidelines have been adhered to, and a copy of the ethical clearance certificate should be submitted. Methods of statistical analyses used should be mentioned where relevant.

Results and Discussion: Results: the results should be concisely and logically presented. Repetition of the same results in figures, tables or text should be avoided.
Discussion: data essential for the conclusions emerging from the study should be discussed. Long, rambling discussions should be avoided. The discussion should deal with the interpretation of results. It should logically relate new findings to earlier ones. Unqualified statements and conclusions not completely supported by data should be avoided.
Molecular sequence data, such as gene or rDNA sequences, genome sequences, metagenomic sequences etc. must be deposited in a public molecular sequence repository, such as GenBank, that is part of the International Nucleotide Sequence Database Collaboration (INSDC). The accession numbers obtained must be cited in the text, Table or on Figures of phylogenetic trees of the manuscript.

Conclusion: The conclusion should be brief, highlight the outcomes of the study and should be aligned with the objectives of the study. It should not contain references.

Conflict of interest statement: All authors should include a statement on conflict of interest disclosing any financial or other substantive conflicts of interest that may be construed to influence the results or interpretation of their research. All sources of financial support for the project should be disclosed.

Acknowledgement: Should be brief and made for specific scientific, financial and technical assistance only. If a significant part of the research was performed in an institution other than in those indicated by the authors' affiliations given in the title page, this fact should be acknowledged. All those who have made substantial contribution to the research but do not qualify to be authors should be acknowledged.

***References* :**
The JNSF uses APA (7th Edition) reference style from July 2024
All research work of other authors, when used or referred to or cited, should be correctly acknowledged in the text and in the References.
All the references in the text should be in the list and vice versa

Citing references in the text:
- References to the literature must be indicated in the text and tables as per the Author-Year System, by the author's last name and year, in parenthesis (i.e. Able, 1997) or (Able & Thompson, 1998).
- Citation to work by more than two authors should be abbreviated with the use of et al. (i.e. Able *et al*., 1997).
- Multiple publications by the same first author in the same year should be coded by letters, (i.e. Thompson, 1991a, 1991b,1992,1993).
- Multiple citations of different authors should be made in chronological order and separated by a semicolon, (i.e. Zimmerman *et al*., 1986; Able *et al*., 1997).

Citing references in the List of references:
- The list of References should be arranged in alphabetical order based on the last name of the first author.
- In APA 7th ed., **up to 20 authors** should be included in a reference list entry. Write out the last name and first initial(s) for each contributor.

   Example for 2–20 authors:

   Wright, A., Komal, G., Siddharth, D., Boyd, G., Cayson, N., Beverley, K., Travers, K., Begum, A., Redmond, M., Mills, M., Cherry, D., Finley, B., Fox, M., Ferry, F., Almond, B., Howell, E., Gould, T., Berger, B., Bostock, T., & Fountain, A. (2020). Styling royalty. London Bridge Press.

- For references with more than 20 authors, after listing the 19th author replace any additional author names with an ellipsis (…) followed by the final listed author's last name and first initial(s).

   Example for 21+ authors:

   Kalnay, E., Kanamitsu, M., Kistler, R., Collins, W., Deaven, D., Gandin, L., Iredell, M., Saha, S., White, G., Woolen, J., Zhu, Y., Chelliah, M., Ebisuzaki, W., Higgins, W., Janowiak, J., Mo, K.C., Ropelewski, C., Wang, J., Leetmaa, A., … Joseph, D. (1996). The NCEP/NCAR 40-year reanalysis project. Bulletin of the American Meteorological Society, 77(3), 437-471. http://doi.org/fg6rf9

- All the initials of the author must be given after the last name and the year of publication should follow in parentheses.
- This should be followed by the full title of the referred publication.
- When journal articles are listed, the journal name should be given in full and in italics and followed by the volume number, issue number in parentheses and then the inclusive pages.
- Where there are several publications by the same author(s) and published in the same year they should be differentiated by adding a lower-case letter after the year.

   Example

   Clarke, P. N., & Fawcett, J. (2014a). Life as a mentor. *Nursing Science Quarterly*, 27(3), 213-215. https://doi.org/10.1177/0894318414534 492
   Clarke, P. N., & Fawcett, J. (2014b). Life as a nurse researcher. *Nursing Science Quarterly*, 27(1), 37-41. https://doi.org/10.1177/08943 18413509708

- Digital object identifiers (DOIs) should be included for all references where available.

Details about this reference style can be obtained from below links
- https://apastyle.apa.org/style-grammar-guidelines/references
- https://apastyle.apa.org/style-grammar-guidelines/references/examples
- https://libguides.jcu.edu.au/apa

Abbreviations and Symbols: Unless common, these should be defined when first used, and not included in the abstract. The SI System of units should be used wherever possible. If measurements were made in units other than SI, the data should be reported in the same units followed by SI units in brackets, e.g. 5290 ft (1610 m).

Formulae and Equations: Equations should be typewritten and quadruple spaced. They should be started on the left margin and the number placed in parentheses to the right of the equation.

Nomenclature: Scientific names of plants and animals should be printed in italics. In the first citation, genus, species and authority must be given. e.g. *Borassus flabellifer* Linn. In latter citations, the generic name may be abbreviated, for example, *B. flabellifer* L.

Tables and figures: Tables and Figures should be clear and intelligible and kept to a minimum, and should not repeat data available elsewhere in the paper. Any reproduction of illustrations, tabulations, pictures etc. in the manuscript should be acknowledged.

Tables: Tables should be numbered consecutively with Arabic numerals and placed at the appropriate position in the manuscript. If a Table must be continued, a second sheet should be used and all the headings repeated. The number of columns or rows in each Table should be minimized. Each Table should have a title, which makes its general meaning clear, without reference to the text. All Table columns should have explanatory headings. Units of measurement, if any, should be indicated in parentheses in the heading of each column. Vertical lines should not be used and horizontal lines should be used only in the heading and at the bottom of the table. Footnotes to Tables should be placed directly below the Table and should be indicated by superscript lower case italic letters ([a], [b], [c], etc.).

Figures: All illustrations are considered as figures, and each graph, drawing or photograph should be numbered consecutively with Arabic numerals and placed at the appropriate position in the manuscript. Any lettering to appear on the illustrations should be of a suitable size for reproduction and uniform lettering should be used in all the Figures of the manuscript. Scanned figures or photographs should be of high quality (**300 dpi**), to fit the proportions of the printed page (12×17 cm). Each figure should carry a legend so that the general meaning of the figure can be understood without reference to the text. Where magnifications are used, they should be stated.

Units of measurement

Length: km, m, mm, μm, nm

Area: ha, km^2, m^2
Capacity: kL, L, mL, μL
Volume: km^3, m^3, cm^3
Mass: t, kg, g, mg, μg

Time: year(s), month(s), wk(s),

d(s), h, min, s
Concentration: M, mM, N, %,
 g/L, mg/L, ppm
Temperature: °C, K
Gravity: x g

Molecular weight: mol wt

Others: Radio-isotopes: 32P
Radiation dose: Bq
Oxidation-reduction potential: rH
Hydrogen ion concentration: pH